SAPIENZA
UNIVERSITÀ DI ROMA

Sapienza University of Rome

Department of Mechanical and Aerospace Engineering
PhD in Aeronautical and Space Engineering

Thesis For The Degree Of Doctor Of Philosophy

Experimental data-driven reduced-order modeling of nonlinear vertical sloshing for aeroelastic analyses

Thesis Advisor
Prof. Franco Mastroddi

Candidate
Marco Pizzoli
1463683

Academic Year MMXIX-MMXXII (XXXV cycle)

"These days even reality has to look artificial."
- James G. Ballard, Kingdom Come

Abstract

This thesis focuses specifically on the study of nonlinear sloshing effects caused by large tank motions in a direction perpendicular to the free liquid surface with emphasis on aeronautical applications. Sloshing is a phenomenon that typically occurs in aircraft tanks as they are subjected to loads caused by gusts, turbulence and landing impacts. This type of sloshing leads to a noticeable increase in overall structural damping, yet it is generally not modeled in the design phase of modern aircraft. The identification and study of such dissipative effects may enable the development of less conservative aircraft configurations in the future, allowing for increasingly lighter structures and reduced environmental impact. The present thesis proposes a combined experimental and numerical approach aimed at obtaining reduced-order models for vertical sloshing, to be subsequently integrated into aeroelastic modeling and applications for the assessment of their effects on overall performance. An experimental campaign is first carried out to characterise the nonlinear dissipative behaviour of vertical sloshing for different filling levels. Specifically, a controlled electrodynamic shaker is employed to provide vertical displacement by means of sine-sweep excitation. By exploiting vertical harmonic motion, it is shown how the frequency and amplitude of the imposed excitation significantly influence the dissipative capabilities of the sloshing liquid. The same experiment is used to create a database - with an acquisition phase that considers vertical sloshing as an isolated system - to build a neural-network-based reduced-order model. The dynamics to be modeled is considered as a black box process, leading to the identification of a surrogate model driven only by input/output signals, regardless the knowledge of the internal dynamics. In order to assess the capability of the identified reduced order model for sloshing, the same tank used to generate the training data is mounted at the free end of a cantilever beam to create a new experimental setup in which a fluid-structure interaction scenario is expected. Indeed, this experiment provides experimental data for the validation of the identified dynamic model by comparison with numerical data. The comparison is carried out using a dynamic virtual simulation model corresponding to the experiment, in which the numerical model of the beam interacts with the reduced-order model simulating the sloshing dynamics. Finally, the experimentally validated reduced-order model is used in two different aeroelastic applications - wing prototype and flying wing model - to finally predict the dissipative effects induced by vertical sloshing on the aeroelastic response. Aeroelastic response analyses under pre- and post-critical conditions showed how the vertical sloshing dynamics helps to alleviate the dynamic loads due to severe gusts while providing limit cycle oscillation beyond the flutter margin.

Keywords: Vertical Sloshing, Nonlinear Reduced Order Models, Neural networks, Experimental Tests, Aeroelastic response, Flexible Aircraft.

Contents

List of Figures

List of Tables

Summary of the thesis

Large passenger aircraft are generally subjected to a wide range of loads during flight and ground operations that cause significant deformation of the wings, especially during the most severe loading phases. This can lead to sloshing of the fuel stowed in the wing tanks, whose weight is comparable to that of the structural components. The standard engineering practices for aircraft design do not consider the effect of the fuel movement within the wing tanks for the determination of the aircraft design loads. The typical aircraft development cycle includes two major tests for the identification and validation of the dynamic characteristics of the aircraft structure: Ground Vibration Test (GVT), which is performed before the first flight (the aircraft is made to vibrate by mechanical means so that its structural behaviour, including damping, can be measured) and Flutter Flight Test (FFT), usually performed via prescribed oscillatory motion of the aircraft control surfaces when flying at speed close to the design envelope of the aircraft. However, these qualification tests are usually held after the architecture of the fuel tank has reached an advanced design stage, thus severely limiting the amount of changes that can be made.

This thesis is framed within the H2020 project SLOshing Wing Dynamics (SLOWD), which studies fuel sloshing as a method to reduce loads in aircraft wings by increasing effective damping. It also aims to identify structural parameters for maximizing fuel slosh-induced damping to overcome the main shortcomings of current industrial practices: unnecessary conservatism in calculating design loads (resulting in oversizing the structure) and maximizing the benefits associated with slosh-induced dissipative effects. Preliminary work by some project partners (Ref. [1]) has indeed shown that sloshing promotes an overall increase in response damping characteristics for a cantilever beam on which tanks are mounted (made to emulate an isolated half-wing model).

The main objective of the thesis is to adopt an integrated multidisciplinary approach that has attention on the energy dissipation effects associated with fuel sloshing within aircraft tanks and thus assess their effects on overall aeroelastic stability and response under maneuvering conditions. This is accomplished by carrying out four distinct activities in accordance with the objectives of the project:

- Experimental characterisation of sloshing dissipative behavior in scaled tanks.

- Development of Reduced Order Models (ROMs) for sloshing based on high-fidelity data collected through experimental testing.
- Validation of identified ROMs with experimental tests that explore the interaction between sloshing and structural dynamics.
- Integration of sloshing ROMs into aeroelastic systems (such as commercial wing prototypes or research aircraft) in order to evaluate the effects of stowed fluid movement on stability and response to external loads.

Sloshing in aeronautical applications: a literature review

The term sloshing refers to any movement of the free liquid surface inside its tank. This phenomenon is caused by any disturbance applied to a partially filled tank. The sloshing problem generally involves estimating the hydrodynamic pressure distribution, forces and moments exerted by the liquid on the internal walls of the tank. Depending on the type of excitation received by the tank - in terms of intensity and/or direction relative to the walls, the motion of the liquid can occur in different ways including planar, rotational, symmetric, chaotic and many more. Thus, it is possible to distinguish different types of sloshing. In

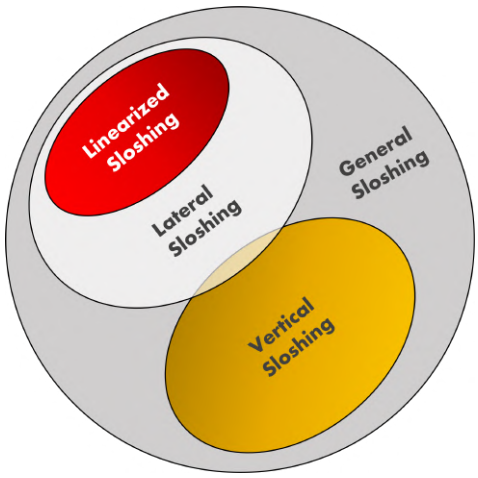

Figure 1: Classification of sloshing dynamics

order to facilitate the understanding and modeling of this complex dynamic, a classification of sloshing has been defined according to the type of motion exhibited by the free liquid surface and the direction along which the tank is excited (see Fig. 1). The first defined category is *vertical sloshing*, which occurs as a result of tank motion perpendicular to the plane of the liquid free surface, *i.e.*, parallel to the gravity force direction. The second is referred to as *lateral sloshing* and is related to latero-rotational motions of the tank. Depending on tank

motion magnitude, the internal dynamics of the liquid may be more or less violent, to the point of exhibiting highly nonlinear behaviour. This can cause the two defined sloshing categories to merge into a small region representing those situations in which the nonlinearities combine the behaviour one would individually expect from each. A further category within lateral sloshing is also defined, whereby the free surface of the liquid is *linearised* on the basis of the application of small lateral or rotational tank excitations. It is possible in this case to estimate the natural frequencies of the liquid free surface since the small perturbations that move the tank do not cause its fragmentation. In fact, surface motion can ideally be represented as a combination of sloshing modes having their own natural frequencies.

The one that is mainly treated in the present thesis is the nonlinear vertical sloshing in rigid tanks. It is a phenomenon induced by high vertical acceleration of the tank, that is, perpendicular to the free liquid surface and parallel to the direction of the gravitational field. At very low excitation levels, the free surface tends to remain flat and not break. By increasing the level of vertical acceleration some fluid modes can become unstable depending on the oscillation frequency (Refs. [2–5]). It is indeed possible to define sloshing modes also for the vertical category, however they can only occur by directly perturbing the free surface of the liquid and not the tank from the outside. This is a nonlinear sloshing effect that is related to so-called Faraday waves (Ref. [6]). They refer to nonlinear standing waves, which appear on liquids enclosed by a tank excited vertically with a frequency, close to twice the natural frequency of the free liquid surface (parametric resonance). Mathieu's equations mathematically manage to describe this effect, presenting solutions that can be stable or unstable depending on the excitation parameters and the type of liquid (Ref. [7]). The boundaries of stability are usually given in a chart known as Ince–Strutt diagram (Ref. [8]). These boundaries are set at excitation frequencies corresponding to subharmonics (twice the natural sloshing frequency) or harmonics (equal to the modal sloshing frequency) and enclose regions of instability. Outside these regions, the free liquid surface is stable. Nonlinearities also generate fluid fingers that can reach the ceiling of the tank. By increasing the level of acceleration even more, the transition to a completely chaotic regime takes place. Indeed, higher values of vertical acceleration trigger Rayleigh-Taylor instabilities (Refs. [3, 9]), determining a chaotic flow regime with air/liquid mixing. At this level of excitation, coherent structures related to the sloshing modes are no longer recognised due to free surface fragmentation. Moreover, turbulence, impacts with the tank ceiling, and continuous free surface generation (surface tension effect) are responsible for additional energy dissipation, which does not depend on resonances with sloshing modes as is the case with Farady waves (Refs. [10–13]). The overall interaction of elastic potential energy of the structure containing the fluid and fluid energy lead to a noticeable increase in the effective damping of the motion of the structure interfacing with the sloshing tank. The energy dissipation occurs due to the phase shift between the sloshing forces when the fluid impacts on the tank roof and the movement imposed on the tank, and

its amount is interpreted to be mainly linked to the intensity of the impacts. More in details, filling level and surface tension seem to play a key role to this behaviour, since affect the relative acceleration of the floating fluid droplets can reach with respect to the tank walls, thus exchanging momentum with the container. This suggests that, when the tank is set on motion with high accelerations, the characteristic length to be considered for vertical slosh dynamics is the tank height rather than the lateral dimension as in traditional sloshing analyses. Nonlinear vertical sloshing can thus be considered a kind of energy sink. When a tank is vertically excited with harmonic motion, it can be evidenced that the induced dissipation depends strongly on both the *amplitude* and *frequency* of the imposed motion. This is also supported by an experimental study conducted in this thesis (and published in Ref. [14]) that investigated the dissipative behavior of vertical sloshing by considering a small sized tank set in harmonic motion by an electromechanical shaker.

Sloshing can be characterised by other nonlinear effects - not considered in this thesis - that are not necessarily related to vertical motion. Among these it is worth mentioning *rotary sloshing*, a type of dynamics that modifies the tank response and may cause instabilities of the tank walls (Refs. [15, 16]) and sloshing induced by g-Jitter that are typically encountered aboard a spacecraft in micro-gravity condition (Ref. [17]). Liquid propellant sloshing dynamics can also have a significant influence on the stability and controllability of launchers and satellites (see Ref. [18]). In this context, Ref. [19] introduced a nonlinear sloshing damping factor to obtain prediction of the limit cycles oscillations magnitude due to adverse control-slosh interaction in liquid propelled space vehicles. Nonlinear sloshing effects plays an important role in naval applications, where extremely high impact pressures can occur on the tank walls in gasoline tankers and ship cargo tanks (Ref. [20]). Vertical sloshing is, however, the most interesting for aeronautical applications since the external loads typically acting on these structures cause a motion of the wing tanks that has a dominant component in the direction orthogonal to the free surface of the stowed fuel, because the typical perturbations occurring on a flying aircraft are of such nature. Thus, this dominant category does not allow the description of local tank rotations due to wing bending, as well as centrifugal effects due to shortening. (which, although irrelevant at the level of fluid-structure interaction for small perturbations, can generate effects on a fluid stowed on the tank Ref. [21]). Furthermore, the above effects are negligible if a box-shaped tank is considered, as it is the case adopted in the present thesis.

Linearised lateral sloshing is also considered in the thesis, but without the modeling that will be devoted exclusively to vertical sloshing. In fact, the effects of this linearised dynamics in aeroelastic applications will be evaluated using descriptive models already existing in the literature. This sloshing dynamics will be considered together with the vertical one in the reduced order description, assuming that they are decoupled and their effects can be summed directly. In other words, the total sloshing force will be defined as the sum of the forces

associated with the two phenomena. Indeed, the motion of the liquid free surface favours a coupling between the first sloshing modes and the dynamics of the structure interfacing with the tank. Nevertheless, the rigid tank assumption allows coupling effects related to possible walls deformations to be neglected (Refs. [22, 23]). In fact, in aeronautical applications, fluid lateral motion can cause the early onset of flutter instability. Studies on the effects of lateral sloshing on the aeroelastic behaviour of aircraft can be found in Ref. [24], where the lateral sloshing is modeled via mass-spring-damper mechanical model, in [25] where an hydroelastic added-mass model is used, in [26] where a Linearised Frequency Domain (LFD) approach is employed, and in [27] where the an Equivalent Mechanical Model for sloshing is used by showing the effects on aeroelastic and flight mechanics stability as well. The reduced-order model used to describe linear sloshing in the present thesis relies on the analytical formulation provided in Ref. [2] and its further development in Ref. [15], according to which a realistic representation of linearised liquid dynamics inside containers with simplified geometry can be approximated by an equivalent mechanical model, whose parameters can be suitably related with the physical quantities obtained from the linearised potential flow theory (Ref. [28]).

Methodology, objectives and activities description

The present thesis exploits a combined experimental and numerical approach to *i)* characterise nonlinear vertical sloshing, *ii)* model it by obtaining surrogate models with a reliable level of accuracy and *iii)* study its effects in aeroelastic applications through the modular integration of different acting dynamics. Thus, the study of nonlinear vertical sloshing is focused on two main aspects: characterisation and modeling. The first problem is primarily aimed at understanding the physics behind the phenomenon and focusing its dissipative characteristics. The second aspect is fundamental allow the integration of the developed sloshing model with the flying-aircraft system. Indeed, the aim is to identify nonlinear reduced-order models (ROMs) of vertical sloshing to be subsequently integrated into numerical simulation models to allow the study of the effects on the global response of the system.

Figure 2 summarises in a diagram the logic behind the approach adopted during the development of the work, highlighting the timing of each activity - defined by the vertical arrow pointing downwards. The left-hand side of the diagram highlights the experiments developed with the main purpose of studying vertical sloshing. While on the right-hand side are the activities related to numerical modeling and the applications studied. It is important to specify that the experimental and numerical analyses are strongly connected by the choice to perform data-driven modeling. As will be described later, experimental tests have in fact a dual role in this work. They are a tool for investigating the physics of the phenomenon and they allow to collect high-fidelity data for the identification of a digital-twin to be used in aircraft integrated numerical simulations.

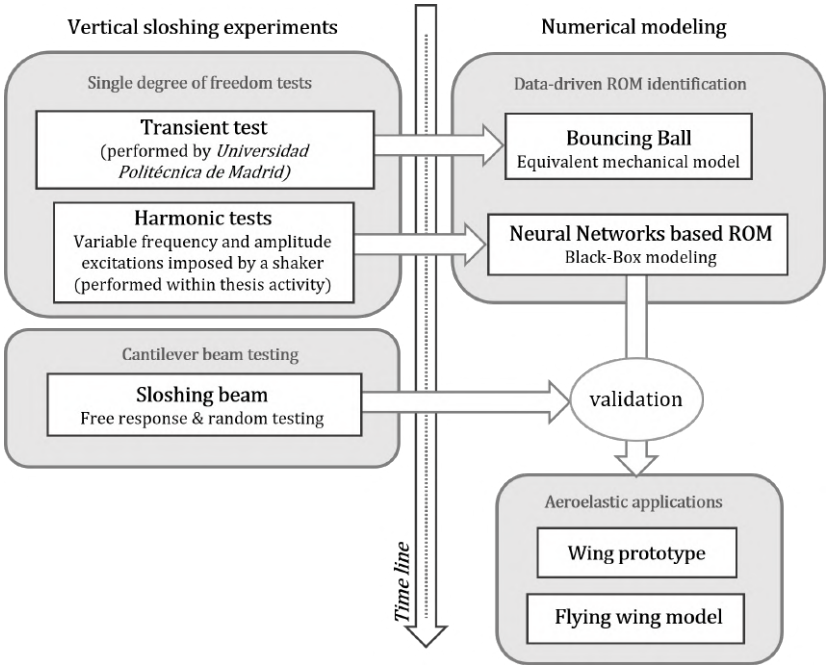

Figure 2: Thesis flowchart

According to the schedule of the SLOWD project, the thesis activity was focused on obtaining a reduced order model for vertical sloshing. In particular, the baseline modeling request was ensuring that the same dissipative behavior of vertical sloshing is accurately reproduced. This can be achieved only after experimental or numerical analyses - with high-fidelity computational fluid-dynamic (CFD) simulations - designed to fully characterise the physics to be modeled by identifying the damping induced to the system. Some members of the SLOWD consortium designed experiments to reduce the complexity of the analysis and isolate the vertical component of sloshing motion (Refs. [29, 30]). These experimental tests aimed to satisfy two main objectives: first, to create a complete database to test numerical models to be developed within the project and, secondly, to understand the complexity of liquid sloshing in the context where turbulence and violent impacts have a dominant role. Within the SLOWD project, numerical analyses on vertical sloshing were also conducted. In particular, multi-physics interface tools are presented in Refs. [31, 32] to accurately describe the coupling between structural dynamics and sloshing. These tools are capable of performing analyses by coupling structural finite element solvers with sloshing CFD solvers based on volume-of-fluid (VOF) or smoothed particle hydrodynamics models (SPH). These two methodologies were respectively tested in Refs. [33, 34] and Refs. [35–37]), with the aim of obtaining reliable numerical tools for the prediction of violent sloshing loads and the dissipation mechanisms induced by them. Nevertheless, the modeling performed in this initial phase of thesis activity involved acceleration data measured in the sloshing experiment

carried out by one of the project partners in the laboratories of the *Universidad Politécnica de Madrid* (UPM) (see Ref. [29]), as shown in Fig. 2. The experimental facility consists of an elastically scaled single degree of freedom (SDOF) mass-spring system coupled with the slosh dynamics within a hydrodynamically scaled tank. Experimental data were measured in transient tests corresponding to a free response problem to an initial condition. An equivalent mechanical model (EMM) of a *bouncing ball* is then built to emulate the fluid behavior inside the tank - specifically the impacts with the tank wall - and provide a numerical model of a tank isolated from the structure on which it is possible to perform simulations with any kind of excitation and that can be used for multi-disciplinary applications. Existing linear sloshing ROMs in the literature are inherently based on potential fluid theory or small lateral perturbations (see Refs. [2, 23, 28, 38]) and do not provide an estimate of the impulsive forces that nonlinear vertical sloshing dynamics produce. In the framework of the SLOWD project, a bouncing ball model capable to reproduce the impact mechanisms has been proposed also in Ref. [39]. These bouncing ball models provide fast prediction of sloshing forces, but since they are obtained by fitting the induced damping on the free response of a single degree of freedom experimental system, they do not generally provide consistent results when working at frequencies different from those used in their identification.

To refine the characterisation of vertical sloshing, a new experimental campaign was developed by employing a linear actuator to impose a controlled vertical sinusoidal motion on the sloshing system. Compared to the transient case described above, where free vertical vibrations following a step-release are used, there are several advantages of using a linear actuator to study sloshing-induced damping, the most important being: *i)* the ability to focus and isolate a single sloshing mode in a controllable manner, *ii)* the ability to study a sloshing mode of interest under periodically steady-state conditions characterised by harmonic inputs within certain range of the input frequencies and amplitudes and *iii)* the minimisation of the various parasitic effects such as dry friction and spatial motion irregularity. The SDOF experimental harmonic campaign, presented in [14], took place in the structural dynamics laboratory of La Sapienza University in Rome and it was conducted to investigate the dissipative behaviour of the fluid sloshing inside a tank set in vertical motion. A controlled electrodynamic shaker is employed to provide vertical displacement by means of sine-sweep excitation: the considered frequency and amplitude ranges are such to characterise the dissipation introduced by the fluid in conditions of small perturbations (low values of gravity acceleration g) as well as at high accelerations. Under these conditions where the imposed acceleration is high, dissipative phenomena become the most intense as the free surface of the fluid breaks up and impact mechanisms with the tank walls arise. The experiment consist of a box-shaped tank - partially filled with water - with dimensions chosen in order to trigger slamming with the tank roof following Rayleigh-Taylor instabilities. The test design provides that three different filling levels are taken into consideration. The dynamic load at the interface between the

shaker and the tank is measured by two load cell sensors. Thanks to such measures and the acceleration measurements is possible to evaluate the work done by sloshing, which is related to the pressure exerted by the liquid on the tank walls. The exchanged work corresponds to the dissipated energy that vertical sloshing provides during the tank motion. Harmonic test results show that the dissipation induced by sloshing depends strongly and nonlinearly on both the amplitude and frequency of the imposed excitation. Moreover, the filling level plays a key role as it is linked to the path that the fluid droplets must go through to impact the tank ceiling. As the filling level increases, the extent - in the frequency and amplitude domain - of the region in which high values of dissipated energy occur increases. However, the case with the highest dissipation values is the one corresponding to the half-filled tank. The experiment also shows how the acceleration imposed on the tank is the dominant parameter in defining the dissipative behaviour of sloshing. In fact, the dissipation mechanisms is less efficient before and beyond some acceleration values. Comparable results are obtained in Ref. [40], where a similar experiment was carried out by imposing a controlled harmonic motion on the tank with varying frequency and amplitude. This study also shows that sloshing-induced dissipation exhibits a maximum in amplitude and frequency domain before being saturated.

Consequently, from the perspective of modeling, vertical sloshing can not simply be described by means of linear viscoelastic models in which the loss of energy depends only on the oscillation frequency (see Ref. [41]) such as fractional derivatives and finite states for the damping (see Ref. [42]). Similarly, nonlinear models such as the bouncing ball are also unable to model the damping characteristic effectively, given the way they are identified and the strong dependence of the phenomenon on the frequency and amplitude of the imposed motion. Reliable nonlinear predictive models are therefore necessary to simulate the impact the sloshing forces have on the dissipation of the elastic energy.

To obtain a model of this kind, the thesis work explores methodologies for identifying dynamic systems through machine-learning approaches. Machine learning methods can be regarded as *data-driven* optimisation and regression techniques that are ideal for high-dimensional and multi-objective optimisation problems with constraints. Given its wealth of data - collected during every stage of design and testing - aerospace engineering is an ideally suited field for modern data-driven machine learning techniques (Ref. [43]). With an ever-increasing capacity to collect and store data (Ref. [44]), we have entered a new era in which scientific analysis is conducted with data-driven hypotheses. This kind of model discovery becomes a new paradigm (Ref. [45]), which does not replace but complements established modes of theoretical, experimental and numerical investigation.

Machine learning algorithms can be grouped into *supervised* and *unsupervised* learning methods, based on the extent to which the training data is labeled (see Ref. [46]). The supervised approach requires that the training data have labels. In other words, this is equivalent to saying that an input data corresponds to a specific output (also referred to as

target). Unsupervised learning, on the other hand, determines the underlying structure of a dataset without labels. In this thesis, supervised learning algorithms are used with the aim to obtain a parameterized function that maps input data onto outputs, by minimising a loss function built as the difference between targets and model estimates. There are numerous techniques to learn the structure and parameters of these mappings, including linear and nonlinear regression, genetic programming and neural networks (Ref. [47]). In addition, machine learning algorithms can incorporate known physics, such as invariances, symmetries, conservation laws, and constraints. These cases are referred to as *physics-informed* machine learning applications (Ref. [48]).

Vertical sloshing dynamics is considered in this work as a black box process, leading to the identification of a surrogate model by the means of those signals that will be assumed as inputs and outputs regardless the knowledge of the internal dynamics. In addition, the collection of data adequately covering the input space is essential for the model training. Specifically, the same experimental setup designed to characterise dissipation in harmonic motion is used to get experimental data for the identification of a nonlinear ROM that takes advantage of neural networks properties. Artificial neural network (ANNs) can be seen as a parallel distributed processors made up of the so called neurons: simple processing units, having the natural capability of storing accumulated knowledge, and then, make it available for subsequent use. In particular, knowledge is acquired by the network from its environment through a learning process, and then stored by synaptic weights. Neural networks have proven to be a powerful tool in modeling nonlinear systems (Ref. [49–51]). Indeed, they can adequately handle complex high-dimensional input-output mappings (see Refs. [52–55]). According to Refs. [56, 57], neural networks can be used for modeling purposes as a static nonlinear approximator (mapping function) of a dynamic model that also employs a filter bank containing delay lines for the input signals. In other words, in this type of model, the neural network provides an estimate of the output at a certain instant of time, based on the input values at previous instants (regressors). The network can also be fed with the measured or estimated outputs at previous times (through feedback for the latter). Depending on what the mapping function receives as input, different types of models can be defined in the context of system identification. Nonlinear Autoregressive model with eXogenous input (NARX) (see Refs. [52, 58]), Nonlinear Output Error (NOE) model (see Ref. [59]) and Nonlinear Finite-Impulse-Response (NFIR) models (see Refs. [60–62]) are amongst the most popular nonlinear black-box model classes. The first two respectively consider the regressors of the targets and the output estimated by the model itself as additional inputs. Whereas, NFIR models only relies on delayed input values to capture the system dynamics.

Neural networks use is increasingly popular in aeroelastic applications, where complex fluid-structure interactions are expected. References [63–65] proposed a neural network approach to predict unsteady aerodynamics loads for nonlinear aeroelastic analysis.

As for applications where sloshing is involved, Refs. [66, 67] already introduced the use of machine learning theory for real-time prediction of the sloshing loads in cargo containers. A data-driven ROM of the free liquid surface motion is developed in Ref. [68] to reduce the time consumption for reconstruction of fluid dynamics in comparison with the standard viscous-flow methods, by exploring several strategies including proper orthogonal decomposition (POD) (Ref. [69]), locally linear embedding (Ref. [70]) and topological data analysis (Ref. [71]). Real-time predictions of the fluid response are also obtained from a ROM constructed by means of thermodynamics-informed data-driven learning in Ref. [72]. The proposed method infers the constitutive behavior of the fluid from video sequences of the sloshing phenomena. Reference [73] used neural networks to adaptively calibrate the associated damping coefficient of fully-nonlinear liquid sloshing simulation in floating liquefied natural gas (FLNG) tanks. A convolutional neural network (CNN) based methodology (see Ref. [74]) is employed in Ref. [75] for the identification of the noise induced by interactions of fluid inside the tank under various driving conditions of a vehicle. The use of an artificial neural network method is also featured in Ref. [76] to obtain effective prediction of impact loads due to sloshing in an offshore vessel. Reference [77] proposed the use of machine learning surrogates based on recurrent neural networks (RNNs) (outlined in Ref. [78]) to predict both external aerodynamic and sloshing loads for describing the coupled motion of the combined airfoil and fuel tank system. Training data for the RNN identification are generated using high fidelity CFD analysis.

As already mentioned, this thesis uses experimentally measured data to train a neural-network-based dynamic model, selecting the best performing structure after sensitivity analyses (NFIR and NOE structures are selected for this purpose). Specifically, the data-acquisition phase reflects an *open-loop* problem, where the process to be identified - vertical sloshing - is considered as an isolated system that enables to obtain data. The strategy employed to generate data for the training consists in imposing vertical displacements to the tank by means of an electromechanical shaker by slowly varying the frequency and output of the motion. The latter strategy is referred to as *Variable Frequency and Amplitude* (VFA). The neural network based ROM is then validated in a complex fluid structure interaction environment. A new experimental setup is designed in which the same tank used to generate the training data is mounted at the free end of a cantilever beam. This particular set up is referred to as the *sloshing beam problem*, and the experimental data generated for comparison and validation will be provided by free response and random testing. The comparison is carried out using a dynamic virtual simulation model that conforms to the *closed-loop* logic of the experiment, in which the numerical model of the beam interacts with the reduced-order model simulating the sloshing dynamics.

As shown in Fig. 2, the final perspective of the thesis is the integration of the validated sloshing ROM into aeroelastic systems to investigate its effects on the response under pre-

critical and post-critical conditions. To this end, a scaling law is introduced in order to use the identified model also in actual applications which may have tanks with different dimensions. Two different applications are considered: the first, consists of a commercial wing prototype of a single-aisle aircraft, while the second is a flying wing (see Refs. [79, 80]) in which both flight dynamics and aeroelasticity are involved. It is worth noting that the latter also involves the integration of reduced-order models for linear lateral sloshing (see Refs. [2, 15, 28]) to evaluate also the effects on aircraft stability. In particular, it is assumed that sloshing forces can be decomposed into a lateral part with linearised behavior and a vertical part with extremely nonlinear behavior by neglecting their mutual interactions. Numerical modeling is implemented in Simulink®, resulting in a hybrid model that combines a differential linear problem (for aeroelasticity, flight dynamics, and linear sloshing) with a data-driven model (nonlinear vertical sloshing). Response analyses under pre- and post-critical aeroelastic conditions have illustrated how the vertical sloshing dynamics helps to alleviate the dynamic loads following severe gusts while providing limit cycle oscillations beyond the linear flutter margin. In addition, stability analyses for the flying wing have shown how the coupling between linear sloshing and aircraft aeroelasticity and flight dynamics contributes to modify the overall stability scenario.

Outline of the thesis

The development of the thesis activities followed the timeline illustrated in Fig. 2. However, they are presented here using a different logic, with a body of three main chapters devoted respectively to the experimental activity of energy characterisation, the identification of nonlinear reduced-order models for vertical sloshing, and related aeroelastic applications. Supporting appendices are also included. Specifically, the thesis is organised as follows:

In Chap. 1, introduces the vertical sloshing problem for rigid tanks and the analytical procedure for obtaining the forces to which it gives rise. Secondly, the experimental campaign carried out to characterise the dissipative behaviour induced by this phenomenon when the tank is set in harmonic motion with different excitation frequencies and amplitudes is presented. The experimental analysis is performed as the tank filling level varies, in order to show how the amount of dissipation varies with the mass of liquid considered.

In Chap. 2, the data-driven procedures for identifying nonlinear vertical sloshing reduced-order models are presented. The first part is devoted to the so called "bouncing ball", an equivalent mechanical model identified using experimental data from transient tests measured in a single-degree-of-freedom sloshing experiment. The same experiment presented in Chap. 1 is again used to create a database aimed at identifying a nonlinear reduced-order model based on neural networks. The second part of the Chapter then shows the training process of this model together with its validation based on comparison with experimental data. The

latter are measured through a further experiment, in which the same tank used to generate the data is mounted on a cantilever beam to simulate a fluid-structure interaction problem. The final part introduces a numerical procedure to scale up the identified model in order to be able to use it in applications where tanks of different sizes are expected.

In Chap. 3, the neural-network-based ROM is used in two aeroelastic applications to evaluate the effects that vertical sloshing induces on the overall system response. The first case study consists of a commercial wing prototype of a single-aisle class aircraft, while the second is a flying wing. In the latter, the additional effect of lateral linear sloshing is also considered, using equivalent mechanical models already present in the literature (see Appendix D).

In Appendix. A, an analytical overview of linear mechanical systems is given in order to simply introduce the dimensional and non-dimensional quantities with which dissipated energy can be measured.

In Appendix. B, a theoretical background on artificial neural networks with radial basis functions as activation functions is presented.

In Appendix. C, the results of an initial attempt to utilise nonlinear dynamic system identification techniques based on the use of neural networks are shown. In particular, the performance of a neural network trained with low-fidelity data obtained by simulating the bouncing ball in harmonic motion for different frequency and amplitude values is presented.

In Appendix. D, the theoretical background underlying the construction of equivalent mechanical models for sloshing in the case of small lateral or rotational perturbations of the rectangular tank is given.

Appendix. E presents a linearised vertical sloshing model based on the assumption that sloshing forces can be described as viscous damping forces with coefficients that can be derived from experimental sloshing data.

Chapter 1

Experimental characterisation of sloshing tank dissipative behaviour

In this chapter, the general problem of vertical sloshing is first presented, together with the analytical procedure assessing the procedure used to measure the sloshing forces exchanged between fluid and tank. Second, a method for characterising and measuring the dissipation caused by this phenomenon is presented by vibrating the tank that contains the sloshing fluid with a harmonic motion. The results concerning the experimental study of the dissipative behaviour of vertical sloshing are part of the work published in Ref. [14]. The chapter concludes with a discussion on sloshing effective mass concept, which was introduced in Ref. [81].

1.1 Measurement of sloshing force on a rigid tank having harmonic vertical motion

In this section, the problem of vertical sloshing is described in general terms, referring to a configuration involving a rigid tank containing a liquid. In particular, an analytical procedure is defined in order to measure the sloshing forces. When a partially filled tank is set in vibration with a motion perpendicular to its base (considering for simplicity that the shape of the tank is parallelepiped), mechanisms can be triggered that lead the stowed liquid to impact with its internal walls. The pressure generated during impacts will represent the force the liquid exerts on the structure, *i.e.* the sloshing force. The description of vertical sloshing therefore requires a procedure to be defined for the estimation of these actions. The aim is to show how this objective is closely linked to the type of motion imposed on the tank. For this reason, the steady-state harmonic motion is the most suitable to derive a formulation that allows us to estimate the sloshing forces. Figure 1.1 shows a rigid tank, partially filled with a liquid, subjected to vertical motion (*i.e.* perpendicular to the free surface of the liquid).

The stowed liquid is portrayed at one of the moments immediately following the application of motion. This type of shape has been found in several experimental campaigns (See Ref. [82]). The displacement field of the rigid tank is given by:

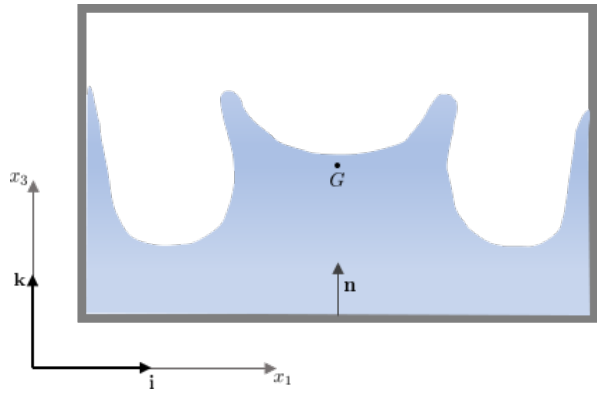

Figure 1.1: Partially filled rigid tank subjected to vertical motion.

$$\mathbf{u}\left(\mathbf{x};t\right)=u\left(t\right)\mathbf{k} \tag{1.1}$$

where $\mathbf{k}$ is the vertical unit vector and $u\left(t\right)$ is an assigned tank time law for the vertical rigid motion. If $\mathbf{x}\in V_t$ (rigid body domain) indicates the position of the tank material point in the reference configuration and V_t the volume tank domain, one has in general

$$\rho\frac{D^2\mathbf{u}}{Dt^2}\left(\mathbf{x};t\right)=\mathrm{div}\mathbf{T}\left(\mathbf{x};\mathrm{t}\right)+\rho\mathrm{g}\mathbf{k} \tag{1.2}$$

where ρ is density of the solid tank material. By integrating the previous expression on the volume occupied by the tank particles and then projecting it on vector $\mathbf{k}$ one has

$$\left[\iiint_{V_t}\rho\frac{D^2\mathbf{u}}{Dt^2}\mathrm{d}\mathcal{V}-\iiint_{V_t}\mathrm{div}\mathbf{T}\mathrm{d}\mathcal{V}-\mathrm{g}\iiint_{\mathrm{V_t}}\rho\mathbf{k}\mathrm{d}\mathcal{V}\right]\cdot\mathbf{k}=0 \tag{1.3}$$

By introducing the mass of the dry tank M and applying the divergence theorem one has:

$$\left[M\ddot{u}\mathbf{k}-\oiint_S\mathbf{t}\mathrm{d}S-Mg\mathbf{k}\right]\cdot\mathbf{k}=0 \tag{1.4}$$

that could be rewritten as:

$$M\ddot{u}-\left[\oiint_S\mathbf{t}\mathrm{d}S\right]\cdot\mathbf{k}-Mg=0 \tag{1.5}$$

where $\mathbf{t}=\mathbf{t}_s+\mathbf{t}_e$ represents the surface forces, whose two contributions are specifically:

- $\mathbf{t}_s = -p\mathbf{n}$ are the surface forces due to the sloshing fluid (p is the fluid pressure; note that no shear forces are assumed on the internal tank walls $\mathbf{t}_s = -p\mathbf{n} + \sigma_{shear}\tau \simeq -\mathbf{pn}$)
- $\mathbf{t}_e$ it is related to the applied external forces: $\iint_S \mathbf{t}_e \cdot \mathbf{k} \mathrm{d}S =: F_{ext}$, where F_{ext} is the vertical applied external force.

Therefore

$$M\ddot{u} + \left[\iint_S p\, \mathbf{n} \cdot \mathbf{k} \mathrm{d}S\right] - Mg = F_{ext}(t)$$

$$M\ddot{u}(t) - F_{S_z}(u(t)) - Mg = F_{ext}(t) \tag{1.6}$$

where F_{S_z} is the vertical sloshing force which depend by the imposed rigid body motion time law $[u(t), \dot{u}(t), \ddot{u}(t)]$. Eq.(1.6) can be rewritten as follows

$$F_I - F_{S_z} - F_G - F_{ext} = 0 \tag{1.7}$$

where $F_I = M\ddot{u}$, $F_{S_z} = -\iint_S p\, \mathbf{n} \cdot \mathbf{k} \mathrm{d}S$, $F_G = Mg$, so highlighting a balancing in vertical direction of the inertial, sloshing, weight and external forces performed on the tank.

As we shall see, in this chapter, an experimental activity will be presented in which the vertical motion $u(t)$ is imposed by means of an elettrodynamical shaker that allows to get $F_{ext}(t)$ as external force ensuring the imposed motion. The work performed by the forces expressed in Eq.(1.7) in the vertical direction z in a time period $[t_1, t_2]$ is given by

$$\int_{z(t_1)}^{z(t_2)} (F_I - F_{S_z} - F_G - F_{ext})\, dz = 0 \tag{1.8}$$

where $dz = \dot{u}\, dt$.
As mentioned above, we use steady harmonic motion to deduce the sloshing force. In this case, the law of motion $u(t)$ imposed on the tank is expressed as follows:

$$u(t) = u_0 \sin(\Omega t) \tag{1.9}$$

where u_0 and Ω represent respectively the amplitude and the frequency of the displacement excitation. The work done by the forces acting on the tank in a generic associated time cycle $T = 2\pi/\Omega$ in a steady harmonic motion could be derived by considering Eq. 1.8, that is

$$\int_t^{t+T} [M\ddot{u}(t) - F_{S_z}(u(t)) - Mg - F_{ext}(t)]\, \dot{u}(t)\, dt = 0$$

$$-\int_t^{t+T} F_{S_z}(u(t))\, \dot{u}(t)\, dt = \int_t^{t+T} F_{ext}(t)\, \dot{u}(t)\, dt \tag{1.10}$$

It should be noted that the work done by the inertial and the weight forces in a generic cycle in steady state harmonic motion are identically equal to zero. Thus, if the work performed by the external forces were measurable, this would be directly the work performed by the sloshing fluid on the tank. The importance of this simple relationship relies in the fact that it shows that the energy dissipated by the sloshing fluid in the left hand side of Eq. 1.10 equals the energy subtracted to a structure interfacing with the tank. The characterisation of this work can thus be referred to as a source of damping for the structure.

1.2 Experimental case study and set-up

A method is now presented to characterise the dissipation caused by vertical sloshing in harmonic motion, exploiting an experimental setup involving a tank dynamically vibrated by a shaker. Given the tank geometry, the quantification of the energy dissipated by the fluid is performed for different values of oscillation amplitudes and frequencies in order to quantify the sloshing nonlinear dissipative behaviour. These two parameters characterise ideal unsteady harmonic boundary conditions that a vertically vibrating structure can impose to the walls of a tank with which it interfaces triggering slosh dynamics. The considered frequency and amplitude ranges are such to characterise the dissipation introduced by the fluid in conditions of small perturbations (low values of g) when Faraday waves occur with a limited dissipative capability as well as at high accelerations with the complete fragmentation of the free surface with the occurrence of intense impacts between liquid and tank ceiling. A proper metric for the definition of dissipative energy is introduced thus mapping the damping introduced by the slosh dynamics corresponding to different filling levels. The proposed metric is inspired by works like the one presented in Ref. [83] where suitable energy maps were used for prediction and control strategies applied to aeroelastic airfoil response to gusts. This experimental campaign took place in the structural dynamics laboratory of the University of Rome La Sapienza.

The experimental testbed is a box-shaped tank made in Plexiglass with a height of $h = 27.2$ mm and base of sides $l_1 = 117.2$ mm and $l_2 = 78.0$ mm. The dimensions are chosen in order to trigger slamming with the tank roof after Rayleigh-Taylor instabilities. The test design provides that three different filling levels featured by $\alpha = h_f/h$ (with h_f the liquid depth) are taken into consideration, *i.e.*, $\alpha = 0.50$ (case 1, reference), $\alpha = 0.25$ (case 2) and $\alpha = 0.75$ (case 3), to which correspond the following non-dimensional liquid depths: $h_f/l_1 = 0.116$ (case 1), $h_f/l_1 = 0.058$ (case 2), $h_f/l_1 = 0.174$ (case 3). The liquid tested in each of the cases listed is water. Table 1.1 provides the sloshing frequencies analytically evaluated for the considered liquid depths for non-ideal fluids (See Ref. [3]). The indices l and m indicate the order modes considering that the modal deflection of the free surface is $S_{l,m}(x, y) = \cos(\frac{l\pi x}{l_1}) \cos(\frac{m\pi y}{l_2})$. For the sake of conciseness only the symmetric modes frequencies are provided in Tab. 1.1.

		Case 1	Case 2	Case 3
		$\alpha = 0.50$	$\alpha = 0.25$	$\alpha = 0.75$
l	m	Sloshing natural frequencies [Hz]		
2	0	2.909	2.179	3.295
0	2	4.093	3.234	4.411
2	2	4.716	3.850	4.972
4	0	5.091	4.240	5.307
4	2	5.984	5.219	6.116
6	0	6.809	6.160	6.886
0	4	6.817	6.170	6.893
2	4	7.079	6.471	7.142
6	2	7.381	6.818	7.432
4	4	7.789	7.285	7.827

Table 1.1: Analytical frequencies of the first ten symmetric sloshing modes for all the considered filling level cases.

The tank is placed over a controlled electrodynamic shaker able to impose vertical sinusoidal displacement starting from a lower frequency of 5 Hz and able to reach 25 mm peak-to-peak displacement amplitude. The dynamic load at the interface between shaker and tank is measured by two PCB 208C03 load cells (See Fig. 1.2), placed in the middle of the long side of the tank base. The overall force exchanged by tank and shaker, that is F_{ext} introduced in Sec. 1.1, is the sum of the two load cells. The system is also equipped with two redundant PCB 352C22 accelerometers placed at the opposite corners of the tank upper closing side and with a control accelerometer used by the shaker sine-sweep controller. The comparison between the data of the accelerometer used for sine-sweep control and the other two over the tank roof confirmed the considered experimental testbed rigidly behaved throughout all the tests carried out.

1.3 Identification of sloshing dissipated energy from frequency sweep excitation

In order to estimate the energy dissipated by the liquid, it is necessary to derive the sloshing forces, *i.e.* those forces that the liquid exerts on the walls of the tank as a result of its vertical dynamic excitation. The identification of the sloshing forces is carried out under sine-sweep excitation regime. The curves showed in Fig. 1.3 illustrate the paths of the frequency-amplitude pairs run through the sine-sweep tests. Specifically the first run starts from O_1 frequency-amplitude point ending at F_1 point (branch $O_1 - F_1$); similar trends are considered for the branches (*i.e.* the runs) $O_2 - F_2$, $O_3 - F_3$ and $O_4 - F_4$. The other branches start from O_4 thus reaching the final points F_5, F_6 and so on, but initially following the dashed line

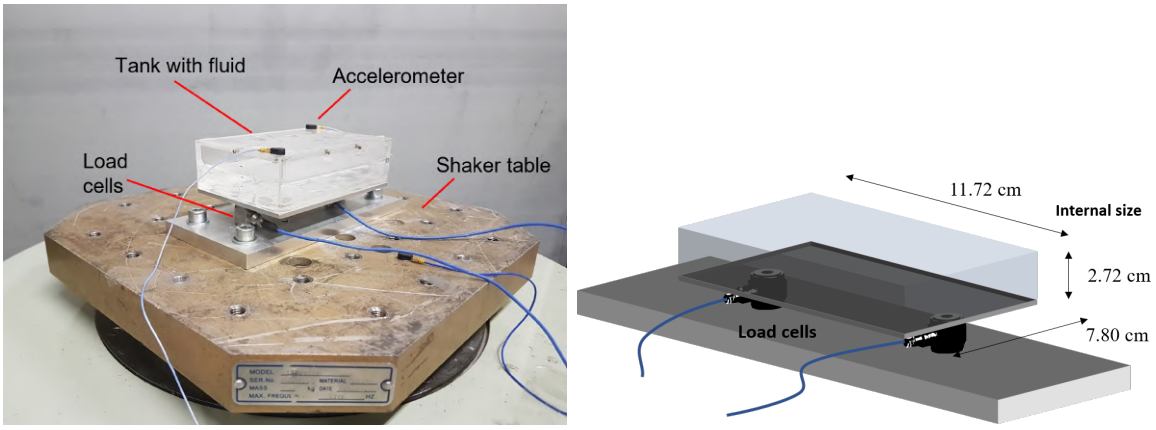

(a) Experimental Set-up (b) Layout

Figure 1.2: Experimental configuration considered for characterising the energy dissipated by vertical sloshing

indicating a displacement of about 12.5 mm due to the aforementioned shaker limits. The right hand side axis indicates the experimental time showing the sweep goes from 5 Hz to 20 Hz in 240 s, where the value of the instantaneous frequency is a function of the time depends on the initial value of the frequency Ω_i and the octave rate R_Ω such that:

$$\Omega(t) = \Omega_i e^{\log 2R_\Omega t} \tag{1.11}$$

As a consequence, once the acceleration amplitude profile $a_0[\Omega(t)]$ is provided, it is possible to get the imposed vertical acceleration

$$\ddot{u}(t) = a_0[\Omega(t)]\cos\big[\phi(\mathrm{t})\big] \tag{1.12}$$

where $\phi(t)$ is the instantaneous phase defined as

$$\phi(t) = \frac{\Omega_i}{\log 2R_\Omega} e^{\log 2R_\Omega t} \tag{1.13}$$

For the evaluation of the work exchanged per unit cycle during the experimental test, we need to find the time domain boundaries of each cycle. This can be identified by finding the time instants t_n such that $\phi(t_n) = 2n\pi$, or considering Eq. 1.13:

$$t_n = \frac{1}{\log 2R_\Omega} \log\left(\frac{\log 2R_\Omega 2n\pi}{\Omega_i}\right) \tag{1.14}$$

By averaging over a user defined number of cycles $2P$ we get the work exchanged by fluid and shaker at any instant t_n:

$$W\big(\Omega(t_n), a_0(t_n)\big) = \frac{1}{2P}\int_{t_{n-P}}^{t_{n+P}} F_{S_z}(\Omega(\tau), a_0(\tau))\,\dot{u}(\tau)\,\mathrm{d}\tau \tag{1.15}$$

The dissipated energy is measured by centering in t_n and averaging in a number of cycles $2P$. However, Eq. 1.15 is evaluated in a subset of time instant t_k with $k = n/M$ where M indicates the number of cycles between a sample and the following (see Fig. 1.4). It is worth pointing out that the ratio between M and $2P$ represents the overlapping between the distance between the t_k points and the width of the window of the integral. In this analysis, the set values of P and M are 6 and 24, respectively. Therefore no overlapping is present among the windows centred at the considered time instants t_k. It should be noted that Eq. 1.15 subtends what was obtained in Eq. 1.10. In fact, in this case, since the motion is harmonic, the work done by the force F_{ext}, measured by the load cells, is equal to the work done by the sloshing forces F_{S_z}. Although the work done by the two forces is the same, they are not exactly equal. Indeed, the sloshing force F_{S_z} is equal to the sum of the signals measured by the load cells (hence, F_{ext}) from which is subtracted the inertial contribution, which in harmonic motion does not contribute to the work, associated with the structural mass resting on the cells (Plexiglass and metal support plate).

The results of the present activity can be also reported in a non-dimensional form. The non-dimensionalised version of the operational parameters introduced in the present analysis, that is the non-dimensional frequency $\bar{\omega}$ and the amplitude of the vertical motion $\bar{u}$ are introduced as it follows:

$$\bar{\omega} = \frac{\Omega}{\sqrt{g/h}} \tag{1.16}$$

$$\bar{u} = \frac{u_0}{h} \tag{1.17}$$

The present definition of the nondimensional frequency comes from the findings (see Sec. 1.4) that sloshing resonances (low acceleration) have little influence on dissipated energy compared to the regime in which the impacts between liquid and tank ceiling occur (high acceleration). In the case of harmonic motion, this non-dimensionalisation makes the product $\bar{u}\,\bar{\omega}^2 = a_0/g$, the main parameter conditioning the possibility of Rayleigh-Taylor instability in the case of an ideal fluid, independent of the geometrical parameters of the tank and fluid depth. Indeed, alternative definitions of non-dimensional frequency (such as normalisation with respect to a reference resonant frequency, see Ref. [84]) would modify the iso-acceleration lines in the domain $\bar{u} - \bar{\omega}$. The non-dimensional work exchanged between the tank and the shaker is

defined as:

$$\bar{W} = \frac{W}{m_l u_0^2 \Omega^2} \tag{1.18}$$

where m_l is liquid mass and the denominator represent a reference energy that can be interpreted as the kinetic energy of the system (by considering just the mass of the liquid). The non-dimensional dissipated energy defined in Eq. 1.18 can also be related to the concept of the loss factor (presented in Appendix A), which allows a metric for dissipation to be defined. It is worth noting that the provided non-dimensional results take into consideration only the operational parameters $\bar{\omega}$ and $\bar{u}$ without considering the dependency of the phenomenon with respect to parameters more addressed to the physics and tank size like free surface effects and viscosity.

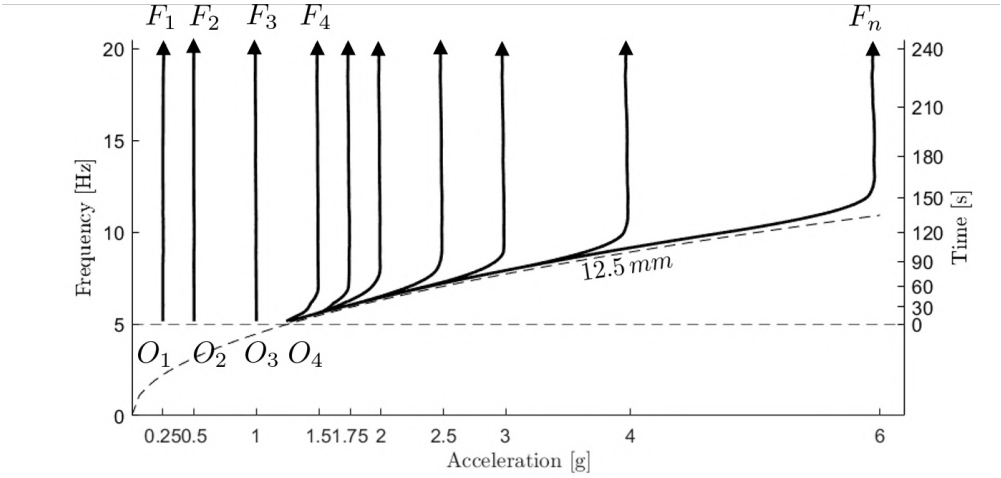

Figure 1.3: Frequency-amplitude pairs spanned during different sine sweep tests.

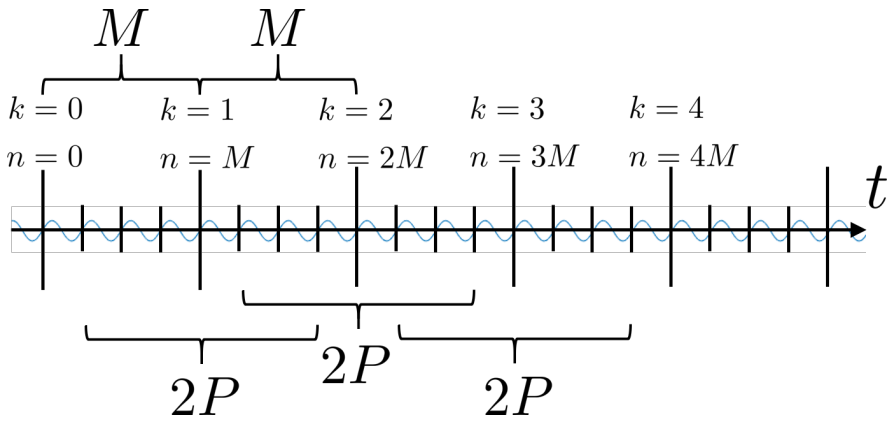

Figure 1.4: Discretization of time and averaging strategy for dissipated energy evaluation.

Point	$a_0(t_k)[g]$	$\Omega(t_k)/(2\pi)$ [Hz]	t_k [s]
1	1.5	9.0	102.3
2	1.5	13.0	166.0
3	1.5	17.0	212.5
4	3.0	9.0	102.3
5	3.0	13.0	166.0
6	3.0	17.0	212.5

Table 1.2: Reference points on which the results are provided.

1.4 Experimental results

Several experimental tests have been carried out which allowed to map the energy dissipated by the fluid for different filling levels on a frequency-amplitude domain. For each of the considered filling levels (*i.e.* , $\alpha = 0.50$, $\alpha = 0.25$ and $\alpha = 0.75$), frequency sine-sweep tests were carried out with acceleration amplitudes between 0.25 g and 6 g (See. Fig. 1.3). The excitation frequency varies, starting from a value of 5 Hz, up to a maximum of 20 Hz, following the time law expressed in Eq. 1.11. Figure 1.5 shows the same result but using the acceleration amplitude instead of the displacement one. The arrows indicate the direction followed by the frequency sweep during the test. The minimum (0.25 g) and maximum (6 g) iso-acceleration curves therefore define the domain where the energy dissipated by the fluid inside the tank is experimentally identified. Furthermore, 6 red dots are highlighted in Fig. 1.5. They are representative of the 6 frequency-amplitude pairs reported in Tab. 1.2 selected to show quantitatively the results in terms of measured sloshing forces and hysteresis cycles.

The dissipated energy is evaluated by considering a time interval centred in the time instant t_k and having as extremes $t_k - P$ and $t_k + P$, where $2P$ is the number of cycles considered, set to 12 (See Fig. 1.4). Thus, in the results that will be hereafter provided, it should be remembered that when referring to the energy dissipated at an instant t_k (and in turn, we are assuming a pair $\Omega(t_k) - a_0(t_k)$) we are not considering a single time instant but we are averaging in a $2P$-wide time interval.

1.4.1 Fluid-dynamics regimes characterisation

This section provides a qualitative characterisation of the different fluid-dynamics regimes. For the sake of conciseness only the reference filling level case $\alpha = 0.50$ is here taken into account. Figure 1.6 shows 12 snapshots of the sloshing behaviour at different values of acceleration and frequency, containing also the same points from Tab. 1.2. In this flow regime, it is hardly possible to relate the sloshing modes in Tab. 1.1 to those in Fig. 1.6, since, the Faraday waves can respond synchronously with the tank displacement as well as at 0.5 and 1.5 of the excitation frequency when the tank is set on vertical motion. Figures 1.6(a) to 1.6(d) refer to

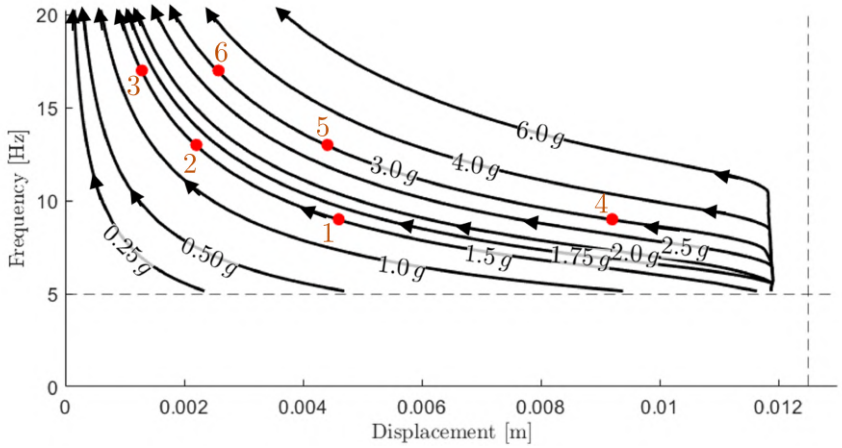

Figure 1.5: Scheme of the runs performed to identify the dissipated energy maps. Six red bullets indicate the reference points presented in Tab. 1.2.

the test with acceleration equal to $0.5\,g$, for frequency values that corresponds respectively to 6, 9, 13 and 17 Hz. For this acceleration value, Rayleigh -Taylor instability is not triggered and, therefore, the liquid does not experience any free surface breakage. Rather we see Faraday waves that are generated inside the tank, that may softly impact the tank ceiling (see Figures 1.6(b) and 1.6(c)). By increasing the frequency, surface tension stabilises the free surface and impacts no longer occur (see Fig. 1.6(d)).

Next, when the acceleration values are further than $1\,g$ we notice the transition to a more chaotic regime of the fluid, where the free surface breaks. This is noticeable in Figures 1.6(e) to 1.6(h), which are related to an acceleration level of $1.5\,g$. In particular, for frequency values equal to 6 and 9 Hz, the fluid violently impacts the tank ceiling and it is no longer possible to identify coherent structures of the fluid (see Figs. 1.6(e) and 1.6(f)). By increasing the frequency, more precisely at 13 Hz, a transition to a new standing waves regime is noticed with impacts occurring with less intensity (see Fig. 1.6(g)). Figure 1.6(h) shows that above a certain frequency value there is no longer presence of impacts. Finally, when the tank is set in motion at high acceleration values (*i.e.* with an acceleration of $3g$, see Figures 1.6(i) to 1.6(l)), the fluid inside the tank behaves chaotically for the whole considered range of frequencies.

1.4.2 Filling level case 1: $\alpha = 0.50$ (reference)

The filling level case $\alpha = 0.50$ is the first case considered in this analysis. Figure 1.7 shows the trend over time of the sloshing forces corresponding to the points highlighted in Tab. 1.2. These data are normalised with respect to the maximum of the corresponding inertial force of the liquid, that is equal to $m_l a_0$. Note that no filtering procedure was used on the measured time signals. The time intervals in which the trend of the sloshing forces is shown are precisely those having an amplitude defined by $[t_k - P, t_k + P]$. Figure 1.8 shows the hysteresis cycles

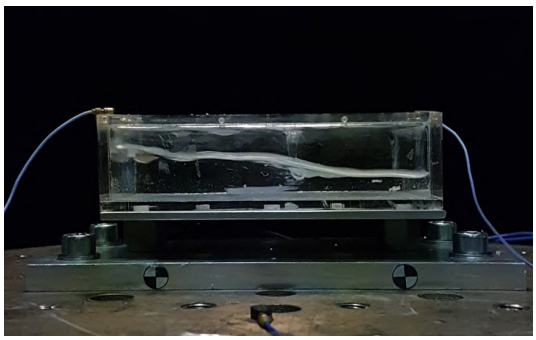

(a) $a_0 = 0.5g$, $f = 6Hz$

(b) $a_0 = 0.5g$, $f = 9Hz$

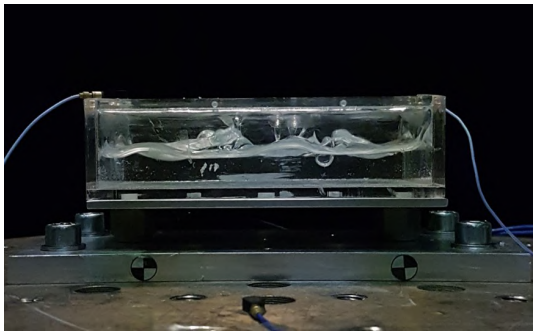

(c) $a_0 = 0.5g$, $f = 13Hz$

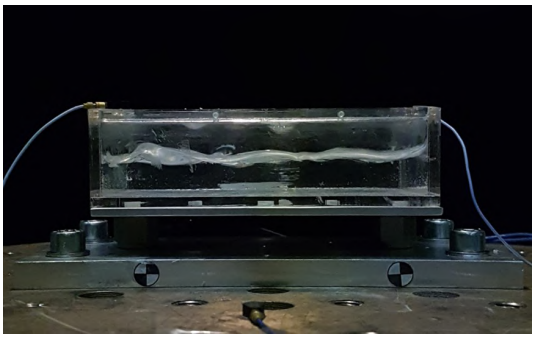

(d) $a_0 = 0.5g$, $f = 17Hz$

(e) $a_0 = 1.5g$, $f = 6Hz$

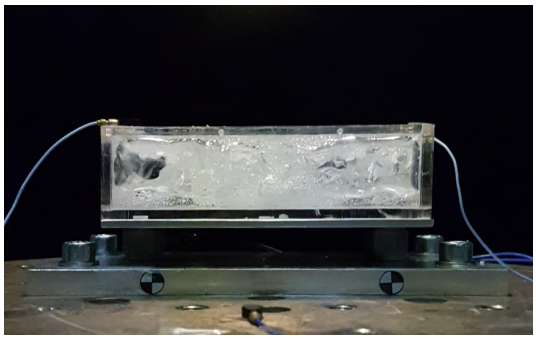

(f) $a_0 = 1.5g$, $f = 9Hz$

obtained by plotting the variation of the sloshing force (normalised with respect to $m_l a_0$) with respect to the harmonic displacement of the tank (that is normalised with respect to the maximum vertical displacement u_0). The area enclosed by the cycles represents the dissipated work at the specific acceleration-frequency pair. It should also be noted that multiple periods are considered in the hysteresis cycle plots. Figure 1.9 shows the trend of the dissipated energy as a function of the frequency sweep for the reference cases with acceleration equal to $1.5g$ and $3.0g$. In particular, the vertical bars in this figure represent the values of the dissipated work evaluated at the selected time intervals centred at t_k (and therefore, at $\Omega(t_k) - a_0(t_k)$). The bars corresponding to the three reference frequencies already indicated above are

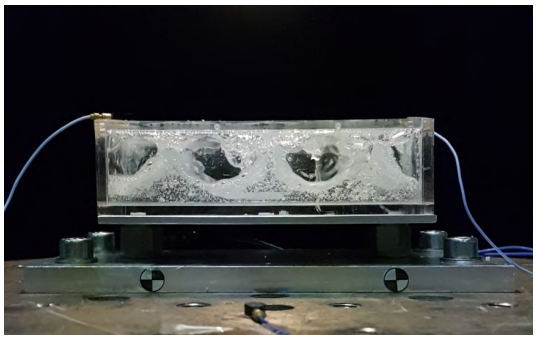

(g) $a_0 = 1.5g,\ f = 13Hz$

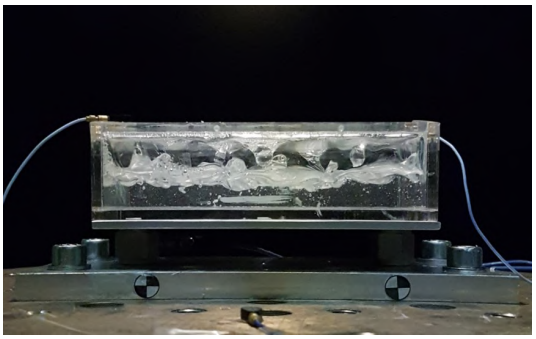

(h) $a_0 = 1.5g,\ f = 17Hz$

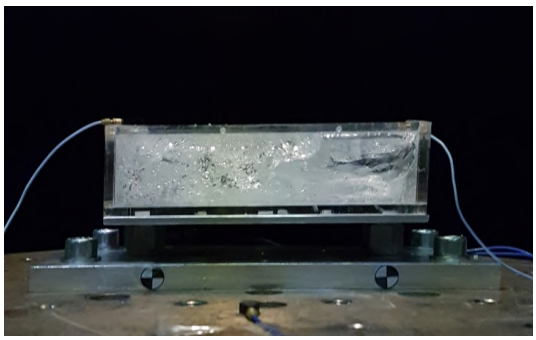

(i) $a_0 = 1.7g,\ f = 6Hz$

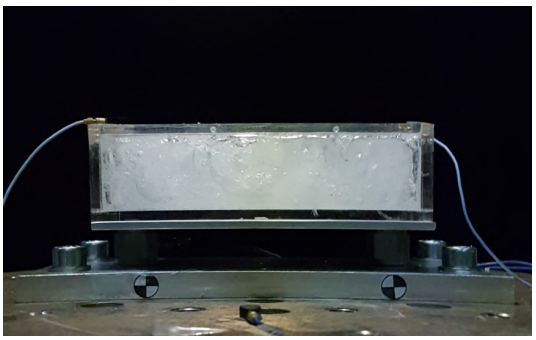

(j) $a_0 = 3g,\ f = 9Hz$

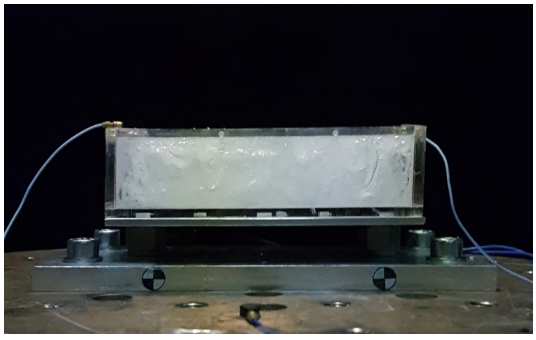

(k) $a_0 = 3g,\ f = 13Hz$

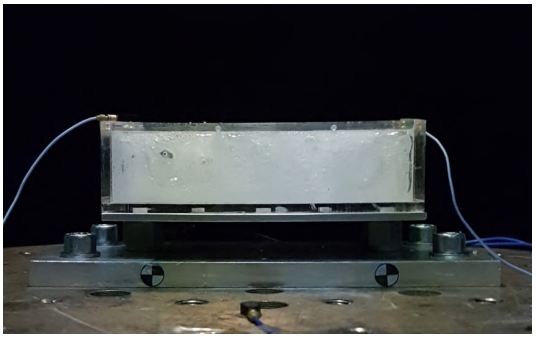

(l) $a_0 = 3g,\ f = 17Hz$

Figure 1.6: Snapshots of the sloshing response at different values of acceleration and frequency for the case $\alpha = 0.50$.

highlighted in red. On the other hand, the dashed orange curve corresponds to the trend of the acceleration amplitude. Note that, the generic bar corresponding to the frequency $\Omega(t_k)$ will be associated to a vertical displacement of the tank equal to $a_0(t_k)/\Omega^2(t_k)$.

By extending this process of evaluating the dissipated energy to all $\Omega(t_k) - a_0(t_k)$ pairs spanned during the experimental tests, an appropriate interpolation of the data based on the radial basis function is performed in order to represent the dissipated energy on a continuous domain as shown in Fig. 1.10. The result of this interpolation allows us to obtain a map of the dissipated energy as a function of frequency and displacement as depicted in Fig. 1.11. The iso-acceleration curves considered for the tests and the six red dots representing the red vertical bars shown in Fig. 1.9 are superimposed on the continuous variation of the energy. The darker regions on the map correspond to the highest values of the dissipated work, while the white regions are those in which the dissipated energy is practically zero. Indeed, in this last region the work done by the sloshing forces is negligible given the lack of Rayleigh-Taylor instability which lead to violent impacts of the fluid with the walls of the tank.

The non-dimensional energy dissipated by the slosh dynamics $\bar{W}$ (as in Eq. 1.18) is represented by means of the maps in Fig. 1.12 (where blue points provides the reference to the snapshots illustrated in Sec. 1.4.1). Both dimensional and non-dimensional axes are depicted for comparison with the dimensional map. The magenta horizontal line in the graph represents the double of the frequency $\omega_{2,0}$ associated with the first symmetrical mode $S_{2,0}$ (see Tab. 1.1). The non-dimensional map assumes very little values at the very low acceleration when fluid motion experiences Faraday waves that are not so effective in dissipating energy. After the 1 g iso-acceleration, we assist to a gradual increase to higher dissipation level in conjunction with the transition to a more chaotic regime. It is worth noting that the trend is not simply dependent on the imposed acceleration and that $\bar{W}$ achieves a maximum for acceleration close to 4 g in a range $\bar{\omega} = 3 - 5$ and $\bar{u} = 0.2 - 0.4$. The presence of maximum dissipation values as a function of both amplitude and frequency can be interpreted as owed to two causes: on the one hand, *i)* the increase in frequency of motion brings to the response of sloshing modes exhibiting greater curvature. As a consequence, the surface tension delays the free surface breakage and the water droplets impact more softly the tank ceiling. On the other hand, *ii)* above a certain value of acceleration, the generation of a homogeneous air/liquid mixture tends to reduce the overall phase shift between the sloshing forces and the imposed motion.

1.4.3 Filling level case 2: $\alpha = 0.25$

The second set of experiments concerns the filling level case $\alpha = 0.25$. The same set of results and analyses of the case $\alpha = 0.50$ have been obtained, where the decrease in water level considerably influences dissipation. Figure 1.13 shows the trend of the dissipated energy as a function of the frequency sweep for the considered acceleration values $1.5g$ and $3.0g$. Figure

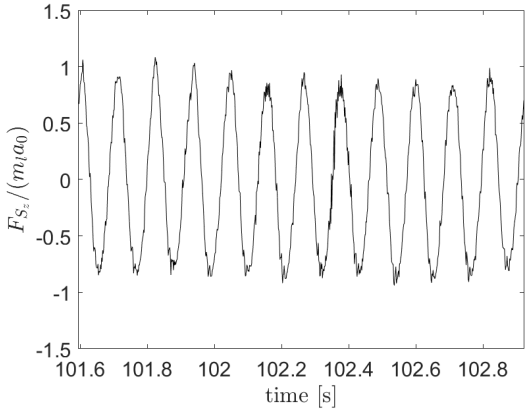

(a) $a_0 = 1.5g,\ f = 9Hz$

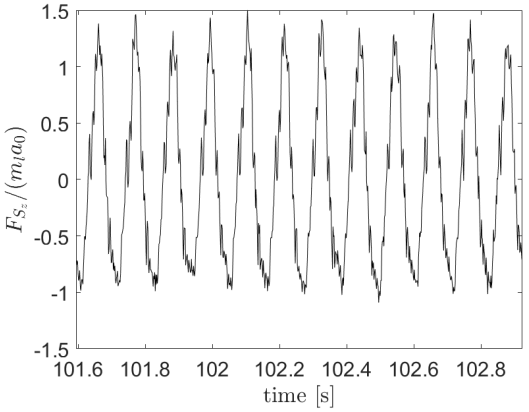

(b) $a_0 = 3g,\ f = 9Hz$

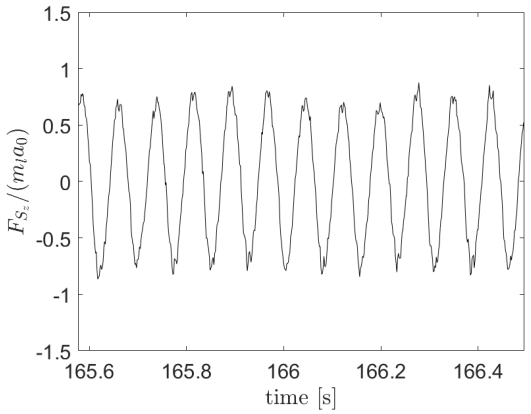

(c) $a_0 = 1.5g,\ f = 13Hz$

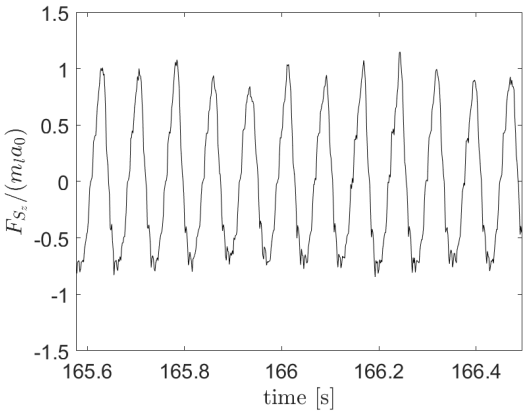

(d) $a_0 = 3g,\ f = 13Hz$

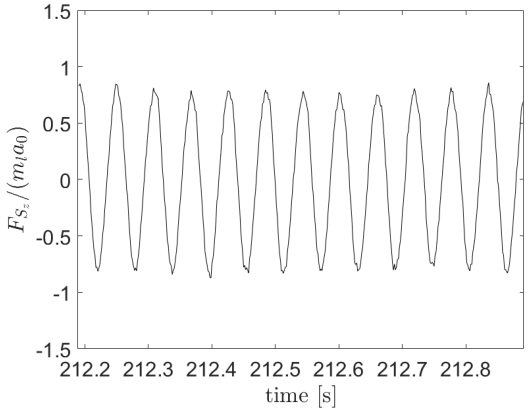

(e) $a_0 = 1.5g,\ f = 17Hz$

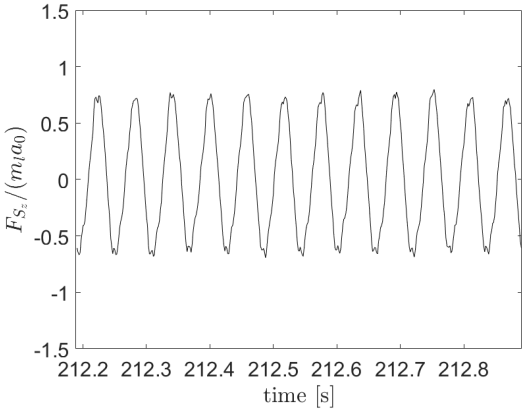

(f) $a_0 = 3g,\ f = 17Hz$

Figure 1.7: Sloshing force for the fill level case 1: $\alpha = 0.50$.

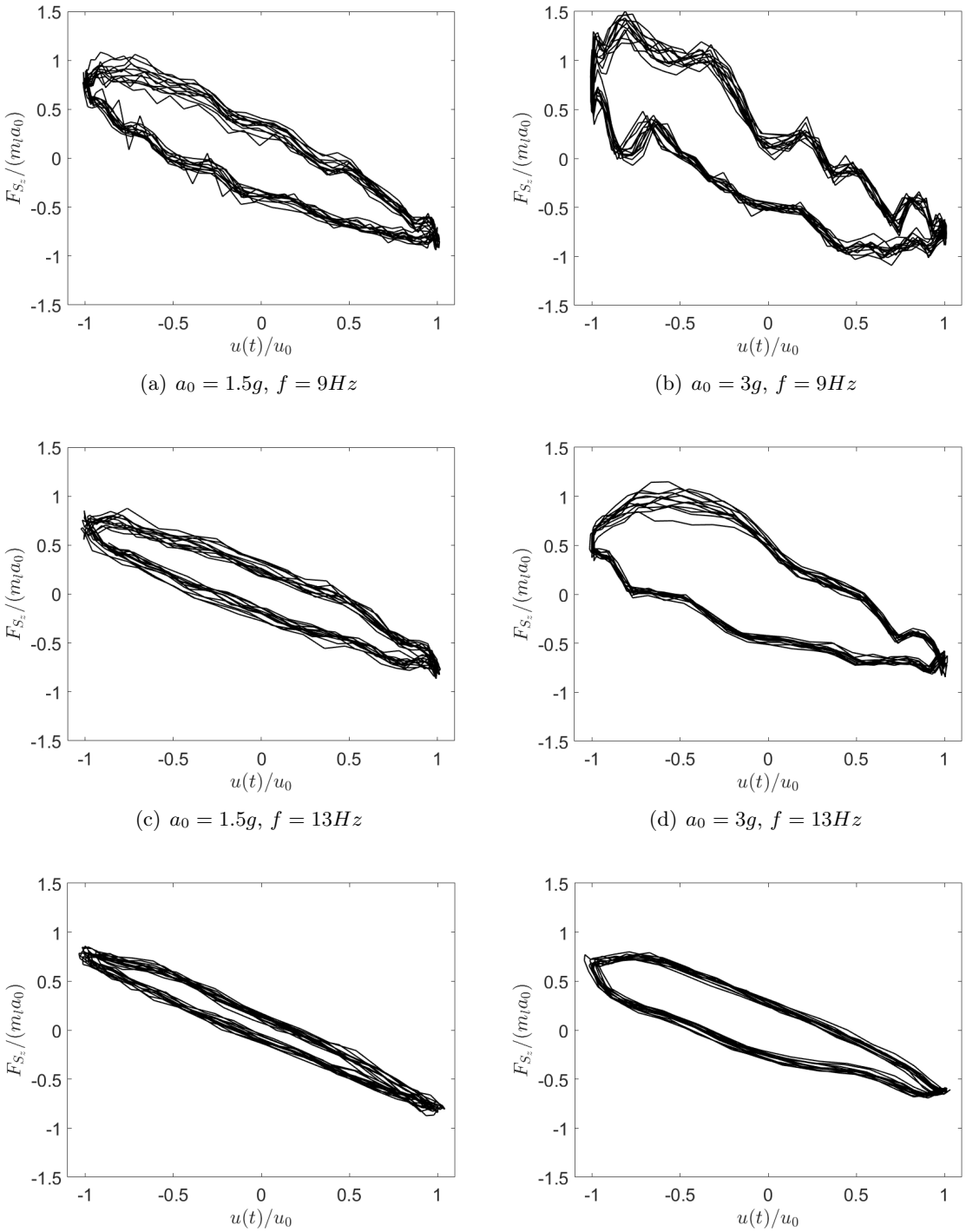

(a) $a_0 = 1.5g,\ f = 9Hz$

(b) $a_0 = 3g,\ f = 9Hz$

(c) $a_0 = 1.5g,\ f = 13Hz$

(d) $a_0 = 3g,\ f = 13Hz$

(e) $a_0 = 1.5g,\ f = 17Hz$

(f) $a_0 = 3g,\ f = 17Hz$

Figure 1.8: Hysteresis cycles for the fill level case 1: $\alpha = 0.50$.

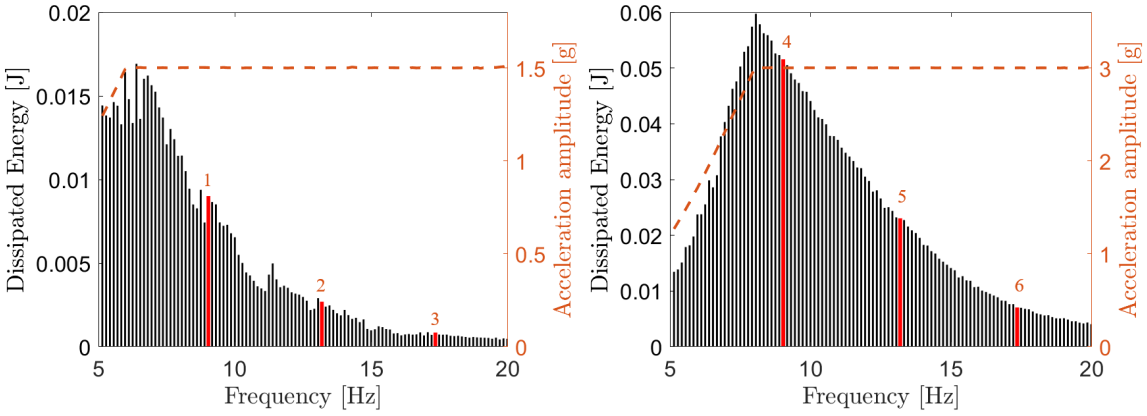

(a) $a_0 = 1.5g$ (b) $a_0 = 3g$

Figure 1.9: Dissipated energy for the fill level case 1: $\alpha = 0.50$. Red bars indicate the reference points.

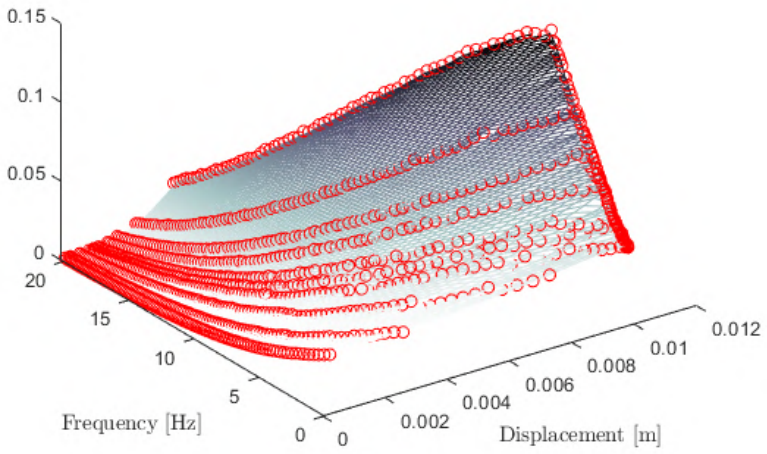

Figure 1.10: Interpolation of data by employing radial basis functions for the fill level case 1: $\alpha = 0.50$. Red circles indicate the data used for the interpolation.

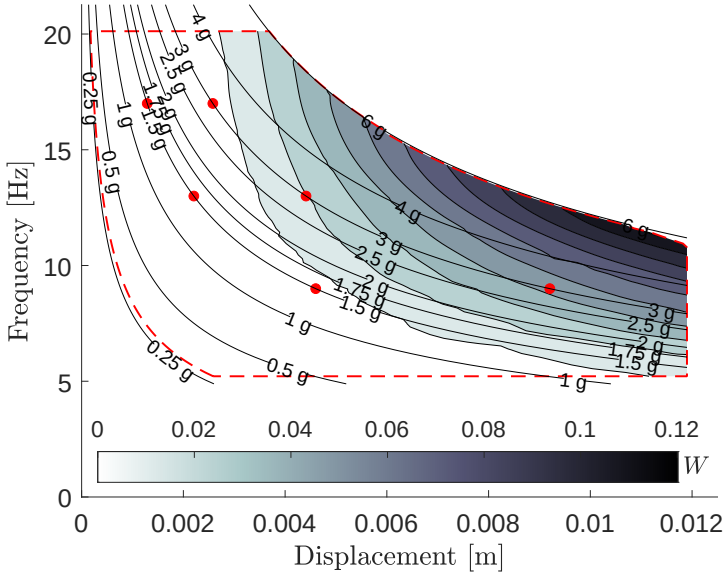

Figure 1.11: Dissipated energy for the fill level case 1: $\alpha = 0.50$. Red bullets indicate the reference points presented in Tab. 1.2.

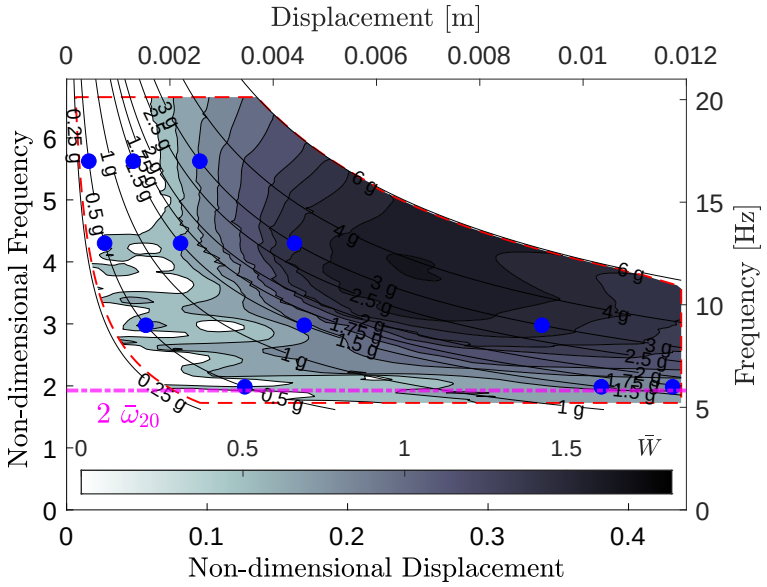

Figure 1.12: Non-dimensionalised dissipated energy for the fill level case 1: $\alpha = 0.50$. Blue bullets indicate the twelve snapshots presented in Fig. 1.6.

1.14 provides the interpolated values of dissipated energy. Similarly to the case $\alpha = 0.50$, the non-dimensional dissipated work is provided in Fig. 1.15 as a function of non-dimensional frequency and amplitude. The decrease of liquid depth brings to the reduction of the frequency $\omega_{2,0}$ as it can be noticed from the horizontal magenta line. It has similar features as in Fig. 1.12, but unlike the case $\alpha = 0.50$, the fluid fingers generated by the Faraday waves have less chance to impact on the tank ceiling because the distance between the free surface at rest and the ceiling is larger, resulting in less dissipation at smaller displacement amplitudes.

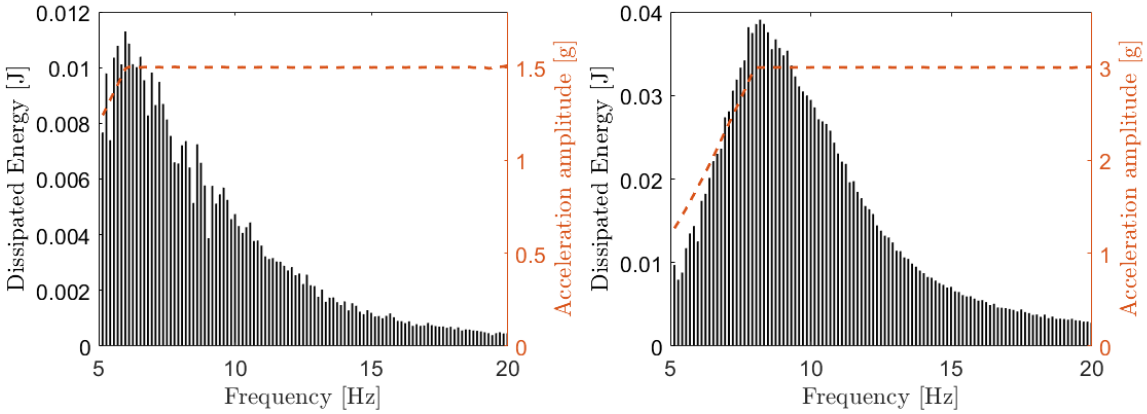

(a) $a_0 = 1.5g$ (b) $a_0 = 3g$

Figure 1.13: Dissipated energy for the fill level case 2: $\alpha = 0.25$.

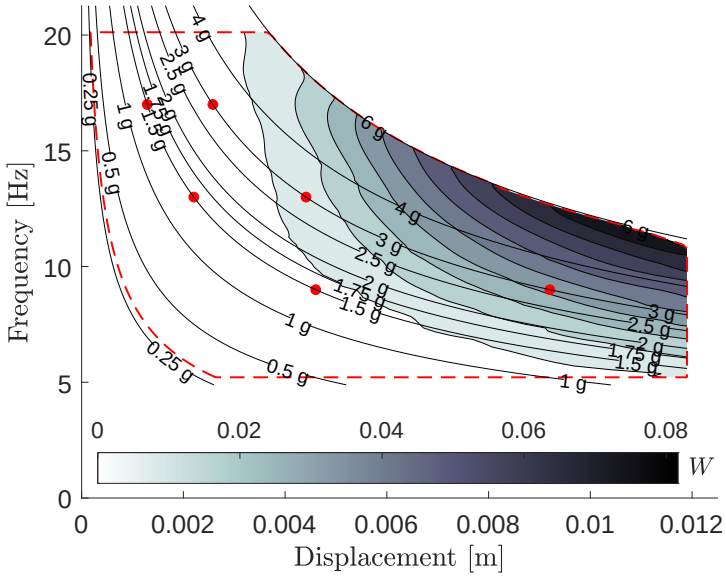

Figure 1.14: Dimensional dissipated energy for the fill level case 2: $\alpha = 0.25$.

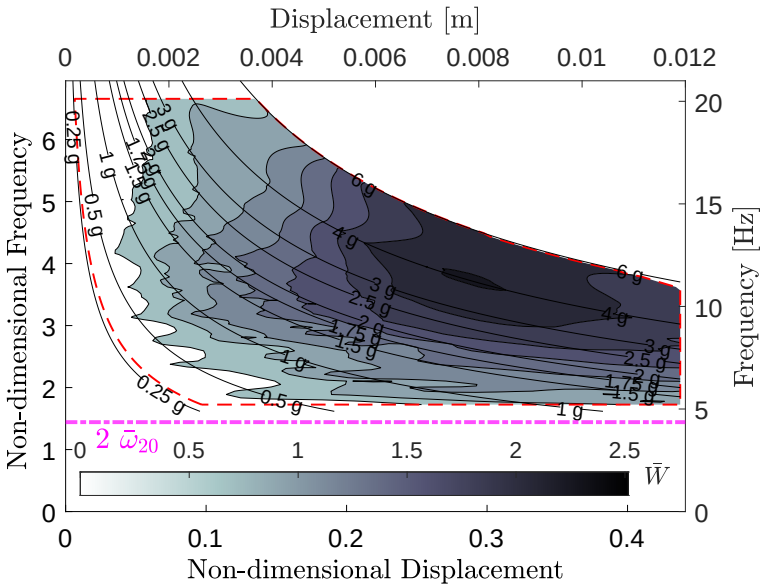

Figure 1.15: Non-dimensionalized dissipated energy for the fill level case 2: $\alpha = 0.25$.

1.4.4 Filling level case 3: $\alpha = 0.75$

The last set of experiments concerns the case with $\alpha = 0.75$. Figure 1.16 shows the trend of the dissipated energy as a function of the frequency sweep for the considered acceleration values $1.5g$ and $3.0g$. Figure 1.17 provides the interpolated values of dissipated energy. Again, the non-dimensional dissipated work is provided in Fig. 1.18 as a function of non-dimensional frequency and amplitude. As opposed to the cases $\alpha = 0.50$ and $\alpha = 0.25$, the map of non-dimensional dissipated work tends to be more homogeneous since, on one hand there is less dissipation at higher values of acceleration since the distance that the liquid can travel inside the tank is shorter (due to the higher filling level) and the liquid particles are unable to get accelerated at a relative speed value such as to generate violent impacts. On the other hand, at lower frequencies the fingers generated by Faraday waves can easily reach the tank ceiling.

1.4.5 Sensitivity to filling level

A sensitivity analysis to the filling level is performed on the dissipation of the fluid. Figure 1.19 shows the trend of dissipated energy for the three filling levels considered in the present work for the cases with $1.5g$ and $3g$ vertical acceleration, respectively, and by varying different frequencies. It can be noticed that the case $\alpha = 0.50$ filling level, is generally the more disruptive in terms of dissipated energy by varying both frequency and amplitude (except for the case of $17\,Hz$) confirming the results obtained in Refs. [10, 30].

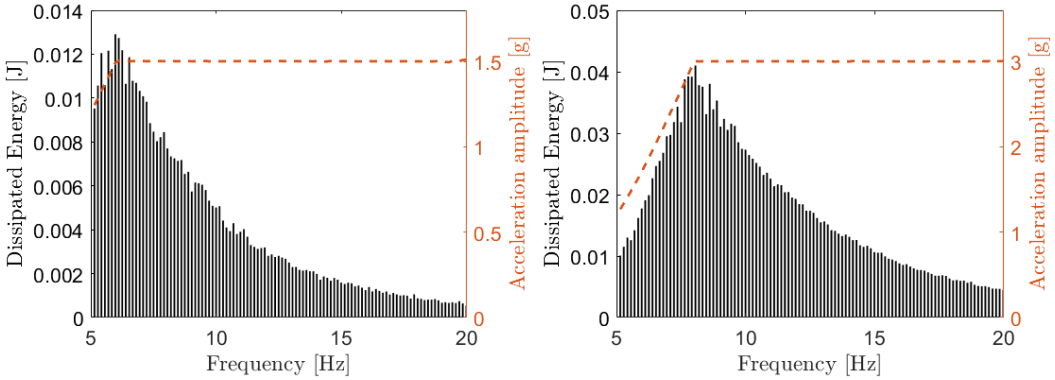

(a) $a_0 = 1.5g$ (b) $a_0 = 3g$

Figure 1.16: Dissipated energy for the fill level case 3: $\alpha = 0.75$.

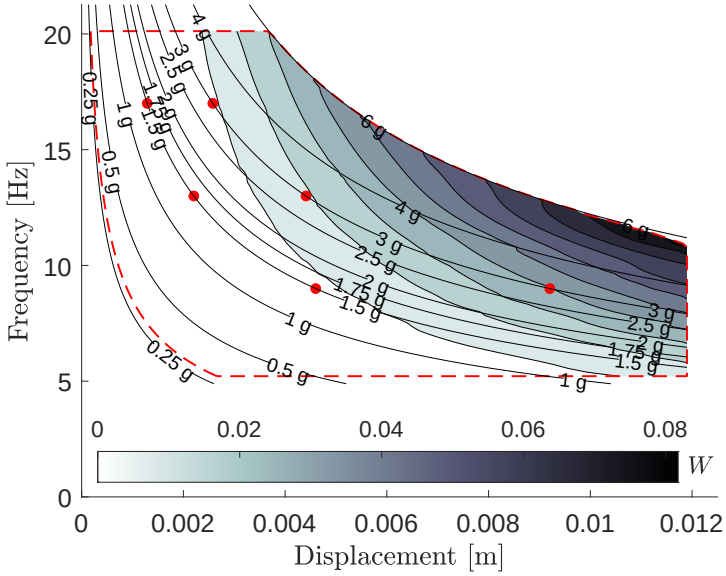

Figure 1.17: Dissipated energy for the fill level case 3: $\alpha = 0.75$.

To better understand the mechanisms that regulate energy dissipation, Fig. 1.20 shows the isolines with 85% of the maximum of $\bar{W}$ for three considered filling level cases, highlighting how the region in the displacement-frequency domain where most of the dissipation occurs evolves as a function of the filling level.

This figure shows the location of the maximum dissipation region in the frequency and amplitude domain and its extension. Vertical sloshing provides always maximum dissipation beyond 1 g of acceleration. The maximum relative dissipation seems to be linked to the oscillation amplitude values owe to a sort of spatial synchronisation of the movement of the

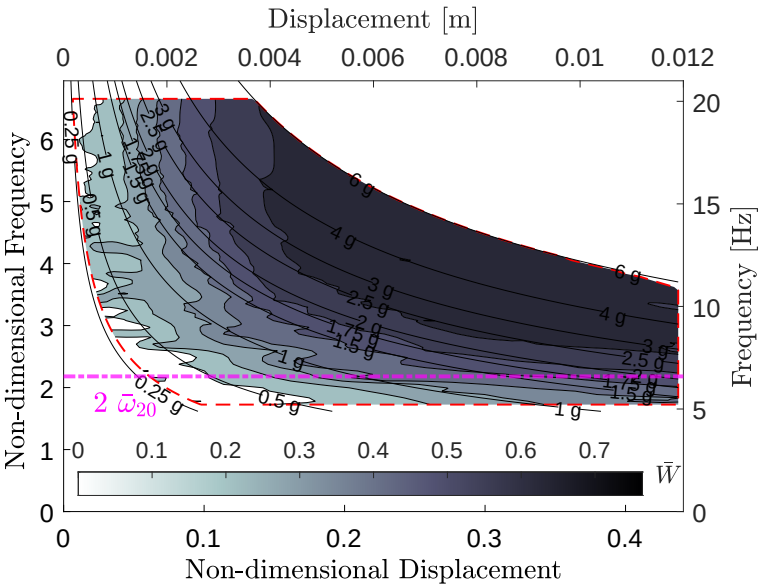

Figure 1.18: Non-dimensionalised dissipated energy for the fill level case 3: $\alpha = 0.75$.

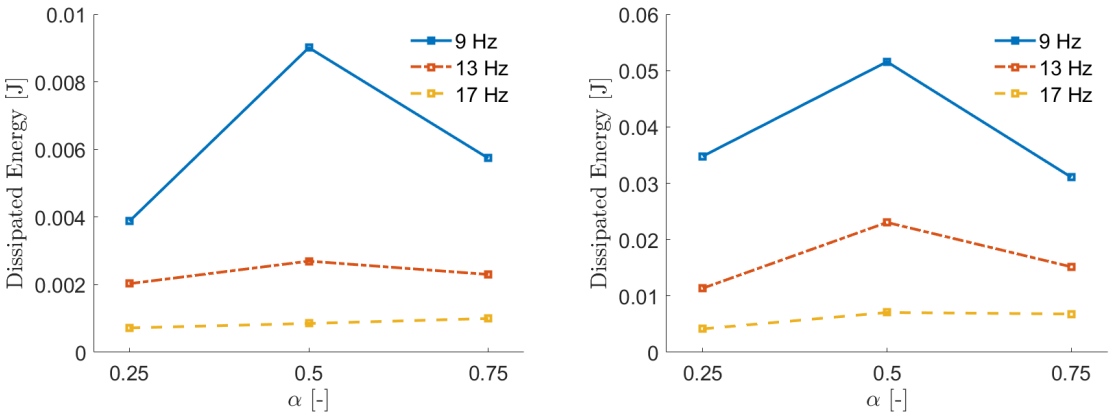

(a) $a_0 = 1.5g$ (b) $a_0 = 3.0g$

Figure 1.19: Sensitivity analysis on the dissipated energy to different water filling levels.

fluid with that supplied to the tank. The filling level plays a key role as it is linked to the path that the fluid droplets must go through to impact the tank ceiling. Maximum dissipation isolines are all comprises in the region $\bar{u} = 0.2 - 0.3$ but the case $\alpha = 0.25$ seems to present higher dissipation values at higher displacement with respect to the case $\alpha = 0.75$, featured by a greater distance between the free surface and the tank ceiling. Furthermore, the greater the α, the greater the extension of the zone of maximum dissipation, probably due to increased likelihood of droplets to reach the ceiling.

In conclusion, the processed results showed that the energy dissipated by the sloshing

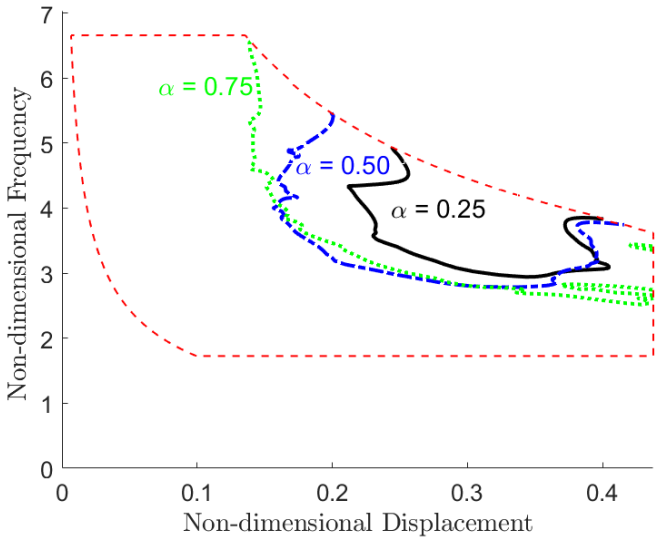

Figure 1.20: Isolines with 85% of maximum of $\bar{W}$ for $\alpha = 0.25$, $\alpha = 0.50$ and $\alpha = 0.75$.

forces highly depends on the intensity of the excitation. More in details, a low dissipation level has been noted for acceleration values lower than 1 g beyond which there is a transition to a regime in which resonant modes are no longer visible (at least at lower frequencies). The $\bar{W}$ dissipated energy maps are not simply monotonically dependent on the amplitude levels of the vertical acceleration. Indeed, surface tension and viscosity seem to play a role in stabilising the free surface at higher frequency range even at acceleration values higher than $1\,g$. Moreover, beyond a certain level of acceleration (around $4\,g$) the dissipation mechanisms become less effective. The sensitivity analysis conducted on the filling level showed that among the three cases considered, the intermediate case, *i.e.* $\alpha = 0.50$ was the most significant in terms of dissipated energy. This suggests that, according with the tank size, the energy dissipated by the fluid is a trade-off between the fluid mass and the path to be covered by the liquid before impacting to the tank walls: the lower the filling level, the higher is the path for the liquid particle for being accelerated (relatively to tank walls) before the impact with the ceiling, whereas, on the other hand, a lower filling level means a lower slamming mass.

1.5 Sloshing-effective mass fraction concept

This section introduces a further contribution to the study of vertical sloshing, again based on the experimental analysis presented in the previous sections. The experimental data obtained allowed us to define another non-dimensional quantity, named *sloshing-effective mass fraction* β. Its identification is performed by applying phasor theory to the dynamics of vertical sloshing and then considering a linear approximation of it.

The sloshing force F_{S_z} can be decomposed as follows:

$$F_{S_z} := F_{S_z}(u(t),t) \;=\; -m_l\,\ddot{u}(t) + \Delta f_{S_z}(u(t),t) \tag{1.19}$$

where $m_l\,\ddot{u}(t)$ is a purely inertial contribution associated with the mass m_l of liquid contained in the tank and Δf_{S_z} is a non-conservative force contribution, nonlinear function of the history of the tank vertical displacement $u(t)$, denoted as *dynamic sloshing force*.
In vertical steady harmonic motion, the response of a nonlinear system provides a nonlinear sloshing force such that its Fourier transform is not uniquely defined as a simple spectral line. However, filtering the response about the excitation frequency preserves the most of the signal properties and can be used here to interpret the role and the origin of the dissipate energy and effective mass.

Let's suppose that, given the amplitude of the motion u_0 and the frequency Ω, it is possible to linearize the dynamic sloshing force by assuming:

$$\Delta f_{S_z}(u(t),t) \cong -\beta(\Omega,u_0)\,m_l\,\ddot{u}(t) - \gamma(\Omega,u_0)\,\dot{u}(t) \tag{1.20}$$

where $[\beta(\Omega,u_0)\,m_l]$ is an additional term with respect to the frozen liquid model (*i.e.* where the liquid is not free to move in the tank) and $\gamma(\Omega,u_0)$ is a quantity that provides the dependency of the sloshing force with respect to the vertical input velocity $\dot{u}(t)$. Both β and γ generally depend on the frequency and amplitude of the motion.

Let us therefore consider that the vertical mtion $u(t)$ imposed on the tank is purely steady harmonic and expressed as $\check{u} = u_0\,e^{j\Omega t}$. The output in response from the liquid is the following dynamic sloshing force $\Delta\check{f}_{S_z} = Fe^{j(\Omega t+\varphi)}$, with F and φ, respectively being its amplitude and the phase shift with respect to the tank motion. In this case, Eq. 1.20 gives:

$$\Delta\check{f}_{S_z} = -\Big(-\beta(\Omega,u_0)m_l\Omega^2 + \gamma(\Omega,u_0)j\Omega\Big)\check{u} \tag{1.21}$$

Thus, Eq. 1.21 yields

$$\frac{\Delta\check{f}_{S_z}}{m_l\Omega^2\check{u}} \;=\; \beta(\Omega,u_0) - j\frac{\gamma(\Omega,u_0)}{m_l\Omega} \tag{1.22}$$

$$\frac{\Delta\check{f}_{S_z}}{\Omega\check{u}} \;=\; \beta(\Omega,u_0)m_l\Omega - j\gamma(\Omega,u_0) \tag{1.23}$$

By respectively taking the real and imaginary part of Eqs. 1.22 and 1.23, one obtains

$$\beta(\Omega,u_0) \;=\; \frac{F}{m_l\,\Omega^2\,u_0}\cos(\varphi) \;=\; \Re\Big[\frac{\Delta\check{f}_{S_z}}{m_l\,\Omega^2\,\check{u}}\Big] \tag{1.24}$$

$$\gamma(\Omega,u_0) \;=\; -\frac{F}{\Omega\,u_0}\sin(\varphi) \;=\; -\Im\Big[\frac{\Delta\check{f}_{S_z}}{\Omega\,\check{u}}\Big] \tag{1.25}$$

The dynamic sloshing force Δf_{S_z} can be expressed also as a function of the relative acceleration $\Delta\ddot{u}_{l_G}$ of the fluid center of mass with respect to tank. Indeed, assuming $\mathbf{u}_l$ the displacement field of the the fluid continuum and $\mathbf{T}$ the stress tensor, the Cauchy momentum (conservation) equation projected in vertical direction $\mathbf{k}$ provides

$$\left[\iiint_V \rho\frac{D^2\mathbf{u}_l}{Dt^2}\mathrm{d}V - \iiint_V \mathrm{div}\mathbf{T}\mathrm{d}\mathrm{V} - \mathrm{g}\iiint_\mathrm{V}\rho\mathbf{k}\mathrm{d}\mathrm{V}\right]\cdot\mathbf{k} = 0 \tag{1.26}$$

Assuming $\mathbf{u}_l = u\,\mathbf{k} + \Delta\mathbf{u}_l$, being u the vertical displacement of the tank and $\Delta\mathbf{u}_l$ the relative displacement of each fluid point of the domain, and using the divergence theorem, one has:

$$m_l\ddot{u} + \iiint_V \rho\frac{D^2\Delta\mathbf{u}_l}{Dt^2}\mathrm{d}V = -F_{S_z} + m_l g \tag{1.27}$$

Neglecting the hydrostatic contribution and considering the dynamic sloshing force given by $\Delta f_{S_z} = F_{S_z} + m_l\ddot{u}$, it is possible to obtain:

$$\Delta f_{S_z} = -m_l\Delta\ddot{u}_{l_G} \tag{1.28}$$

that is, the dynamic sloshing forces depends on the relative motion of the fluid center of mass.

The motion of the fluid center of mass is therefore given by $\Delta\check{u}_{l_G} = u_{l_0}e^{j(\Omega t+\varphi)}$ where $u_{l_0} = F/(m_l\Omega^2)$ is the amplitude of the relative motion of the fluid center of mass with respect to the tank. This way, it is possible to recast the sloshing effective mass variation ratio as:

$$\beta(\Omega, u_0) \;=\; \Re\Big[\frac{\Delta\check{f}_{S_z}}{m_l\,\Omega^2\,\check{u}}\Big] \;=\; \Re\Big[\frac{\Delta\check{u}_{l_G}}{\check{u}}\Big] = \frac{u_{l_0}}{u_0}\cos(\varphi) \tag{1.29}$$

Thus, the variation of the sloshing-effective mass assumes the meaning of the ratio between the amplitude of the phased relative motion of the fluid center of mass and the tank motion amplitude.

Based on what has just been demonstrated, it is possible to correlate the nondimensional dissipated energy $\bar{W}$ already presented in the previous sections with the coefficient γ. By combining Eqs. 1.15, 1.18, 1.19 and 1.20, for the linearised harmonic motion the nondimensional

dissipated energy $\bar{W}$ can be expressed as follows:

$$\begin{aligned}
\bar{W} = \frac{W}{m_l u_0^2 \Omega^2} &= \frac{1}{m_l u_0^2 \Omega^2} \int_{cycle} \Delta f_{S_z}(\Omega(\tau), u_0(\tau))\, \dot{u}(\tau)\, \mathrm{d}\tau \\
&\cong \frac{1}{m_l u_0^2 \Omega^2} \int_{cycle} -\left[\gamma(\Omega(\tau), u_0(\tau))\, \dot{u}(\tau)\right]\, \dot{u}(\tau)\, \mathrm{d}\tau \\
&= -\frac{1}{m_l u_0^2 \Omega^2} \int_{cycle} \gamma(\Omega(\tau), u_0(\tau))\, (u_0\, \Omega)^2\, \cos^2(\Omega\, \tau)\, \mathrm{d}\tau \\
&= -\frac{\gamma}{m_l} \int_{cycle} \cos^2(\Omega\, \tau)\, \mathrm{d}\tau \\
&= -\frac{\pi\gamma}{m_l \Omega} = \frac{\pi F}{m_l \Omega^2 u_0} \sin(\varphi) = \pi \frac{u_{l_0}}{u_0} \sin(\varphi)
\end{aligned} \tag{1.30}$$

From Eqs. 1.29 and 1.30, we can estimate the relative amplitude u_{l_0} and phase shift φ of the fluid center of mass displacement from which we can interpret the role of dissipated energy and sloshing-effective mass. Note that in Eq. 1.30, the work done by sloshing forces is only associated with the dynamic sloshing force Δf_{S_z}, as inertial contributions make no contribution in harmonic motion. A Fourier transform of the sloshing forces $\Delta \tilde{f}_{S_z}(\Omega)$, as well

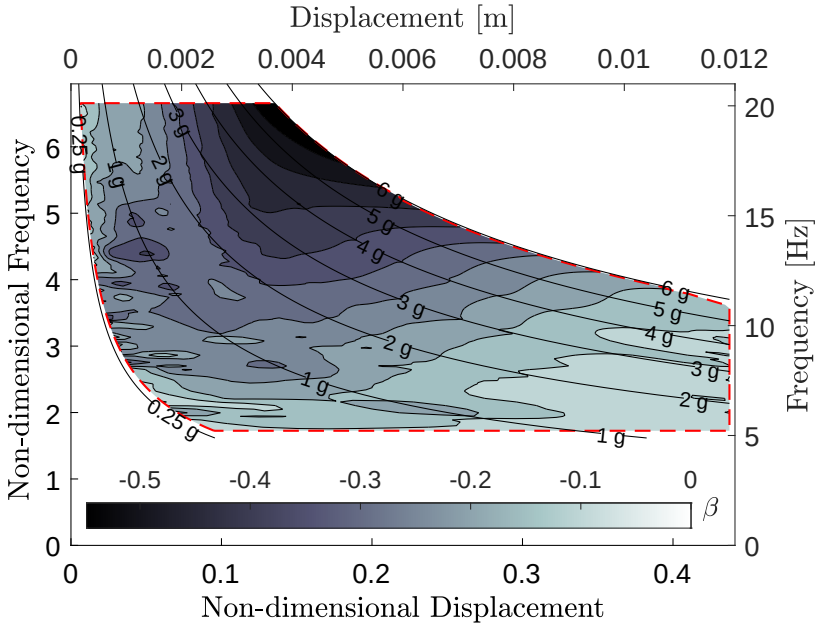

Figure 1.21: Experimental sloshing-effective mass fraction β

as the vertical tank motion $\tilde{u}(\Omega)$ at the excitation frequency Ω, can be used instead of the

phasors for experimentally measured harmonic signals. By exploiting these Fourier transforms and the developments demonstrated in this section, it is possible to identify a map for the effective sloshing mass fraction β as the non-dimensional operational parameters vary (as has already been done for dissipated energy). The result is shown in Fig. 1.21.

The identified $\beta(\bar{\omega}, \bar{u})$ results to be negative throughout the interest frequency-amplitude domain. Therefore, the relative motion of fluid center of mass is always counter-phased with respect to the tank.

Summary

In this chapter the experimental characterisation of the vertical sloshing dissipative behaviour was addressed for a box-shaped tank by means of an experimental campaign using a seismic harmonic excitation on the tank. A controlled electrodynamic shaker was employed to provide high amplitude seismic excitation to the tank thus obtaining the interface forces exchanged between the tank and the shaker. The present work provided that the energy dissipated by the sloshing fluid inside the tank can be related to a source of damping for a structure that interfaces with the tank. A procedure based on the hysteresis behaviour of the sloshing forces was used to evaluate the dissipated energy for a wide range of operative conditions. The type of excitation consisted of a sine-sweep covering a range of amplitudes and frequencies defined by the limits of the electrodynamic actuator and by the characteristics of the phenomenon. The interface force and tank acceleration were used to identify, on one hand, the sloshing forces and, on the other hand, the dissipative behaviour of the sloshing forces for different amplitude-frequency pairs according with dimensional and non-dimensional definition of the evaluated dissipated energy. The analyses were repeated for three different filling levels, *i.e.* $\alpha = 0.50$, $\alpha = 0.25$ and $\alpha = 0.75$. The processed results showed that the energy dissipated by the sloshing forces highly depends on the intensity of the excitation. More in details, a low dissipation level has been noted for acceleration values lower than 1 g beyond which there is a transition to a regime in which resonant modes are no longer visible (at least at lower frequencies). The $\bar{W}$ dissipated energy maps are not simply monotonically dependent on the amplitude levels of the vertical acceleration. Indeed, surface tension and viscosity seem to play a role in stabilising the free surface at higher frequency range even at acceleration values higher than $1\,g$. Moreover, beyond a certain level of acceleration (around $4\,g$) the dissipation mechanisms become less effective. A sensitivity analysis was finally conducted on the filling level having shown that among the three cases considered, the intermediate case, *i.e.* $\alpha = 0.50$ was the most significant in terms of dissipated energy. This suggests that, according with the tank size, the energy dissipated by the fluid is a trade-off between the fluid mass and the path to be covered by the liquid before impacting to the tank walls: the lower the filling level, the higher is the path for the liquid particle for being accelerated (relatively to tank walls) before the impact with the ceiling, whereas, on the other hand, a lower filling

level means a lower slamming mass. The provided energy maps can help to predict the nonlinear behaviour of structures containing tanks subjected to high vertical accelerations. In addition, following an approach similar to the one in Ref. [83], these maps can help to predict the amplitude of limit cycle oscillations before performing computationally expensive fluid-structure interaction simulations. The concept of the sloshing-effective mass fraction was also introduced. By means of a linearisation, it was possible to experimentally identify this nondimensional parameter, showing that sloshing introduces also inertial effects that leads to a correction of the liquid mass that actively participates in the dynamics.

Chapter 2

Nonlinear Reduced Order Models (N-ROMs) for Vertical Sloshing

This chapter describes the non-linear reduced-order models (N-ROMs) that have been developed and identified to obtain virtual twins capable of adequately representing the vertical sloshing dynamics of a fluid contained within a tank. In the first part, the bouncing ball model is presented, consisting of an equivalent mechanical model able to emulate the impact mechanisms inherent in vertical sloshing - which are most responsible for dissipation. Most of the results for this model were presented in Ref. [85]. The second part deals with the reduced order model based on neural networks. Together with its experimental validation, the scaling law introduced in order to use this ROM in applications with tanks of different sizes is also presented. This part draws mainly on the work presented in Refs. [81, 86].

2.1 Equivalent Mechanical Model (EMM) for vertical sloshing: the *Bouncing Ball* model

A realistic representation of the liquid dynamics inside closed tanks can be approximated by an equivalent mechanical model. Equivalence is meant in the sense of equal resultant forces (and moments) acting on the tank walls. Exploiting this principle, it was decided to design a reduced-order model equivalent to the strongly nonlinear dynamics that can occur when a tank containing some liquid inside it, is subjected to violent vertical (and therefore perpendicular to its base) excitations. Under these circumstances, a series of impacts are triggered between the liquid and the tank ceiling (and floor), which contribute greatly to dissipating much of the energy that is supplied to the system through excitation. Observing this physical phenomenon, a conceptual similarity emerged with the motion dynamics of a ball bouncing on flat ground. For this reason, a mathematical model has been developed that can reproduce the behavior of a bouncing ball. It involves the use of a system of masses,

springs and dampers capable of both reproducing the mechanism of impact of the liquid in the tank, and the dissipation induced under the same conditions. In the *bouncing ball* model, equivalence is therefore realized by ensuring that sloshing forces can be replaced by the forces exchanged between the tank walls (floor and ceiling) and the ball itself during impacts. The energy balance after each impact is negative due to the presence of a viscoelastic element inside the ball that characterizes energy dissipation. The bouncing ball model is illustrated in Fig. 2.1. The system is ideally represented as a rigid bubble without mass properties that has

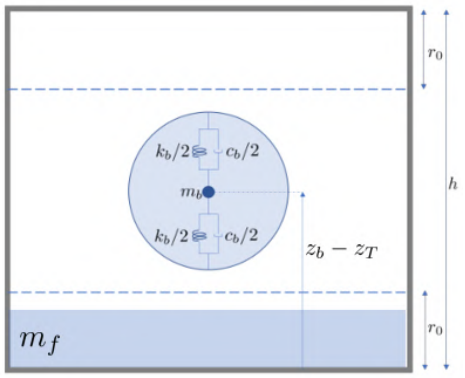

Figure 2.1: Bouncing ball model and its representation inside a box-shaped rigid tank.

a concentrated mass inside hanged to its wall by means of a spring-damper system. A portion of the fluid total mass is considered associated with the ball m_b, whereas another portion is considered frozen m_f, namely attached to the wall. The parameter β, which can take values between zero and 1, is introduced to indicate the mass fraction of frozen liquid. Specifically, we have $m_f = \beta\, m_l$, while the remaining mass of the liquid is dedicated exclusively to the ball as $m_b = (1-\beta)\, m_l$. When the rigid bubble touches the ceiling or the floor of the tank, the impact condition is verified so causing viscoelastic forces exchanged between the case and the bouncing ball. The equation of motion of the bouncing ball can be thus summarized as follows

$$m_b \ddot{z}_b = -m_b g + F_b(z_b(t), z_T(t)) \tag{2.1}$$

where F_b is the viscoelastic force exchanged at the wall, $z_T(t)$ represents the motion of the tank whereas $z_b(t)$ is the absolute vertical motion of the bouncing ball (to be understood as the vertical displacement of the ball mass m_b, which is located in its geometric center when the internal springs and dampers are at rest). In this framework, it is convenient to introduce

a new variable $s(t)$ as:

$$s(t) = \begin{cases} z_b(t) - z_T(t) - r_0 & \text{if } z_b(t) < z_T(t) + r_0 \\ z_b(t) - z_T(t) - h + r_0 & \text{if } z_b(t) > z_T(t) + h - r_0 \\ 0 & \text{elsewhere} \end{cases} \tag{2.2}$$

where r_0 is the radius of the rigid bubble and h is the height of the tank. When the condition, $z_b(t) < z_T(t) + r_0$ occurs, the ball is in the impact region with the floor of the tank. Whereas, the condition $z_b(t) > z_T(t) + h - r_0$ is related to impact with the ceiling. The new variable $s(t)$ is null when the ball finds itself in the suspension or floating phase, where there is no impact. In addition, the variable $\nu(t) = \dot{z}_b(t) - \dot{z}_T(t)$ is introduced. It follows that we can define the viscoelastic forces as

$$F_b(z_b(t), z_T(t)) = F_b(s(t), \nu(t)) = k_b\, s(t) + c_b\, \nu(t) \tag{2.3}$$

where k_b and c_b are, respectively the stiffness and damping associated to the bouncing ball. It is worth to notice that $k_b = \hat{k}_b\, f_{nl}(s)$ may eventually be, in turn, nonlinear function of $s(t)$ by introducing a penalty function $f_{nl}(s)$, defined as

$$f_{nl}(s) = 1 + \frac{\alpha s^2}{(r_0 - |s|)} \tag{2.4}$$

that avoid the ball to go out by the limits of the tank. Then, the inertial and hydrostatic contributions associated with the frozen mass are subtracted from the viscoelastic force to obtain the overall sloshing force $F_s(s(t))$ exchanged between the tank and fluid mass inside it:

$$F_s(s(t), \nu(t)) = F_b(s(t), \nu(t)) - m_f[\ddot{z}_T(t) + g]. \tag{2.5}$$

In order for the described mathematical model to be representative of real vertical sloshing dynamics, its design parameters must have specific values. The parameters that define the bouncing ball are stiffness $\hat{k}_b$, damping c_b, penalty function coefficient α, frozen mass fraction β, and radius r_0. These can be determined by implementing identification or optimization procedures based on the use of experimental data or high-fidelity fluid dynamics data. The next section shows a procedure for identifying a reduced-order model for vertical sloshing based on the bouncing ball, exploiting experimental data in which a partially water-filled tank is mounted in a one-degree-of-freedom structural mechanical system.

2.1.1 Identification of a bouncing ball model based on transient response experimental data

The bouncing ball model should be designed to have parameters that ensure the surrogate model will replicate the same dissipative behavior of sloshing dynamics. As mentioned above, this requires reliable data. The work presented next involves the use of data from sloshing transient experimental tests carried out in the laboratories of the *Universidad Politécnica de Madrid* (UPM). The experimental object consists of an elastically scaled single degree of freedom mass-spring system coupled with the slosh dynamics within a hydrodynamically scaled tank. The equivalent mechanical model of a bouncing ball is then used to emulate the fluid behavior inside the tank (specifically the impacts with the tank wall) and provide a numerical model of a tank isolated from the structure on which it is possible to perform simulations with seismic excitation.

Description of the UPM experiment set-up

A picture of the experimental setup at the Model Basin Research group sloshing laboratory of the UPM and a simplified outline are both shown in Fig. 2.2. This tank is scaled to reflect the dimensions of real wing tanks. In order to scale down an actual wing to the SDOF test it is important to consider the dimensional analysis of the problem. Applying the Π theorem to a reference variable, for example the dissipated power by the fluid, one can find a dimensional relation between this variable and several non-dimensional numbers, such as, the Reynolds number, Froude number, filling level, etc. It is common practice in sloshing problems to perform a Froude scaling (see Ref. [87]), where $Fr = \sqrt{w_0^2 h/Ng}$ is defined based on the maximum acceleration of the problem which is N times the gravity. In the Froude number definition, w_0 is the characteristic angular frequency of the problem, h represents the height of the tank, Ng is the maximum acceleration of the problem, being $N \approx 10$ in this case. Then, a perfect geometrical scaling parameter is considered $\lambda = h_{SDOF}/h_W$ defined as the ratio between the heights of the SDOF tank and the wing tank. For the SDOF sloshing test, a 1:5 scale was selected ($\lambda = 0.2$) which results in a tank geometry of 10x6x6 cm. The scaled tank is filled up to 50 % of its volume with a water mass of $m_l = 0.18$ kg and it oscillates at a characteristic frequency of $f_0 = 6.56$ Hz. Table 2.1 shows the geometric and structural parameters of the components used in the experiment.

The sloshing rig is a SDOF system composed of a mechanical guide that allows the 1 degree of freedom constraint. This guide is attached to a C-shaped wooden structure that holds the tank with a structural mass of $m_s = 2.06$ Kg. Similarly, the C-shaped wooden structure is attached to a set of 6 springs, 3 on the upper side and 3 on the lower side. The lower springs are mechanically embedded into the floor, and on the opposite side the upper set of springs is attached to a metallic plate, having mass $m_p = 0.06$ Kg, that acts as a joint

λ	1:5
Fluid tested	Water
Tank dimensions [cm]	10 x 6 x 6
Filling level [%]	50
Liquid mass m_l [Kg]	0.18
Structural mass m_s [Kg]	2.061
Total mass [Kg]	2.241
Stiffness K [N/m]	3808.8
Characteristic frequency f_0 [Hz]	6.56

Table 2.1: Summary of the parameters used in the Froude scaled SDOF experimental setup.

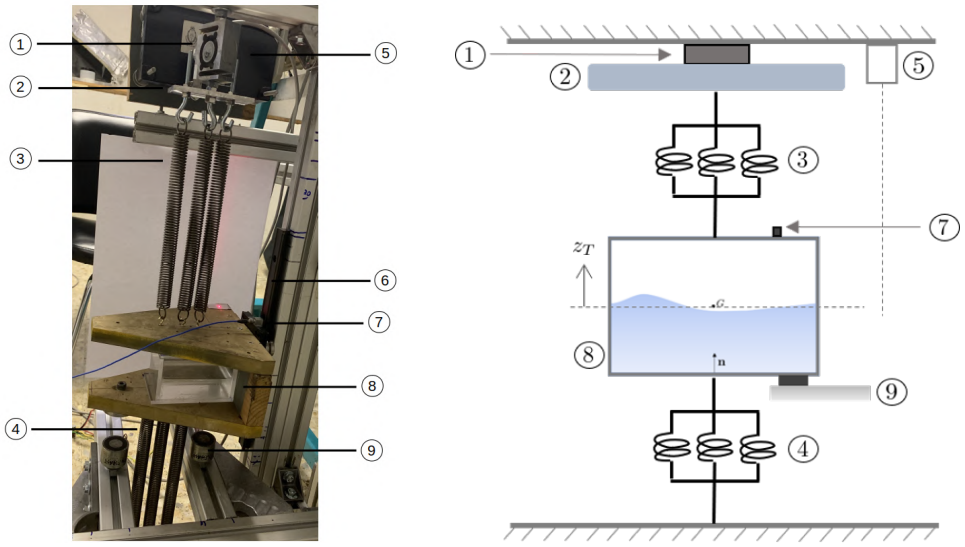

(a) Experimental setup (b) Outline of the setup

Figure 2.2: UPM experiment components: (1) Load cell, (2) Metallic plate (3) Upper springs $k_1 = 1904.4$ N/m, (4) Lower springs $k_2 = 1904.4$ N/m, (5) Laser sensor, (6) Mechanical guide, (7) Accelerometer, (8) Methacrylate tank and C-shaped wooden structure (9) Solenoids for release mechanism.

between them and the the embedded load cell. This setup also includes an accelerometer glued to the C-shaped wooden structure, a laser sensor pointing at the wooden block and two solenoids acting as a release mechanism. The experimental setup presented here can be used to perform free response tests at different initial conditions. Through the use of appropriate sensors, it is possible to acquire measurements. Specifically, the structure can be deflected with an initial amplitude until it is fixed by the action of the solenoids. When the electrical current is turned on, they release the structure triggering the beginning of the experiment where acceleration and position of the tank as well as load cell measurements are recorded allowing the calculation of the sloshing force acting on the system. A more detailed description of the sloshing rig and the sloshing force can be found in Ref. [29].

Bouncing ball model replacing UPM slosh dynamics

In this section a procedure to obtain a bouncing ball that can replace the sloshing liquid inside the experimental tank is presented. The behaviour of the fluid inside the tank is such that it is possible to appreciate impacts of the fluid mass on the tank walls (see Figs. 2.3(b) and 2.3(c)) as well as instants when the most of water mass is floating inside the cavity (see Fig. 2.3(a)). As illustrated in Fig. 2.4, the bouncing ball model aims at reproducing this behaviour. Specifically three different conditions are illustrated representing the ball floating in the tank, and, respectively, the impacts with the ceiling and floor. From Figs. 2.4(b) and 2.4(c) it is possible to appreciate also a graphical representation of the variable s, already introduced in Sec. 2.1.

(a) Floating (b) Ceiling Impact (c) Floor Impact

Figure 2.3: Snapshots of the sloshing experiment.

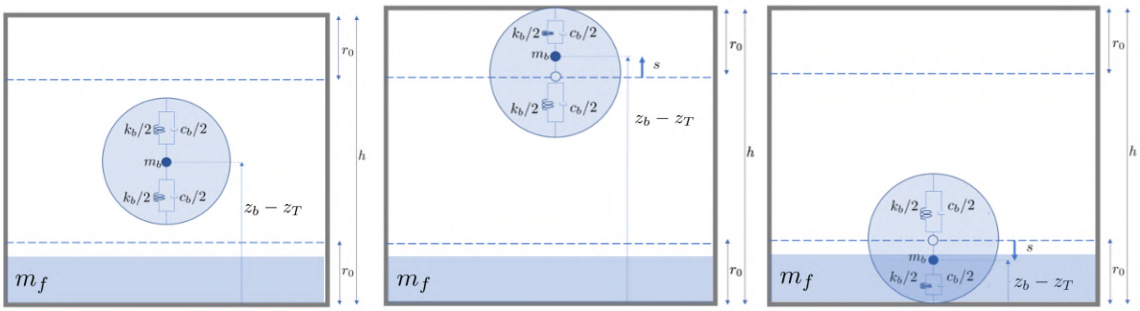

(a) Floating (b) Ceiling Impact (c) Floor Impact

Figure 2.4: Bouncing ball motion phases.

In order to obtain a surrogate model capable of accurately reproducing the dissipative behavior induced by sloshing, a virtual configuration equivalent to the experimental one carried out at the UPM was therefore planned. Figure 2.5 shows a schematic drawing of the configuration to be obtained, in which the bouncing ball replaces the liquid. Obviously, in order for it to actually be an equivalent configuration, it is necessary to determine the param-

eters of the ball that will make it return the same actions that the sloshing liquid manifests in the experiment (mainly to be interpreted as impact forces that induce an additional dissipation). Before presenting the procedure for obtaining the optimal design parameters, the mathematical model for describing the dynamics of the experiment is outlined using the free body diagram of the integrated system shown in Fig. 2.6. The system under consideration

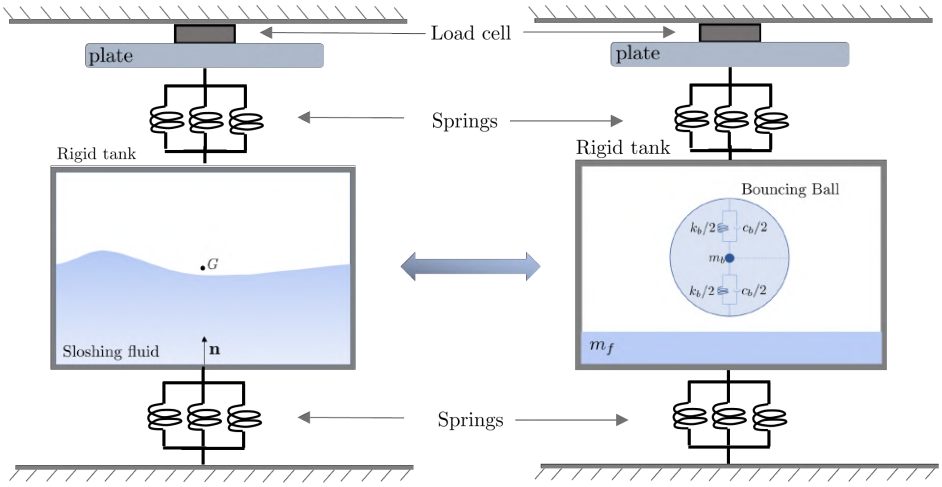

Figure 2.5: Virtual UPM experimental set-up: bouncing ball model instead of the liquid

can be modeled by three components. A rigid tank including the sloshing fluid and therefore, the bouncing ball model (highlighted as body 3 in Fig. 2.6). Then, a load cell having a negligible mass and able to detect, as voltage signal, the compression force $t_1 = t_2$ (body 1) and, finally, a rigid plate elastically linked to the tank, and attached to the load cell (body 2). The individual group of three springs is modeled as a viscoelastic element having a mass,

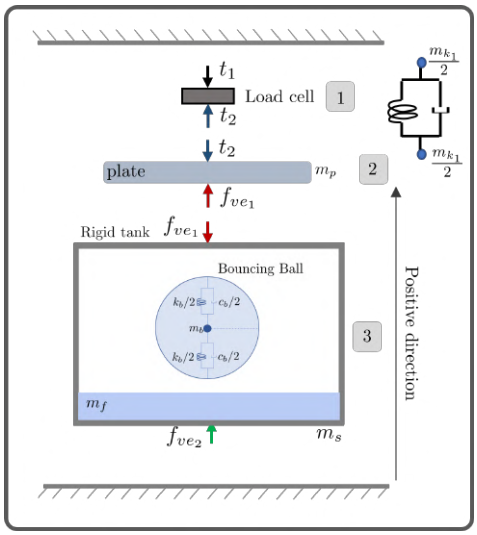

Figure 2.6: Free-body diagram of the virtual experiment

equal to half the total mass of the three springs, concentrated at the ends. The mass of the upper set of springs is m_{k1}, and it is equal to the lower set $m_{k1} = m_{k2} = m_k = 0.42$ Kg. The dampers represent all the mechanical damping in the system, such as the action of the mechanical guide, the drag force of the tank and other minor elements. The equilibrium of the static load cell (body 1) implies that the forces t_1 and t_2 are equal, consequently $t_1 = t_2 = t$. From the equilibrium of the rigid plate (body 2) the following equation is obtained:

$$0 = f_{ve_1} - t - \left(m_p + \frac{m_k}{2}\right) g \tag{2.6}$$

The third equilibrium equation is the one associated with the tank (body 3) and is expressed as follows:

$$\begin{aligned}
\left(m_s + \frac{m_{k_1} + m_{k_2}}{2}\right) \ddot{z}_T &= F_s(s,\nu) - f_{ve_1} + f_{ve_2} - \left(m_s + \frac{m_{k_1} + m_{k_2}}{2}\right) g \\
(m_s + m_k)\, \ddot{z}_T &= [F_b(s,\nu) - m_f(\ddot{z}_T + g)] - f_{ve_1} + f_{ve_2} - (m_s + m_k) g \\
(m_s + m_k + m_f)\, \ddot{z}_T &= F_b(s,\nu) - f_{ve_1} + f_{ve_2} - (m_s + m_k + m_f) g
\end{aligned} \tag{2.7}$$

where, we also considered the internal liquid action, i.e., the sloshing force F_s, provided by the impacts of the bouncing ball and expressed as in Eq. 2.5. Assuming that the damping is mainly due to the mechanical guide and the tank drag force, these forces are distributed symmetrically as part of the viscoelastic elements 1 and 2, as consequence we can consider both elements to be equal, and $f_{ve_1} = -f_{ve_2}$. Now, combining Eq. 2.6 with Eq. 2.7, we get

$$\begin{aligned}
(m_s + m_k + m_f)\, \ddot{z}_T &= F_b(s,\nu) - m_f\, g - 2\left[t + \left(m_p + m_k + \frac{m_s}{2}\right) g\right] \\
(m_s + m_k + m_f)\, \ddot{z}_T &= F_b(s,\nu) - m_f\, g - 2\,(t - t_0)
\end{aligned} \tag{2.8}$$

having defined with t_0 the following static contribution $t_0 = -\left(m_p + m_k + m_s/2\right) g$. The data provided by UPM comes primarily from accelerometer and load cell measurements (together with the measurement of the tank position obtained with the laser). However, while the measured acceleration is precisely $\ddot{z}_T$, the measurement provided by the load cell comes from a correction that takes into account the static contribution t_0 and the inertia force of the springs. Denoting by t_{LC} the provided force signal, defined as $t_{LC} = 2\,(t - t_0) + m_k\, \ddot{z}_T$, Eq. 2.8 becomes

$$(m_s + m_f)\, \ddot{z}_T = F_b(s,\nu) - m_f\, g - t_{LC} \tag{2.9}$$

which in turn can be rewritten in a more generic form, by considering the sloshing force F_s,

as follows:

$$m_s\,\ddot{z}_T = F_s - t_{LC} \tag{2.10}$$

Equation 2.10 is used in Ref.[29] to calculate the sloshing force F_s based on the acceleration measurement and load cell (and it will be exploited to compare the force predicted by the bouncing ball with the experimentally measured sloshing force). In the same reference, an alternative way to consider Eq. 2.7 is introduced. In particular, Newton's second law is applied to the tank assuming that only three forces are acting: linear springs force $K\,z_T$, the sloshing force F_s and a damping force F_D, which is assumed to cause all sources of energy dissipation that are not due to fluid slosh. So, Eq. 2.7 is rewritten by neglecting the mass of the viscoelastic elements and assigning to the actions they exert on the body a linear combination of F_D and $K\,z_T$:

$$m_s\,\ddot{z}_T + F_D + K\,z_T = F_s - m_s\,g \tag{2.11}$$

where $F_D = b_0\,\mathrm{sign}\,(\dot{z}_T) + b_1\,\dot{z}_T$, being b_0 a dry friction coefficient (from Coulomb friction law) and b_1 a structural viscous damping coefficient. The values of these two parameters, identified through a linear fitting in [29], are respectively equal to 0.37 N and 1.58 Kg/s. Considering the bouncing ball instead of the fluid, Eq. 2.11 becomes

$$(m_s + m_f)\,\ddot{z}_T + b_0\,\mathrm{sign}\,(\dot{z}_T) + b_1\,\dot{z}_T + K\,z_T = F_b(s,\nu) - (m_s + m_f)\,g \tag{2.12}$$

Equation 2.12 allows us to model the dynamics of the UPM experiment by considering the ball instead of the fluid. In order to identify the ball parameters, this equation is implemented in a simulation model built in Simulink®, in which the structure and the bouncing ball interact with each other in a closed-loop logic. The flowchart of the overall system (structure and sloshing) is shown in Fig. 2.7 where the input of the structural subsystem is represented by the viscoelastic force exerted by the bouncing ball, while the input of the sloshing subsystem is represented by the vertical rigid displacement z_T and the velocity $\dot{z}_T$ of the tank. Leaving out the hydrostatic contribution, and considering the frozen fluid mass m_f as a liquid mass contribution added to the structure, the structural subsystem is entirely described by the first member of Eq. 2.12. It is worth to notice that the sloshing subsystem can be also studied separately from the structure by assigning a suitable seismic excitation, or connected in a closed loop with the structure.

Bouncing ball tuning via experimental test

2.1.1 The research group at UPM developed and used the experiment described in Sec.2.1.1 to perform free response tests, exploiting a mechanism to release the tank from a given initial

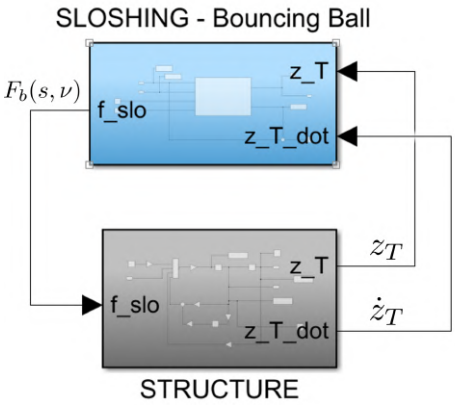

Figure 2.7: Flowchart of the fluid structure interaction problem.

condition. The reference experimental analysis was characterized by an initial displacement equal to $z_T = 0.064$ m. Through an optimization process, the proposed study utilizes acceleration and force data, measured with the accelerometer and load cell during the reference test, to identify and validate the parameters of the bouncing ball. Based on these, the model should be able to reliably reproduce the dissipative behavior of the sloshing liquid as estimated during the experiment. To identify the bouncing ball, the only experimental data that were available were those mentioned above. Consequently, it was necessary to define a metric by which dissipation could be described and quantified, based on these measurements. For this purpose, the metric selected was the instantaneous damping ratio as the representative quantity of dissipation. Specifically, we consider this damping ratio as a function of the acceleration amplitude of the vertical motion of the tank. It is estimated by exploiting the logarithmic decay on the signal over time of the experimental acceleration measured by UPM and shown in Fig.2.8(a). The instantaneous damping ratio evaluated on the experimental

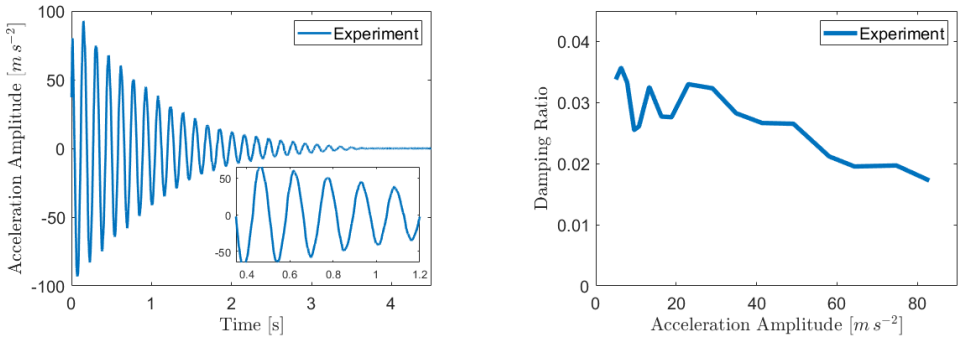

(a) Acceleration (b) Instantaneous damping ratio

Figure 2.8: UPM Experimental acceleration of the tank and estimated instantaneous damping ratio

acceleration data is shown in Fig. 2.8(b). Its value $\zeta^{exp}_{(i,i+1)}$ is assumed to be constant between two consecutive peaks and is evaluated by first selecting the peaks of signal $\ddot{z}_T$ depicted in Fig.2.8(a), and then implementing the following logarithmic decay relation:

$$\zeta^{exp}_{(i,i+1)} = -\frac{\log(\ddot{z}_T(t+\Delta t)) - \log(\ddot{z}_T(t))}{\omega_0 \Delta t} = -\frac{\log(\ddot{z}_T(t_{i+1})) - \log(\ddot{z}_T(t_i))}{\omega_0 \Delta t} = \text{const.} \quad (2.13)$$

where $\omega_0 = 2\pi f_0$ is the natural frequency of the experimental system (see Tab.2.1) and $\Delta t = t_{i+1} - t_i$ is the time interval between two consecutive peaks of the acceleration. To avoid having a piece-wise constant curve, an averaging operation between consecutive constant damping values is performed, providing a continuous curve for damping ζ^{exp}_j (with j being a positive integer index that goes up to number M of samples of the acceleration signal) as the acceleration changes, such as in Fig.2.8(b). This curve of the damping ratio, that is influenced also by the structural damping (viscous and Coulomb), represent the target function to fit. In other words, the bouncing ball, once integrated into the virtual system representing the experiment, should return the same damping estimated with the provided experimental data.

Leveraging the Simulink® model presented in 2.1.1, it is possible to implement the same free response problem as in the reference experiment, with the bouncing ball emulating the dynamics of sloshing liquid impacts. The optimal parameters of the bouncing ball are determined by implementing an optimization process using the simulation model just mentioned. The first step is to collect the vertical acceleration of the tank at each iteration (inside of which the ball bounces and possibly impacts the walls). Then, repeating the procedure already used for the experimental data, the virtual instantaneous damping ratio ζ^{bb}_j as a function of the acceleration signal is determined by using Eq. 2.13. An optimization using a gradient-based method is implemented in Matlab®, aimed at determining the ball parameters that minimize the distance between the two damping curves (experimental and numerical). In other words, the optimal solution is that which minimizes the objective function $J = \sqrt{\sum_{j=1}^{N} \left(\zeta^{exp}_j - \zeta^{bb}_j\right)^2}$. The optimal design parameters are reported in Tab.2.2. They allow to construct a bouncing ball model that is able to return the same dissipative behavior induced by vertical sloshing. In

r_0 [m]	$\hat{k}_b$ [Nm^{-1}]	c_b [Nsm^{-1}]	α [m^{-1}]	β
0.0244	1103.00	13.04	74.04	0.0017

Table 2.2: Optimal parameters of the bouncing ball obtained by tuning the UPM experimental data

fact, as can be seen from Fig.2.9, the identified reduced-order model is able, when integrated into the overall system, to return an acceleration and an instantaneous damping ratio that are practically superimposed on those measured experimentally. By referring to Eqs. 2.9 and 2.10, the force predicted by the bouncing ball can also be compared to the experimentally measured force using load cells. The results are shown in Fig. 2.10, from which it is pos-

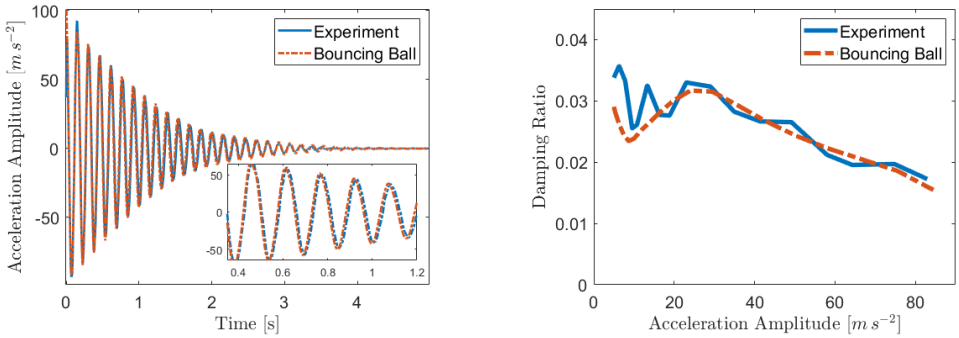

(a) Acceleration (b) Instantaneous damping ratio

Figure 2.9: Acceleration and instantaneous damping ratio provided by the bouncing ball model

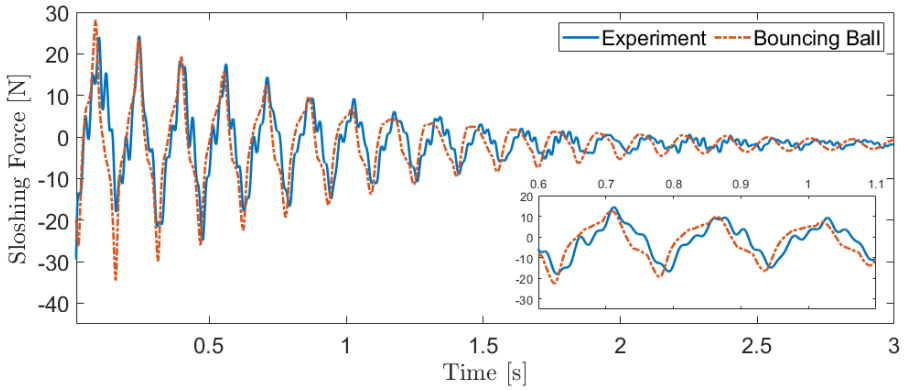

Figure 2.10: Comparison between the sloshing force predicted by the bouncing ball and the one measured from UPM experiment

sible to appreciate how the bouncing ball identified with the optimization process, is able to reproduce with good fidelity the nonlinear behavior of vertical sloshing. However, the force predicted by the ball turns out to be more impulsive than the experimental one and this is due to the impulsive nature of the impacts through which it is modeled.

2.1.2 Characterisation of the nonlinear dissipative behaviour using the bouncing ball model

The bouncing ball model identified in Sec.2.1.1 was able to represent with a good level of accuracy the dissipative actions induced by vertical sloshing in the UPM reference experiment; for this reason, it was decided to use it for a more general characterisation of the sloshing dissipative behaviour. Through the use of the sloshing subsystem (*i.e.* bouncing ball) shown in Fig.2.7 one can easily perform very fast simulations in an *open-loop* mode, testing different types of tank excitation. Since the amount of dissipation induced by the internal dynamics of

the fluid is highly dependent on the amplitude and frequency of the motion imposed on the tank, it is necessary to perform many tests in order to cover a wide region of interest. The first step must be to determine a metric for defining the dissipation. For steady harmonic motion, we can quantify dissipation using a non-dimensional parameter, the loss factor η, defined as follows:

$$\eta := \frac{L_D}{2\pi U_{max}} \tag{2.14}$$

where L_D is the energy dissipated by the sloshing force in a cycle and U_{max} is the maximum elastic (or kinetic) energy of the system (see Appendix A). The objective is then to characterise the dissipation by obtaining a loss factor map in the frequency and amplitude domain of interest. To this end, the bouncing ball subsystem is considered and used to carry out simulations in which the tank containing the equivalent mechanical model is excited with permanent harmonic motion at a fixed frequency and amplitude. More precisely, a large number of simulations are performed for different values of the frequency Ω and amplitude A of the vertical imposed motion, which fall within the following ranges:

$$\begin{aligned} 0.0025\,\text{m} < \quad A \quad &< 0.1\,\text{m} \\ 1.57\,\text{rad/s} < \quad \Omega \quad &< 62.83\,\text{rad/s} \end{aligned}$$

For each of these simulations (with different frequency-amplitude pairs), the sloshing forces produced by the equivalent mechanical model are obtained as output. Once the steady state is reached, the dissipation L_D is evaluated as the work done by the force generated by the bouncing ball on the imposed vertical displacement. This energy quantity will correspond to the area enclosed by the hysteresis cycle in the displacement-force plane (see Appendix A). The cycle shape (with the direction highlighted) for one of the frequency-amplitude pairs taken as an example is shown in Fig. 2.11. By repeating the same process, obtaining the

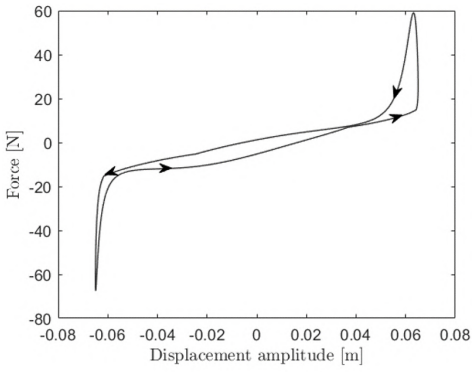

Figure 2.11: Hysteresis cycle generated by the bouncing ball when subjected to steady harmonic motion

hysteresis cycle and evaluating the energy dissipated as the area enclosed by it, for each of the harmonic tests, the dissipation map shown in Fig.2.12(a) is obtained. Black curves representing acceleration iso-lines were also highlighted in it. However, the energy dissipated L_D must be related to the maximum energy supplied to the system (in this case it is an isolated system, in which there is only the tank containing the moving ball). We define this maximum energy U_{max} as the kinetic energy of the system, which can be expressed, for each frequency and amplitude pair, as

$$U_{max} := \frac{1}{2} m_l \, (A\,\Omega)^2 \tag{2.15}$$

Thanks to the definition given in Eq.2.15, it is possible to rewrite the loss factor given in Eq. 2.14 as follows:

$$\eta := \frac{L_D}{2\pi U_{max}} = \frac{L_D}{\pi \, m_l \, A^2 \, \Omega^2} = \eta(A, \Omega) \tag{2.16}$$

Evaluating the loss factor $\eta(A, \Omega)$ for each pair of points in the domain of interest gives the map in Fig.2.12(b). The darker area of the map represents where there is maximum

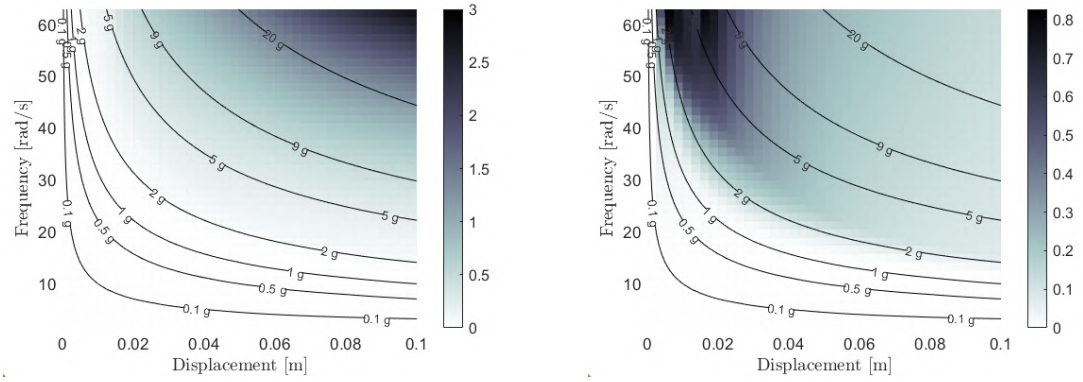

(a) Dissipated Energy L_D

(b) Loss factor η

Figure 2.12: Dissipated energy and loss factor maps obtained with the identified bouncing ball ROM

dissipation (in relation to the energy being supplied). It looks evident how there exists a specific interval of the displacement A (that appears to be between 1 cm and 3 cm) that maximizes the loss factor. Furthermore, one can easily see that the iso-line of acceleration equal to $2g$ acts as a kind of frontier, beyond which dissipation begins to occur. What happens is that, as the acceleration increases above $2g$, the ball starts to detach from the bottom of the tank, possibly resulting in impacts that can be more or less violent. This boundary therefore behaves as a kind of Rayleigh-Taylor stability margin: in real fluids, once a certain value of acceleration is exceeded, chaotic motion and consequent impact with the tank walls are triggered. Figure 2.13 shows the trend of the dissipated energy L_D and the loss factor *eta*

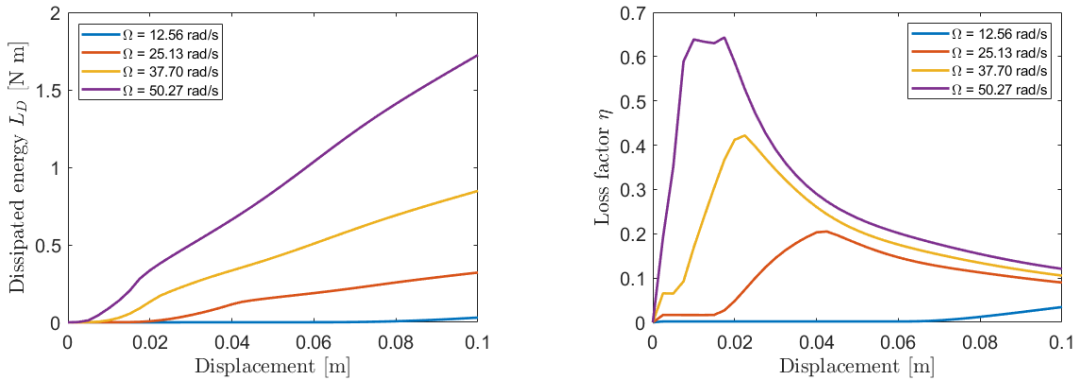

(a) Dissipated Energy L_D (b) Loss factor η

Figure 2.13: Dissipated energy and loss factor for selected frequencies

as the amplitude of the motion varies, for different values of the imposed frequency Ω. From the trends in Fig. 2.13(b) it is even more evident how much the dissipation induced by the bouncing ball (and thus, by sloshing) depends nonlinearly on the frequency and amplitude of the motion. However, we now want to exploit a concept from linear theory to link the loss factor to the damping. In particular, under resonance conditions, the loss factor is found to coincide with twice the instantaneous damping ratio (see Eq.A.22 in Appendix A). This concept is used to compare the two dissipation metrics introduced in relation to the bouncing ball: the instantaneous damping ratio used for the identification and the loss factor for the characterisation of the dissipation in harmonic motion. For the instantaneous damping, we refer to the dashed red curve shown in Fig. 2.9(b), obtained by identifying the parameters of the bouncing ball. This damping curve takes into account not only the damping induced by the bouncing ball, but also those associated with the structure of the experiment: Coulomb and viscous damping (related to the b_0 and b_1 coefficients identified by UPM). In order to isolate the damping associated exclusively with sloshing (*i.e* , bouncing ball), the same simulation of the UPM experiment can be performed with the identified ball, setting the other two damping contributions to zero. The result is shown in Fig. 2.14, where all damping contributions acting in the virtual experiment are compared. Also shown in the same figure is a blue curve representing the instantaneous damping obtained by summing the three separate contributions (sloshing, Coulomb and viscous). This curve is practically superimposed on the dashed red curve corresponding to the same one shown in Fig. 2.9(b). Multiplying by two the values given by the green curve in Fig. 2.14, representing the damping induced by the bouncing ball alone, we obtain a sort of loss factor as the amplitude of the acceleration varies, for the fixed frequency corresponding to the natural frequency of the experimental system. This quantity will be indicated as η_{tr}. From the loss factor map shown in Fig.2.12(b) it is then possible to extract the values obtained at the same frequency of the UPM experiment,

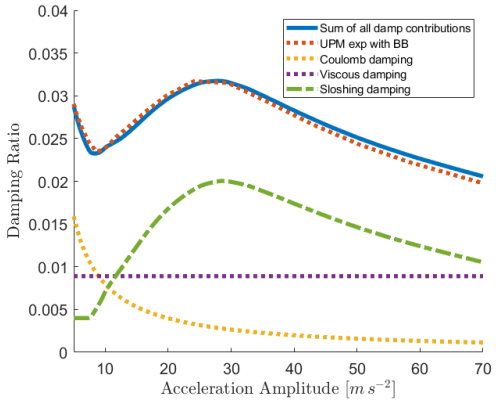

Figure 2.14: Damping contributions in the virtual UPM experiment

indicated as η_{sh}, in order to compare them with η_{tr}. To do this, the following relationship must be implemented

$$\eta_{sh} = \frac{m_l}{(m_l + m_s)} \eta(a, \Omega)\Big|_{\omega_0} = \frac{m_l}{(m_l + m_s)} \eta(a, \omega_0) \tag{2.17}$$

where it has been necessary to consider a corrective mass factor, taking into account the fact that, in order to compare η_{sh} with η_{tr}, it is appropriate to redefine the reference kinetic energy U_{max}. In fact, in the experimental integrated system, the latter is defined as $U_{max} := (m_l + m_s)\, A^2\, \Omega^2/2$. Note also that a is the amplitude of the vertical acceleration and no longer the amplitude of the motion, indicated instead by A. The comparison of the two loss factors is shown in Fig. 2.15, where η_{tr} is the dashed green curve and η_{sh} is the continuous blue one. The two curves almost overlap each other, demonstrating a similarity between the

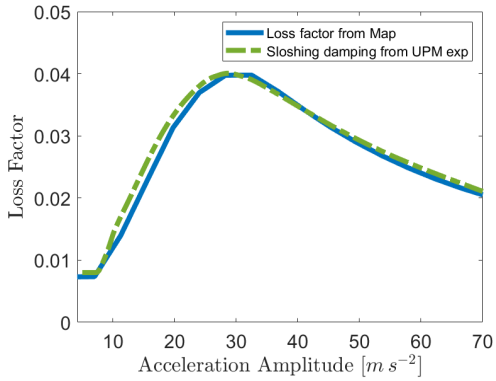

Figure 2.15: Comparison between loss factors: steady harmonic η_{sh} and free decaying η_{tr}

two dissipation metrics used.

In Appendix C, a nonlinear reduced-order model based on a neural network is presented,

trained with the data obtained by simulating the bouncing ball model. It should be noted that this model was identified before the experimental analysis presented in Sec. 1 was conducted. At that time, the only sloshing data available was the experimental free response data provided by UPM. Consequently, following the obtaining of the bouncing ball model, it was decided to exploit the latter to collect low-fidelity data, given its versatility. In other words, the bouncing ball model simulations replaced what in the authors minds should have been represented either by a long experimental campaign designed to investigate the behavior of the fluid or by high-fidelity Computational Fluid Dynamics (CFD) simulations. The good results obtained from this preliminary attempt to use neural network-based identification techniques laid the foundation for what will be shown in the following sections.

2.1.3 Experimental investigation of the bouncing ball ability to estimate dissipation as the frequency varies

The energy dissipated by the sloshing fluid L_d (referred to in the experimental analysis presented in Sec. 1 as work dissipated W) can be expressed by means of the π-theorem as follows:

$$L_d = m_l A^2 \Omega^2 \, \Phi_d \left(\bar{\omega}, \bar{v}, \alpha, Re, Bo, ... \right) \tag{2.18}$$

where, Φ_d is the non-dimensional dissipated energy, equivalent to $\bar{W}$ defined in Sec. 1. Besides the non-dimensional frequency $\bar{\omega} = \Omega / \sqrt{g/h}$ and the non-dimensional velocity $\bar{v} = v / \sqrt{gh}$ (with $v = A\Omega$), L_d is dependent on the fill level α, the Reynolds number $Re = vh/\nu$ (ν kinematic viscosity) that reflects viscosity effects, and the Bond number $Bo = \rho g h^2 / \gamma$ (γ surface tension) that reflects surface tension effects. Furthermore, the choice of non-dimensional operational parameters is arbitrary. Specifically, instead of $\bar{\omega}$ and $\bar{v}$ we could use also the non-dimensional acceleration $\bar{a} = \bar{u}\,\bar{\omega}^2$ and the non-dimensional displacement $\bar{u} = A/h$. The non-dimensional velocity assumes the meaning of Froude number for vertical slosh dynamics (Ref. [29, 30]).

The bouncing ball model can be redefined on the basis of non-dimensional constitutive parameters, exploiting the non-dimensional quantities on which the energy dissipated by sloshing depends. In particular, the five ball parameters defined in Sec.2.1 are redefined in order to be non-dimensional as follows

$$\begin{aligned} \bar{r}_0 &= r_0 / h \\ \bar{k}_b &= \hat{k}_b / (\rho \, g \, S \, \bar{\omega}^2) \\ \bar{c}_b &= c_b / (\rho \, S \, \sqrt{g \, h} \, \bar{\omega}) \\ \bar{\alpha} &= \alpha \, h \\ \bar{\beta} &= \beta \end{aligned} \tag{2.19}$$

where ρ is the liquid density and S is the area of the box-shaped tank base. The non-dimensional parameters defined in Eqs. 2.19 allow a bouncing ball model to be used for different tanks, if the similarity of the non-dimensional frequency $\bar{\omega}$ is guaranteed. The similarity of $\bar{u}$ is implicitly guaranteed when scaling geometric quantities such as h and S, assigning to them the values of the new tank.

As seen in Sec. 2.1.1, the bouncing ball model was identified with transient free response data corresponding to a single frequency (coinciding with the natural frequency of the experimental system considered). However, it is worth investigating how this equivalent mechanical model behaves for frequencies other than the one considered for identification. To this end, the experimental results shown in Sec. 1 are used, which give a more general idea of the dis-

sipative behaviour of vertical sloshing when varying both the frequency and amplitude of the imposed excitation. It should be noted that, the experimental analysis with harmonic tests presented in Sec. 1, was conducted after the one carried out in the UPM laboratories, from which the free response data for the tuning of the bouncing ball was collected. Considering the case with a filling level equal to $\alpha = 0.50$, we refer to the map of non-dimensional dissipated energy depicted in Fig. 1.12, which is shown again below in Fig. 2.16. On the energy map

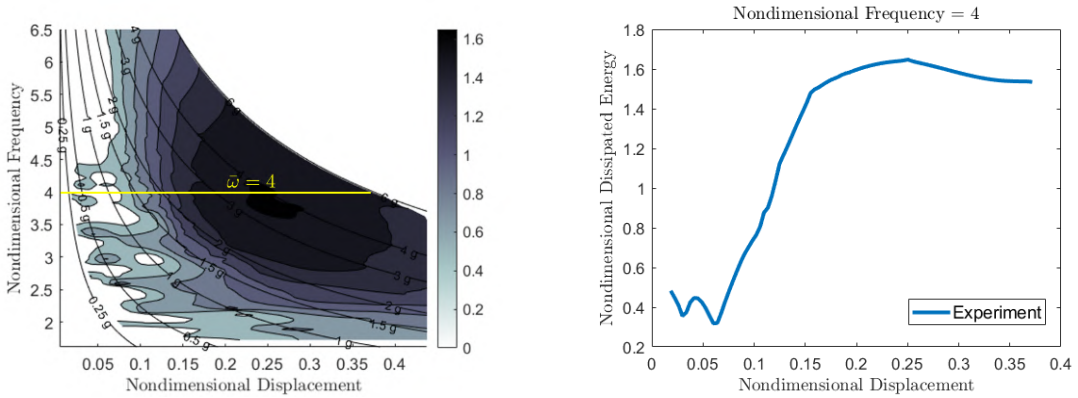

(a) Non-dimensional dissipated energy Φ_d

(b) Φ_d for $\bar{\omega} = 4$

Figure 2.16: Experimental non-dimensional dissipated energy and its trend for $\bar{\omega} = 4$

(see Fig. 2.16(a)), a line is highlighted in yellow, corresponding to the non-dimensional frequency equal to 4. Figure 2.16(b), in turn, shows the trend of the non-dimensional dissipated energy extracted from the points covered by this yellow line. The objective of this study is to implement an optimisation procedure to identify a new bouncing ball with a damping characteristic as similar to the one shown in Fig. 2.16(b) as possible. Once the constitutive parameters of the ball have been obtained, it will be tested at different points in the domain of interest to obtain a map like the experimental one. Then, it will be analysed what is obtained at non-dimensional frequencies other than $\bar{\omega} = 4$.

The identification process cannot be the same as that already seen in Sec. 2.1.1, since in this case there is no structural system (the experimental characterisation of the dissipated energy was carried out using an isolated tank placed on a shaker). However, in order to reproduce a damping like the one in Fig. 2.16(b), the bouncing ball must be excited with decaying harmonic motion (as in the free response of the UPM experiment). For this purpose, a Simulink® model is realised in which the bouncing ball is considered as an isolated system receiving a damped motion as input (in the range of interest defined in Fig. 2.16) defined as follows

$$z_T = c\, e^{-\hat{\zeta}\,\Omega\, t} \cos \Omega\, t \tag{2.20}$$

where c is a coefficient introduced to have an initial condition compliant with the maximum displacement in the map, $\hat{\zeta}$ is an arbitrary damping coefficient, selected to obtain a damped signal, and $\Omega = \bar{\omega}\sqrt{g/h}$ is the frequency corresponding to $\bar{\omega} = 4$, being $h = 2.72$ cm the height of the box-shaped tank used in the shaker-experiment. Assigning the vertical motion defined in Eq. 2.20 to the bouncing ball, the latter respond with a sloshing force F_s defined as in Eq. 2.5. By selecting specific time intervals, the non-dimensional dissipated energy $\Phi_d^{(bb)}$ associated with the bouncing ball can be calculated using the following relationship:

$$\Phi_d^{(bb)} = \frac{1}{m_l\, A^2 \Omega^2} \int F_s \, \mathrm{d}z_T \tag{2.21}$$

A gradient-based optimisation procedure is implemented to find the parameters defined in Eq. 2.19 that minimise the distance between $\Phi_d^{(bb)}$ and $\Phi_d^{(exp)}$ (the blue curve in Fig. 2.16(b)) for $\bar{\omega} = 4$. The optimal non-dimensional parameters obtained are listed in Tab. 2.3 and Fig. 2.17 shows the optimal non-dimensional dissipated energy curve compared to the experimental one.

As demonstrated in the previous sections, the bouncing ball cleverly captures dissipative

$\bar{r}_0$	$\bar{k}_b$	$\bar{c}_b$	$\bar{\alpha}$	$\bar{\beta}$
0.3342	25.28	3.34	52.12	0.0021

Table 2.3: Optimal non-dimensional parameters of the bouncing ball obtained by tuning the shaker-experiment data

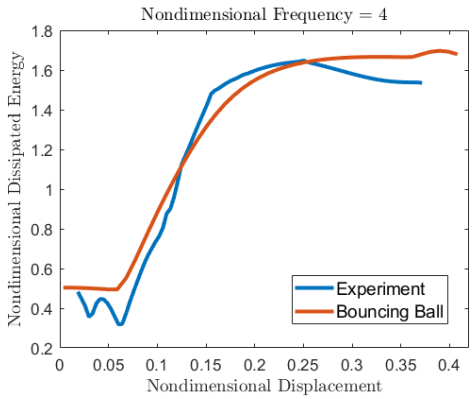

Figure 2.17: Comparison between non-dimensional dissipated energy: experimental $\Phi_d^{(exp)}$ and boucning ball $\Phi_d^{(bb)}$

behaviour at a specific frequency. To understand how it behaves at different frequencies, the same procedure presented in Sec. 2.1.2 is implemented: the new bouncing ball is used for steady harmonic excitation simulations for different amplitude and frequency pairs, with values within the domain of interest; at each simulated operating point, the work (or energy) dissipated by the sloshing forces exerted by the ball is calculated by estimating the area of

the hysteresis cycles in the displacement-force plane. Using this procedure, the bouncing ball with the parameters listed in Tab. 2.3 provides the map for the non-dimensional dissipated energy shown in Fig. 2.18. At $\bar{\omega} = 4$ this map returns what is shown in Fig. 2.17 (in

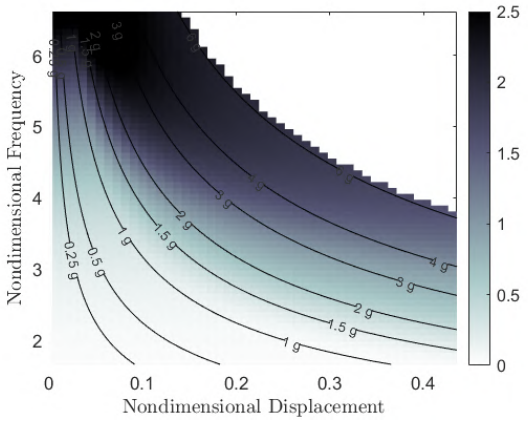

Figure 2.18: Non-dimensional dissipated energy map provided by the bouncing ball obtained by tuning the shaker-experiment data

agreement with what has already been obtained in Fig. 2.15). However, for frequencies other than the one used for identification, the scenario is different. Comparisons of the non-dimensional dissipated energies estimated by the bouncing ball at frequencies different from $\bar{\omega} = 4$ are shown in Fig. 2.19. As can be seen, the bouncing ball cannot accurately estimate the dissipative behaviour induced by vertical sloshing for different frequencies. This leads to the conclusion that this equivalent mechanical model can only be used for applications where the operating conditions are the same as those considered for its identification.

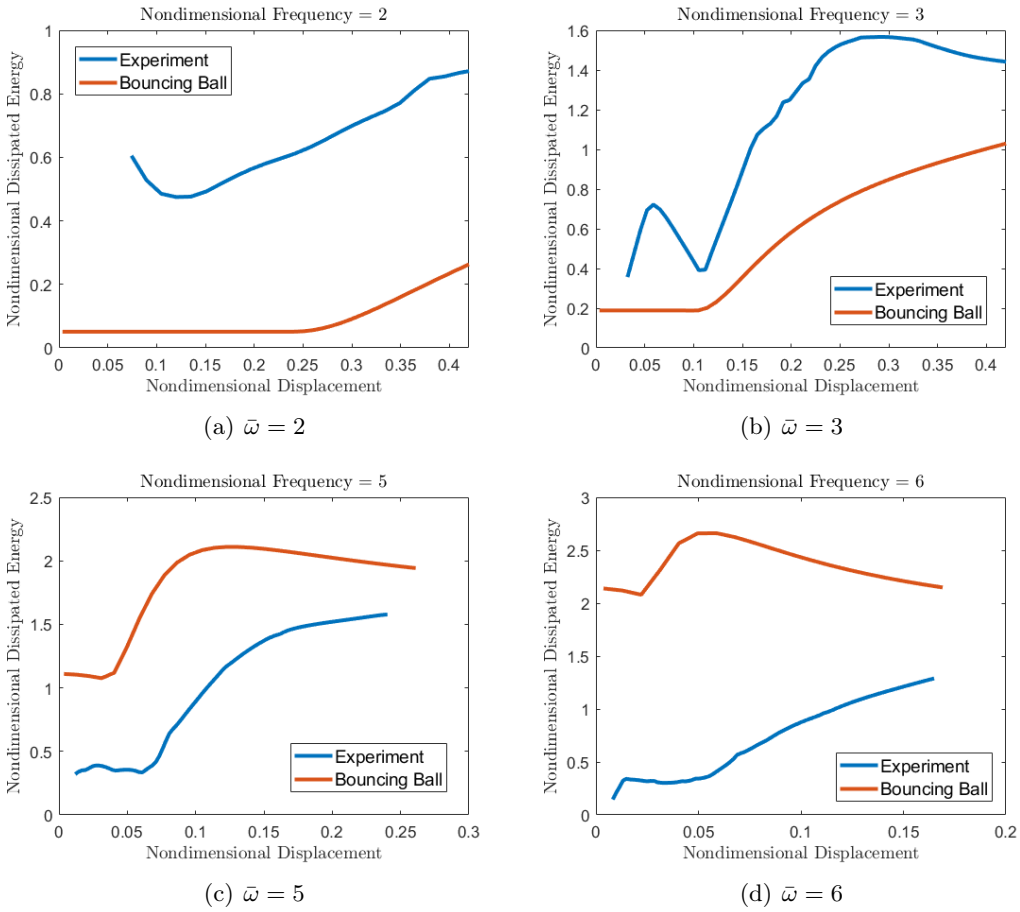

(a) $\bar{\omega} = 2$ (b) $\bar{\omega} = 3$

(c) $\bar{\omega} = 5$ (d) $\bar{\omega} = 6$

Figure 2.19: Bouncing ball model capability to estimate dissipation at different operating frequencies

2.2 Vertical sloshing reduced order modeling with neural network based nonlinear models

Section 2.1.3 highlighted the main limitation of the bouncing ball equivalent mechanical model defined in Sec. 2.1: inaccuracy in estimating dissipative behaviour induced by vertical sloshing at frequencies other than the one considered for model identification. As a result, the bouncing ball is hardly applicable in multi-frequency problems. This awareness led to the exploration of different techniques for the identification of nonlinear systems, searching for solutions that could handle the aforementioned problem.

In order to obtain a model capable of describing the nonlinear dynamics of vertical sloshing, it was decided to use dynamic systems identification techniques based on the use of data and machine learning theory. The dynamics to be modeled can be treated as a black box process, since the relationships linking the quantities that describe it are not known. This leads us to face the problem of identifying a surrogate model, working only with those signals that will

then be selected as inputs and outputs, without knowing the internal dynamics. In addition, for training the model, it is essential to collect data that adequately covers the input space. To this end, input-output data from high-fidelity numerical simulations (CFD) or experiments with varying frequencies and amplitudes are likely to be the most useful for implementing this technique.

An experiment aimed at characterising the dissipative behaviour of vertical sloshing based on harmonic motion, by varying the two operating parameters mentioned above, has already been presented in Sec. 1. The same configuration is used to collect experimental data for the identification of a nonlinear reduced-order model (ROM) that takes advantage of artificial neural networks (ANN) properties (see Appendix B). Specifically, this phase reflects an *open-loop* problem, where the process to be identified, vertical sloshing, is considered as an isolated system that allows to obtain data. The latter will be referred to as harmonic data with Variable Frequency and Amplitude (VFA). Appendix C presents what was an initial attempt to apply these methods in the context of vertical sloshing, but relying on low-fidelity data (obtained by testing the bouncing ball with vertical harmonic excitations for different frequency and amplitude pairs). The model identified consisted of a dynamic feedforward neural network (FFNN).

The purpose of this section is to first describe how the experimental data used for the identification of the new reduced order model are generated. Then, a sensitivity analysis on the neural-network-based model constitutive parameters is carried out to select the structure that most accurately describes the process to be identified. Two main types of models are described and considered for this analysis: one strictly feedforward and another recurrent, in which the output signal is fed to the model as additional input. The model selection is based on comparing the training loss value. After the presentation of the process of identifying the reduced-order model, a further analysis that was conducted in order to validate it experimentally is also introduced. Specifically, a new experimental configuration is set up, in which the same tank used to generate the training data (which also include an additional set of VFA data to help the training avoid overfitting) is mounted at the free end of a cantilever beam. This particular set up will be referred to as the *sloshing beam problem*, and the experimental data generated for comparison and validation will be provided by free response and random testing. To carry out the comparison, a virtual simulation model is designed to conform to the *closed-loop* logic of the experiment, in which the numerical model of the beam interacts with the reduced-order model simulating the sloshing dynamics.

2.2.1 Experimental data collection for ROM identification

The experimental setup presented in Chapter 1 was used to generate a training and validation data set for the identification of a neural-network based ROM capable to predict the desired sloshing forces. The advantage of using this configuration (reproduced in Fig. 2.20)

stems from the fact that it allows the sloshing dynamics to be studied as an isolated system, guaranteeing that its constitutive properties can be highlighted. Two additional harmonic

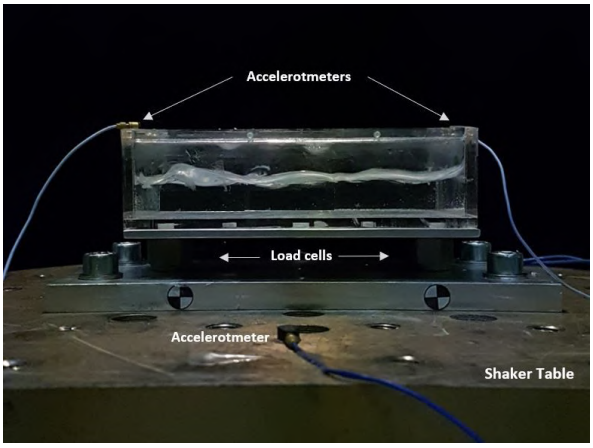

Figure 2.20: Experimental Configuration of the isolated sloshing-tank (see Fig. 1.2).

tests with variable frequency and amplitude (VFA) were performed, by considering the filling level corresponding to the 50 %. Indeed, two tests with acquisition time of $480\,s$ and $240\,s$ are used for the collection of training and validation data. In these experimental tests, the vertical sloshing fluid is considered as an isolated system that receives as input a motion (or acceleration) imposed to the boundary by the electrodynamic shaker and returns as output a force. The excitation provided by the shaker, which is controlled in order to impose a vertical acceleration with the law $\ddot{u} = f(t)\left[\cos(\int_0^t \Omega(\tau)\mathrm{d}\tau)\right]$, was such as to suitably cover the non-dimensional frequency $\bar{\omega}$ and amplitude $\bar{u}$ domain of interest, following the path shown in Fig. 2.21. The choice of this path was dictated by the need to acquire the most representative data possible to describe the dissipation induced by vertical sloshing characterised in Sec. 1.4.2 and shown in Fig. 1.12.

The time series needed for training the neural network were obtained by acquiring sensor measurements. In particular, from the accelerometers we obtain the signal associated with the motion imposed by the shaker, while from the load cells we obtain the force exchanged at the fluid-tank interface. Integrating the acceleration signal yields the velocity signal given by the vertical shaker motion shown in Fig. 2.22(a). This signal assumes the role of the input of neural network model to be identified. On the other hand, load cells are used to acquire the force that is exchanged at the interface between shaker and tank. In this study, sloshing force is decomposed into two contributions (as already defined in Eq. 1.19): the inertial force according to the frozen fuel modeling (Ref. [25]) and the perturbation resulting from the relative motion of the fluid particles within the tank, denoted as *dynamic sloshing force*

$$F_{S_z} \quad = \quad -m_l\,\ddot{u} + \Delta f_{S_z} \tag{2.22}$$

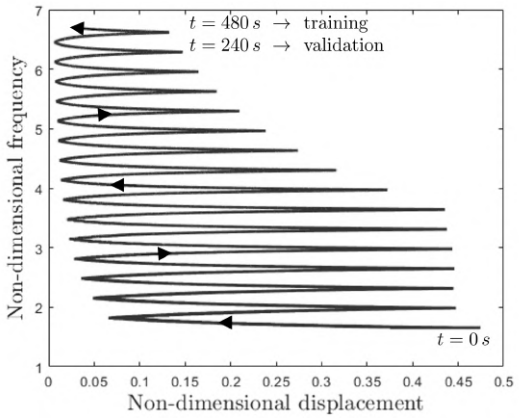

Figure 2.21: Path of the VFA harmonic tests considered for training and validation data collection

where m_l is the overall fluid mass. As the inertial contribution $-m_l\,\ddot{u}$ is linear and conservative with respect to the input, it is convenient to identify directly the dynamic sloshing force Δf_{S_z}. Therefore, in order to obtain the dynamic sloshing force in Fig. 2.22(b), it is necessary to subtract from the force measured by the load cells the inertial contribution of the liquid $-m_l\ddot{u}$ and the supporting structure of the box which lies on top of the load cells. Figure 2.23(a), shows the input signal of the validation data set, obtained with the shorter VFA harmonic test (240 s long), in the frequency-amplitude domain. Figure 2.23(b) shows the trend of the dynamic sloshing force of the validation data set.

2.2.2 Identification of the neural-network-based ROM for vertical sloshing

In order to identify a nonlinear reduced order model for vertical sloshing it was decided to exploit an external dynamics strategy, that is, by far, the most widely used approach for modeling and identifying nonlinear dynamical systems. The name "external dynamics" indicates that the nonlinear dynamic model can be uniquely divided into two parts: a nonlinear static (*i.e.*, memory-less) approximator and an external dynamic filter bank (Ref. [56]). Any function $g(\cdot)$ can be chosen for the static approximator. However, it should be able to cope with relatively high-dimensional mappings, at least for high-order systems (the system order is indicated as m). If filters are chosen as simple time delays and the approximator is chosen as a fully connected neural network, the whole model is usually called a *time-delay neural network* (TDNN). This type of model has the property of being a universal dynamic mapper. Figure 2.24 shows a nonlinear input/output model built using the external dynamics approach, where $x(k)$ and $y(k)$ are the measured input and output data of the process to be identified (at the current discretised time instant k). The estimate of the output produced from the identified model is instead represented by $\hat{y}(k)$. As can be seen from the figure, this approach can generate an output prediction by receiving both past input and output values (if available

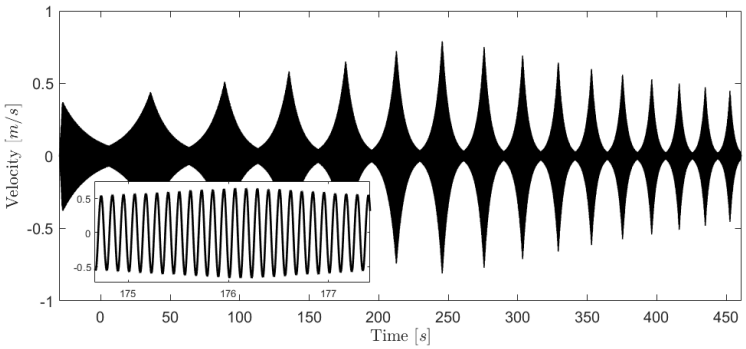

(a) Velocity imposed on the tank

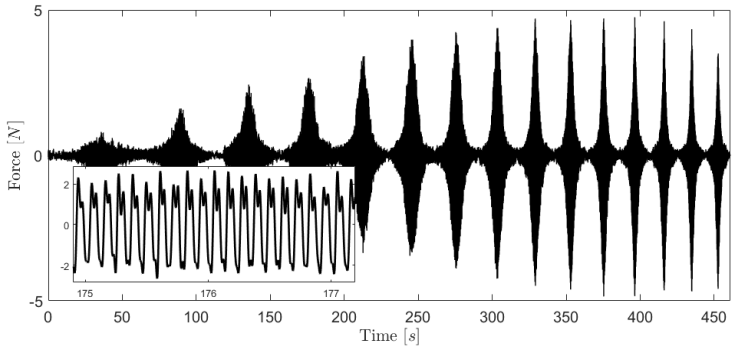

(b) Dynamic sloshing force

Figure 2.22: Input-Output time histories for data-driven ROM training process

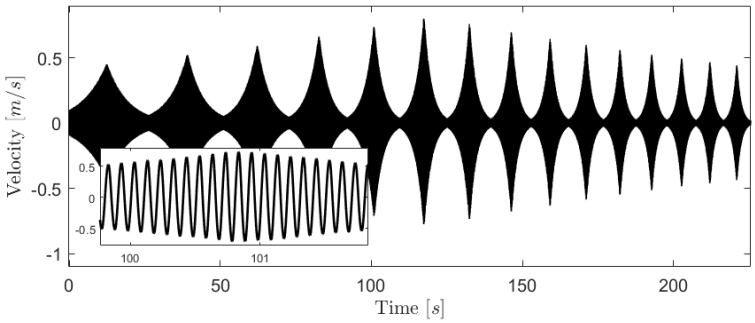

(a) Velocity imposed on the tank

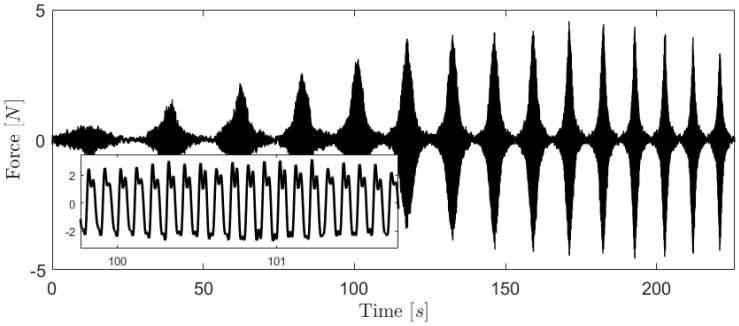

(b) Dynamic sloshing force

Figure 2.23: Input-Output time histories for data-driven ROM validation

during simulations).

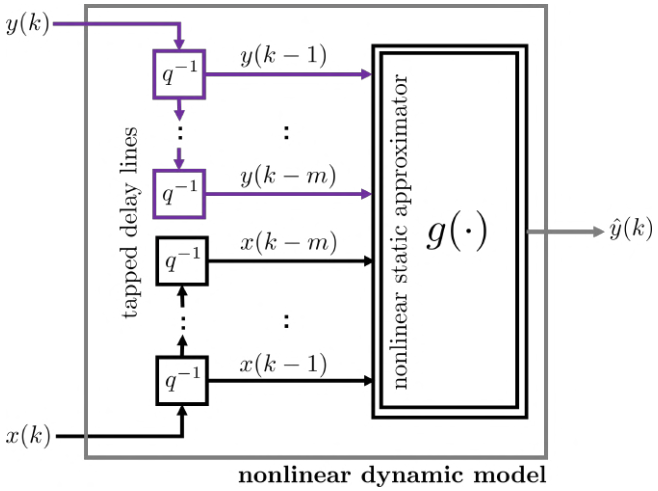

Figure 2.24: External dynamics approach: the model is separated into a nonlinear static approximator and an external filter bank, realised as tapped-delay lines

A nonlinear dynamic model can be used in two configurations: for prediction and for simulation. *Prediction* means that on the basis of previous process inputs $x(k-i)$ and process outputs $y(k-i)$, the model predicts one or several steps into the future. A requirement for prediction is that the process output is measured during operation. In contrast, *simulation* means that the model simulates future outputs on the basis of previous process inputs $x(k-i)$ (and, eventually, also estimated outputs $\hat{y}(k-i)$). Thus, simulation does not require process output measurements during operation. The one-step prediction configuration is called a *series-parallel model*, while the simulation configuration is called a *parallel model*. Figure 2.25 compares the model configuration for prediction (a) and simulation (b).

The two configurations shown in Fig.2.25 cannot only be distinguished for the model architecture but also for the training process. The model is trained by minimising a loss function dependent on the error $e(k) = y(k) - \hat{y}(k)$. For the series-parallel model, $e_{sp}(k)$ is called the equation error, and for the parallel model, $e_p(k)$ is called the output error.

The model that performs the prediction is purely *feedforward* (i.e., the information is propagated from the input to the output without any feedback). While, the simulation model, beyond being feedforward (in the case in which the static approximator receives in input only the passed values of the input), can be also *recurrent*, if the feedback of the output predicted from the same model is considered. All nonlinear dynamic input/output models can be written in the following form

$$\hat{y}(k) = g\left(\boldsymbol{\varphi}(k)\right) \tag{2.23}$$

where $\boldsymbol{\varphi}(k)$ is the regression vector containing previous and possibly current process inputs, previous process or model outputs, and previous prediction errors. So basically the vector of

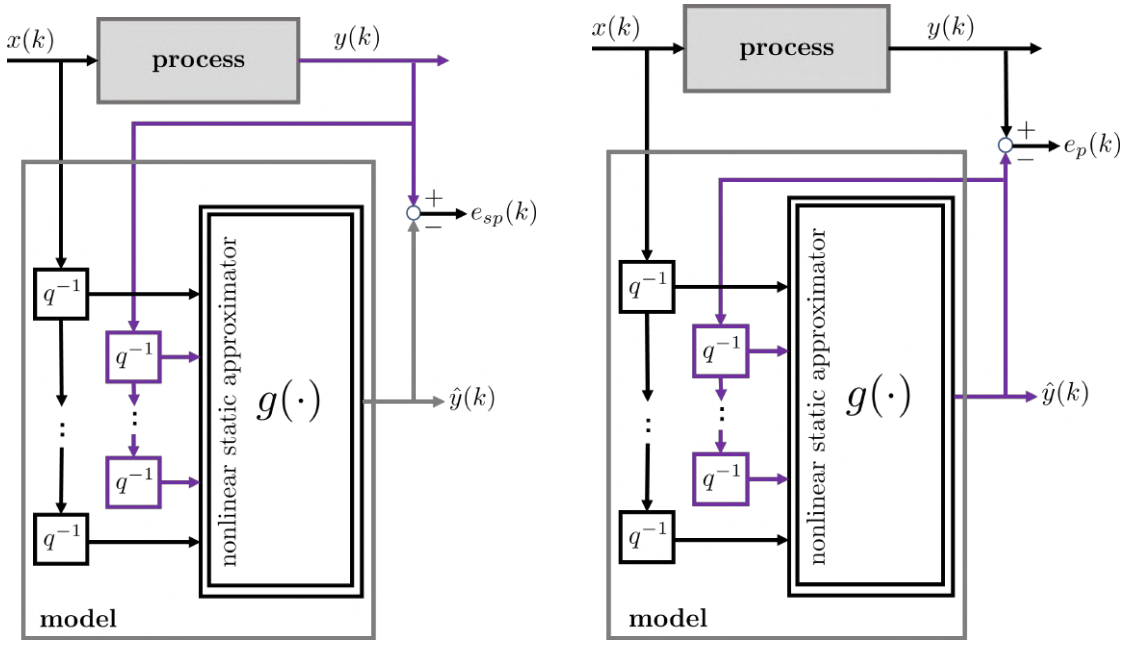

(a) Prediction with a series-parallel model

(b) Simulation with a parallel model

Figure 2.25: External dynamics approach models: (a) series-parallel. (b) parallel

regressors collects within it all the signals that come out of the tapped-delay lines and are then fed to the approximator. Two types of models can be distinguished: with and without output feedback.

The regression vector $\boldsymbol{\varphi}(k)$ of the models with output feedback contains previous process or model outputs and possibly prediction errors. The three most common nonlinear model structures are NARX (nonlinear autoregressive model with exogenous inputs), NARMAX (nonlinear autoregressive moving average model with exogenous input) and NOE (nonlinear output error model):

- NARX: $\boldsymbol{\varphi}(k) = [x(k-1)\cdots x(k-m)\ \ y(k-1)\cdots y(k-m)]^{\mathrm{T}}$
- NARMAX: $\boldsymbol{\varphi}(k) = [x(k-1)\cdots x(k-m)\ \ y(k-1)\cdots y(k-m)\ \ e(k-1)\cdots e(k-m)]^{\mathrm{T}}$
- NOE: $\boldsymbol{\varphi}(k) = [x(k-1)\cdots x(k-m)\ \ \hat{y}(k-1)\cdots \hat{y}(k-m)]^{\mathrm{T}}$

The NARX model is trained in series-parallel configuration and the NOE model is trained in parallel configuration. The NARMAX model requires both process outputs $y(k-i)$ and model outputs $\hat{y}(k-i)$ contained in $e(k-i)$. One drawback of models with output feedback is that the choice of the dynamic order m is crucial for the performance and no really efficient methods for its determination are available. Another disadvantage of output feedback is that, in general, stability cannot be proven for this kind of model. Generally, however, the user is left with extensive simulations in order to check stability.

In opposition to these drawbacks, models with output feedback compared with those without output feedback have the strong advantage of being a very compact description of the process. As a consequence, the regression vector $\boldsymbol{\varphi}(k)$ contains only a few entries, and thus the input space for the approximator $g(\cdot)$ is relatively low dimensional.

The NARX model should be used for training if the model is to be applied for prediction. The NARX model minimises exactly this prediction error and is simpler to train than NOE. On the one hand, the NOE model is advantageous because it yields the optimal simulation error, which is exactly the goal of modeling. The NARX model is simpler to train. A recommended strategy (see Ref. [56]) is to train a NARX model first and possibly utilize it as an initial model for a subsequent NOE model optimization. The training of an NOE model independently of the chosen approximator always requires nonlinear optimization schemes with a quite complex gradient calculation due to their recurrent structure. In contrast to NARX models, an NOE model can discover an *error accumulation* that might lead to inferior accuracy or even model instability.

When no output feedback is involved, the regression vector $\boldsymbol{\varphi}(k)$ contains only previous or filtered inputs. The number of required regressors for models without output feedback is significantly higher than for models with output feedback. Therefore, only approximators that can deal well with high-dimensional input spaces can be applied. The most important model is the NFIR (nonlinear finite impulse response model):

- NFIR: $\boldsymbol{\varphi}(k) = [x(k-1)\ x(k-2) \cdots x(k-m)]^{\mathrm{T}}$

This type of model bypasses all the problems of previous models, mainly related to the presence of feedback. The price to be paid for the missing feedback is that the dynamic order m has to be chosen very large to describe the process dynamics properly. Theoretically, the dynamic order must tend to infinity ($m \to \infty$). Since NFIR models are not recurrent but purely feedforward, their stability is ensured (Ref. [49]), although an NFIR model can represent an unstable process for the first m sampling instants in a step or impulse response.

In the analysis to be presented in this section, only simulation-oriented models are considered in order to identify a digital-twin for vertical sloshing. Therefore, only parallel models, such as the NFIR model and the NOE model, will be tested to conduct a sensitivity analysis on their constituent parameters, aimed at identifying the best performing model. The NFIR model's static approximator will only receive as input the vertical velocity passing through the delay lines, whereas the NOE model's static approximator, in addition to receiving the velocity, will also be fed with the predicted dynamic sloshing force (once it has passed through the delay lines). The static approximator of both considered model types is precisely a neural network having a hidden layer and an output layer. Normalised radial basis functions are employed as activation functions in all nodes of the hidden layer, while the output layer consists of a simple linear function (see Appendix B for more details). By using Gaussian activation

functions, neural networks are ensured to be universal approximators, due to their inherent properties (Ref. [88]). The reliability of the models is assessed based on the training loss value, that is the Mean Squared Error (MSE).

The *velocity-force* input-output data obtained with the VFA harmonic experimental tests have been used for the training of the networks. The algorithm used consists of *Levenberg-Marquardt* backpropagation implemented in Matlab® through the *trainlm* function (Ref. [89]). The networks learn directly from the training data shown in Fig.2.22, while the validation data, shown in Fig.2.23, are not involved in the process of estimating its weights. All the tested models underwent a training process that stops after the error rate on the validation data increase continuously for more than 6 epochs. NFIR models are trained directly in their original form, while NOE models require an intermediate step. Specifically, a NARX model having the NOE desired structure - but using feedback from the measured output rather than the predicted output - is first trained. The weights obtained from the NARX training are then used to initialise the NOE recurrent network training process. Sensitivity analysis is performed considering for NFIR models 3 different filter banks with 50, 60 and 70 delay lines for the input velocity and with a variable number of hidden layer neurons from 5 to 40. While for NOE models the only architectures that in our trials guaranteed stability are those having 2 delay lines for both velocity and predicted output and a number of hidden layer neurons equal to 10, 15 and 20. The results of the sensitivity analysis are shown in Fig. 2.26, in terms of the trend of MSE as the number of neurons and selected delay lines changed. Each MSE

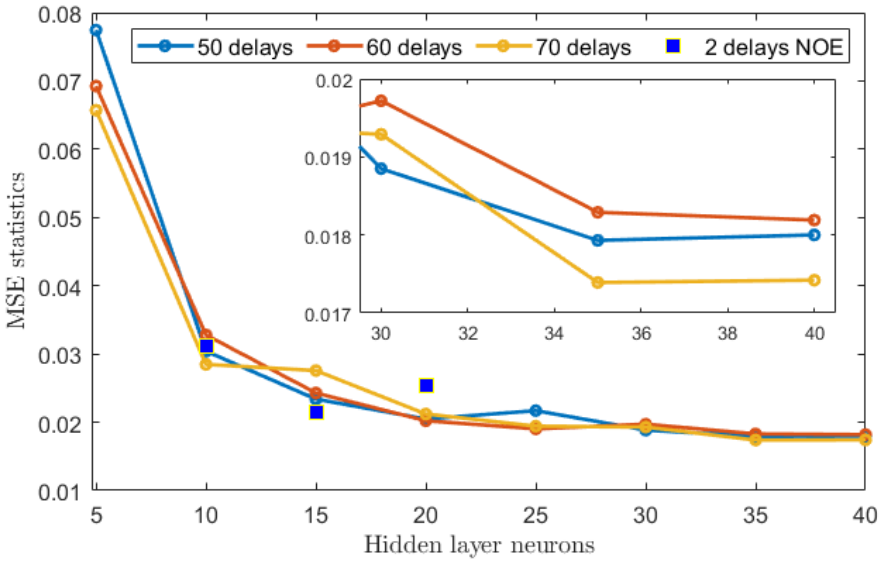

Figure 2.26: Sensitivity analysis for NFIR and NOE models with varying number of neurons and number of delay lines.

displayed is equal to the average of the MSE computed on the training data and the validation

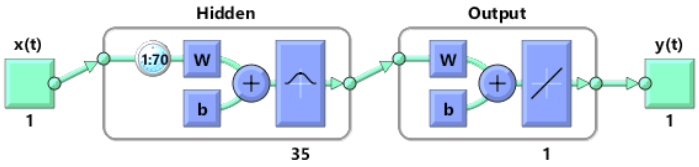

Figure 2.27: Architecture of the identified Time-Delay Neural Network: NFIR model with 70 tapped delay lines and 35 hidden layer neurons

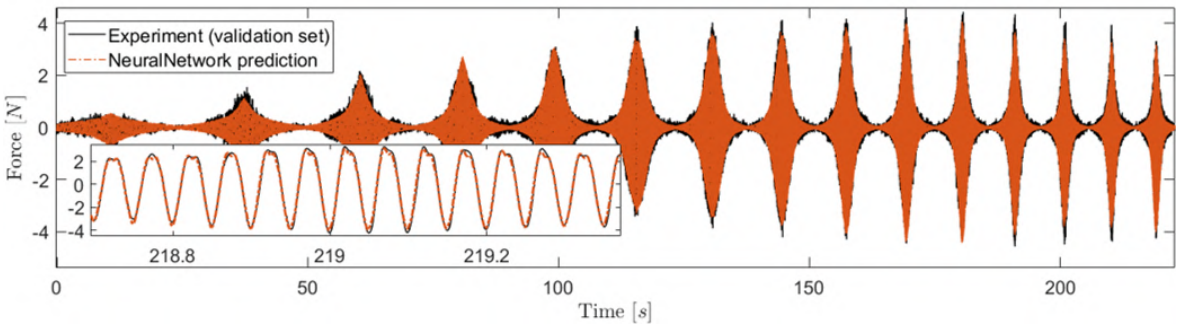

Figure 2.28: Comparison between the output predicted by the identified neural network and the experimental time history of the force used for the validation

data obtained at the end of the training process. Figure 2.26 shows that as the number of neurons increases, the NFIR models perform much better than the only stable NOE models identified. Since the convergence looks to be reached for the NFIR models after 35 neurons, the model with 70 tapped delay lines and 35 neurons results to be the candidate for being used in FSI simulations. The architecture of this model is shown in Fig.2.27. The selected network was then converted into a Simulink® block to simulate it and obtain predictions for the output. Figure 2.28 shows the dynamic sloshing force (in red) that the network predicts when it is excited with a velocity equal to that used for the validation data set generation (see Figs. 2.23(a)), compared to the validation force (in black). From the comparison figure, it looks like the identified network is able to accurately replace the nonlinear behaviour of sloshing.

Finally, by performing tests varying the frequency and amplitude of excitation in the domain of interest, the sloshing dissipated energy was evaluated based on the predictions provided by the neural network. The result is the nondimensional dissipated energy map shown in Fig. 2.29, that is in good agreement with the experimental map shown in Fig. 1.12, thus demonstrating that the neural network based ROM is a reliable digital twin of the vertical slosh dynamics.

Good performances can also be achieved with lighter NFIR models - in terms of the number of delays and neurons - having a higher training loss value. In fact, the output predicted by the

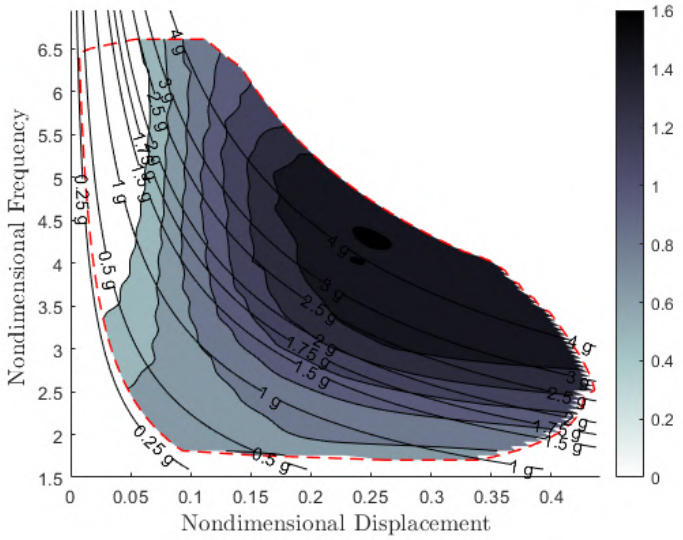

Figure 2.29: Nondimensional Dissipated energy map predicted by the neural-network-based NFIR model

selected model has a fitting [1] of $e_f = 85\%$ with the experimental validation target, whereas, for example, the NFIR model with 60 delay lines and 20 neurons has a slightly lower fitting corresponding to $e_f = 83.4\%$. Moreover, the latter requires a lower computational cost in the simulation phase. Thus, the model with fewer parameters could also be used instead of the one selected to run faster simulations, but with the awareness of having slightly less accurate (but still reasonable) estimates of the dynamic sloshing force.

2.2.3 The sloshing beam problem

This section introduces the experimental strategy used to validate the reduced-order model for sloshing identified in Sec. 2.2.2. Specifically, the section consists of a first part in which the analytical formulation used to describe the problem of a structural system interfacing with vertical sloshing dynamics is presented. The second part on the other hand, describes a new experimental setup representing the sloshing beam problem. This is used to generate data to be used as a benchmark for the experimental validation of the identified model.

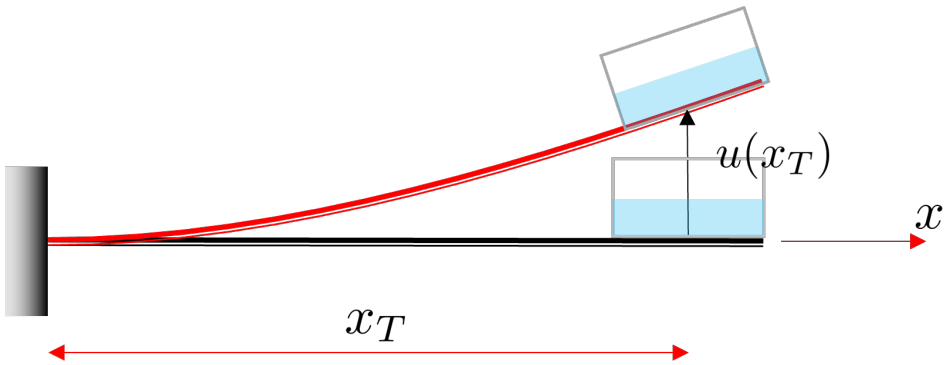

Figure 2.30: Sloshing beam problem.

Analytical formulation of the sloshing beam integrated system

In this section, the mathematical formulation for the dynamic description of the sloshing beam system shown in Fig. 2.30 is presented. The problem consists of a cantilever beam characterized by a purely vertical linear displacement field, with a partially filled tank placed at its free end. The latter is assumed perfectly symmetrical with respect to the vertical plane passing through the elastic center. The structural transversal displacement for a one-dimensional bending beam $u(x,t)$ can be expressed as

$$u(x,t) \simeq \sum_{n=1}^{N} \psi_n(x) q_n(t) \tag{2.25}$$

where $\psi_n(x)$ is the n-th mode of vibration of the structure and $q_n(t)$ is the n-th modal coordinate describing the body vertical displacement in time. This analysis uses a modal representation involving a finite number of modes N, which corresponds to describing the system in a limited frequency band. Considering the displacement representation defined in Eq. 2.25 for the beam dynamics, one has the following Lagrange equations of motion in terms of N modal coordinates $q_n(t)$:

$$\mathsf{M}\ddot{\mathsf{q}} + \mathsf{K}\mathsf{q} = \mathsf{g} + \mathsf{f}^{(ext)} \tag{2.26}$$

where $\mathsf{M} = \mathrm{diag}(m_1, m_2, \ldots m_N)$ and $\mathsf{K} = \mathrm{diag}(k_1, k_2, \ldots k_N)$ are, respectively, the modal mass and stiffness diagonal matrices, whereas $\mathsf{g} = [g_1, g_2, \ldots, g_N]^{\mathrm{T}}$ is the vector of the generalised *sloshing* forces non-linearly induced by the elastic motion q. The $\mathsf{f}^{(ext)}$ is the vector

[1] An evaluation of the goodness of fit between the neural network prediction $\hat{\mathsf{y}}$ and the target signal y can be performed by employing the error function e_f defined as follows

$$e_f := 100 \times \left(1 - \frac{\|\mathsf{y} - \hat{\mathsf{y}}\|}{\|\mathsf{y} - \hat{\mathsf{y}}_m\|}\right) \tag{2.24}$$

where $\hat{\mathsf{y}}_m$ is the mean value of the predicted output.

of the current external forcing terms. The natural frequency of the n-th mode is indicated as $\omega_n = \sqrt{k_n/m_n}$.
The n-th component of $\mathbf{g}$ is the projection of the liquid-induced internal pressure distribution p_S on each n-th modal shape ψ_n by integrating the inner product on the n-th tank wet surface $\mathcal{S}_{tank}$ as in the following ($\mathbf{n}$ unit normal vector to $\mathcal{S}_{tank}$ and $\mathbf{k}$ vertical unit vector)

$$g_n = -\oiint_{\mathcal{S}_{tank}} p_S \; \mathbf{n} \cdot \mathbf{k} \, \psi_n \, d\mathcal{S} \tag{2.27}$$

By assuming a rigid tank identified by its geometrical centre, Eq. 2.27 can be recast as:

$$g_n = f_S \, \psi_n(x_T) + m_S \, \varphi_n(x_T) \tag{2.28}$$

where f_S and m_S are, respectively, the sloshing force and moment applied in the geometric centre of the tank x_T, whereas $\varphi_n(x_T)$ is the n-th modal rotation of the point x_T. The dynamic sloshing force Δf_{S_z} is a nonlinear function of the history of the tank vertical displacement $u(\mathbf{x}_T, t)$.
Assuming that the moment m_S about the geometric center of the tank is negligible, and considering the decomposition of the sloshing force as in Eq. 2.22, Eq. 2.28 can be recast as:

$$g_n = -\sum_{k=1}^{N} m_l \, \psi_n(x_T) \, \psi_k(x_T) \, \ddot{q}_k + \psi_n(x_T) \, \Delta f_{S_z} \tag{2.29}$$

It is worth to remind that the dynamic sloshing force Δf_{S_z} is a non-conservative force that is a nonlinear function of the history of the tank vertical displacement and corresponds to the output used for training the neural network in Sec. 2.2.2.

Experimental test case of the sloshing beam

The tank presented in Sec. 2.2.1, used to generate the data for the identification of the reduced-order model, is placed at the end of a cantilever beam in order to obtain a new experimental configuration, shown in Fig. 2.31, aimed at studying the interaction between the liquid stowed in the box and the beam. The vertical sloshing dynamics and the beam structural dynamics interface with each other, defining a *closed-loop* problem, through the motion imposed by the structure and the load provided by the liquid impacting with the internal walls of the tank. These two actions are measured by means of accelerometers and load cell sensors properly placed on the experimental system (see Fig. 2.31). The beam is $74\,cm$ long, $10\,cm$ large, $1\,cm$ thick. Table 2.4 shows the main modal quantities of the first three modes of vibration of the cantilever beam in the configuration with frozen liquid, defined as the case in which $\Delta f_{S_z} = 0$. In experimental practice, this reference configuration, useful for assessing the effects that sloshing induces on the system response, was realized by replacing

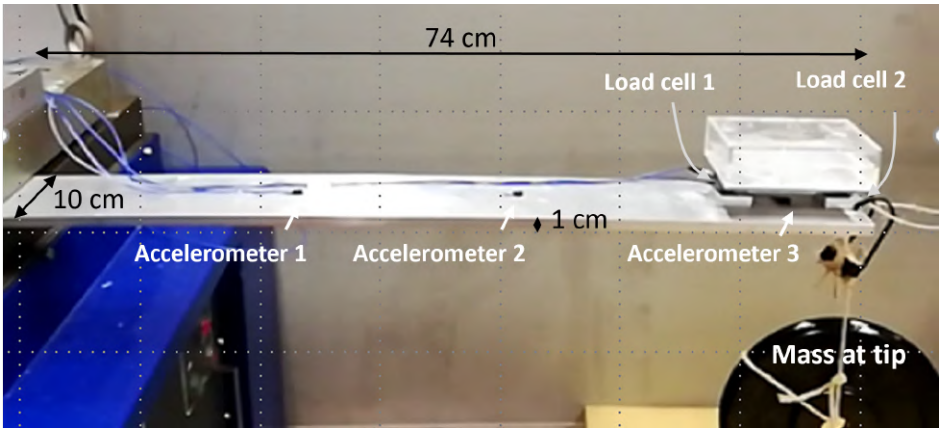

Figure 2.31: Layout of the experimental FSI problem

Mode	Experimental		Numerical	
n	$f_n^{(exp)}$ [Hz]	ζ_n [%]	$f_n^{(num)}$ [Hz]	m_n [kg]
1	10.87	0.32	10.87	0.8956
2	79.06	0.90	78.31	1.0692
3	223.15	1.76	226.5	0.9655

Table 2.4: Experimental and numerical natural frequencies f_n, modal damping coefficients ζ_n and modal masses m_n of the cantilever beam with frozen liquid at the free end.

the liquid with an equivalent non-sloshing mass. The experimental natural frequencies $f_n^{(exp)}$ are listed, as well as the numerical frequencies $f_n^{(num)}$ derived by a structural model updating process. In addition, the table also shows the experimental modal damping coefficients. The modal masses of the beam are also listed based on the numerical model obtained with the structural updating process.

The sloshing beam presented in this section is used to obtain experimental reference data that can be used to validate the identified reduced-order model. Free response data as well as random seismic excitation at the root provided by the shaker are used to assess the identified ROM performances.

Free response analysis

Similarly to Refs. [10], a free-response problem was considered in this work, where an initial displacement is assigned to the free end of the beam. With the release of the beam tip, the interaction between liquid and structure is triggered. The free response results are shown in Fig. 2.32 showing the effects induced by sloshing on the system response compared to the frozen case. A weight of 7 kg (see Fig. 2.31) was used to provide an initial vertical displacement of the beam tip of 1.46 cm that provide initial acceleration in line with the

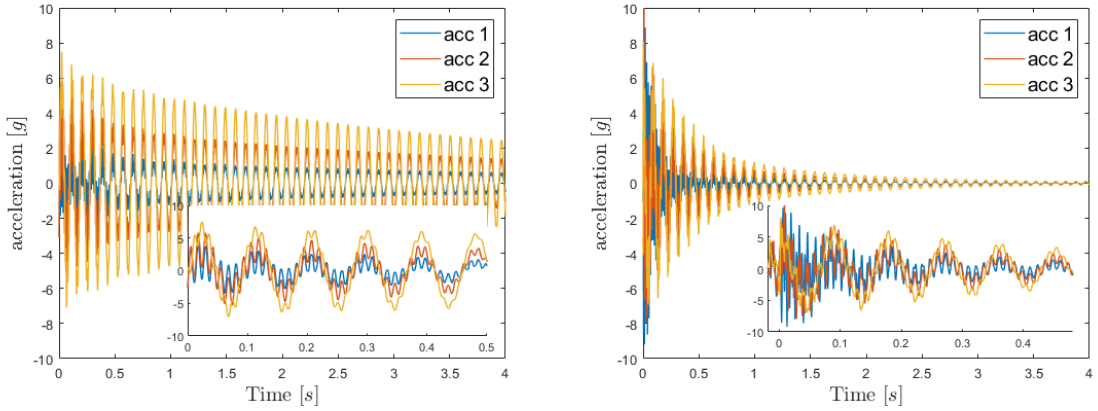

(a) Frozen case

(b) Sloshing case

Figure 2.32: Comparison between acceleration signals measured by the sensors in the case where the liquid is considered as frozen (a) and in the case where it is free to move (sloshing) (b).

maximum acceleration provided during the training process. Figure 2.32 shows the time trends of the free acceleration response signals measured by the accelerometers for the frozen case in Fig. 2.32(a) and the sloshing case in Fig. 2.32(b)). The impacts of the liquid with the ceiling of the tank, which occur in the initial stages of the response, lead to considerable dissipation of energy, resulting in more damped responses than in the frozen case. This can also be appreciated from Fig. 2.33, in which two different instants of the sloshing beam response are shown. In particular, in the first instants of the response, the liquid impacts violently with the ceiling of the tank (see Fig. 2.33(a)) inducing considerable damping in the response. Once the initial phase of the response is over, the fluid transitions to a regime characterized by the presence of standing waves (see Fig. 2.33(b)). It is also possible to consider a further comparison by identifying the modal content from accelerometer responses. Indeed, by exploiting the modal filtering technique (see Ref. [90]) on the measured acceleration signals, the modal accelerations of the cantilever beam can be extracted. The comparison of the first three modal accelerations of the frozen case with that of the sloshing case is provided in Fig. 2.34. The interaction between sloshing and structural dynamics provides effects on damping the dynamics of the first mode of vibrations, whilst is less effective on the second mode and looks to have a detrimental on the third mode.

Random analysis

In addition to the free response test, other experiments were conducted in which the same configuration presented in Sec. 2.2.3 is subjected to seismic excitation. To this end, the beam root is attached to the electromechanical shaker as described in Ref. [91].

Three $90s$ long experimental tests were performed, corresponding to three different levels

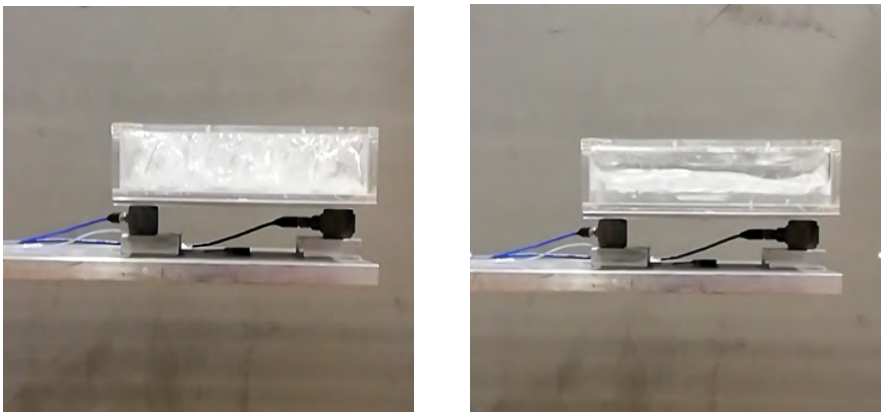

(a) $t = 0.65\,s$ (b) $t = 2.45\,s$

Figure 2.33: Frames of the sloshing beam free response in two different time instants

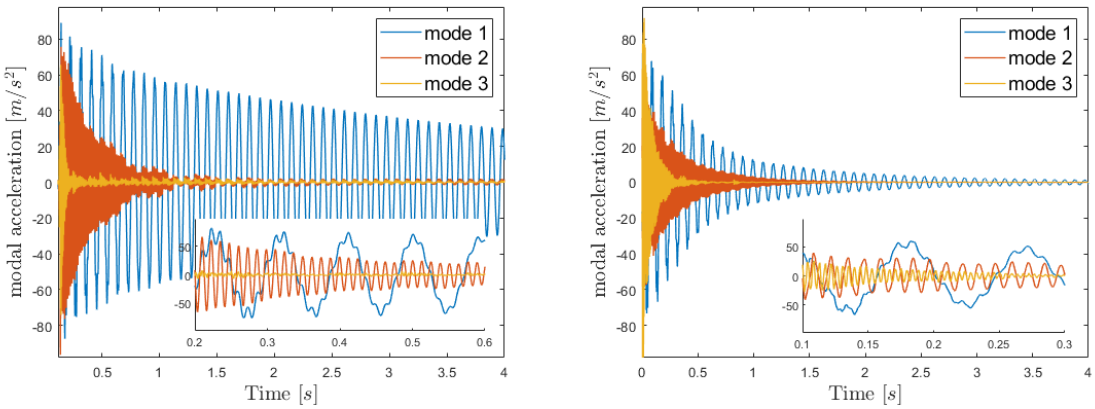

(a) Frozen case (b) Sloshing case

Figure 2.34: Comparison between modal accelerations of frozen (a) and sloshing (b) cases.

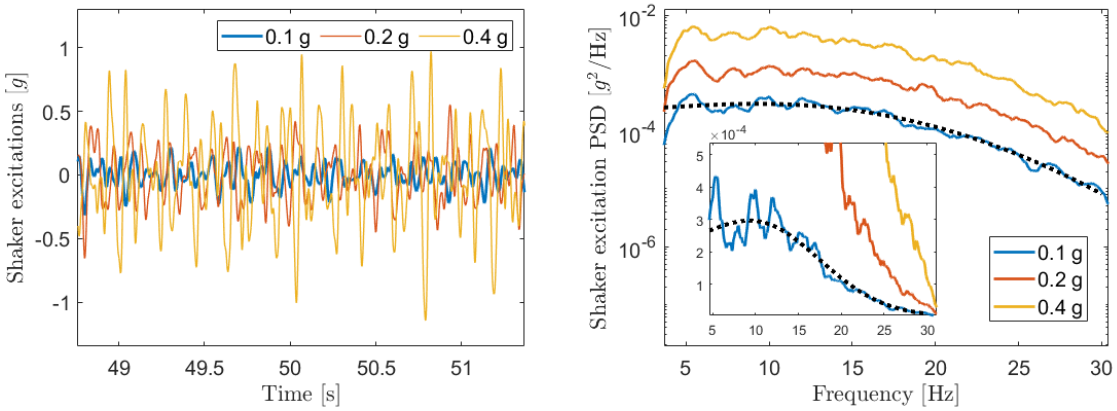

(a) Time signals

(b) Power spectral densities (PSD)

Figure 2.35: Seismic excitations imposed by the shaker (RMS: 0.1 g, 0.2 g, 0.4 g)

of vertical random excitation, with a root-mean-square (RMS) acceleration value of 0.1 g, 0.2 g and 0.4 g. Figure 2.35 shows the three controlled accelerations imposed by the shaker at the beam root. More in details, Fig. 2.35(a) shows the trend of the acceleration signals over time (for a limited time window), while Fig. 2.35(b) shows their power spectral densities (PSD) as a function of the frequency, in which the inset plot shows a zoom on the PSD having RMS equal to 0.1 g, compared with a black dashed curve representing the assigned theoretical Gaussian spectrum expressed as follows

$$S(f) = \frac{A}{\sigma\sqrt{2\pi}}\left[e^{-(f-f_0)^2/2\sigma^2} + e^{-(f+f_0)^2/2\sigma^2}\right] \tag{2.30}$$

where A is the amplitude, σ is the standard deviation and f_0 is the center of the distribution. Sloshing response data is collected by means of accelerometers and load cells placed on the beam as shown in Fig. 2.31. Figure 2.36 shows the tank accelerations measured for each of the three considered RMS levels, in the case where the liquid is free to slosh. It is possible to appreciate that the seismic excitation imposed on the beam is amplified by the beam's dynamics, leading to acceleration values that, for the case with RMS level equal to 0.4g, reach at most a value of 6 g at the tank location. This value is in line with the maximum acceleration covered by the identification process.

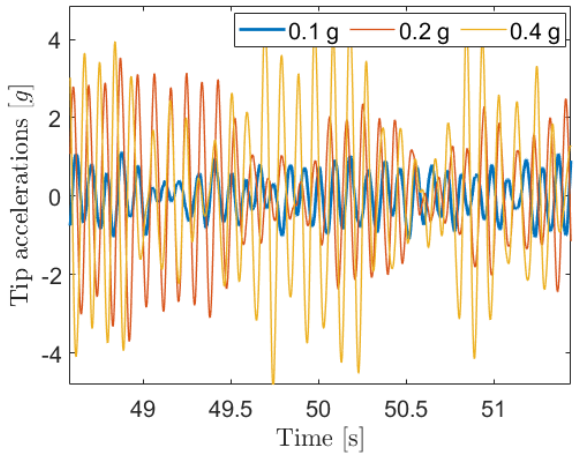

Figure 2.36: Tank accelerations measured in the sloshing case, following the application of the shaker random excitations (RMS: 0.1 g, 0.2 g, 0.4 g)

2.2.4 Results of the experimental validation

The neural-network-based NFIR model identified in Sec. 2.2.2 is experimentally validated using the data obtained with the experimental set-up presented in Sec. 2.2.3. In this section, the numerical procedure implemented in order to evaluate the performance of the model by comparison with experimental data is presented. The logic employed in this activity is to implement a digital twin of the experimental configuration in Fig. 2.31.

For this purpose, a simulation model was built in Simulink®, representing the the sloshing beam problem as shown in Fig. 2.37. The block *structure* in Fig. 2.37(a) contains the modal description of the cantilever beam implementing Eq. 2.26, while the block *sloshing* detailed in Fig. 2.37(b) include the neural network ROM architecture. It provides the dynamic sloshing forces Δf_{S_z} when it receives as input the history of the elastic velocity evaluated at the tank position x_T. The gains before and after the network in Fig. 2.37(b) (the blue block) allow, respectively, for the transformation of modal velocities in tank vertical velocity as $\dot{u}(x_T) = \sum_m \psi_m(x_T)\dot{q}_m(t)$, and the projection of the dynamic sloshing force on the modes of vibration to obtain the generalized sloshing forces $\psi_n(x_T)\,\Delta f_{S_z}$.

The numerical model of the sloshing beam problem was used to replicate the same responses of the experimental set-up presented in Sec. 2.2.3. The results used for the experimental validation of the surrogate model are shown next, starting with those related to the free response problem presented in Sec. 2.2.3.

Figure 2.38(a) shows the predicted numerical acceleration at the center of tank x_T compared with that obtained by the corresponding experiment. On the other hand, Fig. 2.38(b) shows the comparison of time histories of the interface forces exchanged between the structure and the tank. The curves are practically superimposed for both acceleration at tank location

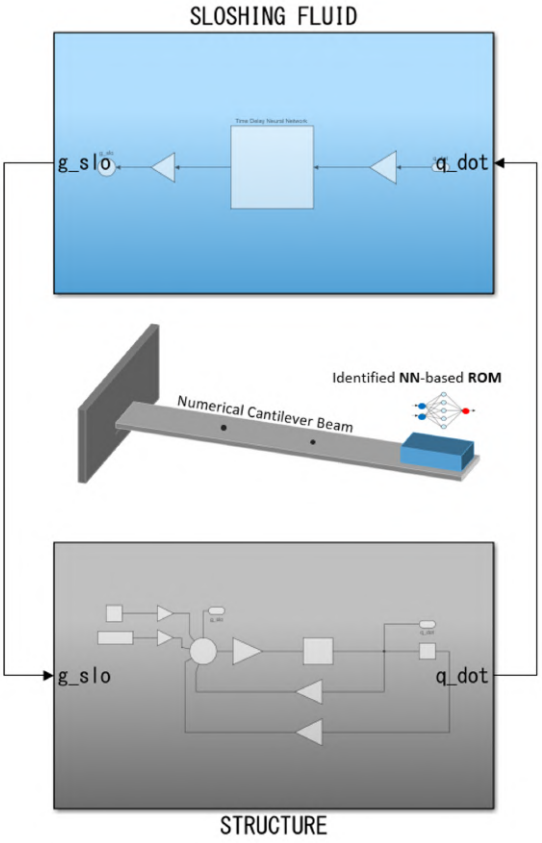

(a) FSI model plant

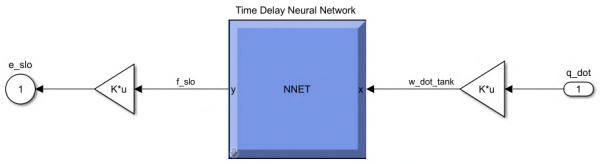

(b) Neural network plant

Figure 2.37: Simulink® model representing the sloshing beam experiment

and interface force. Figure 2.38(c) shows the comparison between the experimental dynamic sloshing force and that predicted numerically by the network. The two curves are in good agreement with each other, except for the first cycles of the response in which the load cells seems to incorrectly measure the sloshing forces (likely due to the impulsive release mechanism in the initial phase of the response). By taking advantage of the modal filtering technique, it is possible to isolate the first mode of vibration from the experimental and numerical acceleration signals shown in Fig. 2.38(a). Once the dynamics of the first mode of vibration has been isolated, the instantaneous damping ratio can be evaluated by considering the envelope through logarithmic decay. Then, since the envelope decreases monotonically, the damping can be parameterized as a function of the vertical acceleration of the tank as shown in Fig. 2.39 that provides the comparison between experimental and numerical instantaneous damping. Since the model is trained using harmonic input, it is limited in providing a perfect estimate of the damping at the very initial transient - first two cycles at high acceleration amplitudes - but the neural-network-based ROM looks to provide perfect superimposition in the prediction of the nonlinear damping induced by slosh dynamics in the rest of the response. Indeed, when high vertical accelerations are involved triggering Rayleigh-Taylor instabilities and impacts with the tank ceiling, the system promptly reaches a steady regime. The difference at the first cycles - in which the NN model appears to be anyway conservative with respect to the experimental response in terms of damping - is likely to be linked with the time needed for the inertial forces to win the surface tension and fragment the free surface. The problem of introducing such an effect on the training process is still open. In the Appendix E these same results are compared with those obtained by modeling the vertical sloshing force by means of linearised viscous damping.

Concerning random analysis, the seismic excitation is implemented by considering the model in the non-inertial frame of reference and modeling a generalized force $\mathsf{f}^{(ext)}$ determined by the fictitious forces such as

$$f_n^{(ext)} = -\int_0^l \mu(x)\psi_n(x)\,\mathrm{d}x\,a_s \tag{2.31}$$

where a_s is the controlled vertical acceleration imposed by the shaker at the beam root and $\mu(x)$ the beam linear density. On the other hand, the input to the neural network needs to be expressed in the inertial frame of reference, and thus equal to $\dot{u}(x_T) + v_s$ where $\dot{u}(x_T)$ is the tank vertical velocity in the non-inertial frame of reference and v_s the drag speed. Fig. 2.40 compares the estimated and measured tank acceleration signals over time for each of the three considered seismic tests. Again, the experimental response measured in the sloshing case (blue curve) is compared with the acceleration predicted by the sloshing beam simulation (red dot-dashed curve) obtained considering the same a_s as in Fig. 2.35(a). In order to compare the effects that sloshing has on the random response of the system over time, the response in

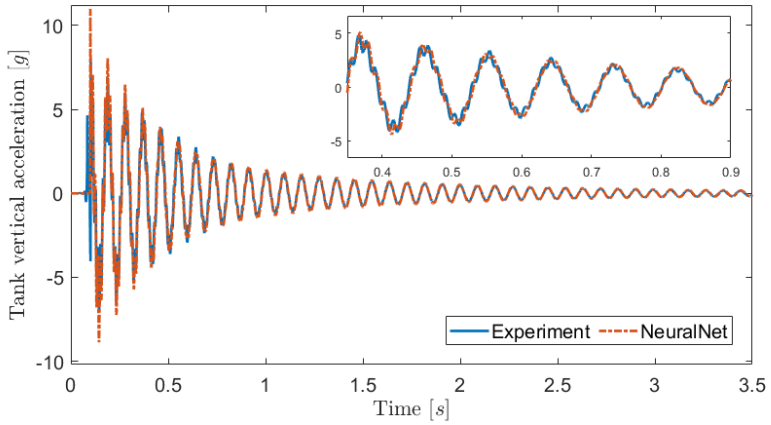

(a) Acceleration at the tank location

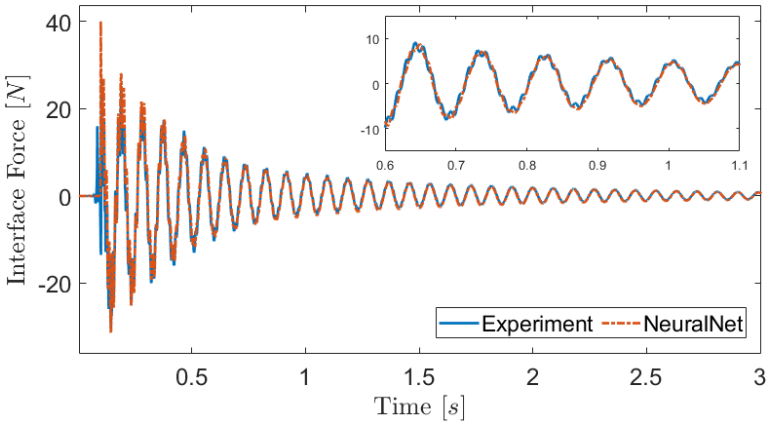

(b) Interface force

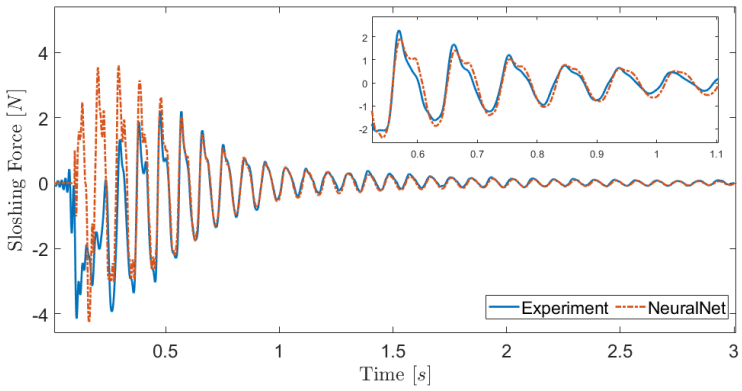

(c) Sloshing force

Figure 2.38: Comparison between network predictions and experiments for vertical acceleration of a tank, interface force and sloshing force.

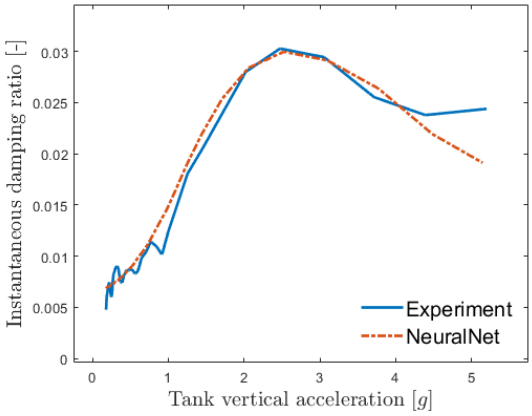

Figure 2.39: Instantaneous damping ratio of the first mode of vibration as a function of the acceleration amplitude.

the frozen case obtained numerically with the same experimental input (black dotted curve) is also represented. This is more representative of the experimental counterpart given the difficulty of assigning the same random signal for two different experimental tests. In the time intervals selected for the representation of the results, it can be noticed that the NFIR model identified in Sec. 2.2.2, once integrated into the equivalent virtual sloshing-beam model, is able to return a reasonable estimate of the sloshing beam response. This is mainly due to the predominantly mono-harmonic nature of the random response, which is consistent with that of the VFA harmonic experimental data used to train the neural network. However, as can be seen from the inset plots in Fig. 2.40, the response is less accurate at low amplitudes. This may be related to the lack of zero crossings at some points, which, based on the training data used, may cause the model to fail in its predictions. However, the numerical response is very close to the experimental response when compared with the frozen case numerical response that still includes experimentally derived damping values. This is also corroborated by Fig. 2.41, which shows the comparisons of the power spectral densities (using Welch method, Ref. [92]) of the tank acceleration for the different RMS cases. In fact, the PSDs associated with the numerical frozen case (black) present a clearly higher peak than that of the sloshing curves (blue). Comparing these with the (red) curves obtained by simulating the sloshing-beam with the integrated data-driven ROM, it can be noticed that qualitatively the identified ROM is able to return the same level of dissipation at the system resonance frequency.

Although it is quite clear that the damping level depends on the amplitude of the tank vertical oscillation, PSDs are next used to make an average estimate of the modal damping of the first vibration mode as a function of the intensity of the input random signal. To this end, for each of the curves in Fig. 2.41, a modal fitting procedure is implemented based on the least-squares rational function estimation method (Ref. [93]). Table 2.5 shows the obtained damping ratios, in which it can be noticed that the experimental case of sloshing turn out

	Damping ratio ζ_1 [%]		
RMS	Experiment	NeuralNet	Frozen
$0.1\,g$	2.70	2.20	0.54
$0.2\,g$	2.54	2.38	0.51
$0.4\,g$	2.43	2.95	0.31

Table 2.5: Comparison between estimated modal damping ratios

to provide similar to those predicted with ROM, emphasizing the capability of the identified model to adequately reproduce the dissipative behavior induced by vertical sloshing. Also for this other type of test, Appendix E provides a comparison with results obtained by modeling the sloshing force using a linear viscous damping model.

It is worth noting that, similar results to those presented in this section can also be obtained with the NFIR model with 60 delay lines and 20 neurons. Indeed, the latter has predictive capabilities comparable to those of the selected model, ensuring an accurate representation of the dissipative behaviour of nonlinear vertical sloshing (as already mentioned in Sec. 2.2.2). Having a lighter structure (in terms of hyperparameters, such as delays and neurons) it may be suitable for use in applications that require a higher computational cost. In fact, it will be used in the aeroelastic applications presented in Chap. 3 to study and evaluate the effects of vertical sloshing on system response.

2.2.5 Scaling procedure for actual applications

The experimental data used to train the neural network were obtained with the set-up presented in Sec. 2.2.1. The dimensions of the box-shaped tank used in the experiment are different than those of the tanks considered in actual aeroelastic applications. It is therefore desirable to introduce a scaling law that allows the identified reduced-order model to be used even for tanks with dimensions other than the original ones. Before describing the procedure by which NFIR model scaling is implemented, it is necessary to reintroduce the concepts presented in Sec. 1.4.2 and Sec. 1.5. In particular, referring to the case with the 50 % fill level, the maps of the non-dimensional dissipated energy Φ_d and the sloshing-effective mass fraction β (shown in Fig. 1.12 and Fig. 1.21, respectively) are re-presented in Fig. 2.42 in the non-dimensional frequency $\bar{\omega} = \Omega/\sqrt{g/h}$ and the non-dimensional velocity $\bar{v}$ domain. The second operating parameter is expressed as $\bar{v} = v/\sqrt{gh}$ (with $v = \Omega\, u_0$, being u_0 the amplitude of the vertical imposed motion) that, for the vertical slosh dynamics assumes the meaning of Froude number (Ref. [29, 30]).

Figure 2.42(a) provides the non-dimensional dissipated energy $\Phi_d = L_d/(m_l u_0^2 \Omega^2)$ in a vertical harmonic motion $u = u_0 \cos(\Omega t)$ as a function of the non-dimensional frequency $\bar{\omega}$

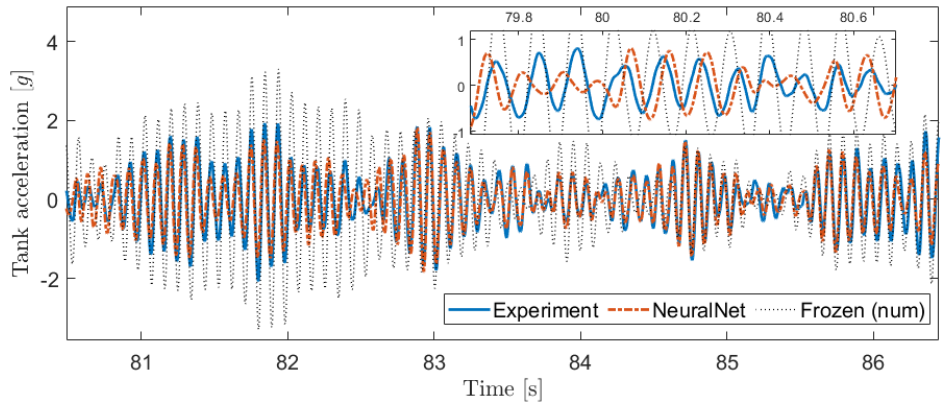

(a) RMS: 0.1 g

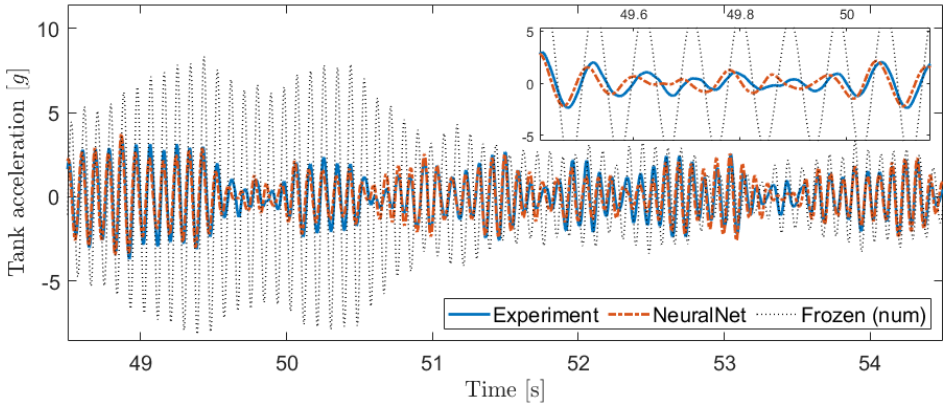

(b) RMS: 0.2 g

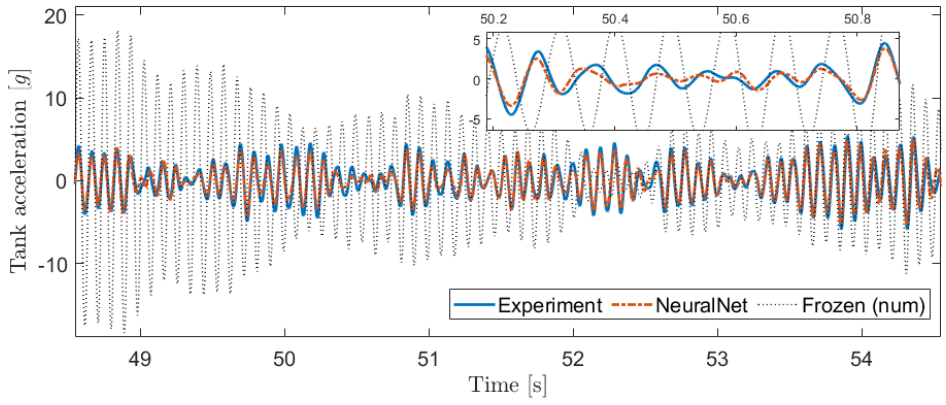

(c) RMS: 0.4 g

Figure 2.40: Comparison between the numerical tank accelerations predicted by the virtual sloshing beam model with NFIR model and with frozen liquid and the experimental one measured in the sloshing case.

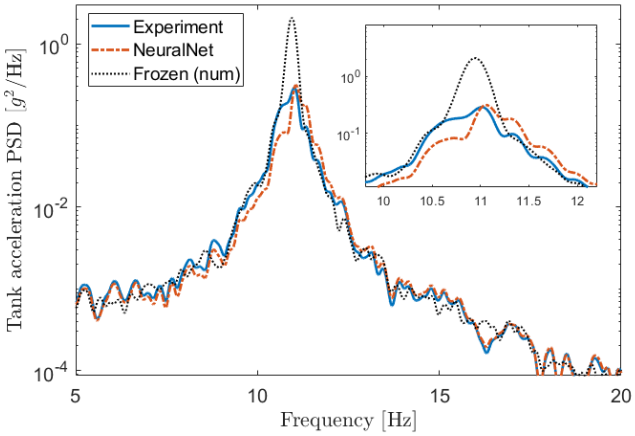

(a) RMS: 0.1 g

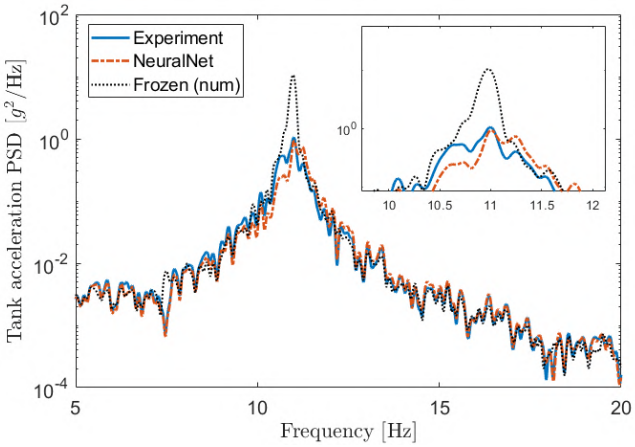

(b) RMS: 0.2 g

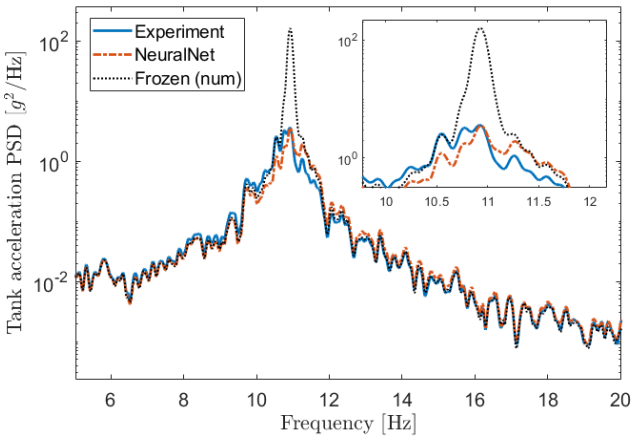

(c) RMS: 0.4 g

Figure 2.41: Comparison between the PSDs of the tank acceleration predicted by the virtual sloshing beam model with NFIR model and with frozen liquid and those of the experimental sloshing case.

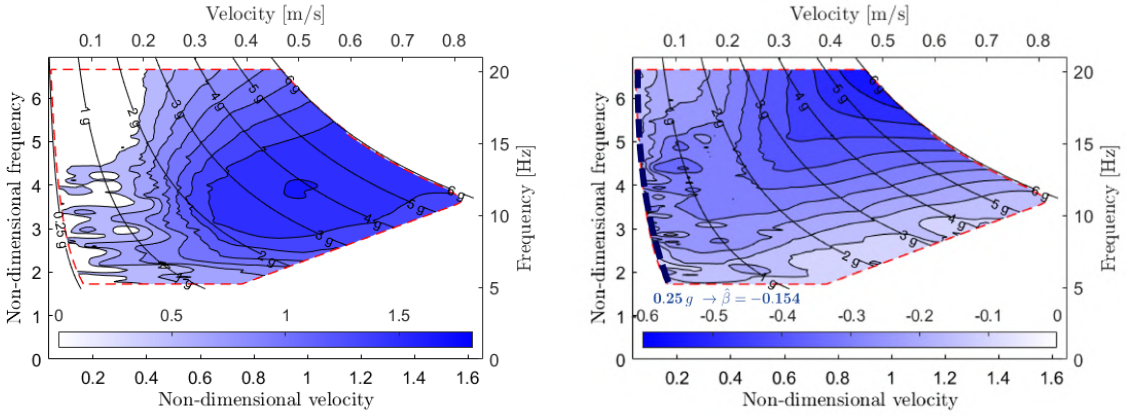

(a) Non-dimensional dissipated energy Φ_d

(b) Sloshing-effective mass fraction β

Figure 2.42: Maps of the Identified dissipated energy and Sloshing-effective mass fraction.

(not to be confused with the reduced frequency k for the unsteady aerodynamics) and velocity $\bar{v}$. Figure 2.42(b) shows the variation of the sloshing-effective mass fraction β in the same domain. As described in Sec. 1.5, this quantity can be identified by assuming the linear approximation of the dynamic sloshing force (removing the effects of the super-harmonics) and performing the ratio between the Fourier transform of the dynamic sloshing force and the related frozen mass force (see Eq. 1.29). The non-dimensional dissipated energy map predicted by the identified NFIR model in the frequency-velocity domain of interest (already presented in Fig. 2.29 in the frequency and amplitude domain) is shown in Fig. 2.43(a). Similarly, Fig. 2.43(b) presents, in the same domain, the variation of β predicted by the ROM. Comparing Fig. 2.43 with Fig. 2.42, it can be seen that the identified dynamic model is able to capture both the dissipative behaviour and the mass effect induced by vertical sloshing.

As already mentioned in Sec. 2.1.3 the energy dissipated by the sloshing fluid L_d can be expressed by means of the π-theorem as

$$L_d \;=\; m_l\, u_0^2\, \Omega^2 \Phi_d \left(\bar{\omega}, \bar{v}, \alpha, Re, Bo, ...\right) \tag{2.32}$$

Besides the non-dimensional frequency $\bar{\omega}$ and velocity $\bar{v}$, L_d is dependent on the fill level α, the Reynolds number $Re = vh/\nu$ (ν kinematic viscosity) that reflects viscosity effects, and the Bond number $Bo = \rho g h^2/\gamma$ (γ surface tension) that reflects surface tension effects. Since the operational parameters $\bar{\omega}$ and $\bar{v}$ only cover a subspace of the space spanned by the non-dimensional parameters influencing the sloshing-induced energy dissipation, it is necessary to formulate the following hypotheses before scaling the NN-based ROM:

- the non-dimensional dissipated energy is assumed to be mainly dependent on the non

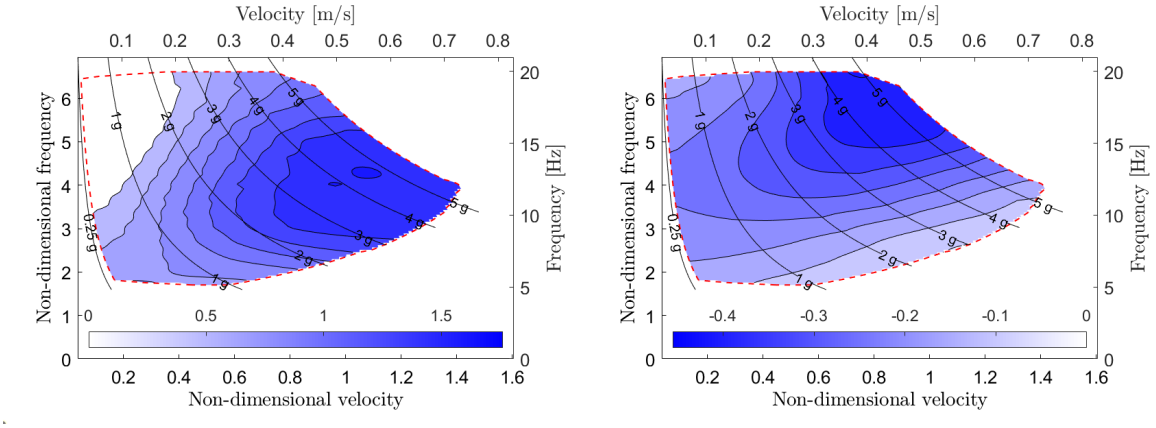

(a) Nondimensional dissipated energy Φ_d

(b) Sloshing-effective mass fraction β

Figure 2.43: Nondimensional Dissipated energy and sloshing-effective mass fraction maps predicted by the neural-network-based NFIR model

dimensional velocity (Froude) and non-dimensional frequency. Other parameters more related to physical properties of the fluid (Reynolds and Bond) are assumed to play a secondary role.

- The principal dimension is assumed to be the tank height h (Ref. [29]). Tank base area is not assumed to be important.
- For each filling level α a different identification is required.

Although these hypotheses are only partially supported by experiments and numerical evidences [29, 82], it is reasonable to assert them to scale the obtained data for the eight tanks embedded within the structure. Indeed, a variation in the dimensionless parameters of Reynolds (at high Reynolds values) and Bond seems to provide a negligible influence on the dissipative capabilities during violent vertical sloshing phenomena (Ref. [82]). The re-scaled ROM must therefore work in similarity of non-dimensional velocity and non-dimensional frequency as well as non-dimensional dissipated energy in order to replace the sloshing model with a neural network capable of reproducing the real dissipative behavior. Figure 2.44 shows the Simulink® implementation of the neural network unit and the scaling gain. More in details, from the non-dimensional frequency similarity between the experiment $\bar{\omega}^{(exp)}$ and the *i-th* tank $\bar{\omega}^{(i)}$, we obtain:

$$\frac{\Omega^{(exp)}}{\sqrt{g/h^{(exp)}}} = \frac{\Omega^{(i)}}{\sqrt{g/h^{(i)}}} \Longrightarrow dt^{(i)} = dt^{(exp)} \sqrt{\frac{h^{(i)}}{h^{(exp)}}} \tag{2.33}$$

Thus, a proper time rate translator is used within the simulation (see Fig. 2.44) to make the neural network working with a time rate compliant with the one used for its identification.

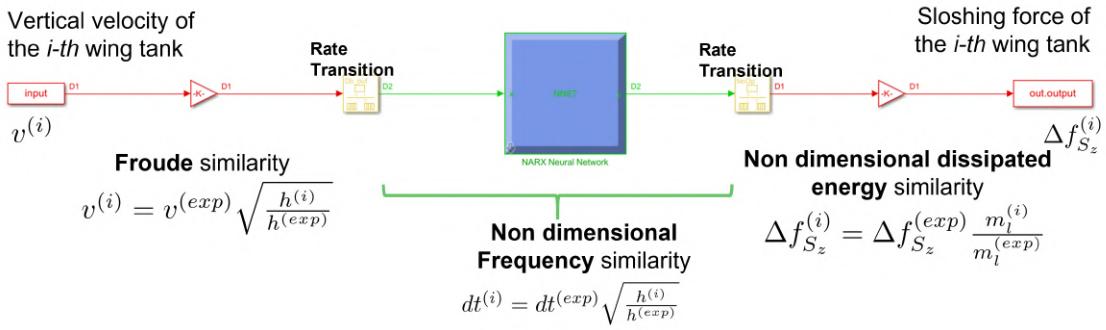

Figure 2.44: Scaling procedure implemented in Simulink®.

Furthermore, the similarity of the non-dimensional velocity (Froude) of the vertical motion yields:

$$\frac{v^{(exp)}}{\sqrt{gh^{(exp)}}} = \frac{v^{(i)}}{\sqrt{gh^{(i)}}} \Longrightarrow v^{(i)} = v^{(exp)}\sqrt{\frac{h^{(i)}}{h^{(exp)}}} \tag{2.34}$$

that provides a gain to the vertical tank velocities before the call to the neural network (see Fig. 2.44). Assuming the similarity of the non-dimensional dissipative function Φ_d and that $L_d = \int_{cycle} \Delta f_{S_z} d\,u$ we obtain:

$$\Delta f_{S_z}^{(i)} = \Delta f_{S_z}^{(exp)} \frac{m_l^{(i)}}{m_l^{(exp)}} = \Delta f_{S_z}^{(exp)} \frac{\rho_k V^{(i)}}{\rho_w V^{(exp)}} \tag{2.35}$$

where ρ_k and ρ_w are the density of kerosone and water, respectively, whereas $V^{(i)}$ and $V^{(exp)}$ are the volume of the *i-th* wing tank and experimental tank, respectively. Equation 2.35 provides the gain for the dynamic sloshing forces to be applied after the call to the neural network within the simulation framework (see Fig. 2.44). This scaling procedure is able to take into account different liquids with respect to that used for data generation. In this scaling procedure, velocity and displacements of the tank are adjusted according to tank size, but the maximum accelerations achievable when the tank works in similarity with the tank used for the network identification are retained. It is worth noting how this scaling procedure assumes a perfectly box-shaped tank. In addition, the dependence of the dissipative characteristics of vertical sloshing with respect to aspect ratios (the other two dimensions of the tank with respect to its height) is not considered in this procedure.

Summary

A neural-network-based nonlinear finite impulse response model (NFIR), resulting from a sensitivity analysis aimed at finding the most performing network, was selected to construct the

surrogate model for vertical sloshing. An experimental validation procedure of the identified model was presented. To this end, an experimental setup consisting of a cantilever beam with a tank mounted at its free end was realised. The latter is the same as that used to generate the training data. By performing free response and seismic tests, FSI experimental data were collected to be used as a benchmark for validating the nonlinear identified ROM when integrated in an equivalent virtual model to account for the effects of vertical sloshing. The comparisons for the free response case showed that the time histories of the numerical acceleration at the end of the beam and sloshing forces are in good agreement with the experimental data. The estimated instantaneous damping ratio validates the good capabilities of the identified model to accurately reproduce the dissipative behavior induced by vertical sloshing. The random analyses also yielded good results and showed a satisfactory level of accuracy for the time response in each of the considered excitation cases. By comparing the damping coefficients estimated in the frequency domain, it was possible to assess the neural network capability to provide the same levels of dissipation as experimentally given by vertical sloshing in random FSI testing. The nonlinear neural network-based model identified in this section allows it, unlike an equivalent mechanical model such as the bouncing ball, to be used for different applications, and thus, for different operating frequencies. However, the data used for training, although covering a wide region in the frequency and amplitude domain, is characterised by having, instantaneously, a dominant harmonic. This means that the applications in which the neural network can be used (returning good force estimates) should not have multi-harmonic effects. Consequently, future developments should include a new identification process that uses experimental data from stochastic tests to train a model capable of capturing these features as well.

Chapter 3

A numerical investigation of the sloshing effects in aeroelastic applications

A thorough understanding of the effects of sloshing on aircraft dynamic loads is of great relevance for the future design of flexible aircraft to be able to reduce their structural mass and environmental impact. Indeed, the high vertical accelerations caused by the vibrations of the structure can lead to the fragmentation of the fuel free surface. Fluid impacts on the tank ceiling are potentially a new source of damping for the structure that has hardly been considered before when computing the dynamic loads of the wings. This chapter presents the application of sloshing reduced-order models to aeroelastic test cases, with the aim of investigating their effects on response under pre- and post-critical conditions.
Section 3.1 presents an aeroelastic analysis in which vertical sloshing is integrated into a flexible wing model in order to study its effects on the response for different loading conditions. The related results are reported in [81]. Section 3.2 presents an investigation of the combined effects of linear and nonlinear sloshing on the stability and aeroelastic response of a flying wing. This second part is published in Ref. [94].

3.1 Nonlinear sloshing integrated aeroelastic analyses of a research wing prototype

The subject of this section is an aeroelastic model consisting of research wing used to investigate the nonlinear vertical sloshing effects on the aeroelastic response under pre-critical and post-critical conditions. The vertical sloshing dynamics is modeled with the neural-network-based ROM presented in Sec. 2.2. However, its integration into the aeroelastic model is done by implementing the scaling procedure introduced in Sec. 2.2.5, considering that the

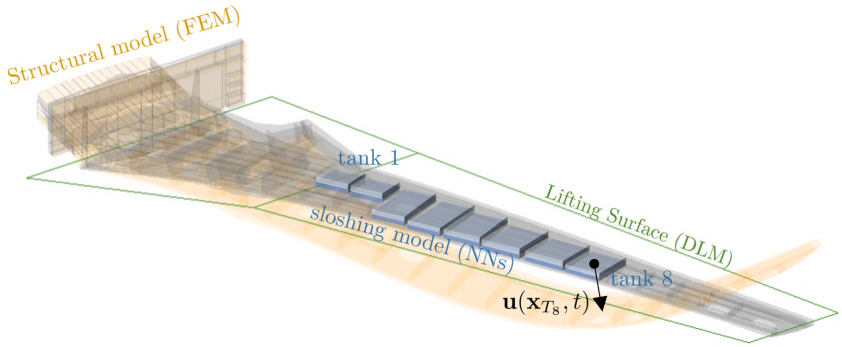

Figure 3.1: Research wing aeroelastic/sloshing modeling.

wing tanks have different dimensions to those of the experimental set-up used to generate the ROM training data. The results concern the aeroelastic response of the wing to gust input under pre-critical (flutter) conditions as well as post-critical conditions highlighting the onset of limit cycle oscillations caused by sloshing. Moreover, the load alleviation performances are assessed for a typical landing input.

3.1.1 Aeroelastic and sloshing modeling of the wing prototype

A sloshing/aeroelastic wing is modeled in this section using a hybrid approach that combines a linear differential problem (aeroelasticity) with a data-driven model (sloshing). More in details, the numerical testbed is represented by a prototype wing model with dimensions typical of a single-aisle commercial aircraft wing. Figure 3.1 shows the finite element model (FEM), along with the lifting surface discretised by means of doublet lattice method (DLM), and the position of the eight tanks integrated within the wing box. Since no data were available to generate the aerodynamic model, the lifting surface was generated by taking into account the typical values of single aisle commercial aircraft. Figure 3.2 shows the wing first six modes of vibration in the case of *dry* structure, that is the case in which tanks are empty. Dry modes are assumed to be the shape functions in order to avoid considering different FEM models depending on the fill level (even though the case with 50% fill level is considered in the present analysis). A box-shaped, rigid structure is approximated for each of the eight tanks embedded within the wing-box. Their dynamic behaviour is condensed in a point placed in the geometric centre of the tank and their motion is based on a weighted average of the motion of the surrounding nodes. The wing structural displacements $\mathbf{u}(\mathbf{x}, t)$ can be expressed by the spectral decomposition

$$\mathbf{u}(\mathbf{x}, t) \simeq \sum_{n=1}^{N} \boldsymbol{\psi}_n(\mathbf{x}) q_n(t) \tag{3.1}$$

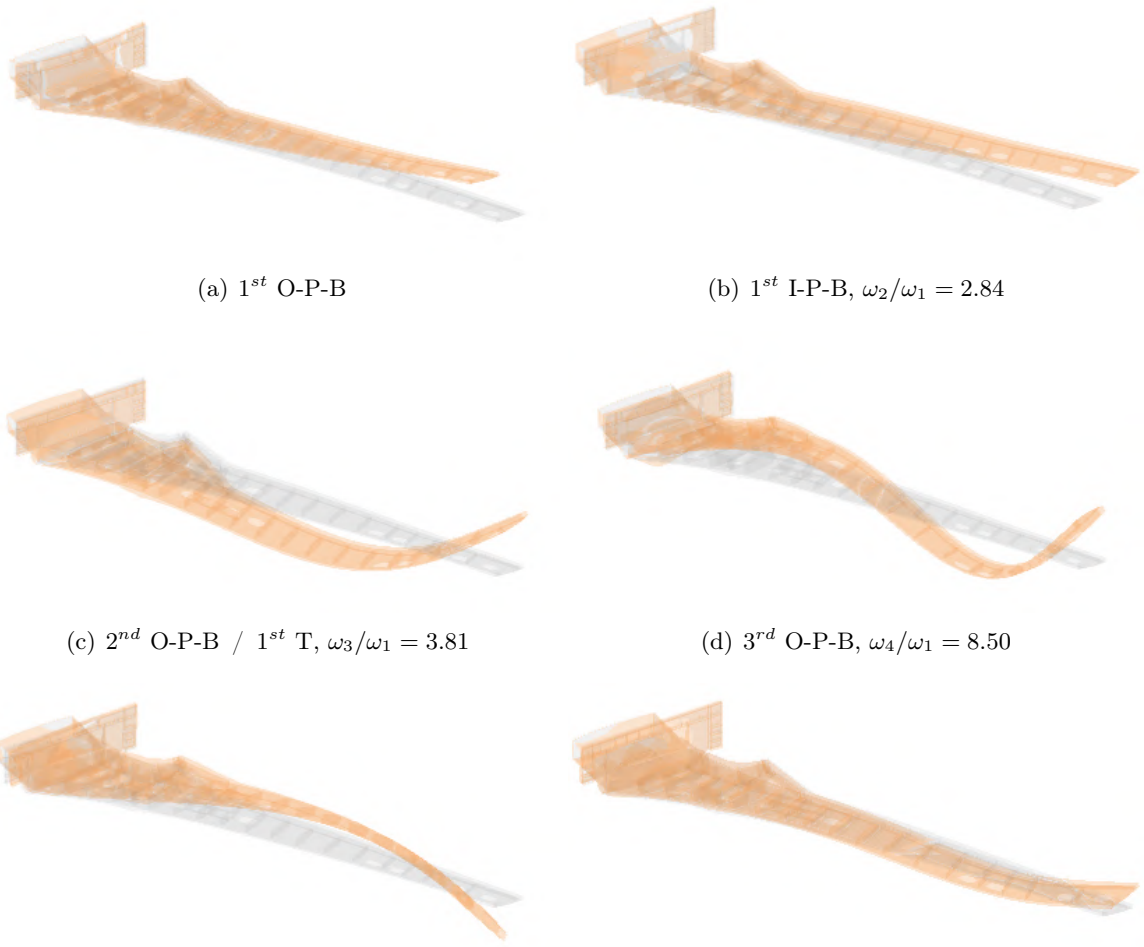

(a) 1^{st} O-P-B

(b) 1^{st} I-P-B, $\omega_2/\omega_1 = 2.84$

(c) 2^{nd} O-P-B / 1^{st} T, $\omega_3/\omega_1 = 3.81$

(d) 3^{rd} O-P-B, $\omega_4/\omega_1 = 8.50$

(e) 1^{st} T / 2^{nd} I-P-B, $\omega_5/\omega_1 = 10.42$

(f) 2^{nd} T / 2^{nd} O-P-B, $\omega_6/\omega_1 = 11.79$

Figure 3.2: Mode shapes of the wing model with their natural frequencies. O-P-B = Out-of-plane bending mode, I-P-B = In plane bending mode, T = torsional mode.

where $\boldsymbol{\psi}_n(\mathbf{x})$ are the modes of vibrations of the structure and $q_n(t)$ are the generalised coordinates describing the body deformation in time. Note that a space-discretisation for the structure is assumed by including a finite number N of modes in the analysis, *i.e.,* a frequency-band-limited unsteady process. Considering this representation for aircraft wing dynamics, one has the following Lagrange equations of motion in terms of N modal coordinates $q_n(t)$

$$\mathsf{M}\ddot{\mathsf{q}} + \mathsf{K}\mathsf{q} = \mathsf{e} + \mathsf{g} + \mathsf{f}^{(ext)} \tag{3.2}$$

where $\mathsf{q} = [q_1, q_2, \ldots, q_N]^{\mathrm{T}}$ is the modal coordinates vector, M and K are, respectively, the modal mass and stiffness (diagonal) matrices provided by FEM solver, whereas $\mathsf{e} = [e_1, e_2, \ldots, e_N]^{\mathrm{T}}$ and $\mathsf{g} = [g_1, g_2, \ldots, g_N]^{\mathrm{T}}$ are, respectively, the generalized *aerodynamic* and *sloshing* forces induced by the elastic motion. The $\mathsf{f}^{(ext)}$ is the vector of the current external forcing terms which includes gust and landing force. The generalised aerodynamic forces (due to the aircraft motion only) are generally computed as a function of the reduced frequency $k = \omega b/U_\infty$ (with b semi-chord and U_∞ free stream velocity) and Mach M_∞ domain (see Ref. [95]) as:

$$\tilde{\mathsf{e}} = q_D\, \mathsf{Q}(k, M_\infty)\, \tilde{\mathsf{q}} \tag{3.3}$$

where $\mathsf{Q}(k, M_\infty)$ is the generalised aerodynamic forces matrix, q_D is the dynamic pressure and the symbol $\tilde{}$ is used to represent the Laplace/Fourier transforms. For a fixed value of M_∞, the following rational function approximation for the unsteady aerodynamics

$$\mathsf{Q}(k) \approx \mathsf{A}_0 + jk\mathsf{A}_1 - k^2\mathsf{A}_2 + jk\mathsf{C}\Big(jk\mathsf{I} + \mathsf{P}\Big)^{-1}\mathsf{B} \tag{3.4}$$

is typically considered to transform an integro-differential problem into a pure differential problem (see Ref. [96]). The coefficients of the matrices in Eq. 3.4 are obtained by applying a minumum criterion on the error between the aerodynamic matrix evaluation and its interpolating form. This translates into finding those coefficients that minimise the following norm:

$$\min_{\mathsf{A}_0,\mathsf{A}_1,\mathsf{A}_2,\mathsf{C},\mathsf{B},\mathsf{P}} \left(\sum_{i=1}^{N_k} \left\| \mathsf{A}_0 + jk_i\mathsf{A}_1 - k_i^2\mathsf{A}_2 + jk_i\mathsf{C}\Big(jk_i\mathsf{I} + \mathsf{P}\Big)^{-1}\mathsf{B} - \mathsf{Q}(k_i) \right\|^2 \right) \tag{3.5}$$

where N_k is the number of reduced frequencies with which the unsteady aerodynamics is seeded. As a consequence of the rational function approximation, the aerodynamic forces can be recast in time domain as

$$\mathsf{e} = q_D\, \mathsf{A}_0\, \mathsf{q} + q_D\, \frac{b}{U_\infty}\, \mathsf{A}_1\, \dot{\mathsf{q}} + q_D (\frac{b}{U_\infty})^2\, \mathsf{A}_2\, \ddot{\mathsf{q}} + q_D\, \mathsf{C}\, \mathsf{a} \tag{3.6}$$

$$\dot{\mathsf{a}} = \frac{U_\infty}{b}\, \mathsf{P}\, \mathsf{a} + \mathsf{B}\, \dot{\mathsf{q}} \tag{3.7}$$

where a is the vector of the aerodynamic finite states, able to describe the linearised wake dynamics. At the same time, the generalised sloshing forces vector g can be expressed as a sum of contributions $\mathsf{g}^{(i)}$ of individual tanks:

$$\mathsf{g} = \sum_{i=1}^{N_T} \mathsf{g}^{(i)} \tag{3.8}$$

with N_T the number of tanks. The *n-th* component of $\mathsf{g}^{(i)}$ is the projection of the fluid pressure distribution p_S evaluated on the wet tank surface $\mathcal{S}_{tank}^{(i)}$ on each *n-th* modal shape $\boldsymbol{\psi}_n$ as in the following ($\mathbf{n}$ unit normal vector to $\mathcal{S}_{tank}^{(i)}$)

$$g_n^{(i)} = -\oiint_{\mathcal{S}_{tank}^{(i)}} p_S \; \mathbf{n} \cdot \boldsymbol{\psi}_n \, d\mathcal{S} \tag{3.9}$$

By assuming a rigid tank identified by its geometrical centre, Eq. 3.9 can be recast as:

$$g_n^{(i)} = \mathbf{f}_S^{(i)} \cdot \boldsymbol{\psi}_n(\mathbf{x}_{T_i}) + \mathbf{m}_S^{(i)} \cdot \boldsymbol{\varphi}_n(\mathbf{x}_{T_i}) \tag{3.10}$$

where $\mathbf{f}_S$ and $\mathbf{m}_S$ are, respectively, the sloshing force and moment applied in the geometric centre of the tank $\mathbf{x}_{T_i}$, whereas $\boldsymbol{\varphi}_n(\mathbf{x}_{T_i})$ is the *n-th* modal rotation of the point $\mathbf{x}_{T_i}$. In this study, sloshing force is decomposed into two contributions: the inertial force according to the frozen fuel modeling (Ref. [25]) and the perturbation resulting from the relative motion of the fluid particles within the tank. Assuming there is only a vertical perturbation $\Delta f_{S_z}^{(i)}$, the sloshing force $\mathbf{f}_S$ and moment $\mathbf{m}_S$ about the geometric centre of the *i-th* tank are given by:

$$\mathbf{f}_S^{(i)} = -\sum_{k=1}^{N} m_l^{(i)} \left[\boldsymbol{\psi}_k(\mathbf{x}_{T_i}) - \mathbf{d} \times \boldsymbol{\varphi}_k(\mathbf{x}_{T_i})\right] \ddot{q}_k + \mathbf{i}_3 \Delta f_{S_z}^{(i)} \tag{3.11}$$

$$\mathbf{m}_S^{(i)} = -\sum_{k=1}^{N} \left(\mathbf{I}_l^{(i)} \boldsymbol{\varphi}_k(\mathbf{x}_{T_i}) - m_l^{(i)} \mathbf{d} \times \left[\boldsymbol{\psi}_k(\mathbf{x}_{T_i}) - \mathbf{d} \times \boldsymbol{\varphi}_k(\mathbf{x}_{T_i})\right] \right) \ddot{q}_k \tag{3.12}$$

where $\mathbf{d}$ is the offset between the geometric centre of the tank and the liquid centre of mass, $\mathbf{i}_3$ is the vertical unit vector and $\mathbf{I}_l$ is the inertia tensor of the frozen fluid. $\Delta f_{S_z}^{(i)}$ is the already defined dynamic sloshing force: a non-conservative force that is a nonlinear function of the history of the tank vertical displacement $u(\mathbf{x}_{T_i}, t)$. By considering Eqs. 3.11 and 3.12, Eq. 3.10 can be recast as:

$$g_n^{(i)} = -\Delta m_{nk}^{(i)} \, \ddot{q}_k + \mathbf{i}_3 \cdot \boldsymbol{\psi}_n(\mathbf{x}_{T_i}) \, \Delta f_{S_z}^{(i)} \tag{3.13}$$

where the components $\Delta m_{nk}^{(i)}$ provides a further non-diagonal contribution to the mass matrix given by the inertia of the fluid. The aeroelastic/sloshing modeling is therefore implemented in Simulink® as illustrated in Fig. 3.3. The aeroelastic blocks are purely differential whereas

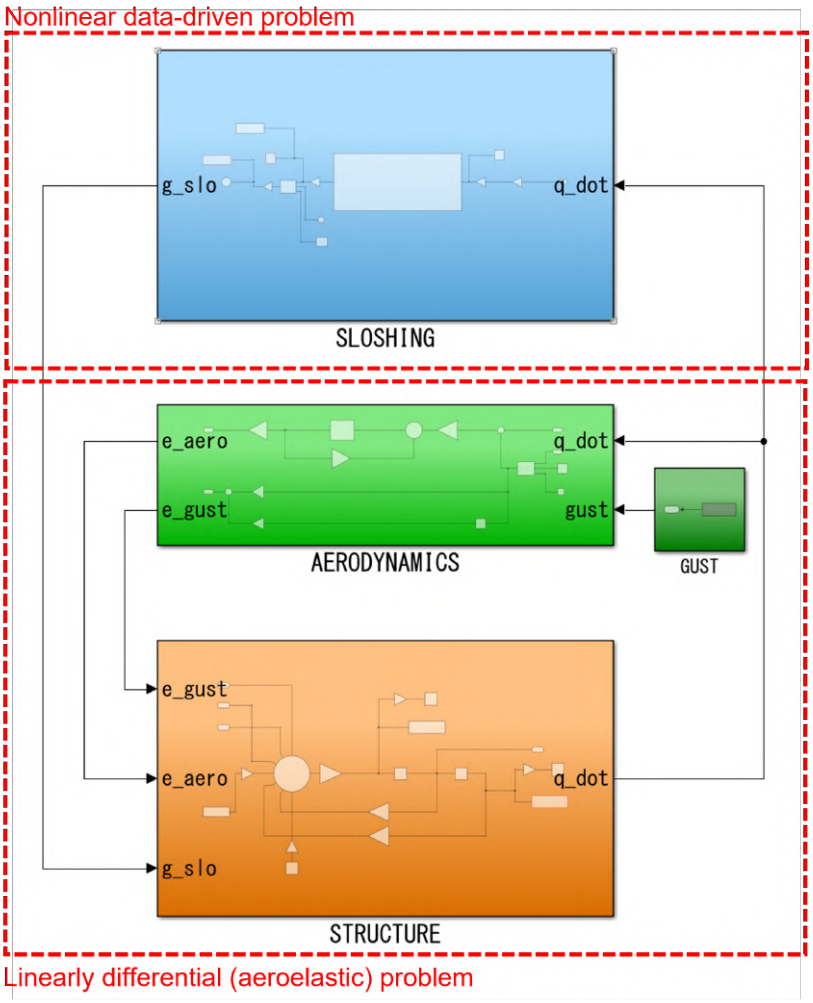

Figure 3.3: Aeroelastic/sloshing modeling in Simulink®.

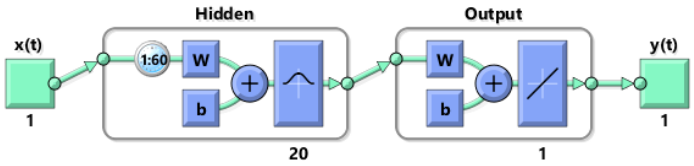

Figure 3.4: Identified NFIR model with 60 tapped delay lines and 20 hidden layer neurons

the sloshing block is modeled with the data-driven neural-network-based ROM identified in Sec. 2.2. Specifically, the NFIR model with 60 delay lines and 20 neurons is used, due to its greater efficiency in terms of simulation time (as already discussed in Sec. 2.2.2). This model is shown in Fig. 3.4. However, the experimental data used to train the neural network were obtained with the set-up presented in Sec. 2.2.1. The dimensions of the box-shaped tank used in the experiment are smaller than those of the eight tanks in the wing model under investigation. Therefore, the scaling law introduced in Sec. 2.2.5 is applied to the identified reduced order model for vertical sloshing in order to use it in this aeroelastic application.

3.1.2 Wing aeroelastic response analyses

Before performing the aeroelastic response of the wing, a stability analysis is performed by evaluating the poles of the linearised aeroelastic system between 250 m/s and 360 m/s and considering fixed the Mach number $M_\infty = 0.85$ and the air density $\rho_\infty = 0.9\,\mathrm{kg/m^3}$. Twelve vibration modes are employed for the aeroelastic analyses whereas 200 aerodynamic states were used for the rational function approximation of the unsteady aerodynamics. An additional modal damping of 5% is introduced into the analysis only for vibration modes whose dry nondimensional frequency with respect to the size of the wing bigger tank was greater than the nondimensional frequency limit of the sloshing identification process, namely when $f_n/\sqrt{g/h_1} > 6.72$. The root locus of the aeroelastic system (frozen configuration $\Delta f_{S_z}^{(i)} = 0$) is shown in Fig. 3.5 in which the vibration modes from which the different branches originate are annotated. The flutter instability occurs at $U_\infty = U_F = 319.3\,\mathrm{m/s}$ from the branch that originates from the first bending mode (see Fig. 3.2(a)), whereas the flutter frequency is $\omega_F = 1.95\,\omega_1$. The critical mode mainly consists of a coupling between the first vibration mode (1^{st} O-P-B) and the third mode (2^{nd} O-P-B / 1^{st} T) that consists also of a slight torsion of the aerodynamic sections.

The effects induced by the sloshing-effective mass fraction, can result critical for aeroelastic responses close to the flutter margin. In Ref. [97], a preliminary investigation of the mass effects associated with vertical sloshing has already been carried out. A reference value $\hat{\beta} = -0.154$ is obtained by averaging among the experimental values obtained at low level of acceleration ($0.25g$), namely for the quasi-linear sloshing regime (with reference to the experimental sloshing-effective mass fraction distribution shown in Fig. 2.42(b)). Nonetheless, a

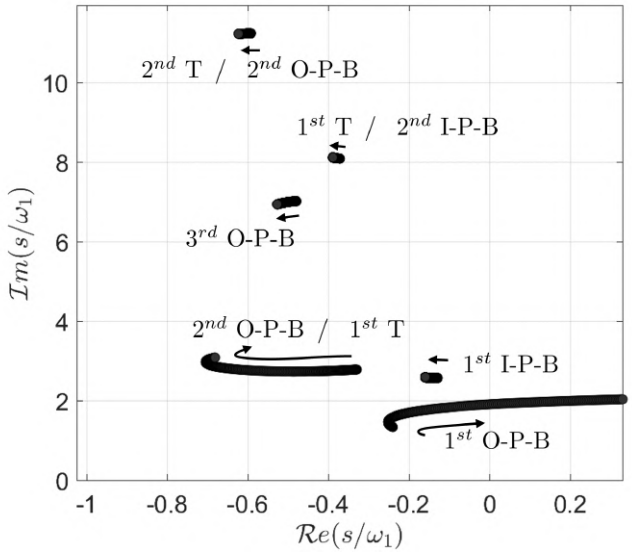

Figure 3.5: Root Locus of the wing aeroelastic system.

small uncertainty in defining the exact amount of liquid in the tank during the experiment (presented in Sec. 1.4.2) affects this value. Figure 3.6 shows the trend of the flutter speed as a function of the filling level α, where the green square represents the speed value in the case a fuel mass correction is used to take into account the sloshing effective mass at small perturbances, namely by assuming

$$\Delta f_{S_z}^{(i)} = \hat{\beta}\, m_l^{(i)} \sum_{n=1}^{N} \mathbf{i}_3 \cdot \boldsymbol{\psi}_n(\mathbf{x}_{T_i}) \ddot{q}_n \tag{3.14}$$

that can be integrated in Eq. 3.13.

Aeroelastic response analyses to vertical gust are then performed for different velocities in the neighborhood of the flutter speed where the response is less damped and the sloshing may play a role of paramount relevance on damping aeroelastic vibrations. Since the neural network is trained considering a time history made of a sequence of simply-harmonic input with different frequency and amplitude values (see Fig. 2.22), it follows that the proposed sloshing model works consistently when the input velocity has a dominant harmonic. The external aerodynamics plays a key role on filtering a single mode that has a pole with a smaller real part making the proposed ROM suitable to study most of the aeroelastic response analyses (like the aeroelastic response to discrete gusts). Specifically, in this analysis we consider the following standard gust profile:

$$w_g(t) = \frac{1}{2} w_{g_a} \Big[1 - \cos\left(\frac{2\pi U_\infty t}{L_g} \right) \Big] \tag{3.15}$$

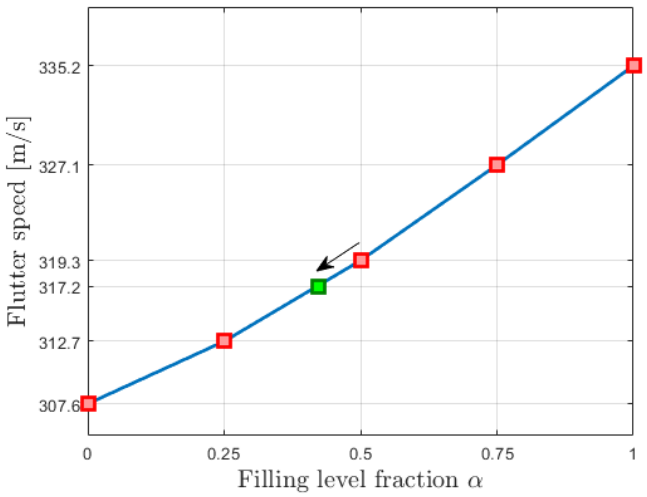

Figure 3.6: Flutter speed as a function of the filling level fraction α.

where w_{g_a} is the gust amplitude. The reference value for the gust length measured in chord length b is $L_g = 25\,b$. Spatially, the gust is assumed to be constant throughout the wing domain.

Two models are compared, namely the *frozen fuel* model and the *sloshing fuel* model that employs the neural network to replace slosh dynamics. Three different flight conditions are considered, that is $U_\infty = 266\,\mathrm{m/s}$ and $U_\infty = 315\,\mathrm{m/s}$, before the flutter margin as evaluated by the frozen fuel model, and $U_\infty = 321\,\mathrm{m/s}$ in flutter condition. The gust amplitude w_{g_a} is assigned in order to do not make the vertical acceleration overcome the limit of $6\,g$ at the tank locations which would violate the range of applicability of the network. Different gust intensities are employed to highlight the increase of the sloshing induced damping at high response amplitudes or the onset of limit cycle oscillations.

The first analysis is performed at a free stream velocity of $U_\infty = 266\,\mathrm{m/s}$, with a gust intensity of $w_{g_a} = 6\,\mathrm{m/s}$. Figure 3.7(a) compares the wing response of the sloshing fuel model with the frozen fuel model in terms of tip acceleration. Despite the aerodynamic damping is high, the role of sloshing is evident since the sloshing fuel model results in a more damped response due to presence of the fluid impacting inside the tanks. Moreover, The response of the dynamic sloshing forces, obtained by exploiting the neural network-based ROM, can be observed in Fig. 3.7(b).

Then, the flight speed is brought close to the flutter margin, at a free stream velocity of $U_\infty = 315\,\mathrm{m/s}$, with a gust intensity of $w_{g_a} = 3\,\mathrm{m/s}$. Figure 3.8(a) compares the wing tip response of the sloshing fuel model with the frozen fuel model. Even though, the structure is closer to the flutter margin, it can be noticed how the beneficial influence of the damping introduced by sloshing dynamics helps to alleviate the gust response. Again, the response of

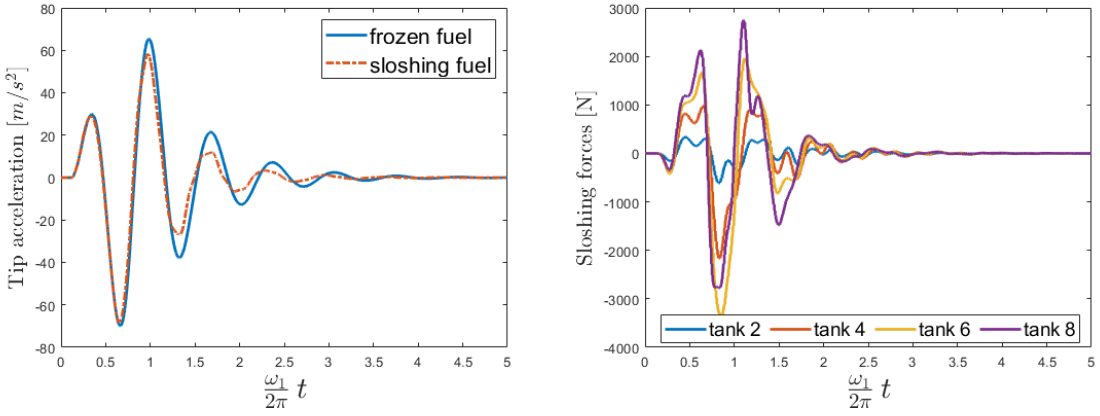

(a) Tip vertical acceleration

(b) Dynamic sloshing forces

Figure 3.7: Gust response analysis for $U_\infty = 266$ m/s.

the dynamic sloshing forces, obtained by exploiting the neural network-based ROM, can be observed in Fig. 3.8(b). Appendix E shows the same results compared with what is obtained by modeling vertical sloshing by experimentally characterised linearised viscous damping.

The post-critical gust response analysis is performed after the flutter speed limit evaluated with the frozen fuel model, that is $U_\infty = 321$ m/s, with a gust intensity of $w_{g_a} = 1.5$ m/s. The wing tip response is shown in Fig. 3.9(a) comparing the two considered cases. The linear frozen case results in a fluttering response with diverging exponential envelope, whilst the sloshing case develops a limit-cycle oscillation (LCO). This LCO is determined by the nature of the sloshing forces, which become highly dissipative when the acceleration of the tank increases (Rayleigh-Taylor instabilities occur above 1 g). Figure 3.10 compares the response of the sloshing fuel model for two different gust amplitudes, that is $w_{g_a} = 0.15$ m/s and $w_{g_a} = 2.5$ m/s. Within the range of maximum allowable vertical acceleration at the tank locations (given by the identification process), the response of the wing converges to the same limit cycle oscillation.

More in general, the response analysis to small disturbances ($w_{g_a} = 0.15$ m/s) is carried out spanning from 316 m/s to 323 m/s. Figure 3.11 shows the Hopf bifurcation diagram of the limit-cycle oscillation of the wing tip displacement. Despite the nonlinear stabilising contribution of the sloshing forces, the system is nevertheless unstable after a flight speed slightly lower 323m/s. This denotes the presence of an unstable branch coexisting with the stable one identified by the numerical simulations. Moreover, because the sloshing forces are primarily dissipative, the unstable branch cannot exist before the flutter speed. It is worth noting that the limit cycle oscillations of the stable branch exist in a range of displacement amplitude that generally structures of this type can withstand in terms of maximum allowable stresses. Moreover, sloshing is able to provide a limit cycle response up to a velocity which is

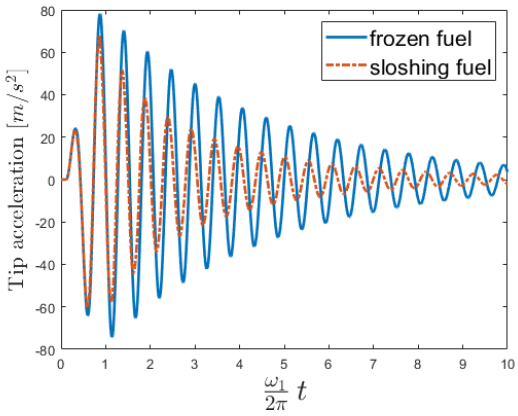

(a) Tip vertical acceleration

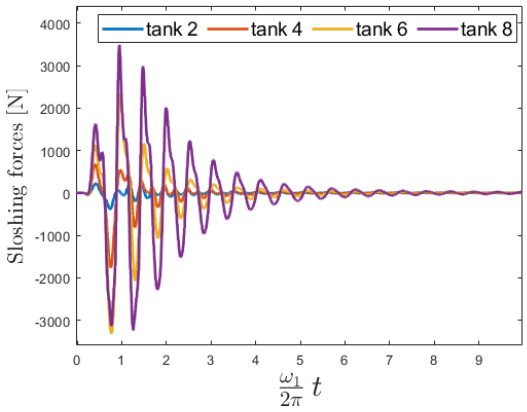

(b) Dynamic sloshing forces

Figure 3.8: Gust response analysis for $U_\infty = 315$ m/s.

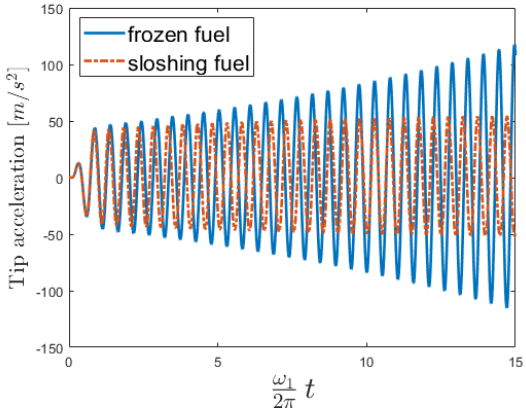

(a) Tip vertical acceleration

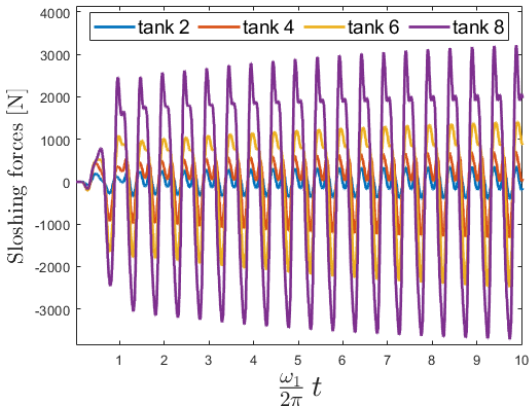

(b) Dynamic sloshing forces

Figure 3.9: Gust response analysis for $U_\infty = 321$ m/s.

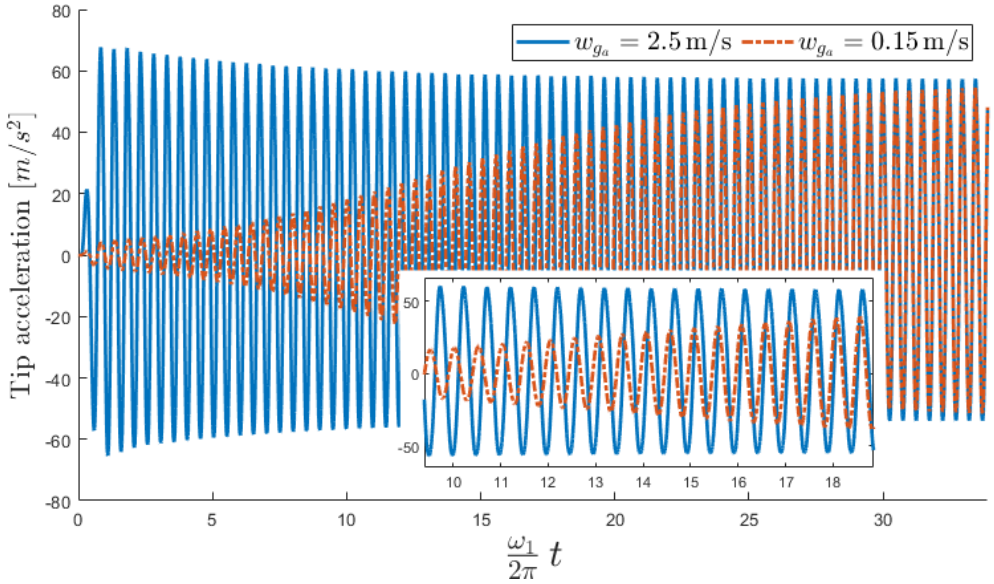

Figure 3.10: Gust response analysis for $U_\infty = 321$ m/s considering two different gust amplitudes.

slightly greater than the linear flutter speed. Therefore, for flutter analyses, this effect must be weighed against other uncertainties from structural and aerodynamic modelling.

Figure 3.12(a) shows a contour plot of the energy exchanged between the structure and external aerodynamics per cycle as a function of the amplitude of the response and flight speed in case the response were solely determined by the unstable branch of the root locus in Fig. 3.5, or $\mathsf{q}(t) \approx \mathsf{w}_1 a_1(t) + c.c.$ [1]. The blue colour indicates the region in which the aerodynamics subtract energy from the structure (positive damping, stable), whereas the red-one indicates that the structure is absorbing energy from the aerodynamics (negative damping, flutter condition).

On the other hand Fig. 3.12(b) provides the energy exchanged by the internal sloshing fluid with the structure summarising the effects of the eight tanks by dimensionalisation and the sum of the map in Fig. 2.42(a). This energy map, similarly to the one in Fig. 3.12(a), is based on the tracking of the critical eigenvector and frequency. By increasing the flight speed, the map is not defined at the higher amplitude because of the increase of the considered aeroelastic frequency. The dissipative nature of sloshing is thus highlighted (positive damping, stabilising effect).

[1] From mode tracking we obtain the eigenvector $\mathsf{w}_{1_{track}}(U_\infty)$ corresponding to unstable branch as a function of the flight speed (that is normalised in order to have real and unit displacement at tip $\longrightarrow a_1$ assumes the meaning of the tip displacement) and the associated frequency $\omega_{1_{track}}(U_\infty)$. Therefore, the following quantity yields the energy exchanged by the structure and the external aerodynamics in a cycle with angular frequency $\omega_{1_{track}}$:

$$L_{aero}(U_\infty, a_1) = \pi\, a_1^2\, \frac{1}{2}\rho U_\infty^2\, \mathcal{I}\Big\{ \mathsf{w}_{1_{track}}^{\mathsf{T}}\, \mathsf{Q}\big(\frac{\omega_{1_{track}}\, b}{U_\infty}\big)\, \mathsf{w}_{1_{track}} \Big\} \tag{3.16}$$

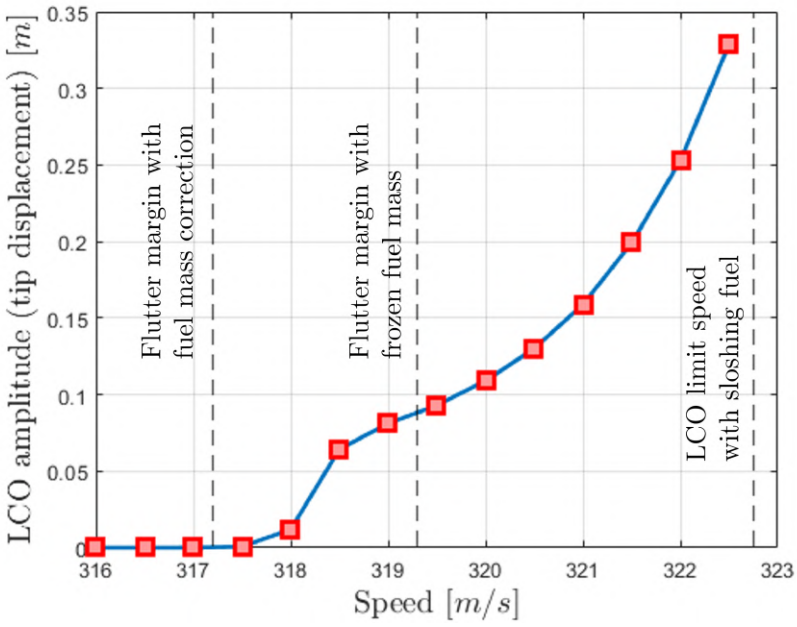

Figure 3.11: Bifurcation diagram.

The energy exchanged between the structure and the fluids (external aerodynamics and sloshing) can be computed by integrating the maps in Figs. 3.12(a) and 3.12(b) (see Fig. 3.12(c)). This figure is overlaid with the LCO bifurcation in Fig. 3.11. The zero-energy isoline should represent the locus of points at which fuel sloshing dissipates as much energy as the aerodynamics induces onto the structure, and thus represents the LCO bifurcation obtained directly from the energy map analysis (Ref. [83]). Note that the LCO bifurcation identified by simulation is similar to the one obtained by energy consideration but it is shift of about 2 m/s due the inertial effects of the fluid in the tank that anticipate the onset of flutter (as shown in Fig. 3.11). Considering the dissipative nature of sloshing, the total energy exchanged between structure and fluid before the flutter speed will always result in positive damping. Moreover, as a result of the saturation of the dissipated energy, an unstable branch may result with vertical asymptote at flutter speed. This *a-priori* post-critical analysis based on energy maps shows that the neural-network-based ROM is capable to reproduce the behaviour of the slosh dynamics when integrated in a complex aeroelastic computational environment.

3.1.3 Landing response analysis

The last analysis is performed considering landing condition with a reference free stream velocity equal to $U_\infty = 150\,\mathrm{m/s}$ and Mach $M_\infty = 0.43$. The simplified landing modeling is

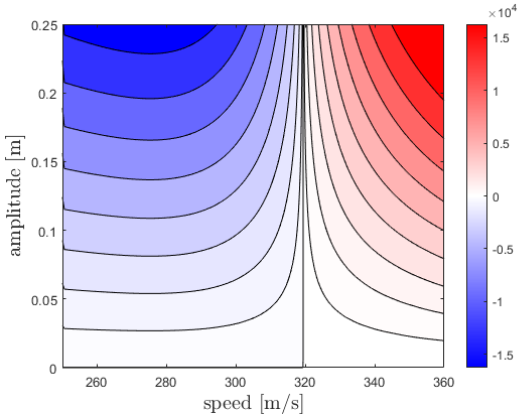

(a) Aeroelastic energy map

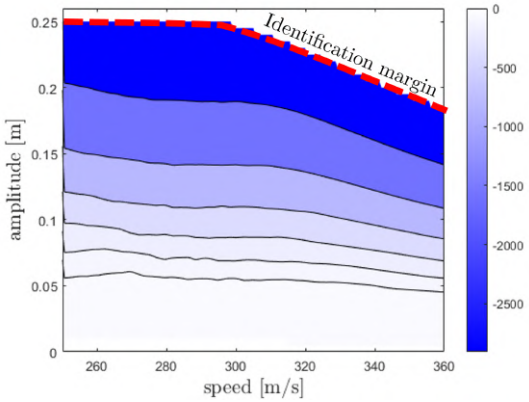

(b) Dissipated energy map by the sloshing forces

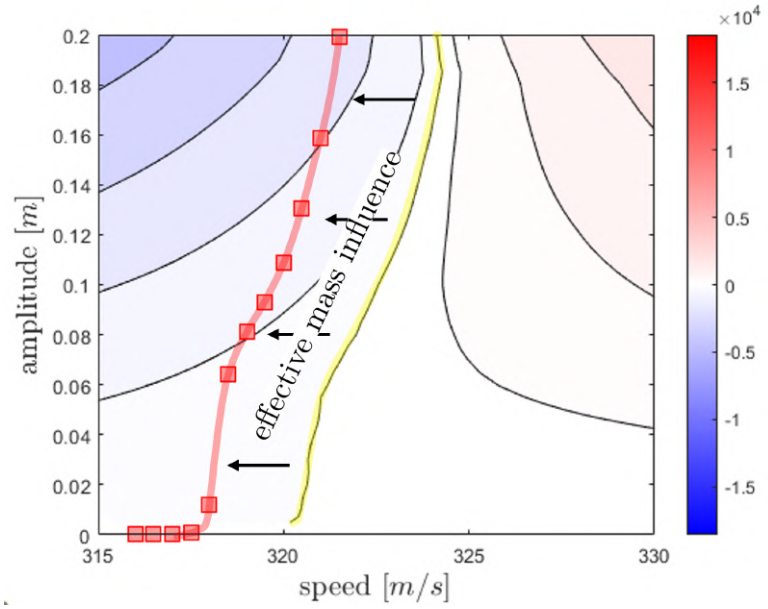

(c) Energy map of the full integrated system (with the LCOs)

Figure 3.12: Energy maps of the wing aerolastic system.

accounted in modal coordinates by specializing the external forces $\mathsf{f}^{(ext)}$ in Eq. 2.26:

$$\mathsf{f}^{(ext)} = \mathsf{b}\,\ddot{u}_{z_f} \tag{3.17}$$

where $\ddot{u}_{z_f}$ is the vertical acceleration of the fuselage and therefore of a system moving according with the wing. Moreover, the *n-th* component of the input vector b is obtained by:

$$b_n = \frac{M_{ac}}{2}\,\mathbf{i}_3 \cdot \boldsymbol{\psi}_n(\mathbf{x}_{lg}) - \iiint_V \rho_m\,\mathbf{i}_3 \cdot \boldsymbol{\psi}_n\,\mathrm{d}V \tag{3.18}$$

where $M_{ac}/2$ is the aircraft half mass, $\mathbf{x}_{lg}$ is the position of the landing gear, ρ_m is the material density, and V is the material volume. The first term in Eq. 3.18 represents the mutual force between the landing gear and the ground, whereas the second term is the fictitious force given by the deceleration of the wing reference system with respect to the ground.

The present simplified modeling is based on the following hypotheses: *i)* the vertical acceleration of the landing gear is assumed equal to the fuselage vertical acceleration; *ii)* there exists only a one way coupling between the dynamics of the fuselage and the wing dynamics; *iii)* ground effects and high-lift devices are not accounted. Using an operational landing acceleration measured at the fuselage of a typical aircraft, the analysis is conducted for the two models taken into account. Figure 3.13(a) compares the wing tip response of the sloshing fuel model with the frozen fuel model. Slosh dynamics provides a bit more damped response with respect to the frozen fluid model. Moreover, Fig. 3.13(b) shows the response of the dynamic sloshing forces.

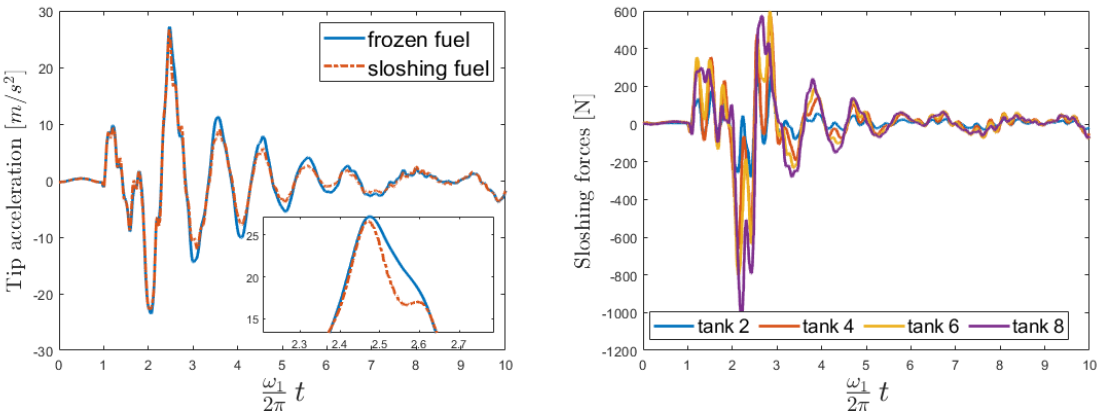

(a) Tip vertical acceleration

(b) Dynamic sloshing forces

Figure 3.13: Landing response analysis.

Summary

A hybrid modeling was used to predict the aeroelastic/sloshing response of a wing prototype model. The coefficients of the aeroelastic model were obtained by a standard linear aeroelastic solver whilst a data-driven approach was used to obtain slosh dynamics which were subsequently incorporated into the aeroelastic framework. The vertical sloshing dynamics was considered using neural networks trained with experimental data from a scaled tank. The neural-network based ROM was properly scaled for being integrated into the aeroelastic system considering the current tank dimensions.

The results concerned the damping performance under pre-critical conditions as well as the limit cycle oscillation caused by the sloshing. In fact, sloshing is the only nonlinear phenomenon modeled in the present work and has proven to be effective in providing an additional margin of stability in post-critical conditions. The characterisation of the limit cycle bifurcation provides results in line with those originally presented in Refs. [98, 99] for a simplified aeroelastic model in wind tunnel. Finally, the effect of sloshing in aircraft landing was also investigated showing the increased damping of the structural response.

3.2 Linear and nonlinear sloshing integrated aeroelastic analyses of a flying wing

This section presents the integration of both linear and nonlinear sloshing ROMs into a flexible aircraft model, where flight dynamics and aeroelasticity are involved. It is assumed that sloshing forces can be decomposed into a lateral part with linearised behavior and a vertical part with extremely nonlinear behavior by neglecting their mutual interactions. The present work mainly relies on the approach described in [100], where the fully coupled equation of motion of the aircraft have been derived by assuming practical mean axes (PMA) constraints. The structure is modeled using the finite element method (FEM), whereas the doublet lattice method (DLM) is used to describe the unsteady aerodynamics (see Ref. [95]). Using the rational polynomial function approximation, the unsteady aerodynamics is recast into a pure differential expression that requires a new set of aerodynamic state space variables (see Ref. [101]). The linear sloshing resembled in this analysis occurs during rotations or lateral motions of the tank. Studies on the effects of lateral sloshing on the aeroelastic behaviour of aircraft can be found in Ref. [24], where the lateral sloshing is modelled via mass-spring-damper mechanical model, in [25] where an hydroelastic added-mass model is used, in [26] where a linearized frequency domain (LFD) is employed, and in [27] where the an Equivalent Mechanical Model for sloshing is used by showing the effect on aeroelastic and flight mechanics stability as well. The reduced-order model used to describe linear sloshing in this study relies on the analytical formulation provided in Ref. [2] and its further development in Ref. [15],

according to which a realistic representation of linearised liquid dynamics inside containers with simplified geometry can be approximated by an equivalent mechanical model, whose parameters can be suitably related with the physical quantities obtained from the linearised potential flow theory (Ref. [28]). The integration of linear sloshing, described by means of an EMM, introduces additional state variables (analogous to aerodynamics), so representing latero-rotational sloshing dynamics (see Appendix D for more details). Nonlinear vertical sloshing, on the other hand, is a phenomenon caused by accelerations perpendicular to the the liquid free surface, which interacts with the aeroelastic model by providing a nonlinear force contribution that depends on the vertical excitation of the aircraft tanks. The vertical sloshing dynamics is modeled with the neural-network-based NFIR model having 60 delay lines and 20 neurons introduced in Sec. 2.2. The combined effect of linear and nonlinear sloshing dynamics is modeled by adding the two contributions they make to the system. The reference aircraft is the Body Freedom Flutter (BFF) (whose model is proposed in Ref. [79] and a flutter suppression strategy also proposed in Ref. [80]) in two different cases or configurations. The first one has only one tank that is partially filled with a low density liquid and placed beneath the aircraft center of mass whereas the second case has two rectangular tanks symmetrically placed beneath the wings. Sloshing and frozen mass (in which liquid is just a ballast) models are compared to quantify the sloshing effects on aircraft aeroelastic behavior. Stability analyses show how the coupling between linear sloshing, aircraft aeroelasticity, and flight dynamics contributes to modify the overall aircraft stability scenario. Nonlinear response aeroelastic analyses provide that dynamic loads alleviation is achieved when vertical (nonlinear) sloshing is also included in the overall aeroelastic model. Moreover, limit cycle oscillations arise after the onset of flutter due to the dissipative characteristics of vertical sloshing.

3.2.1 Flexible aircraft with sloshing integrated modeling

The present modeling is based on the formulation presented in Refs.[27, 100], in which the rigid body degrees of freedom are associated with the so-called practical mean axes (PMAs), characterised by having the PMA frame origin in the instantaneous center of mass and the orientation of the principal axes invariant with respect the deformations. The linearised elastic deflections are described as a combination of unconstrained aircraft mode shapes in the PMAs thus relaxing the inertial formulation.

The equations of motion for the conservation of momentum and angular momentum and

the equations of the structural dynamics are given by:

$$\begin{aligned} m\frac{\mathrm{d}\mathbf{v}_{\mathsf{G}}}{\mathrm{d}t} &= \mathbf{f}_{\mathsf{T}} \\ \frac{\mathrm{d}\mathbf{h}_{\mathsf{G}}}{\mathrm{d}t} &= \mathbf{m}_{\mathsf{G}} \\ m_n\ddot{q}_n + k_n q_n &= f_n \qquad n = 1, \ldots, N_m \end{aligned} \tag{3.19}$$

where $\mathbf{v}_{\mathsf{G}}$ and $\mathbf{h}_{\mathsf{G}}$ are the centre of mass velocity and the angular momentum respectively, m is the total mass, $\mathbf{f}_{\mathsf{T}}$ and $\mathbf{m}_{\mathsf{G}}$ are the aerodynamic force and moment, respectively, whereas q_n denotes the n-th modal coordinate, m_n, k_n, and f_n are the n-th modal mass, stiffness and generalized force and N_m is the number of flexible modes included in the analysis. The equations of motion (3.19) are then recast with respect a body frame of reference and linearised around a level flight aeroelastic trim condition:

$$\begin{aligned} m\frac{\mathrm{d}\mathbf{v}_{\mathsf{G}}}{\mathrm{d}t} = m\dot{\mathbf{v}}_{\mathsf{G}} + \boldsymbol{\omega}\times\mathbf{v}_{\mathsf{G}} \approx m\Delta\dot{\mathbf{v}}_{\mathsf{G}} - \mathbf{v}_{\mathsf{G}_e}\times\Delta\boldsymbol{\omega} = \Delta\mathbf{f}_{\mathsf{T}} \\ \frac{\mathrm{d}\mathbf{h}_{\mathsf{G}}}{\mathrm{d}t} = \frac{\mathrm{d}\mathbf{J}\boldsymbol{\omega}}{\mathrm{d}t} + \boldsymbol{\omega}\times\mathbf{J}\boldsymbol{\omega} \approx \mathbf{J}\Delta\dot{\boldsymbol{\omega}} = \Delta\mathbf{m}_{\mathsf{G}} \\ m_n\Delta\ddot{q}_n + k_n\Delta q_n = \Delta f_n \qquad n = 1, \ldots, N_m \end{aligned} \tag{3.20}$$

where $\mathbf{J}$ is the inertia tensor, and $\boldsymbol{\omega}$ is the angular velocity. It is worth noting that, if a linearization around a trimmed straight flight solution is performed, the inertial coupling terms in Ref. [100] can be neglected.

The variables associated to a second order dynamics are grouped in the following vector:

$$\Delta\eta = \left\{\Delta\mathsf{x}_{\mathsf{G}}^{\mathsf{T}}, \Delta\Theta^{\mathsf{T}}, \Delta\mathsf{q}^{\mathsf{T}}\right\}^{\mathsf{T}} \tag{3.21}$$

where

$$\begin{aligned} \Delta\mathsf{x}_{\mathsf{G}} &= \{\Delta x_{\mathsf{G}},\, \Delta y_{\mathsf{G}},\, \Delta z_{\mathsf{G}}\}^{\mathsf{T}} \\ \Delta\Theta &= \{\Delta\phi,\, \Delta\theta,\, \Delta\psi\}^{\mathsf{T}} \end{aligned} \tag{3.22}$$

are respectively the perturbation vectors of the center of mass coordinates in inertial frame of reference and of the Euler angles. Moreover, the perturbation vector of the modal coordinates is given by

$$\Delta\mathsf{q} = \{\Delta q_1,\, \ldots,\, \Delta q_{N_m}\}^{\mathsf{T}} \tag{3.23}$$

Nevertheless, the equations of motion of the aircraft are expressed in a non inertial frame of reference. Indeed, the following vector is defined

$$\Delta\nu = \left\{\Delta\mathsf{v}_{\mathsf{G}}^{\mathsf{T}}, \Delta\omega^{\mathsf{T}}, \Delta\dot{\mathsf{q}}^{\mathsf{T}}\right\}^{\mathsf{T}} \tag{3.24}$$

where $\Delta \mathsf{v}_{\mathsf{G}} = \{\Delta u, \Delta v, \Delta w\}^{\mathsf{T}}$ and $\Delta\omega = \{\Delta p, \Delta q, \Delta r\}^{\mathsf{T}}$ are the translational and angular velocities in the PMAs coordinate system, respectively. The linearised relation between $\Delta\eta$ in Eq. (3.24) and $\Delta\nu$ is expressed as

$$\Delta\dot{\eta} = \Delta\nu + \mathsf{T}_1^* \Delta\eta \tag{3.25}$$

with

$$\mathsf{T}_1^* = \begin{bmatrix} \mathsf{0}_{3\times3} & -\hat{\mathsf{V}}_{\mathsf{G}_e} & \mathsf{0}_{3\times N_m} \\ \mathsf{0}_{3\times3} & \mathsf{0}_{3\times3} & \mathsf{0}_{3\times N_m} \\ \mathsf{0}_{N_m\times3} & \mathsf{0}_{N_m\times3} & \mathsf{0}_{N_m\times N_m} \end{bmatrix}, \quad \hat{\mathsf{V}}_{\mathsf{G}_e} = \begin{bmatrix} 0 & 0 & 0 \\ 0 & 0 & -U_\infty \\ 0 & U_\infty & 0 \end{bmatrix} \tag{3.26}$$

where $\mathsf{0}_{\bullet\times\bullet}$ are zero matrices with suitable number of rows and columns. Equation 3.26 allows to highlight the link between the variables expressed in the PMAs and those defined in the inertial reference system (being T_1^* a square matrix with dimension $N = 6 + N_m$). Taking into account the external action of aerodynamics and sloshing dynamics, the system of Eqs. (3.20) can be rewritten as follows:

$$\mathsf{M}\,\Delta\dot{\nu} + \mathsf{D}\,\Delta\nu + \mathsf{K}\,\Delta\eta \;=\; \mathsf{e} + \mathsf{g} + \mathsf{f}^{(ext)} \tag{3.27}$$

where M, D and K are, respectively, the modal mass, damping and stiffness (diagonal) matrices of the flexible aircraft, whereas $\mathsf{e} = [e_1, e_2, \ldots, e_N]^{\mathsf{T}}$ and $\mathsf{g} = [g_1, g_2, \ldots, g_N]^{\mathsf{T}}$ are, respectively, the generalized *aerodynamic* and *sloshing* forces induced by the aircraft motion. These forces are generally defined as projection of physical applied force fields (aerodynamics and sloshing) on the assumed rigid and flexible mode shapes. In the present paper the wing body is assumed to be locally rigid in the neighborhood of the tank (see Refs. [14, 23]) and therefore, the force field projection becomes a scalar product (see later Eq. 2.29). The $\mathsf{f}^{(ext)}$ is the vector of the current external forcing terms like the gust excitation. The description of the aircraft motion in the PMA non-inertial reference requires accounting for the projection of the weight force on the aircraft body reference. Under the assumption of small perturbation with respect to the trimmed configuration, such a contribution was modelled as an additional stiffness term included inside K.

The generalised aerodynamic force vector is generally computed as a function of the reduced frequency $k = \omega b/U_\infty$ (with b semi-chord and U_∞ free stream velocity) and Mach number M_∞ domain (see Ref. [95]) as:

$$\tilde{\mathsf{e}} = q_D\, \mathsf{Q}(k, M_\infty)\, \Delta\tilde{\eta} \tag{3.28}$$

where $\mathsf{Q}(k, M_\infty)$ is the generalised aerodynamic forces matrix, q_D is the dynamic pressure and the symbol $\tilde{}$ is used to represent the Laplace/Fourier transforms. For a fixed value of

M_∞, the same rational function approximation for unsteady aerodynamics presented in Eq. 3.4 is considered. Introducing the aerodynamic states vector a and exploiting the definition of inverse Fourier transform, the aerodynamic forces can be recast in time domain as:

$$\mathsf{e} = q_D\,\mathsf{A}_0\,\Delta\eta + q_D\,\frac{b}{U_\infty}\,\mathsf{A}_1\,\Delta\nu + q_D(\frac{b}{U_\infty})^2\,\mathsf{A}_2\,\Delta\dot{\nu} + q_D\,\mathsf{C}\,\mathsf{a} \tag{3.29}$$

$$\dot{\mathsf{a}} = \frac{U_\infty}{b}\,\mathsf{P}\,\mathsf{a} + \mathsf{B}\,\Delta\nu \tag{3.30}$$

In this work, the effect of two different sloshing dynamics is considered. The first is present when small lateral displacements and rotations are imposed on the tanks. In these cases, the dynamics can be considered linear (Ref. [23]) and give rise to sloshing generalised loads referred to as g_l. The second is instead nonlinear, and its action g_{nl} is triggered as a result of large vertical perturbations imposed on the tanks. Thus, the generalised sloshing forces vector g is composed as a sum of contributions $\mathsf{g}^{(i)}$ of individual tanks:

$$\mathsf{g} = \sum_{i=1}^{N_T} \mathsf{g}^{(i)} = \sum_{i=1}^{N_T} \left(\mathsf{g}_l^{(i)} + \mathsf{g}_{nl}^{(i)}\right) \tag{3.31}$$

with N_T the number of tanks.

The linear contribution is due to the presence of lateral standing waves and is modelled using equivalent mechanical models that allow the force and moment exerted by the liquid, following the application of a small lateral displacement or rotation. The lateral sloshing forces for each tank in Laplace domain are expressed by means of a generalised sloshing forces matrix $\mathsf{G}(s)^{(i)}$ as

$$\tilde{\mathsf{g}}_l^{(i)} = \bar{\mathsf{G}}(s)^{(i)}\Delta\tilde{\eta} \tag{3.32}$$

Appendix D provides the formulation of the linear lateral sloshing forces based on the analytical model (Ref. [2]), according with, the generalized sloshing forces can be recast as it follows:

$$\tilde{\mathsf{g}}_l^{(i)} = s^2\,\bar{\mathsf{A}}_s^{(i)}\,\Delta\tilde{\eta} + \left(s^2\bar{\mathsf{B}}_s^{(i)} + \bar{\mathsf{C}}_s^{(i)}\right)\tilde{\mathsf{r}}^{(i)} \tag{3.33}$$

where the linear sloshing modal coordinates $\tilde{\mathsf{r}}^{(i)}$ are introduced as

$$\tilde{\mathsf{r}}^{(i)} = \left[\left(s^2\mathsf{I} + s\mathsf{D}_s^{(i)} + \Omega_s^{2(i)}\right)^{-1}\left(s^2\,\bar{\mathsf{B}}_s^{(i)} + \bar{\mathsf{C}}_s^{(i)}\right)^{\mathrm{T}}\right]\Delta\tilde{\eta} \tag{3.34}$$

and $\bar{\mathsf{A}}_s^{(i)}, \bar{\mathsf{B}}_s^{(i)}, \bar{\mathsf{C}}_s^{(i)}, \mathsf{D}_s^{(i)}$ and $\Omega_s^{2(i)}$ are the coefficient matrices of the lateral sloshing operator. It is worth to mention that $\Omega_s^{2(i)}$ and $\bar{\mathsf{D}}_s^{(i)}$ are, respectively, the natural frequency and damping modal coefficient matrices of the considered linear sloshing modes. The same representation

of the sloshing force can be achieved by a linear frequency domain approach as in Ref. [23, 26]. The inverse Laplace transform of Eqs. 3.32 and 3.34 leads to

$$\mathsf{g}_l^{(i)} = \bar{\mathsf{A}}_s^{(i)} \Delta\ddot{\eta} + \bar{\mathsf{B}}_s^{(i)} \ddot{\mathsf{r}} + \bar{\mathsf{C}}_s^{(i)} \mathsf{r}^{(i)} \tag{3.35}$$

$$\ddot{\mathsf{r}}^{(i)} + \mathsf{D}_s^{(i)} \dot{\mathsf{r}}^{(i)} + \Omega_s^{2(i)} \mathsf{r}^{(i)} = \bar{\mathsf{B}}_s^{(i)\mathsf{T}} \Delta\ddot{\eta} + \bar{\mathsf{C}}_s^{(i)\mathsf{T}} \Delta\eta \tag{3.36}$$

in which the second order dynamics of the sloshing modal coordinates is highlighted.

The nonlinear force contribution is instead related to the *dynamic sloshing force* $\Delta f_{S_z}^{(i)}$ given by the relative acceleration of the liquid particles with respect to the *i-th* tank non-inertial frame (see Ref. [81]). The *n-th* component of $\mathsf{g}_{nl}^{(i)}$ is the projection (following the approximation previously discussed after Eq. 3.27) of the sloshing dynamic force on each *n-th* rigid and elastic modal shape $\boldsymbol{\psi}_n$ as:

$$g_{nl_n}^{(i)} = \boldsymbol{\psi}_n(\mathbf{x}_{T_i}) \cdot \mathbf{i}_3 \, \Delta f_{S_z}^{(i)} \tag{3.37}$$

where $\mathbf{x}_{T_i}$ is the geometrical centre of the *i-th* tank, $\mathbf{i}_3$ is the vertical unit vector of the inertial frame of reference and $\boldsymbol{\psi}_n(\mathbf{x}_{T_i})$ correspond to the *n-th* column of matrix $\mathsf{Z}_t^{(i)}$ (defined in Appendix D).

The formulation is implemented in Simulink® as illustrated in Fig. 3.3, creating a numerical model combining a purely differential linear problem describing flight dynamics, aeroelasticity and linear sloshing, and a data-driven model representing nonlinear vertical sloshing dynamics. As for the wing prototype model, the nonlinear sloshing block contains the NFIR model shown in Fig. 3.4 and appropriately scaled up following the procedure implemented in Sec. 2.2.5. As will be shown in Sec. 3.2.2, in fact, the tanks mounted on the two reference configurations turn out to have different dimensions to those of the box used to generate the training data for the vertical sloshing reduced-order model. It is therefore necessary to use the scaling law in order to use this model in the applications under consideration. Refs. [81, 86] provide further details nonlinear reduced-order modeling based on neural network driven by experimental data obtained with a suitable scaled tank. It is worth noting that the neural network is fed with the tanks vertical velocity expressed in the inertial frame of reference and provides an estimate of the already defined dynamic sloshing force Δf_{S_z}.

3.2.2 Case Studies

The test cases analysed in this study are based on the finite element model (FEM) of the Body-Freedom-Flutter (BFF), an unmanned flying-wing research aircraft model of total mass $M = 5.44\,\mathrm{Kg}$ (without tanks), half-chord $b = 0.2\,\mathrm{m}$, wing span equal to $3.048\,\mathrm{m}$ and projected wing surface area equal to $1.084\,\mathrm{m}^2$. The model takes its name from its flutter mode involving both vibrations and rigid body motion of the aircraft (Ref. [79]). The first six flexible modes,

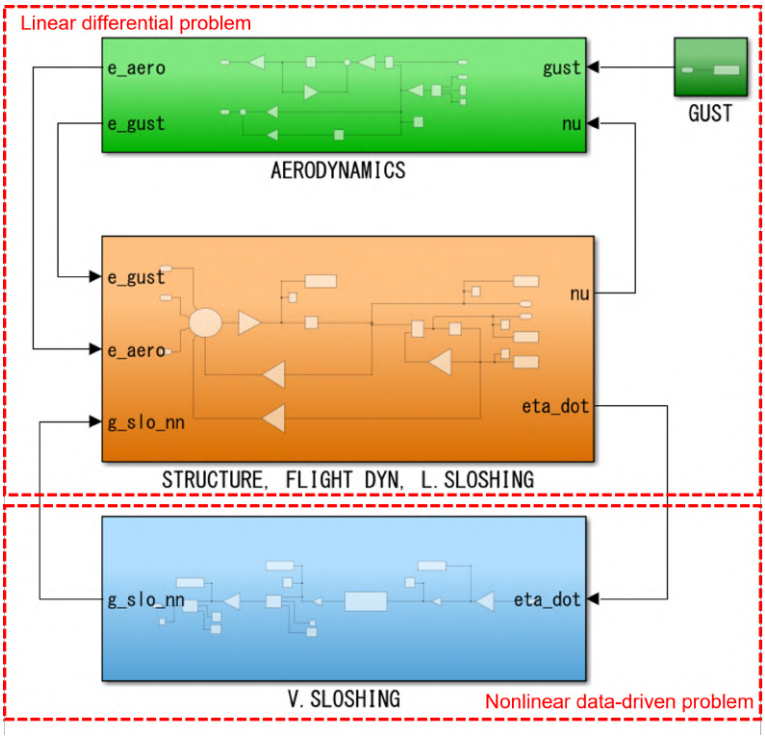

Figure 3.14: Flexible aircraft with linear and nonlinear sloshing modeling in Simulink®.

with their respective frequencies, are shown in Fig. 3.15. The effects of sloshing dynamics on the aircraft are studied in two different configurations, one with a single tank under the center of mass (see Fig. 3.16) and the other with two tanks symmetrically placed under the wings (see Fig. 3.17). The geometric dimensions of the tank of case study 1 (half-filled with a liquid with density $\rho = 650 kg/m^3$) are listed in Tab. 3.1 and are such that the total mass of liquid contained is 25% of the structural mass of the aircraft. This configuration in Fig. 3.16 will be hereafter denoted as case study 1.

Table 3.1: Tank geometry - case study 1

Parameter	Value (m)
side in direction x	0.18
side in direction y	0.18
h (height)	0.13
h_f (filling level 50%)	0.065

In the present analysis, three sloshing modes have been considered in the linear lateral analysis for both the dynamics along x and y (in plane dimensions). The natural frequencies of linear sloshing are reported in Tab. 3.2 (when the tank detached from the structure).

The case study 2 was realised by considering two tanks created by halving the tank shown

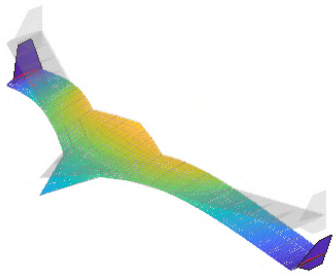

(a) $f_1 = 5.83$ Hz

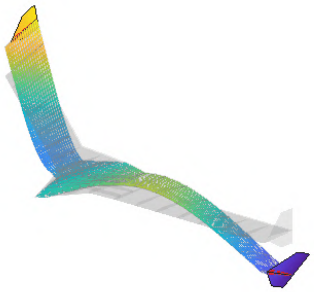

(b) $f_2 = 8.83$ Hz

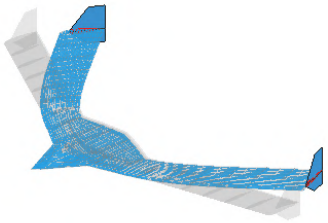

(c) $f_3 = 13.45$ Hz

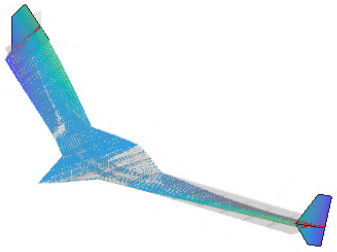

(d) $f_4 = 19.82$ Hz

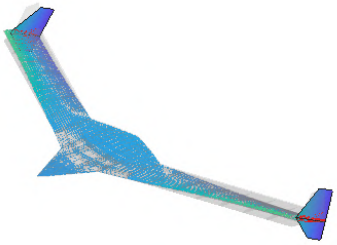

(e) $f_5 = 20.09$ Hz

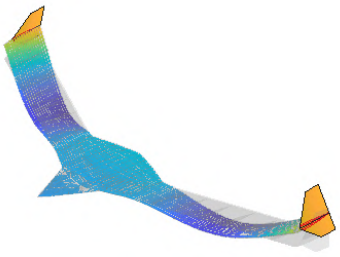

(f) $f_6 = 23.72$ Hz

Figure 3.15: Elastic mode shapes of the model. Captions indicate their natural frequencies.

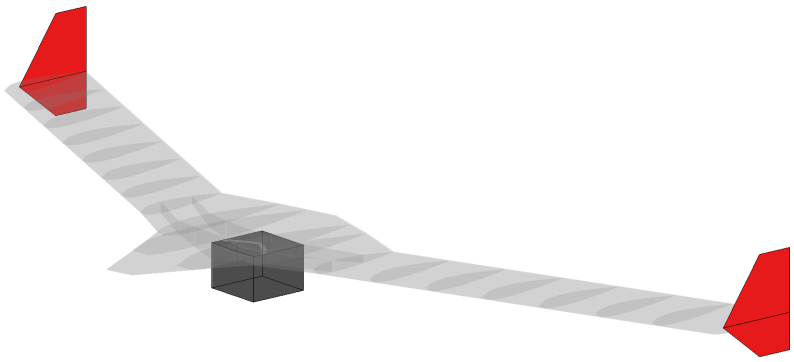

Figure 3.16: Configuration with one box shaped tank placed underneath the BFF center of mass

Table 3.2: Linear sloshing natural frequencies - case study 1

Mode number	Direction	Frequency (rad/s)
1,2	x, y	11.80
3,4	x, y	22.64
5,6	x, y	29.26

in Tab. 3.1 in the y-direction to ensure the same amount of liquid carried by the aircraft (see Tab. 3.3). The natural frequencies of sloshing in this case are different depending on the direction in the tanks plane being considered, as can be seen in Tab. 3.4. This implies the presence of three modal coordinates describing the linear sloshing, referred to as $r_1^{(i)}$, $r_2^{(i)}$ and $r_3^{(i)}$, for both tanks. From a FEM modelling point of view, a node located at the tank

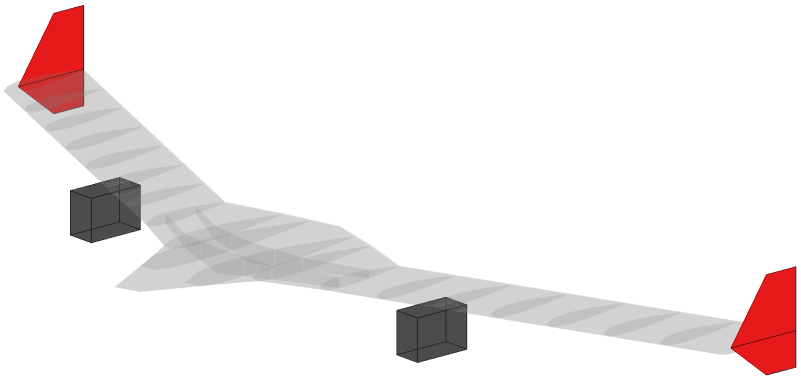

Figure 3.17: Configuration with two box shaped tanks placed under the BFF wings

geometrical center was created and attached to the aircraft structure by means of a rigid body element. On the other hand, the small-disturbance unsteady aerodynamics is modeled via the Doublet Lattice Method (DLM) available in MSC Nastran for unsteady linear aeroelastic

Table 3.3: Tank geometry - case study 2

Parameter	Value (m)
side in direction x	0.18
side in direction y	0.09
h (height)	0.13
h_f (filling level 50%)	0.065

Table 3.4: Linear sloshing natural frequencies - case study 2

Mode number	Direction	Frequency (rad/s)
1	x	11.80
2	y	18.31
3	x	22.64
4	y	32.05
5	x	29.26
6	y	41.38

analysis (Ref. [95]). As can be seen in Fig. 3.14, linear sloshing was included in the same block as the structural and flight dynamics model of the aircraft. Indeed, combining Eqs. (3.27), (3.31) and (3.33) it is possible to obtain an augmented model with additional modal variables represented precisely by the added state-space vector r.

3.2.3 Aeroelastic stability and response analyses

This section presents the stability and response analyses performed for the two configurations presented in Sec. 3.2.2, highlighting the effects of lateral (linear) and vertical (nonlinear) sloshing dynamics with respect to the case where the liquid is frozen ($\mathsf{r} = \mathsf{0}$ and $\Delta f_{S_z} = 0$). The linearised aeroelastic system of the two case studies is used to evaluate the stability scenario of the aircraft between 13 m/s and 30 m/s considering incompressible and sea level flow conditions. On the other hand, gust response analyses at different velocities in the neighbourhood of the flutter speed are performed to investigate the role of sloshing in damping aircraft vibrations. Specifically, the following standard gust profile is considered for both case studies:

$$w_g(t) = \begin{cases} \frac{1}{2} w_{g_a} \left[1 - \cos\left(\frac{2\pi U_\infty t}{L_g} \right) \right] & \text{if} \quad 0 < t < \frac{L_g}{U_\infty} \\ \mathsf{0} & \text{if} \quad t \geq \frac{L_g}{U_\infty} \end{cases} \tag{3.38}$$

where w_{g_a} is the gust amplitude and b the chord length. The set value of the gust length is $L_g = 25\, b$. Spatially, the gust is assumed to be constant throughout the wing domain. Four models will be compared for both case studies, namely the *frozen fuel* model, the *lateral (linear) sloshing* model, the *vertical (nonlinear) sloshing* model, and the *full sloshing* model,

in which both types of sloshing considered in this analysis are accounted.

Test case 1

The stability scenario of the aircraft model in the frozen liquid configuration (blue diamonds) is compared in Fig. 3.18 with that in which lateral sloshing is considered in the formulation (red squares). Figure 3.18(b) highlights the additional poles representing linear sloshing dynamics, along with rigid-body dynamics. Lateral sloshing slightly worsens the stability of the aircraft with respect to the frozen fuel case. In fact, the flutter speed U_F slightly decreases from 18.95 m/s to 18.8 m/s. This corresponds to a slight change in the critical frequency ω_F, which increases from 23.53 rad/s (3.74 Hz) to 23.82 rad/s (3.79 Hz). In both configurations, the critical mode occurs due to the coupling between the *short period* mode and the first vibration mode. The crossing of the imaginary axis occurs with the pole originating from the branch of the first mode (see Fig. 3.18(a)). Furthermore, sloshing dynamics have a non-negligible effect on *dutch roll* and *phugoid*, making the latter less stable and very close to the imaginary axis. On the other hand, the higher frequency poles are only minimally affected and show no particular changes compared to the frozen case. Two different flight conditions

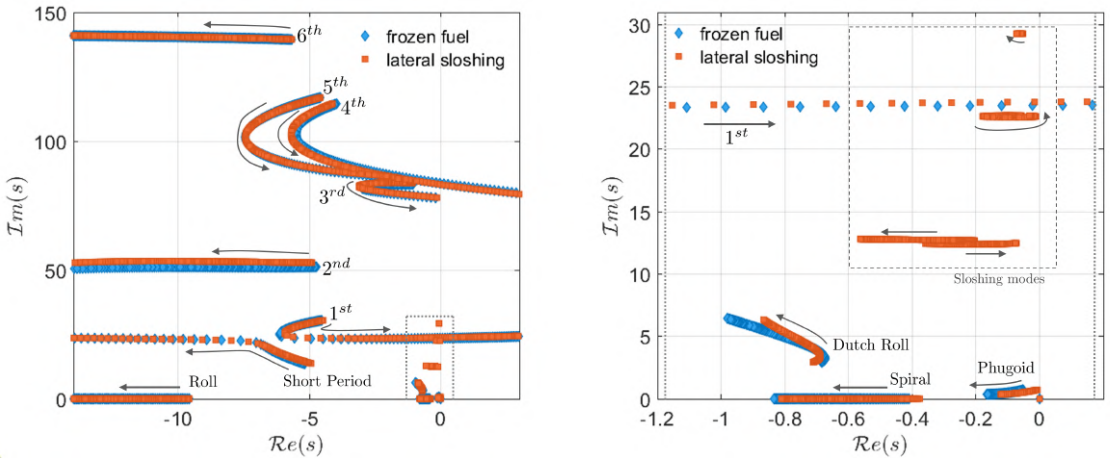

(a) Root locus of the integrated system

(b) Focus on the rigid body and sloshing modes

Figure 3.18: Root locus with linear sloshing - test case 1

are considered for the gust response analysis, that is $U_\infty = 18$ m/s (*i.e.*, before the flutter speed of the linear sloshing and the frozen fuel models), and $U_\infty = 19.35$ m/s (after flutter onset). Moreover, the dependency of the vertical sloshing induced damping by the response magnitude is investigated by taking into account different gust amplitudes. The first analysis is performed at a free stream velocity of $U_\infty = 18$ m/s, with a gust intensity of $w_{g_a} = 2.5$ m/s. Being slightly under pre-critical conditions (speed equal to 95% and 96% of the flutter speeds

of the frozen and lateral sloshing models), the response is expected to be slightly damped. Figure 3.19(a) compares the aircraft responses of the four considered models in terms of local angle of attack (AoA = $\Delta w/U_\infty$). Similarly, Fig. 3.19(b) shows the comparison in terms of the response of the first dry vibration mode q_1, whose values have meters as units when normalised to unit displacement. A reasonable result is the ability of vertical sloshing dynamics to make the aeroelastic response more damped than in the frozen case due to the sloshing impacts that occur in the tank. It also leads to a change in the frequency of the response, which is lower than in the frozen case. Linear sloshing does not introduce dissipative effects into the response, but induces a slight increase in frequency (in the same way as the critical frequency). Figure 3.20 shows the time trends of the nonlinear dynamic sloshing force for the vertical and full sloshing models. The forces almost overlap because the neural network-based reduced-order model receives a similar tank velocity as input for both models. The particularly nonlinear response in the first three cycles is caused by the impacts between the fluid and the tank walls. Finally, Fig. 3.21 shows comparisons between the responses of the first two added sloshing modes (in x-direction) in the linear and full sloshing models. The modes in question do not appear to be influenced by aeroelastic or rigid-body dynamics, but solely by the initial condition imposed by the external gust. The vertical sloshing effect dampens the second mode response for a few seconds, before becoming irrelevant. Sloshing modes in the y-direction are not affected by the gust and therefore do not exhibit active dynamics. The response analysis is then performed at $U_\infty = 19.35\,\mathrm{m/s}$ in developed flutter condition with a gust amplitude of $w_{g_a} = 0.3\,\mathrm{m/s}$. Being under flutter conditions (the speed is 2% and 3% higher than flutter speeds of the frozen and lateral sloshing models, respectively), the response is expected to be unstable with exponential envelope. The local angle of attack and the first mode responses are shown in Figs. 3.22(a) and 3.22(b) comparing the effects that the four considered models have on the flying wing post-critical response. The linear sloshing model as well as the frozen fuel configuration results in a unstable response. In contrast, vertical sloshing helps prevent the response from growing indefinitely, favoring the onset of limit cycle oscillations (LCOs). This behaviour is determined by the nature of the nonlinear sloshing forces, which become highly dissipative when the acceleration of the tank increases. In the case of a combined effect of the two sloshing dynamics, the oscillation amplitude is greater than in the case of only vertical sloshing.

Test case 2

Figure 3.23 shows the results of the stability analysis conducted for the second case study, both for the frozen model (blue diamonds) and for the linear sloshing model (red squares). The stability scenario of the frozen model is different from that of test case 1. In fact, to ensure the static stability of the two-tank configuration, it was necessary to place them under the wings with some offset in the longitudinal direction. Such a tank location emphasizes the

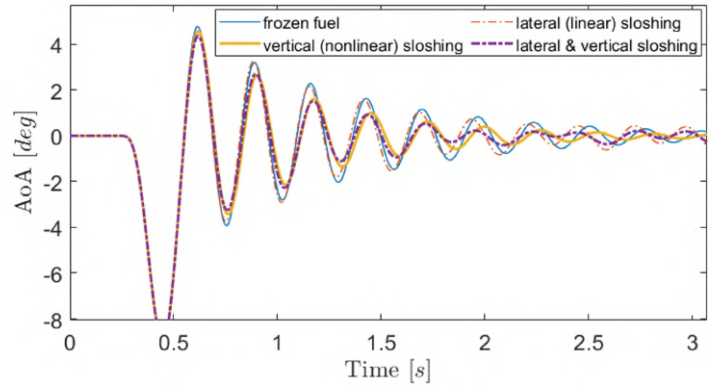

(a) Local angle of attack

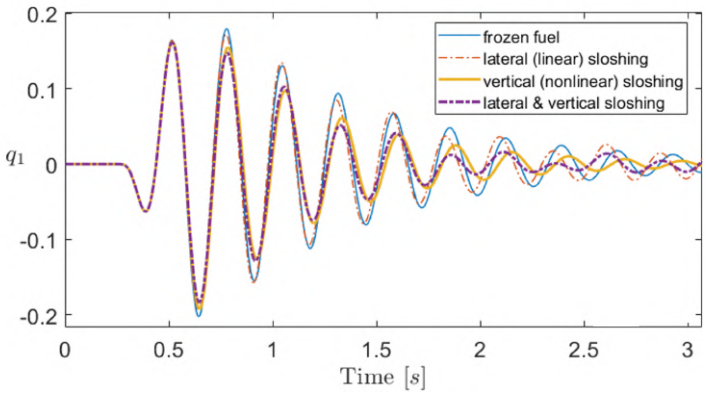

(b) First structural mode

Figure 3.19: $U_\infty = 18\,\mathrm{m/s}$ and $w_{g_a} = 2.5\,\mathrm{m/s}$ - test case 1

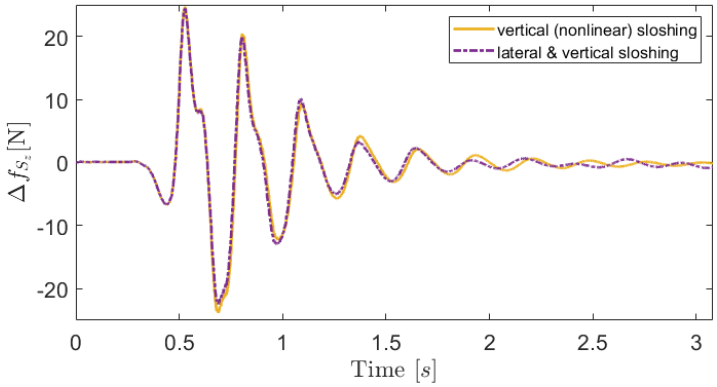

Figure 3.20: Dynamic sloshing force for $U_\infty = 18\,\mathrm{m/s}$ and $w_{g_a} = 2.5\,\mathrm{m/s}$ - test case 1

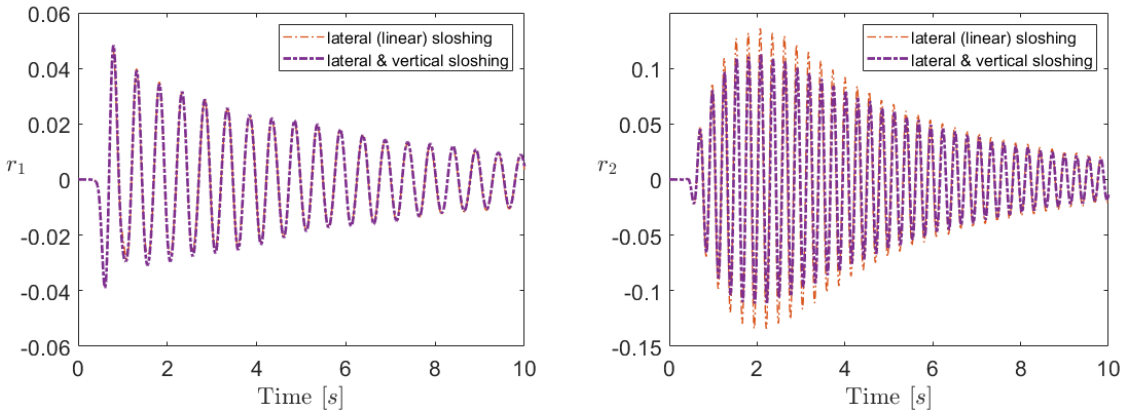

(a) First mode (dir. x)

(b) Second mode (dir. x)

Figure 3.21: Sloshing modes for $U_\infty = 18\,\mathrm{m/s}$ and $w_{g_a} = 2.5\,\mathrm{m/s}$ - test case 1

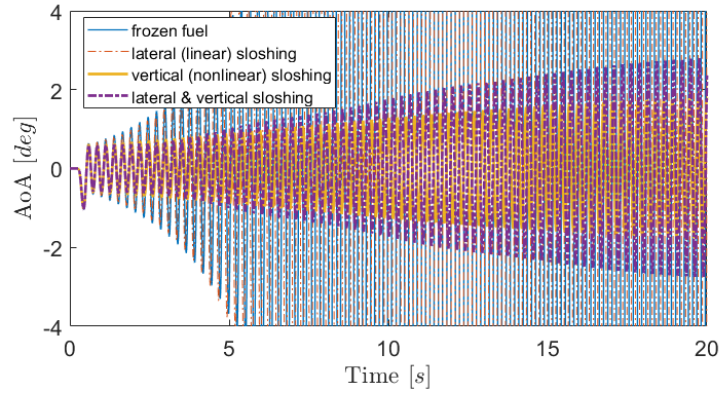

(a) Local angle of attack

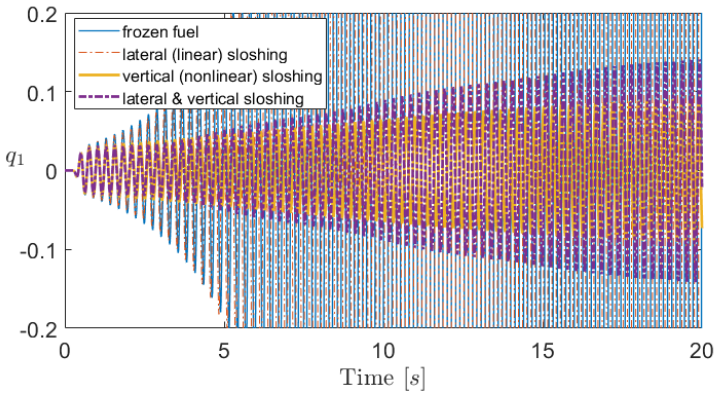

(b) First structural mode

Figure 3.22: $U_\infty = 19.35\,\mathrm{m/s}$ and $w_{g_a} = 0.3\,\mathrm{m/s}$ - test case 1

coupling between the torsional mode (fourth mode) and the anti-symmetrical bending mode (second mode). For the frozen model, flutter instability occurs at $U_\infty = U_F = 20.86\,\text{m/s}$ with the branch that originates from the *short period* (see Fig. 3.23(a)), whereas the flutter frequency is $\omega_F = 22.7\,\text{rad/s}\,(3.61\,\text{Hz})$. The critical mode occurs due to thecoupling between the the *short period* and *first vibration* mode. Note also that the third mode becomes unstable at a flight speed of $U_\infty = 22.65\,\text{m/s}$, which corresponds to the a frequency value equal to $48.22\,\text{rad/s}\,(7.67\,\text{Hz})$. Lateral sloshing introduces poles that go to significantly affect the dynamics of the aircraft. Figure 3.23(b) highlights rigid body dynamics and the added dynamics of linear sloshing. One of the latter crosses the imaginary axis at a low velocity equal to $U_\infty = 16.2\,\text{m/s}$, making the system slightly unstable. The presence of the sloshing dynamics makes the body freedom flutter pole (short period mode) more stable augmenting the flutter margin to $U_\infty = 21.71\,\text{m/s}$ ($\omega = 23.12\,\text{rad/s}$). However, there is also a deterioration in the stability of the third mode, which crosses the imaginary axis at the speed of $U_\infty = 20.94\,\text{m/s}$ ($\omega = 49.13\,\text{rad/s}$) giving rise to a critical bending-torsional mode. Sloshing dynamics also have an impact at low frequency, also going to affect both the frequency and damping of *dutch roll* and *phugoid*.

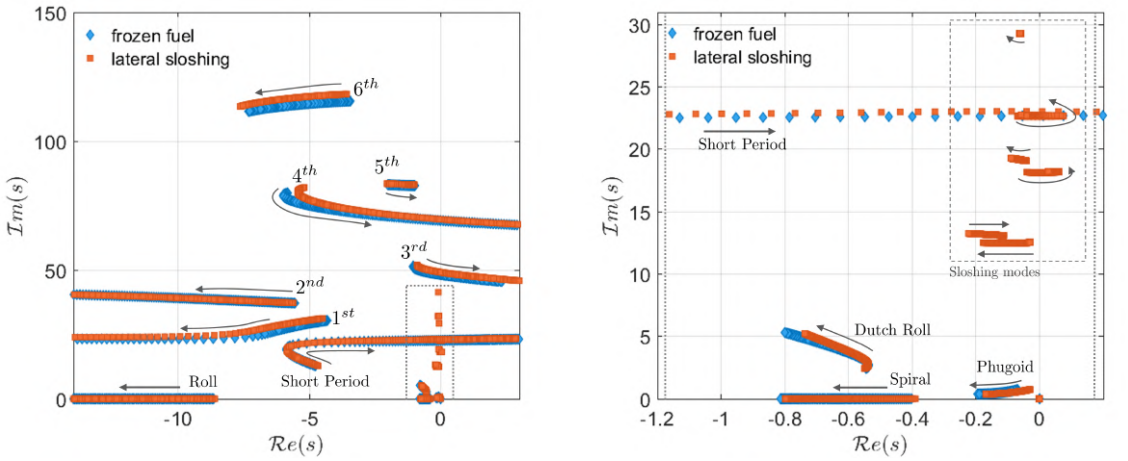

(a) Root locus of the integrated system

(b) Focus on the rigid body and sloshing modes

Figure 3.23: Root locus with linear sloshing - test case 2

Different aeroelastic analyses are considered by varying the speed and gust amplitude. The first analysis is performed at a free stream velocity of $U_\infty = 18\,\text{m/s}$ (speed equal to 86% and 83% of the body freedom flutter mode critical speeds of the frozen and lateral sloshing models, respectively), with a gust intensity of $w_{g_a} = 3\,\text{m/s}$. In this condition (see Fig. 3.23(b)) the model with linear sloshing is unstable due to the crossing of the imaginary axis by a sloshing pole, whilst the frozen fuel model is still stable. The local angle of attack and

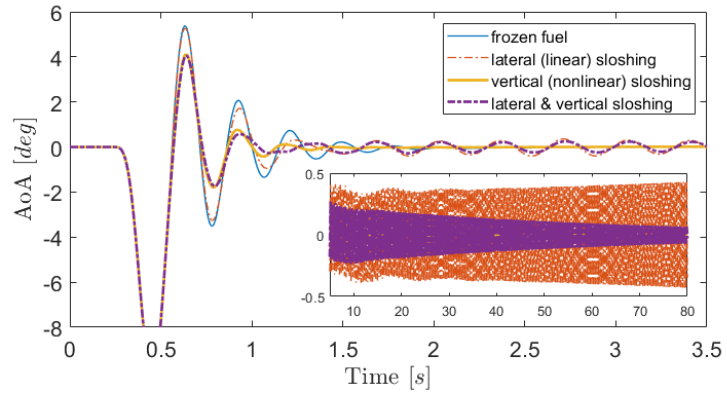

(a) Local angle of attack

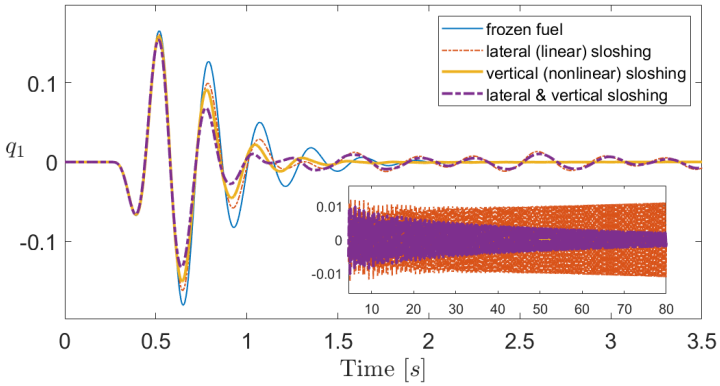

(b) First structural mode

Figure 3.24: $U_\infty = 18\,\mathrm{m/s}$ and $w_{g_a} = 3\,\mathrm{m/s}$ - test case 2

the first structural mode responses are respectively shown in Fig. 3.24(a) and Fig. 3.24(b), comparing the four different models taken into account. Vertical sloshing again contributes to damp the responses of both quantities shown also providing an increase in response frequency. As can be seen from the structural response, linear sloshing provides a damping contribution, which however is not as clear as in the local angle of attack. This makes the full sloshing model the one with the most damped response for the first bending mode. The tail of the response is featured by the trigger of the unstable sloshing dynamics that has small effect also in the structural and flight dynamics components (see inset plots in Fig. 3.24). Albeit very slowly, vertical sloshing succeeds in containing this instability. Increasing oscillations become unphysical as they are associated with sloshing mode. This means that when accounting the nonlinear behaviour of the lateral sloshing (not considered in this work), this dynamics will be limited in oscillation amplitudes. The second gust response analysis is performed at $U_\infty = 21.1\,\mathrm{m/s}$ (speed that is 1% higher than the flutter speed of the frozen fuel model and

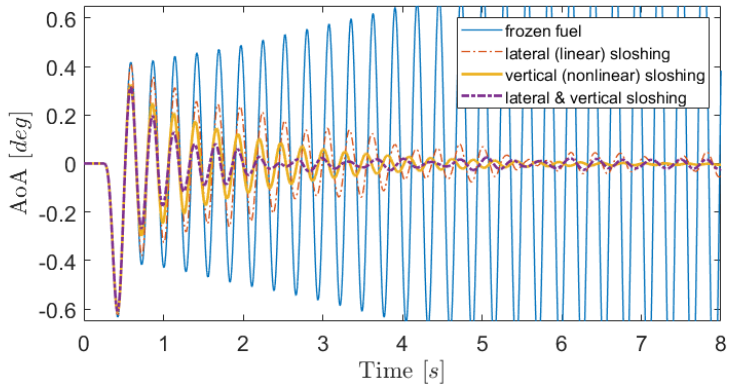

(a) Local angle of attack

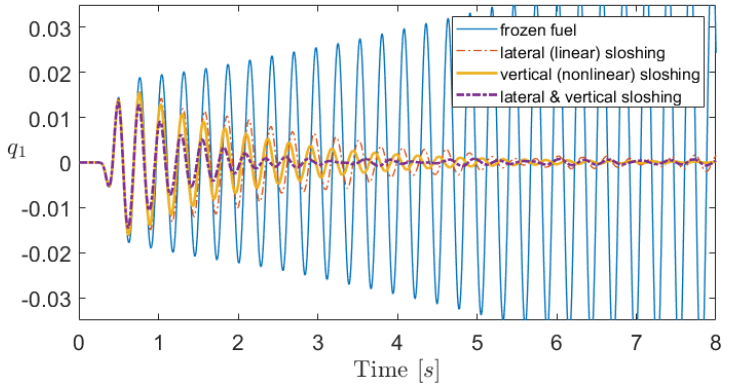

(b) First structural mode

Figure 3.25: $U_\infty = 21.1\,\mathrm{m/s}$ and $w_{g_a} = 0.2\,\mathrm{m/s}$ - test case 2

97% of the body freedom flutter mode critical speed of the lateral sloshing model), with a gust intensity of $w_{g_a} = 0.2\,\mathrm{m/s}$. In this flight condition, the model with linear sloshing is unstable because of the critical bending-torsional mode. Figure 3.25 compares the responses of the four considered models in terms of local angle of attack and Fig. 3.25(b) shows the comparison in terms of the response of modal variable associated to the first bending mode. The frozen case results in a unstable response, whereas the case of vertical sloshing presents a damped response. The model with lateral sloshing is in unstable condition due to the critical bending-torsional antisymmetric mode. However, the applied gust, as symmetric input, is not able to trigger this dynamics. In addition, the body freedom flutter occurs at a higher velocity and this leads to a more damped response. The addition of vertical sloshing, makes the response of the full sloshing case furtherly damped. The last analysis analysis is performed in body freedom flutter condition at $U_\infty = 22.5\,\mathrm{m/s}$ (the speed is 4% and 8% higher than body freedom flutter mode critical speeds of the frozen and lateral sloshing models, respectively)

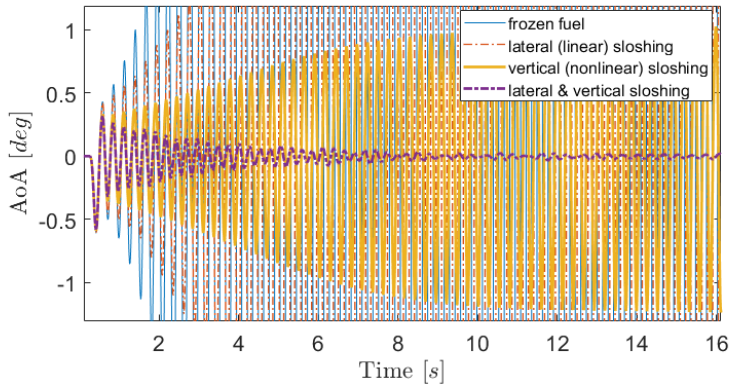

(a) Local angle of attack

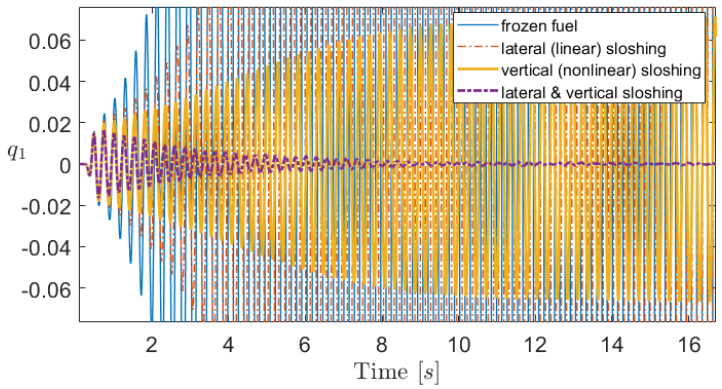

(b) First structural mode

Figure 3.26: $U_\infty = 22.5\,\mathrm{m/s}$ and $w_{g_a} = 0.2\,\mathrm{m/s}$ - test case 2

and $w_{g_a} = 0.2\,\mathrm{m/s}$. The local angle of attack and the first mode responses are shown in Figs. 3.26(a) and 3.26(b) comparing the four considered cases. The linear sloshing model leads to a flutter response with divergent exponential envelope. In contrast, vertical sloshing helps prevent the response from growing indefinitely, favoring the onset of limit cycle oscillations (LCOs). In the full sloshing, the oscillations are damped completely by vertical sloshing and this is due to the additional margin of stability provided by lateral sloshing dynamics.

Summary

In this work the effects of linear and nonlinear sloshing dynamics of fuel inside the tanks on the stability and response of a flexible flying wing model involving flight dynamics and aeroelasticity were studied. The aircraft equations of motion were linearised around a stationary level flight trim condition and recast in time-domain state-space form, thus obtaining a aeroelastic model that includes rigid-body, elastic, and aerodynamic states. Furthermore, the

combined effect of linear and nonlinear sloshing dynamics was modelled by adding directly the two lateral and vertical contributions, respectively, to the aeroelastic system. Linear sloshing was described using an equivalent mechanical model (EMM) capable of restoring the actions exerted by the liquid following latero-rotational perturbations of the tank. Similarly to the modelling of unsteady aerodynamics, the EMM introduced additional states related to the liquid dynamics. Nonlinear vertical sloshing is a phenomenon caused by accelerations perpendicular to the the liquid free surface. Rather than providing a coupling between the dynamics of the free surface and the rest of the system, it can be considered as a kind of mechanical energy sink. Thus, vertical sloshing dynamics was modelled with a neural network-based ROM driven by experimental data. Two case studies were considered, one with one tank placed beneath the aircraft center of mass and another with two tanks simmetrically placed underneath the wings. For the two case studies, the effects of the sloshing dynamics on the stability and response were investigated comparing the cases in which the liquid is assumed as a frozen mass and the cases in which the liquid is allowed to slosh freely. The results showed how linear sloshing dynamics can significantly influence aircraft stability as a result of their coupling with aeroelastic dynamics. Gust response analyses revealed the performance of vertical sloshing to provide additional damping in both pre-critical and post-critical conditions. Indeed, the presence of limit-cycle oscillations after the flutter guarantees an enhanced margin of stability for the system. The modeling presented will allow to verify the effects of sloshing on the stability and response of commercial aircraft, including next-generation configurations that may include large tanks within the fuselage. In addition, the ease with which the presented sloshing reduced order models are scalable will enable to use such models in preliminary aircraft design phase.

Concluding remarks

This thesis is focused on the study and reduced-order modeling of nonlinear sloshing effects caused by large aircraft tank motions in a direction perpendicular to the free liquid surface. These effects were placed in the category referred to as *vertical sloshing*, appropriately defined within the thesis to distinguish different sloshing dynamics according to the type of tank movement. Aircraft are generally subjected to loads caused by gusts, turbulence and landing impacts that excite the wing tanks in a predominantly vertical direction. This type of sloshing results in a noticeable increase in structural damping, which, however, is not taken into account in the design phase of a modern aircraft. The identification and study of such dissipative effects may enable the development of less conservative aircraft configurations in the future, allowing for increasingly lighter structures and reduced environmental impact. The thesis proposed a combined experimental and numerical approach aimed at obtaining reduced-order models for vertical sloshing, to be subsequently integrated into aeroelastic applications for the assessment of their effects on overall performance.

The first step was to create an equivalent nonlinear mechanical model - referred to as *bouncing ball* - capable of emulating the mechanisms of liquid impact with the tank ceiling, as these are primarily responsible for the additional dissipation caused by sloshing. Data measured in time-decaying transient tests of a single-degree-of-freedom sloshing experiment - suitably built to isolate vertical dynamics - were used to identify the model. Despite its ability to reproduce sloshing-induced damping at the frequency for which it has been identified, the *bouncing ball* model cannot accurately estimate dissipation for different frequencies.

Confirmation of this was provided by an experimental campaign performed to characterise the non-linear dissipative behaviour of vertical sloshing for different fill levels. Specifically, a controlled electrodynamic shaker was employed to provide vertical displacement by means of sine-sweep excitation to a partially filled box-shaped tank. This configuration treats the sloshing tank as an isolated system in order to properly investigate vertical sloshing. By exploiting vertical harmonic motion, it has been shown how the frequency and amplitude of the imposed excitation significantly influence the dissipative capabilities of the sloshing liquid.

The same experiment was used to create a database in the frequency and amplitude domain for the identification of a neural-network-based reduced-order model. *Vertical sloshing*

dynamics can be considered as a black box process, which resulted in a surrogate model driven only by input/output signals (tank velocity and sloshing force, respectively). To avoid overfitting in the training process, a validation data set, obtained by performing an additional experimental test with variable frequency and amplitude, was also considered. A neural-network-based Nonlinear Finite Impulse Response model (NFIR), resulting from a sensitivity analysis aimed at finding the most performing network, was selected to construct the surrogate model for vertical sloshing. An experimental validation procedure of the identified model as integrated to a flexible structure was also performed. To this end, a specific experimental setup consisting of a cantilever beam with a tank mounted at its free end was realized. The latter is the same as that used to generate the training data. By performing free response and seismic tests, FSI experimental data were collected to be used as a benchmark for validating the nonlinear identified ROM when integrated in an equivalent virtual model to account for the effects of vertical sloshing. The comparisons for the free response case in the numerical simulation including the identified ROM for the sloshing tank component showed that the time histories of the numerical acceleration at the end of the beam and sloshing forces are in good agreement with the experimental data provided by the FSI coupled experiment. The estimated instantaneous damping ratio validates the good capabilities of the identified model to accurately reproduce the dissipative behavior induced by vertical sloshing. The random seismic excitation for the considered cantilever beam with sloshing tank at tip also yielded good results and showed a satisfactory level of accuracy for the time response in each of the considered excitation cases. Indeed, by comparing the estimated damping coefficients , it was possible to assess the neural network capability to provide the same levels of dissipation as experimentally given by vertical sloshing in random FSI testing.

The experimentally validated reduced-order model was used in two different aeroelastic applications - wing prototype and flying wing model - to assess the dissipative effects induced by vertical sloshing on the response. This was made possible by the definition of a scaling law, which allowed the data-driven ROM to be used even in systems employing tanks with different dimensions. A scaling process is performed by considering tank height as the main dimension and assuming that physical liquid parameters such as Reynolds and Bond numbers play a secondary role to operational parameters (such as Froude and non-dimensional frequency). Both case studies were modeled in Simulink®, resulting in a hybrid model combining a differential linear problem (for aeroelasticity, flight dynamics, and linear sloshing) with a data-driven model (nonlinear vertical sloshing). Response analyses under pre- and post-critical aeroelastic conditions showed how the vertical sloshing dynamics helps to alleviate the dynamic loads following severe gusts while providing limit cycle oscillation beyond the flutter margin. In the specific case of the wing prototype, a post-critical energy analysis was conducted to demonstrate the neural-network-based ROM capability to reproduce the dissipative behaviour of the slosh dynamics when integrated in a complex aeroelastic computational environment.

Moreover, vertical sloshing is able to provide a limit cycle response up to a velocity which is slightly greater than the linear flutter speed stability margin. As for the flying wing, the combined effect of linear and nonlinear sloshing dynamics was modeled by adding directly the two *lateral* and *vertical* contributions, respectively, to the aeroelastic system. Linear sloshing was described using an equivalent mechanical model capable of restoring the actions exerted by the liquid following latero-rotational perturbations of the tank. Similarly to the modeling applied to unsteady aerodynamics for linear aeroelastic applications, the EMM introduced additional states related to the liquid dynamics. Stability analyses showed how linear sloshing dynamics can significantly influence aircraft stability as a result of their coupling with aeroelastic and rigid body dynamics.

Future possible developments to the present thesis activity could include a plan to further study sloshing and its interaction with aircraft structures. The sensitivity of the aspect ratios, shape and number of degrees of freedom to be considered for the synthesis of the sloshing ROMs will be investigated to assess the goodness of the assumptions that were made in the scaling process. One of the aims is to characterise the dissipation induced by sloshing in the presence of combined vertical-rotational motion and evaluate if it is consistent with that obtained in the case of purely vertical motion. This analysis has a key role because wing tanks may exhibit local rotations due to wing bending as well as centrifugal effects due to shortening present in the realistic nonlinear wing bending deformation. Thus, it should be understood whether the purely vertical sloshing category is quite representative of what typically occurs in this type of application. Following this experimental analysis, it will become clear whether the surrogate models identified for purely vertical sloshing can also be used to accurately estimate dissipation in the presence of combined vertical-lateral-rotational violent tank motion. Further developments on the modeling side will include the improvement of the neural-network-based model performances by performing training with stochastic inputs in order to account for multi-harmonic responses. With the support of high-fidelity CFD codes, it will also be possible to create richer data sets, covering a large space in the frequency and amplitude domain in order to simulate large gust scenarios as requested by aircraft certification authorities. In addition, the characterisation of cylindrical or capsular shaped tanks could facilitate the generation of reduced-order models for sloshing of alternative fuels such as hydrogen inside tanks placed in the fuselage as envisioned for some classes of future generation green aircraft.

References

[1] F. Gambioli, A. Chamos, S. Jones, P. Guthrie, J. Webb, J. Levenhagen, P. Behruzi, F. Mastroddi, A. Malan, S. Longshaw, J. Cooper, L. Gonzalez, and S. Marrone. Sloshing Wing Dynamics -Project Overview Sloshing Wing Dynamics – Project Overview. In *Proceedings of 8th Transport Research Arena TRA 2020*, 2020.

[2] H. N. Abramson. The dynamic behaviour of liquids in moving containers with applications to space vehicle technology. *Natl. Aeronaut. Sp. Adm.*, page 464, 1966.

[3] T. B. Benjamin, F. J. Ursell, and G. I. Taylor. The stability of the plane free surface of a liquid in vertical periodic motion. *Proceedings of the Royal Society of London. Series A. Mathematical and Physical Sciences*, 225(1163):505–515, 1954.

[4] S. Douady. Experimental study of the faraday instability. *Journal of Fluid Mechanics*, 221:383–409, 1990.

[5] H. Bredmose, M. Brocchini, D. H. Peregrine, and L. Thais. Experimental investigation and numerical modelling of steep forced water waves. *Journal of Fluid Mechanics*, 490:217–249, 2003.

[6] Raouf A. Ibrahim. Recent Advances in Physics of Fluid Parametric Sloshing and Related Problems. *Journal of Fluids Engineering*, 137(9), 09 2015. 090801.

[7] E. Mathieu. Memoire sur le mouvement vibratoire d'une membrane de forme elliptique. *Journal de Mathématiques Pures et Appliquées*, 13:137–203, 1868.

[8] W. McLachlan, N. *Theory and application of Mathieu Functions.* Oxford University London, 1947.

[9] D. J. Lewis. The instability of liquid surfaces when accelerated in a direction perpendicular to their planes. II. *Proc. R. Soc. London. Ser. A. Math. Phys. Sci.*, 202(1068):81–96, 1950.

[10] F. Gambioli, R. A. Usach, T. Wilson, and P. Behruzi. Experimental Evaluation of Fuel Sloshing Effects on wing dynamics. In *18th Int. Forum Aeroelasticity Struct. Dyn. IFASD 2019*, 2019.

[11] B. Titurus, J. E. Cooper, F. Saltari, F. Mastroddi, and F. Gambioli. Analysis of a sloshing beam experiment. In *International Forum on Aeroelasticity and Structural Dynamics. Savannah, Georgia, USA*, volume 139, 2019.

[12] M. Wright, F. Gambioli, and A. G. Malan. A non-dimensional characterization of structural vibration induced vertical slosh. International Ocean and Polar Engineering Conference, 06 2021. ISOPE-I-21-3211.

[13] M. D. Wright, F. Gambioli, and A. G. Malan. Cfd based non-dimensional characterization of energy dissipation due to verticle slosh. *Applied Sciences*, 11(21), 2021.

[14] F. Saltari, M. Pizzoli, G. Coppotelli, F. Gambioli, J. E. Cooper, and F. Mastroddi. Experimental characterisation of sloshing tank dissipative behaviour in vertical harmonic excitation. *Journal of fluids and structures*, 109:103478, 2022.

[15] R. A. Ibrahim. *Liquid Sloshing Dynamics: Theory and Applications*. EngineeringPro collection. Cambridge University Press, 2005.

[16] F. T. Dodge, D. D. Kana, and H. N. Abramson. Liquid surface oscillations in longitudinally excited rigid cylindrical containers. *AIAA Journal*, 3(4):685–695, 1965.

[17] Y. Kamotani, L. Chao, S. Ostrach, and H. Zhang. Effects of g jitter on free-surface motion in a cavity. *Journal of Spacecraft and Rockets*, 32(1):177–183, 1995.

[18] H. F. Bauer. Stability boundaries of liquid-propelled space vehicles with sloshing. *AIAA Journal*, 1(7):1583–1589, 1963.

[19] J. A. Ottander, R. A. Hall, and J. F. Powers. Practical methodology for the inclusion of nonlinear slosh damping in the stability analysis of liquid-propelled space vehicles. volume 0, 2018.

[20] O. M. Faltinsen and Det Norske Veritas. *Liquid Slosh in LNG Carriers*. DNV publication. Det norske Veritas, Oslo, 1974.

[21] T. Pagliaroli, F. Gambioli, F. Saltari, and J. E. Cooper. Proper orthogonal decomposition, dynamic mode decomposition, wavelet and cross wavelet analysis of a sloshing flow. *Journal of Fluids and Structures*, 112, 2022.

[22] F. D. Fischer and F. G. Rammerstorfer. A refined analysis of sloshing effects in seismically excited tanks. *International Journal of Pressure Vessels and Piping*, 76(10):693–709, 1999.

[23] F. Saltari, A. Traini, F. Gambioli, and F. Mastroddi. A linearized reduced-order model approach for sloshing to be used for aerospace design. *Aerospace Science and Technology*, 108:106369, 2021.

[24] R. D. Firouz-Abadi, P. Zarifian, and H. Haddadpour. Effect of fuel sloshing in the external tank on the flutter of subsonic wings. *Journal of Aerospace Engineering*, 27(5):04014021, 2014.

[25] C. Farhat, E. K. Chiu, D. Amsallem, J. S. Schotté, and R. Ohayon. Modeling of fuel sloshing and its physical effects on flutter. *AIAA Journal*, 51(9):2252–2265, 2013.

[26] M. Colella, F. Saltari, M. Pizzoli, and F. Mastroddi. Sloshing reduced-order models for aeroelastic analyses of innovative aircraft configurations. *Aerospace Science and Technology*, 118:107075, 2021.

[27] M. Pizzoli. Investigation of sloshing effects on flexible aircraft stability and response. *Aerotecnica Missili & Spazio*, 99(4):297–308, Dec 2020.

[28] E. Graham and A. M. Rodriquez. The characteristics of fuel motion which affect airplane dynamics. Technical report, Douglas Aircraft Co. inc., Defense Technical Information Center, 1951.

[29] J. Martinez-Carrascal and L. González-Gutiérrez. Experimental study of the liquid damping effects on a sdof vertical sloshing tank. *Journal of Fluids and Structures*, 100:103172, 2021.

[30] L. Constantin, J. J. De Courcy, B. Titurus, T. C. S. Rendall, and J. E. Cooper. Analysis of damping from vertical sloshing in a sdof system. *Mechanical Systems and Signal Processing*, 152:107452, 2021.

[31] W. Liu, S. M. Longshaw, A. Skillen, D. R. Emerson, C. Valente, and F. Gambioli. A high-performance open-source solution for multiphase fluid-structure interaction. *International Journal of Offshore and Polar Engineering*, 32:1–7, 2022.

[32] S. M. Longshaw, W. Liu, A. Skillen, B. W. S. Jones, A. G. Malan, J. Michel, S. Marrone, and F. Gambioli. A Coupled FSI Framework Using the Multiscale Universal Interface. International Forum on Aeroelasticity and Structural Dynamics, 06 2022.

[33] A. G. Malan, B. W. S. Jones, L. C. Malan, and M. Wright. Accurate Prediction of Violent Slosh Loads via a Weakly Compressible VoF Formulation. volume All Days of *International Ocean and Polar Engineering Conference*, 06 2021. ISOPE-I-21-3210.

[34] B. W. A. Jones, M. D. Wright, A. G. Malan, J. Farao, , F. Gambioli, and S. Longshaw. A high fidelity fluid-structure-interaction model of the airbus protospace slosh damping experiment. In *International Forum on Aeroelasticity and Structural Dynamics 2022*, Online.

[35] S. Marrone, A. Colagrossi, F. Gambioli, and L. González-Gutiérrez. Numerical study on the dissipation mechanisms in sloshing flows induced by violent and high-frequency accelerations. i. theoretical formulation and numerical investigation. *Phys. Rev. Fluids*, 6:114801, Nov 2021.

[36] S. Marrone, A. Colagrossi, J. Calderon-Sanchez, and J. Martinez-Carrascal. Numerical study on the dissipation mechanisms in sloshing flows induced by violent and high-frequency accelerations. ii. comparison against experimental data. *Physical Review Fluids*, 6(11):114802, 2021.

[37] J. Hall, T. Rendall, and C. B. Allen. A two-dimensional computational model of fuel sloshing effects on aeroelastic behaviour. In *31st AIAA Applied Aerodynamics Conference*, 2013.

[38] J. S. Schotté and R. Ohayon. Various modelling levels to represent internal liquid behaviour in the vibration analysis of complex structures. *Computer Methods in Applied Mechanics and Engineering*, 198(21):1913–1925, 2009. Advances in Simulation-Based Engineering Sciences – Honoring J. Tinsley Oden.

[39] J. J. De Courcy, L. Constantin, B. Titurus, T. C. S. Rendall, and J. E. Cooper. Gust loads alleviation using sloshing fuel. In *AIAA Scitech 2021 Forum*, 2021.

[40] L. Constantin, J. J. De Courcy, B. Titurus, T. C. S. Rendall, and J. E. Cooper. Sloshing induced damping across froude numbers in a harmonically vertically excited system. *Journal of Sound and Vibration*, 510:116302, 2021.

[41] M. Eugeni, F. Saltari, and F. Mastroddi. Structural damping models for passive aeroelastic control. *Aerospace Science and Technology*, 118:107011, 2021.

[42] E. Balmes and J. M. Leclère. *Viscoelastic Vibration Toolbox, User's Guide*. 2017.

[43] S. L. Brunton, J. N. Kutz, K. Manohar, A. Y. Aravkin, K. Morgansen, J. Klemisch, N. Goebel, J. Buttrick, J. Poskin, A. W. Blom-Schieber, T. Hogan, and D. McDonald. Data-driven aerospace engineering: Reframing the industry with machine learning. *AIAA Journal*, 59(8):2820–2847, 2021.

[44] T. Hey and A. Trefethen. *The Data Deluge: An e-Science Perspective*, chapter 36, pages 809–824. John Wiley & Sons, Ltd, 2003.

[45] T. Hey, S. Tansley, and K. Tolle. *The Fourth Paradigm: Data-Intensive Scientific Discovery*. Microsoft Research, 2009.

[46] S. L. Brunton and J. N. Kutz. *Data-Driven Science and Engineering: Machine Learning, Dynamical Systems, and Control*. Cambridge University Press, 2019.

[47] I. Goodfellow, Y. Bengio, and A. Courville. *Deep Learning*. MIT Press, 2016. `http://www.deeplearningbook.org`.

[48] G. Karniadakis, Y. Kevrekidis, L. Lu, P. Perdikaris, S. Wang, and L. Yang. Physics-informed machine learning. pages 1–19, 05 2021.

[49] S. O. Haykin. *Neural Networks and Learning Machines*. Pearson, 3 edition, 2009.

[50] J. Sjöberg, H. Hjalmarsson, and L. Ljung. Neural networks in system identification. *IFAC Proceedings Volumes*, 27(8):359–382, 1994. IFAC Symposium on System Identification (SYSID'94), Copenhagen, Denmark, 4-6 July.

[51] S. Chen and S. A. Billings. Neural networks for nonlinear dynamic system modelling and identification. *International Journal of Control*, 56(2):319–346, 1992.

[52] K. S. Narendra and K. Parthasarathy. Identification and control of dynamical systems using neural networks. *IEEE Transactions on Neural Networks*, 1(1):4–27, 1990.

[53] S. Elanayar and Y. C. Shin. Radial basis function neural network for approximation and estimation of nonlinear stochastic dynamic systems. *IEEE Transactions on Neural Networks*, 5(4):594–603, 1994.

[54] A. U. Levin and K. S. Narendra. Identification Using Feedforward Networks. *Neural Computation*, 7(2):349–369, 03 1995.

[55] A. R. Barron. Universal approximation bounds for superpositions of a sigmoidal function. *IEEE Transactions on Information Theory*, 39(3):930–945, 1993.

[56] O. Nelles. *Nonlinear system identification, from classical approaches to neural networks, fuzzy models, and gaussian processes*. Springer, 2 edition, 2021.

[57] S. A. Billings. *Nonlinear System Identification: NARMAX Methods in the Time, Frequency, and Spatio-Temporal Domains*. John Wiley and Sons, 2013.

[58] Y. Ma, H. Liu, Y. Zhu, F. Wang, and Z. Luo. The narx model-based system identification on nonlinear, rotor-bearing systems. *Applied Sciences*, 7(9), 2017.

[59] Q. Zhang. Nonlinear system identification with output error model through stabilized simulation. *IFAC Proceedings Volumes*, 37(13):501–506, 2004. 6th IFAC Symposium on Nonlinear Control Systems 2004 (NOLCOS 2004), Stuttgart, Germany, 1-3 September, 2004.

[60] G. Pillonetto, M. H. Quang, and A. Chiuso. A new kernel-based approach for nonlinearsystem identification. *IEEE Transactions on Automatic Control*, 56(12):2825–2840, 2011.

[61] G. Birpoutsoukis, A. Marconato, J. Lataire, and J. Schoukens. Regularized nonparametric volterra kernel estimation. *Automatica*, 82:324–327, 2017.

[62] S. J. Qin and T. J. McAvoy. Nonlinear fir modeling via a neural net pls approach. *Computers & Chemical Engineering*, 20(2):147–159, 1996.

[63] W. E. Faller and S. J. Schreck. Unsteady fluid mechanics applications of neural networks. *Journal of Aircraft*, 34(1):48–55, 1997.

[64] O. Voitcu and Y. S. Wong. Neural network approach for nonlinear aeroelastic analysis. *Journal of Guidance, Control, and Dynamics*, 26(1):99–105, 2003.

[65] A. Mannarino and P. Mantegazza. Nonlinear aeroelastic reduced order modeling by recurrent neural networks. *Journal of Fluids and Structures*, 48:103–121, 2014.

[66] Y. Ahn, Y. Kim, and S. Kim. Database of model-scale sloshing experiment for lng tank and application of artificial neural network for sloshing load prediction. *Marine Structures*, 66:66–82, 2019.

[67] Y. Ahn and Y. Kim. Data mining in sloshing experiment database and application of neural network for extreme load prediction. *Marine Structures*, 80:103074, 2021.

[68] B. Moya, D. Gonzalez, I. Alfaro, F. Chinesta, and E. Cueto. Learning slosh dynamics by means of data. *Comput. Mech.*, 64(2):511–523, aug 2019.

[69] H. V. Ly and H. T. Tran. Modeling and control of physical processes using proper orthogonal decomposition. *Mathematical and Computer Modelling*, 33(1):223–236, 2001.

[70] S. T. Roweis and L. K. Saul. Nonlinear dimensionality reduction by locally linear embedding. *Science*, 290(5500):2323–2326, 2000.

[71] L. Wasserman. Topological data analysis. *Annual Review of Statistics and Its Application*, 5(1):501–532, 2018.

[72] B. Moya, I. Alfaro, D. González, F. Chinesta, and E. Cueto. Physically sound, self-learning digital twins for sloshing fluids. *PLoS ONE*, 15, 2020.

[73] C. Zhang, J. Tan, and D. Ning. Machine learning strategy for viscous calibration of fully-nonlinear liquid sloshing simulation in flng tanks. *Applied Ocean Research*, 114:102737, 2021.

[74] K. O'Shea and R. Nash. An introduction to convolutional neural networks, 2015.

[75] G. Siva Teja, C. Saurav Vara Prasad, B. Venkatesham, and K. Sri Rama Murty. Identification of sloshing noises using convolutional neural network. *The Journal of the Acoustical Society of America*, 149(5):3027–3041, 2021.

[76] M. A. Mahmud, R. I. Khan, S. Wang, and Q. Xu. Comprehensive study on sloshing impacts for an offshore 3d vessel via the integration of computational fluid dynamics simulation, experimental unit, and artificial neural network prediction. *Industrial & Engineering Chemistry Research*, 59(51):22187–22204, 2020.

[77] S. Srivastava, M. Damodaran, and B. C. Khoo. Machine learning surrogates for predicting response of an aero-structural-sloshing system, 2019.

[78] D. Mandic and J. Chambers. *Recurrent Neural Networks for Prediction: Learning Algorithms, Architectures and Stability*. John Wiley and Sons, 2001.

[79] E. Burnett, C. Atkinson, J. Beranek, B. Sibbitt, B. Holm-Hansen, and L. Nicolai. *NDOF Simulation Model for Flight Control Development with Flight Test Correlation*, pages 2010–7780. 2010.

[80] D. K. Schmidt. Stability augmentation and active flutter suppression of a flexible flying-wing drone. *Journal of Guidance, Control, and Dynamics*, 39(3):409–422, 2016.

[81] F. Saltari, M. Pizzoli, F. Gambioli, C. Jetzschmann, and F. Mastroddi. Sloshing reduced-order model based on neural networks for aeroelastic analyses. *Aerospace Science and Technology*, page 107708, 2022.

[82] J. Calderon-Sanchez, J. Martinez-Carrascal, L. Gonzalez-Gutierrez, and A. Colagrossi. A global analysis of a coupled violent vertical sloshing problem using an sph methodology. *Engineering Applications of Computational Fluid Mechanics*, 15(1):865–888, 2021.

[83] K. Menon and R. Mittal. Aeroelastic response of an airfoil to gusts: Prediction and control strategies from computed energy maps. *Journal of Fluids and Structures*, 97:103078, 2020.

[84] O. M. Faltinsen and A. N. Timokha. *Sloshing*. Cambridge University Press, 2009.

[85] M. Pizzoli, F. Saltari, F. Mastroddi, J. Martínez-Carrascal, and L. González-Gutiérrez. Nonlinear reduced order model for vertical sloshing by employing neural networks. *Nonlinear dynamics*, 2021.

[86] M. Pizzoli, F. Saltari, G. Coppotelli, and F. Mastroddi. Experimental validation of neural-network-based nonlinear reduced-order model for vertical sloshing. In *AIAA Scitech 2022 Forum*, 2022.

[87] R. L. Bass. Modeling criteria for scaled lng sloshing experiments. *Transactions of the ASME Journal of Fluids Engineering*, 107, June 1985.

[88] E. J. Hartman, J. D. Keeler, and J. M. Kowalski. Layered Neural Networks with Gaussian Hidden Units as Universal Approximations. *Neural Computation*, 2(2):210–215, 06 1990.

[89] M. H. Beale, M. T. Hagan, and H. B. Demuth. *Deep Learning Toolbox*. Mathworks, r2020a edition.

[90] L. Meirovitch and H. Baruh. Implementation of modal filters for control of structures. *Journal of Guidance, Control, and Dynamics*, 8:707–716, 1985.

[91] G. Coppotelli, G. Franceschini, F. Mastroddi, and F. Saltari. Experimental investigation on the damping mechanism in sloshing structures. *AIAA Scitech Forum*, N.6 2021-1388 Virtual Event Paper:11–15 & 19–21, January 2021.

[92] P. Welch. The use of fast fourier transform for the estimation of power spectra: A method based on time averaging over short, modified periodograms. *IEEE Transactions on Audio and Electroacoustics*, 15(2):70–73, 1967.

[93] A. Arda Ozdemir and S. Gumussoy. Transfer function estimation in system identification toolbox via vector fitting. *IFAC-PapersOnLine*, 50(1):6232–6237, 2017. 20th IFAC World Congress.

[94] M. Pizzoli, F. Saltari, and F. Mastroddi. Linear and nonlinear reduced order models for sloshing for aeroelastic stability and response predictions. *Applied Sciences*, 12(17), 2022.

[95] E. Albano and W. P. Rodden. Msc/nastran aeroelastic analysis' user's guide. *MSC Software*, 1994.

[96] M. Karpel. Design for active flutter suppression and gust alleviation using state-space aeroelastic modeling. *Journal of Aircraft*, 19(3):221–227, 1982.

[97] B. S. Sykes, A. G. Malan, and F. Gambioli. Novel nonlinear fuel slosh surrogate reduced-order model for aircraft loads prediction. *Journal of Aircraft*, 55(3):1004–1013, 2018.

[98] J. Reese. Some effects of fluid in pylon-mounted tanks on flutter. Technical report, National Advisory Committee for Aeronautics, 07 1955.

[99] J. Sewall. An experimental and theoretical study of the effect of fuel on pitching-translation flutter. Technical report, National Advisory Committee for Aeronautics, 12 1955.

[100] F. Saltari, C. Riso, G. De Matteis, and F. Mastroddi. Finite-element-based modeling for flight dynamics and aeroelasticity of flexible aircraft. *Journal of Aircraft*, 54(6):2350–2366, 2017.

[101] L. Morino, F. Mastroddi, R. De Troia, G. L. Ghiringhelli, and P. Mantegazza. Matrix fraction approach for finite-state aerodynamic modeling. *AIAA Journal*, 33(4):703–711, 1995.

[102] J. Park and I. W. Sandberg. Universal approximation using radial-basis-function networks. *Neural Computation*, 3(2):246–257, 1991.

[103] F. Heimes and B. van Heuveln. The normalized radial basis function neural network. In *SMC'98 Conference Proceedings. 1998 IEEE International Conference on Systems, Man, and Cybernetics*, volume 2, pages 1609–1614, 1998.

[104] J.-S.R. Jang and C.-T. Sun. Functional equivalence between radial basis function networks and fuzzy inference systems. *IEEE Transactions on Neural Networks*, 4(1):156–159, 1993.

[105] R. Babuška and H. Verbruggen. Neuro-fuzzy methods for nonlinear system identification. *Annual Reviews in Control*, 27(1):73–85, 2003.

[106] L. Ljung. *System Identification Toolbox for use with MATLAB.* Mathworks, r2020a edition.

[107] M. Leshno, V. Pinkus, and A. Schocken. Multilayer feedforward networks with a polynomial activation function can approximate any function. *Neural Networks*, 6:861–867, 1993.

[108] D. S. Broomhead and D. Lowe. Radial basis functions, multi-variable functional interpolation and adaptive networks. *Complex Systems*, 2:321–355, 1988.

Appendix A

Damping characterisation for linear harmonic oscillators

Consider a Mass-Spring-Damper linear system excited by a force $F(t)$

$$\begin{aligned} & m\ddot{x}(t) + c\dot{x}(t) + kx(t) \;=\; F(t) \\ & x(0) = 0 \\ & \dot{x}(0) = 0 \end{aligned} \tag{A.1}$$

Dividing by m (indeed, only 2 are the necessary parameters for describing the system, like natural frequency and damping ratio) and defining:

$$\omega_n := \sqrt{k/m},\;\; d = \zeta := c/(2\sqrt{km}) \tag{A.2}$$

one has

$$\begin{aligned} & \ddot{x}(t) + 2\zeta\omega_n\dot{x}(t) + \omega_n^2 x(t) \;=\; \frac{F(t)}{m} \\ & x(0) = 0 \\ & \dot{x}(0) = 0 \end{aligned} \tag{A.3}$$

Considering an harmonic excitation

$$F(t) = A\sin(\Omega t) \quad \text{with} \quad \Omega = 2\pi f \tag{A.4}$$

the *steady state harmonic* response of the system reads

$$x(t) \;=\; |B(\Omega)|\,\sin\left(\Omega t + \chi(\Omega)\right) \tag{A.5}$$

with[1]

$$|B(\Omega)| \;=\; \frac{A/m}{\sqrt{(\omega_n^2-\Omega^2)^2+4\zeta^2\omega_n^2\Omega^2}} \quad \text{and} \quad \chi\,(\Omega) = \arctan\left(\frac{2\zeta\omega_n\Omega}{\Omega^2-\omega_n^2}\right) \tag{A.8}$$

In Figure A.1 the classic plots below show the $|B|$ and χ as function of $\Omega/\omega_n = f/f_n$ for different damping coefficients ζ.

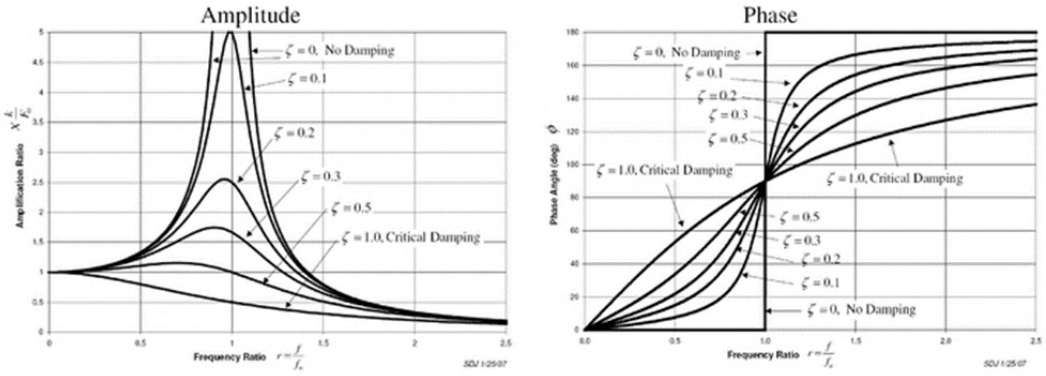

Figure A.1: Amplitude and phase of a standard harmonic damped oscillator system

The velocity can be calculated as (derivative of the displacement):

$$\dot{x}(t) \;=\; \Omega\,|B(\Omega)|\,\cos\left(\Omega t+\chi(\Omega)\right) \tag{A.9}$$

For the work done in a time cycle $T = 1/f$ in steady harmonic motion (see Fig. A.2), using Eq. A.4 and Eq. A.9 for the equation for the velocity, we have:

$$\begin{aligned} W_{cycle} \;&=\; \oint_{cycle} F(t)dx \;=\; \int_0^{T=1/f} F(\tau)\,\dot{x}(\tau)\mathrm{d}\tau \;= \\ &=\; \int_0^{T=1/f} \left[\Omega\,A\,|B(\Omega)|\,\sin(\Omega\tau)\,\cos\left(\Omega\tau+\chi(\Omega)\right)\right]\mathrm{d}\tau \;= \\ &=\; -\pi A\,|B(\Omega)|\,\sin\left[\chi(\Omega)\right] \end{aligned} \tag{A.10}$$

[1]Note also that, by the standard theory, one can also obtain that

$$\sin\chi \;=\; \frac{-c\Omega/m}{\sqrt{(\omega_n^2-\Omega^2)^2+4\zeta^2\omega_n^2\Omega^2}} = \frac{-2\omega_n\Omega\zeta}{\sqrt{(\omega_n^2-\Omega^2)^2+4\zeta^2\omega_n^2\Omega^2}} \tag{A.6}$$

$$\cos\chi \;=\; \frac{\omega_n^2-\Omega^2}{\sqrt{(\omega_n^2-\Omega^2)^2+4\zeta^2\omega_n^2\Omega^2}} \tag{A.7}$$

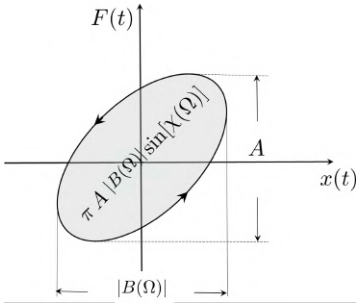

Figure A.2: Work performed by $F(t)$ force in a cycle with time period $T = 1/f$ at steady-harmonic regime

Equation A.10 shows that the work done by the force in a cycle is maximum at resonance, since $|B(\Omega)|$ is maximised and $\chi(\Omega)$ is 90 degrees. Note also that the dissipative conditions are *symmetric* in the neighbourhood of the resonance frequency since the function $|B(\Omega)|$ has here a local maximum (see Fig. A.1) and $\chi(\Omega)$ is a locally linear function for any ζ with value around 90^o and, therefore, $\sin[\chi(\Omega)]$ in Eq. A.10 is also symmetric in the neighbourhood of the resonance.
Considering the first equation of motion, multiplying by the displacement $x(t)$ and integrating during a cycle, we get:

$$\oint_{cycle} [m\ddot{x}(\tau) + c\dot{x}(\tau) + kx(\tau)\,]\,\mathrm{d}x \;=\; \oint_{cycle} F(\tau)dx \tag{A.11}$$

where the right-hand-side has already been calculated. Working on the first and third terms on the left-hand side, we have in harmonic motion, respectively:

$$\oint_{cycle} m\ddot{x}(\tau)\,\mathrm{d}x \;=\; \int_0^{T=1/f} \frac{1}{2} m \frac{d\left(\dot{x}^2\right)}{d\tau}\,\mathrm{d}\tau \;=\; \frac{1}{2} m \int_0^{T=1/f} \mathrm{d}\left(\dot{x}^2\right) \;=\; 0$$

and

$$\oint_{cycle} kx(\tau)\,dx \;=\; \frac{1}{2}\,k \oint_{cycle} \mathrm{d}\left(x^2\right) \;=\; 0$$

Thus, substituting the above equations into Eq. A.11, we have:

$$W_{cycle} \;=\; \oint_{cycle} F(\tau)\mathrm{d}x \;=\; \oint_{cycle} c\dot{x}(\tau)\mathrm{d}x \;=\; -\pi A\,|B(\Omega)|\,\sin\left[\chi(\Omega)\right] \tag{A.12}$$

which implies that the work done by the exciting force in a harmonic cycle is equal to the dissipation due to the viscous forces. Indeed, this can be further demonstrated. If one develop

the above integral, one can identically obtain (see Eq. A.9)

$$\oint_{cycle} c\dot{x}(\tau)\mathrm{d}x \;=\; c\Omega^2|B(\Omega)|^2 \int_0^{T=1/f} \cos^2\left(\Omega\tau + \chi(\Omega)\right)\mathrm{d}\tau \;=\; c\,\pi\,\Omega\,|B(\Omega)|^2$$

Indeed, by substituting into the previous formula the value of coefficient c as obtained from Eq. A.6, one obtains, consistently with Eq. A.10, what follows

$$\oint_{cycle} c\dot{x}(\tau)dx \;=\; -\pi A\,|B(\Omega)|\,\sin\left[\chi(\Omega)\right]$$

It is worth to pointing out that the dissipative model considered here is simple, in that the force is assumed to be proportional to the velocity:

$$f_D(t) = c\dot{x}(t) = 2\zeta\sqrt{km}\,\dot{x}(t) = 2m\zeta\omega_n\,\dot{x}(t) \tag{A.13}$$

However, the conclusions provided by Eq. A.12 are not limited to this kind o damping-force model.

Listed next are the parameters that can be used to define or quantify dissipation in a dynamical system undergoing a harmonic motion:

⋆ *Damping Capacity* : L_d
Dissipated energy in a cycle by the damper or a dissipative force:

$$L_d := \oint_{cycle} f_D\,dx \tag{A.14}$$

⋆ *Specific Damping Capacity* : D
Ratio between the damping capacity L_d and the maximum energy of the overall system in a periodic motion U_{max}

$$D := \frac{L_d}{U_{max}} \tag{A.15}$$

⋆ *Loss Factor* : η
Specific damping capacity per radian

$$\eta := \frac{D}{2\pi} = \frac{L_d}{2\pi U_{max}} \tag{A.16}$$

So, in a harmonic motion is possible to identify a dissipation metric by exploiting the loss factor. However, it is essential to make a distinction between linear systems and nonlinear systems such as vertical sloshing. Indeed, for linear systems, the loss factor is a global characteristic, mainly related to the dissipation capabilities of the system. While for nonlinear systems, it can be considered as a local quantity, or in other terms, a quantity strictly

dependent on the imposed harmonic motion.

Selecting the loss factor as the most representative nondimensional parameter of dissipation in harmonic motion, we go on to derive this parameter for two different dissipative models: linear viscous model and hysteretic model.

Viscous damping model

Consider the Mass-Spring-Damper linear system already discussed in previous sections

$$\ddot{x}(t) + 2\zeta\omega_n\dot{x}(t) + \omega_n^2 x(t) \;=\; \frac{A}{m}\sin(\Omega t) \tag{A.17}$$

where the dissipative model is characterized by having a force defined as that in Eq.(A.13). The *steady state harmonic* response and velocity of this system reads

$$\begin{cases} x(t) \;=\; |B(\Omega)|\,\sin\left(\Omega t + \chi(\Omega)\right) \\ \dot{x}(t) \;=\; \Omega\,|B(\Omega)|\,\cos\left(\Omega t + \chi(\Omega)\right) \end{cases} \tag{A.18}$$

where $|B(\Omega)|$ and $\chi(\Omega)$ are expressed as in Eq.(A.8).
The damping capacity L_d is therefore expressed as follows

$$\begin{aligned} L_d \;&:=\; \oint_{cycle} f_D\,dx \;=\; \int_t^{t+T} f_D\,\dot{x}(\tau)\mathrm{d}\tau \;=\; \int_t^{t+T} \left(2m\zeta\omega_n\,\dot{x}\right)\,\dot{x}\mathrm{d}\tau \;= \\ &=\; \int_t^{t+T} 2m\zeta\omega_n\,\Omega^2\,|B(\Omega)|^2\,\cos^2\left(\Omega\tau + \chi(\Omega)\right)\mathrm{d}\tau \;= \\ &=\; 2m\zeta\omega_n\,\Omega^2\,|B(\Omega)|^2\int_t^{t+T}\frac{1+\cos\left[2\left(\Omega\tau+\chi(\Omega)\right)\right]}{2}\mathrm{d}\tau \;=\; m\zeta\omega_n\,\Omega^2\,|B(\Omega)|^2\,T \;= \\ &=\; 2\pi m\zeta\omega_n\,\Omega\,|B(\Omega)|^2 \end{aligned} \tag{A.19}$$

The maximum energy in a periodic motion U_{max} is defined as the maximum elastic energy

$$U_{max} = \frac{1}{2}kX_0^2 = \frac{1}{2}k|B(\Omega)|^2 \tag{A.20}$$

where X_0 is the maximum amplitude oscillation, that is equal to $|B(\Omega)|$ at permanent sinusoidal regime. So, the specific damping capacity D is

$$D := \frac{L_d}{U_{max}} = \frac{2\pi m\zeta\omega_n\,\Omega\,|B(\Omega)|^2}{\frac{1}{2}k|B(\Omega)|^2} = \frac{4\pi\zeta\omega_n\,\Omega}{\omega_n^2} = 4\pi\zeta\frac{\Omega}{\omega_n} \tag{A.21}$$

Dividing the specific damping capacity by 2π, it is possible to obtain the loss factor η

$$\eta := \frac{D}{2\pi} = 2\zeta\frac{\Omega}{\omega_n} \tag{A.22}$$

It is worth emphasising that, in resonance condition ($\Omega = \omega_n$), the loss factor is twice bigger than the damping ratio ζ.

Hysteretic damping model

Consider a system with a single degree of freedom having a hysteretic damping model which, for a harmonic motion, can be written in the frequency domain as

$$\left(-m\Omega^2 + j\,h + k\right)\tilde{x}(\Omega) = \tilde{F}(\Omega) \tag{A.23}$$

where the term $jh\,\tilde{x}(\Omega)$ is representative of the dissipative force $\tilde{f}_{D_{hys}}$ and $\tilde{F}(\Omega)$ is the harmonic excitation (see Eq.(A.4)). Defining the coefficient $\bar{\eta}$ as the ratio between h and k, the model expressed in (A.23) can be reformulated as

$$m\left[-\Omega^2 + (1 + j\bar{\eta})\,\omega_n^2\right]\tilde{x}(\Omega) = \tilde{F}(\Omega) \tag{A.24}$$

In this case, the *steady state harmonic* response and velocity of this system reads

$$\begin{cases} x(t) \;=\; |B_{hys}(\Omega)|\,\sin\left(\Omega t + \chi_{hys}(\Omega)\right) \\ \\ \dot{x}(t) \;=\; \Omega\,|B_{hys}(\Omega)|\,\cos\left(\Omega t + \chi_{hys}(\Omega)\right) \end{cases} \tag{A.25}$$

where $|B_{hys}(\Omega)|$ and $\chi_{hys}(\Omega)$ are expressed as follows

$$|B_{hys}(\Omega)| \;=\; \frac{A/m}{\sqrt{(\omega_n^2 - \Omega^2)^2 + \bar{\eta}^2\omega_n^4}} \quad \text{and} \quad \chi_{hys}\left(\Omega\right) = \arctan\left(\frac{\bar{\eta}\,\omega_n^2}{\Omega^2 - \omega_n^2}\right) \tag{A.26}$$

The damping capacity $L_{d_{hys}}$ is now expressed as follows

$$\begin{aligned} L_{d_{hys}} \;&:=\; \oint_{cycle} f_{D_{hys}}\,dx \;=\; \int_t^{t+T} f_{D_{hys}}\,\dot{x}(\tau)\mathrm{d}\tau \;=\; \int_t^{t+T}\left(\frac{h}{\Omega}\dot{x}\right)\dot{x}\mathrm{d}\tau \;= \\ &=\; \frac{h}{\Omega}\int_t^{t+T}\Omega^2\,|B_{hys}(\Omega)|^2\,\cos^2\left(\Omega\tau + \chi_{hys}(\Omega)\right)\mathrm{d}\tau \;= \\ &=\; h\Omega|B_{hys}(\Omega)|^2\int_t^{t+T}\frac{1 + \cos\left[2\left(\Omega\tau + \chi(\Omega)\right)\right]}{2}\mathrm{d}\tau \;=\; \bar{\eta}k\Omega|B_{hys}(\Omega)|^2\,\frac{T}{2} = \\ &=\; \pi\bar{\eta}k|B_{hys}(\Omega)|^2 \end{aligned} \tag{A.27}$$

The maximum energy U_{max} is again defined as the maximum elastic energy

$$U_{max} = \frac{1}{2}kX_0^2 = \frac{1}{2}k|B_{hys}(\Omega)|^2 \tag{A.28}$$

So, the specific damping capacity D_{hys} is

$$D_{hys} := \frac{L_{d_{hys}}}{U_{max}} = \frac{\pi\bar{\eta}k|B_{hys}(\Omega)|^2}{\frac{1}{2}k|B_{hys}(\Omega)|^2} = 2\pi\bar{\eta} \tag{A.29}$$

Dividing the specific damping capacity by 2π, it is possible to obtain the loss factor η_{hys}

$$\eta_{hys} := \frac{D_{hys}}{2\pi} = \bar{\eta} \tag{A.30}$$

Therefore, in this case the loss factor coincides with the hysteretic damping coefficient $\bar{\eta}$ and it does not depend by the excitation frequency.

Appendix B

Artificial neural networks (ANN)

Artificial neural network can be seen as a parallel distributed processors made up of the so called neurons (or nodes): simple processing units, having the natural capability of storing accumulated knowledge, and then, make it available for subsequent use. In particular, knowledge is acquired by the network from its environment through a *learning process*, and then stored by synaptic weights. Due to their useful properties and capabilities (Ref. [49]), neural networks are increasingly used in nonlinear system identification. Indeed, they are a powerful tool for approximating nonlinear dynamic systems, even when the system structure is unknown and only input–output data are available, thus allowing a sort of generalized black-box modeling. This appendix describes the structure of neural networks for static modeling.

To talk about nonlinear static models as neural networks, it is necessary to introduce a fundamental concept on which they are based, which, in the context of systems modeling, is called the *basis function formulation*. Static nonlinear models perform a mapping from p inputs x_i contained in the vector $\mathsf{x} = [x_1\, x_2\, \cdots x_p]^T$ to r outputs y_j of the vector $\mathsf{y} = [y_1\, y_2\, \cdots y_r]^T$. Considering for the sake of simplicity a static nonlinear model with only one output (thus a MISO model), it follows that it can be described by the following equation:

$$\hat{y} = g(\mathsf{x}) \tag{B.1}$$

being $g(\cdot)$ the nonlinear function that defines the mapping from the p inputs x_i to the single output denoted as $\hat{y}$. Note that the first member of Eq. B.1 is different from the true output y, precisely because the mapping is only able to provide an estimate of it.
From all possible realizations of this function $g(\cdot)$, almost all alternatives of practical interest can be written in the following basis function formulation:

$$\hat{y} = \sum_{i=0}^{M} \theta_i \, \Phi_i \left(\mathsf{x}, \boldsymbol{\theta}_i^{(n)}\right) \quad \text{with} \quad \Phi_0(\cdot) = 1 \tag{B.2}$$

The output y is modeled as a weighted sum of M basis functions $\Phi_i(\cdot)$. The basis functions are weighted with the linear parameters θ_i, and they depend on the inputs x and a set of nonlinear parameters gathered in vector $\boldsymbol{\theta}_i^{(n)}$. In order to realize a nonlinear mapping, the basis functions have to be nonlinear. Thus, the parameters in $\boldsymbol{\theta}_i^{(n)}$ on which the basis functions depend are necessarily nonlinear. Often models incorporate an offset parameter (sometimes called "bias") that adjusts the operating point. Such an offset can be included in the basis function formulation by the introduction of a "dummy" basis function $\Phi_0(\cdot)$, which is always equal to 1. The basis function formulations can be illustrated as the network shown in Fig. B.1. Generally, the basis functions $\Phi_i(\cdot)$ can be of different type for each node. If all basis functions are of the same type and differ only in their parameters, the network is called an artificial neural network (ANN) or, for short, a neural network (NN). Then the nodes of the network in Fig. B.1 are called neurons (or nodes). In neural network terminology, the struc-

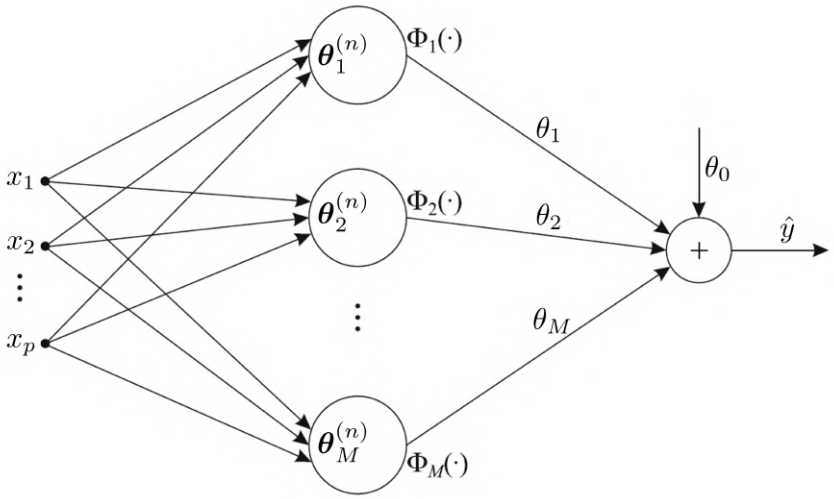

Figure B.1: Network of basis functions $\Phi_i(\cdot)$

ture shown in Fig. B.1 is described as follows. The node at the output is called the output neuron, and all output neurons together are called the output layer (here only a single output is considered, so the output layer consists only of one neuron). Each of the M nodes in the center that realizes a basis function is called the hidden layer neuron, and all these neurons together are called the hidden layer. Finally, the inputs are sometimes denoted as input neurons, and all of them together are called the input layer. However, these neurons only fan out the inputs to all hidden layer neurons and do not carry out any real calculations. For a neural network, the linear parameters associated with the output neuron are called output weights: $\theta_i = w_i$.

The output neuron is usually a linear combination of the hidden layer neurons (basis functions) $\Phi_i(\cdot)$ with an additional offset w_0, which is sometimes called "bias". Each hidden layer neuron output is weighted with its corresponding weight. The two most common neural net-

work architectures are the multilayer perceptron (MLP) and the radial basis function (RBF) network.

The basis functions $\Phi_i(\cdot)$ are generally multidimensional, i.e., their dimensionality is defined by the number of inputs p. For all neural network approaches and many other model architectures, however, the multivariate basis functions are constructed by simple one-dimensional functions. In the neural network context, the one-dimensional function is called the *activation function*. Note that the activation function that maps the scalar $\tilde{x}$ to the neuron output $\tilde{y}$ is denoted in the following by $h(\cdot)$. In contrast, the basis function $\Phi(\cdot)$ characterizes the multidimensional mapping from the neuron inputs to the neuron output and thus depends on the construction mechanism. MLP and RBF networks differ mainly on the grounds of this construction mechanism.

B.1 Radial basis function (RBF) networks

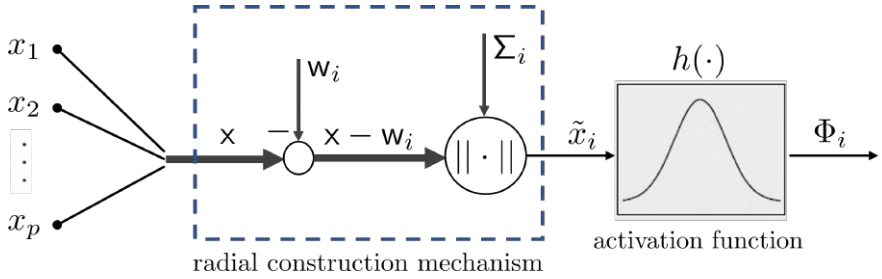

Figure B.2: The i-th hidden neuron of an RBF network

Figure B.2 shows a neuron of an RBF network. Its operation can be split into two parts. In the first part, the distance of the input vector $\mathsf{x} = [x_1\, x_2 \cdots x_p]^T$ to the center vector $\mathsf{w}_i = [w_{i1}\, w_{i2} \cdots w_{ip}]^T$ with respect to the covariance matrix $\mathbf{\Sigma}_i$ is calculated. This is the radial construction mechanism. In the second part, this scalar distance $\tilde{x}$ is transformed by the nonlinear activation function $h(\tilde{x})$. The activation function is usually chosen to possess local character and a maximum at $\tilde{x} = 0$. Typical choices for the activation function are the Gaussian function like

$$h(\tilde{x}) = e^{-\tilde{x}^2} \tag{B.3}$$

The distance $\tilde{x}_i$ is calculated with help of the center w_i and inverse covariance matrix $\mathbf{\Sigma}_i^{-1}$, which are the hidden layer parameters of the i-th RBF neuron

$$\tilde{x}_i = \|\mathsf{x} - \mathsf{w}_i\|_{\mathbf{\Sigma}_i} = \sqrt{(\mathsf{x} - \mathsf{w}_i)^T\, \mathbf{\Sigma}_i^{-1}\, (\mathsf{x} - \mathsf{w}_i)} \tag{B.4}$$

Thus, the basis functions $\Phi_i(\cdot)$ of a Gaussian RBF network are

$$\Phi_i\left(\mathsf{x}, \boldsymbol{\theta}_i^{(n)}\right) = \exp\left(-\|\mathsf{x} - \mathsf{w}_i\|_{\Sigma_i}^2\right) \tag{B.5}$$

where the hidden layer parameter vector $\boldsymbol{\theta}_i^{(n)}$ consists of the coordinates of the center (weights) vector w_i and the entries of the inverse covariance matrix Σ_i^{-1}. For simplicity, we will always consider RBF networks with the inverse covariance matrix equal to the identity matrix $\Sigma_i^{-1} = \mathsf{I}_i$. If several RBF neurons are used in parallel and are connected to an output neuron, the radial basis function network is obtained (see Fig. B.3). In basis function formulation, the RBF network can be written as

$$\hat{y} = \sum_{i=0}^{M} w_i \, \Phi_i\left(\|\mathsf{x} - \mathsf{w}_i\|_{\Sigma_i}\right) \qquad \text{with } \Phi_0 = 1 \tag{B.6}$$

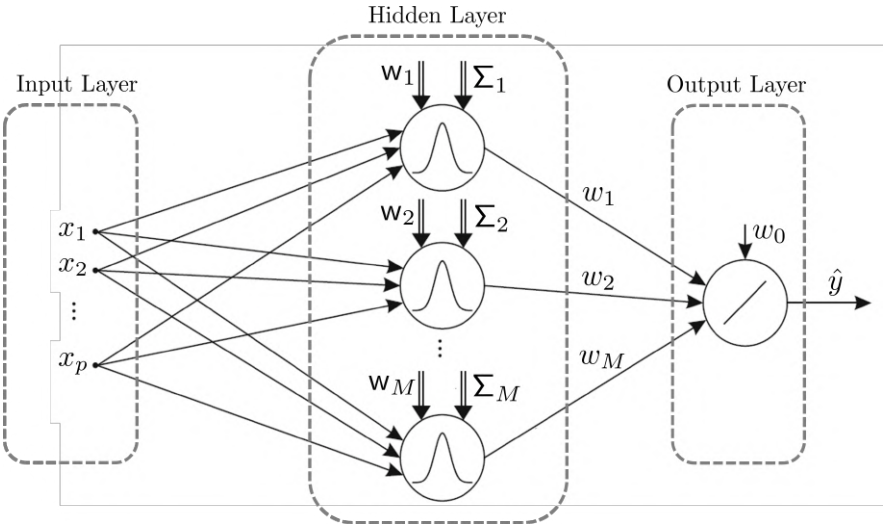

Figure B.3: Radial basis function (RBF) network

with the output layer weights w_i. The hidden layer parameters contain the center vector w_i , which represents the position of the i-th basis function, and the inverse covariance matrix Σ_i^{-1}, which represents the widths and rotations of the i-th basis function. The total number of parameters of an RBF network depends on the Σ_i^{-1}. However, as already mentioned, this matrix will be assumed to be the same as the identity matrix. So it does not generate any additional parameters. The number of output weights is $M + 1$ and the number of center coordinates is Mp. Then, the total number of parameters of an RBF network becomes $(Mp + M + 1)$, where M is the number of hidden layer neurons and p is the number of inputs. Like the MLP, an RBF network is a *universal approximator* (see Refs. [88], [102]). Contrary to the MLP, multiple hidden layers do not make much sense for an RBF network.

In conclusion, an RBF network consists of three types of parameters, *output layer weights* w_i, *centers* (or hidden layer weights) w_i and standard deviations (nonlinear elements of the matrix $\mathbf{\Sigma}_i^{-1}$). These parameters must be determined following an optimisation or training process in order to obtain an RBF neural network model capable of estimating an output $\hat{y}$ that is as accurate as possible. The training of neural networks is generally performed using the *backpropagation* algorithm. This method consists of calculating the gradients of the output of the neural network with respect to its parameters (hence, its weights). There are several versions of this algorithm, and among them are variants that also allow for the inclusion of time dependency for dynamic models (namely, backpropagation through time).

Matlab® also allows the use of a variant of the function defined in Eq. B.3 which is called the normalised radial basis function. This function is equivalent to the classic radial basis one, except that output vectors are normalised by dividing by the sum of the pre-normalised values (see Ref. [103]). In basis function formulation, the normalised radial basis function (NRBF) network can be written as

$$\hat{y} = \sum_{i=1}^{M} w_i \tilde{\Phi}_i \left(\mathsf{x}, \boldsymbol{\theta}_i^{(n)}\right) = \sum_{i=1}^{M} w_i \left(\frac{\Phi_i \left(\|\mathsf{x} - \mathsf{w}_i\|_{\mathbf{\Sigma}_i} \right)}{\sum_{j=1}^{M} \Phi_j \left(\|\mathsf{x} - \mathsf{w}_j\|_{\mathbf{\Sigma}_j} \right)} \right) \quad \text{with} \sum_{i=1}^{M} \tilde{\Phi}_i \left(\cdot\right) = 1 \tag{B.7}$$

It overcome some of the shortcomings of RBF networks, such as the lowering of interpolating capabilities in the case of too small standard deviations. These drawbacks are almost unavoidable for highly dimensional input spaces and cause unexpected non-monotonic behaviour. In addition, the extrapolation behaviour of standard RBF networks, which tends to zero, is undesirable for many applications (Ref. [56]). Under some conditions, normalised radial basis function networks are equivalent to singleton neuro-fuzzy models (Ref. [104]), which exploit a combination of fuzzy logic and neural networks and can be used in the identification of nonlinear systems (see Ref. [105]). Within the thesis, NRBF networks are used to construct reduced-order models to describe the nonlinear dynamics of vertical sloshing.

Appendix C

Neural-network-based ROM driven by bouncing ball data

In order to cover the initial lack of reliable data on vertical sloshing, it was decided to use the bouncing ball model identified in Sec. 2.1.1 to train a reduced-order model based on a neural network. What is shown in this appendix represents the first attempt to use neural networks to identify a nonlinear system. The neural network is trained by exploiting data that are output by low-fidelity bouncing ball model. This equivalent mechanical model is now considered as a black-box to be identified that provides sloshing forces as a function of the history of the assigned vertical displacement. Next, the training process of the neural network and the process of integrating the identified model into the simulation environment will be presented, in order to obtain an integrated model equivalent to the experiment performed by UPM.

C.1 Training phase

The training phase consists in the definition of a neural network able to emulate vertical slosh dynamics represented by the bouncing ball. In this framework, the use of a proper data set is critical, thus requiring an investigation among different types of inputs, after which, the choice fell on a pseudo-harmonic signal with amplitude and frequency slowly varying over time ($z_T = A(t)\sin(\int_0^t \Omega(\tau)\,\mathrm{d}\tau)$). This time law is such as to suitably cover the amplitude-frequency domain of interest as in Fig. 2.12(b), that, in turn, covers the range of accelerations provided by the performed simulations. The time derivative of z_T is used as input for the training. On the other hand, the output consists of the sloshing force that the ball returns when the tank is set on motion. The need to cover the more frequency-amplitude pairs leads to a *data set* represented by time series (velocity as input and sloshing force as output) obtained by only one 200 s long simulation with a sample frequency of 1 kHz. Among the wide variety

of NN architectures, a Feed Forward Neural Network (FFNN) has been considered, in which the information simply propagates from left to right in the network through a manifold of hidden layers. The proposed scheme of the identified neural network is shown in Fig. C.1. It

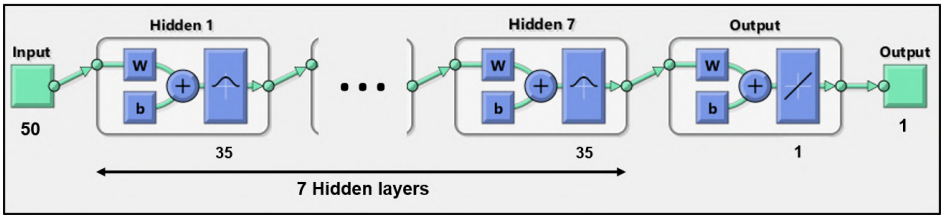

Figure C.1: Feed forward neural network flowchart.

was built in MATLAB using the *system identification toolbox* (see Ref. [106]) and consists of 7 hidden layers with 35 nodes/neurons each. The neural network receives as input a vector R_v of 50 regressors, corresponding to 50 time-delayed velocity values. In other words, one could say that 50 tapped delay lines are considered for the input. The model under consideration thus corresponds to a nonlinear finite impulse response model (NFIR), having a feedforward neural network as static approximator. The regressor vector R_v at time instant t is defined as follows

$$R_v(t) \;=\; [\dot{z}_T(t-1)\;\dot{z}_T(t-2)\cdots\dot{z}_T(t-m)]^{\mathrm{T}} \tag{C.1}$$

where m is the order of the model, that in this case is equal to 50.
This kind of NN is proved to work efficiently by using non-polynomial activation functions like radial basis functions (Refs. [107, 108]). As a consequence, these latter are employed as activation functions in all nodes of the considered hidden layers, whereas the output layer is made up with a simple linear function. The choice of the number of hidden nodes and layers is based on a qualitative sensitivity analysis that did not require the use of specific techniques. Specifically, given the same number of epochs considered in the network training, the selected NN is the one that proved to provide more fitting results when the ROM is introduced in the FSI environment that follows in Sec. C.2. The algorithm used for the training consists of *Bayesian Regularization*, implemented in Matlab® through the *trainbr* function (Ref. [89]), with a fixed number of epochs equal to 1000, in which the mean-squared error performance is observed to converge to a constant value, thus guaranteeing the convergence of the network. The total time spent for the NN training is 44 hours without employing any kind of parallel computing.

C.2 Performance assessment in a fluid-structure interaction problem

Subsequently, the equivalent mechanical model of bouncing ball was replaced by the identified neural-network-based ROM in the simulation framework depicted in Fig. 2.7. The same free response analysis as in the experiments and simulation in Sec. 2.1.1 has been performed. It is worth to highlight that this kind of response has nothing to do with the data used to train the network. Since the sloshing tank system is of the type *single input/single output*, the simulation takes only a few seconds to perform the fluid structure interaction analysis where the sloshing block is replaced with a neural network. Figs. C.2(a), C.2(b) and C.2(c) provide, respectively, the acceleration response, the instantaneous damping ratio as a function of the acceleration envelope, and the sloshing force comparing the experiments, the simulation with the bouncing ball and the one with the neural-network-based ROM. Specifically, Fig. C.2(a) shows that response in terms of acceleration obtained with the NN-based ROM for sloshing is close to the the response obtained with the bouncing ball model (used to train the network) and the experimental response as well. Fig C.2(b) demonstrates the capability of the NN-based ROM to provide a value of the instantaneous damping ratio matching the one of the bouncing ball model at each value of response amplitude even though better performances are noticeable at higher acceleration values. The results show that although the methodology was at its preliminary stage, the NN-based ROM was able to reproduce the behaviour of the model with the bouncing ball and, in turn, also of the experiments. Moreover, as shown in Fig. C.2(c), the neural network is also capable to reproduce the nonlinear behavior of the bouncing ball impact force.

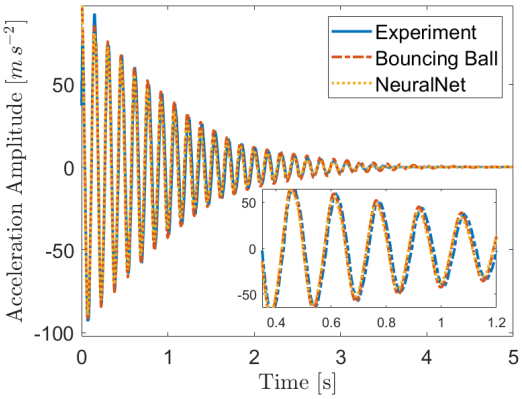

(a) Acceleration free response

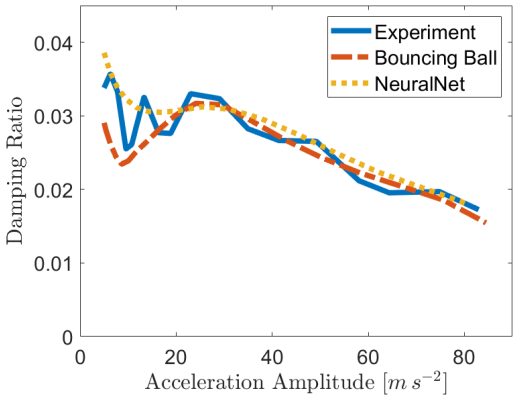

(b) Instantaneous damping ratio

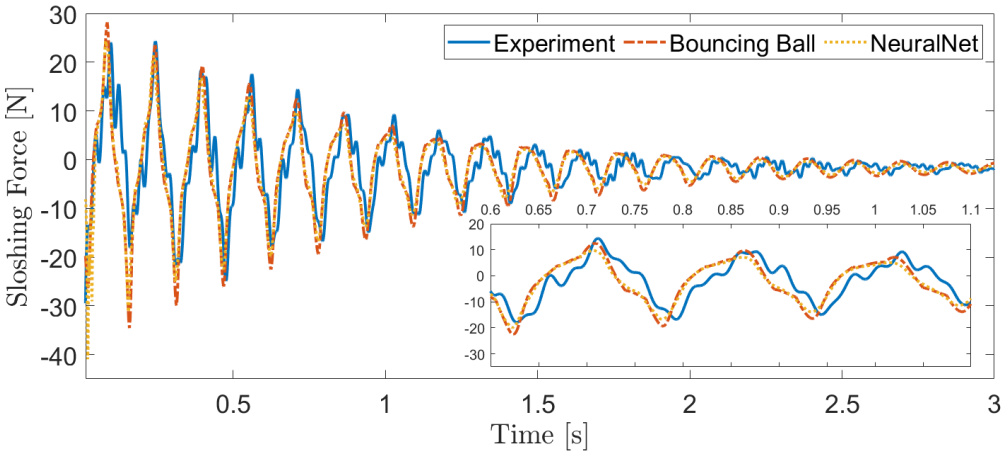

(c) Sloshing Forces

Figure C.2: Comparison between FFNN, Bouncing Ball and experiment.

Appendix D

Equivalent mechanical model for linearised sloshing

The appendix presents the analytical formulation of linear sloshing for potential flows. The linear sloshing dynamics of a quasi-rigid rectangular tank is characterised by the action of lateral forces and moments when the system is perturbed by lateral accelerations and rotations.

Starting from the basic assumptions generally adopted for such analytical models (mainly related to the fluid properties and tank geometry), the procedure here presented considers the formulation in Refs. [2, 15, 28] as a starting point with reference to a rectangular tank geometry. Indeed, the analytical models provide a Laplace domain expression of lateral force and moment about the center of mass of the liquid denoted as G arising by lateral motion Y and rotation $\varphi^{(G)}$ of a 2D tank as a function of the tank size and filling level. Considering a rectangular tank as in Fig. D.1, the force and moment provided by the liquid can be expressed as:

$$
\begin{aligned}
\tilde{F}_y &= s^2\Bigg\{ -\varrho a_t b_t h_f - \sum_{n=0}^{\infty} \frac{\omega_n^2}{g} \frac{8\varrho a_t^3 b_t}{\pi^4(2n-1)^4} \left[\frac{s^2}{s^2+\omega_n^2}\right] \Bigg\}\tilde{Y} + \\
&\quad s^2\Bigg\{ -\frac{\varrho a_t^3 b_t}{12} + \\
&\quad \sum_{n=0}^{\infty} \frac{\omega_n^2}{g} \frac{8\varrho a_t^3 b_t}{\pi^4(2n+1)^4} \left(\frac{h}{2} - \frac{2a_t \tanh[(2n+1)\frac{\pi h_f}{2a_t}]}{(2n+1)\pi} + \frac{g}{\omega_n^2}\right) \left[\frac{s^2}{s^2+\omega_n^2}\right] \Bigg\}\tilde{\varphi}^{(G)} \\
\tilde{M}_x^{(G)} &= s^2\Bigg\{ -\frac{\varrho a_t^3 b_t}{12} + \\
&\quad \sum_{n=0}^{\infty} \frac{\omega_n^2}{g} \frac{8\varrho a_t^3 b_t}{\pi^4(2n+1)^4} \left(\frac{h_f}{2} - \frac{2a_t \tanh[(2n+1)\frac{\pi h_f}{2a_t}]}{(2n+1)\pi} + \frac{g}{\omega_n^2}\right) \left[\frac{s^2}{s^2+\omega_n^2}\right] \Bigg\}\tilde{Y} + \\
&\quad s^2\Bigg\{ -\frac{\varrho g a_t^3 b_t}{12\omega^2} + \sum_{n=0}^{\infty} \frac{8\varrho a_t^3 b_t}{\pi^4(2n+1)^4} \left(\frac{h_f}{2} - \frac{a_t \tanh[(2n+1)\frac{\pi h_f}{2a_t}]}{(2n+1)\pi} + \frac{g}{\omega_n^2}\right) - \\
&\quad \sum_{n=0}^{\infty} \frac{8\varrho h_f^3 b_t}{\pi^4(2n+1)^4} \left(\frac{a_t}{2} - \frac{3h_f \tanh[(2n+1)\frac{\pi h_f}{2a_t}]}{(2n+1)\pi}\right) - \\
&\quad \sum_{n=0}^{\infty} \frac{\omega_n^2}{g} \frac{8\varrho a_t^3 b_t}{\pi^4(2n+1)^4} \left(\frac{h_f}{2} - \frac{2a_t \tanh[(2n+1)\frac{\pi h_f}{2a_t}]}{(2n+1)\pi} + \frac{g}{\omega_n^2}\right)^2 \left[\frac{s^2}{s^2+\omega_n^2}\right] \Bigg\}\tilde{\varphi}^{(G)}
\end{aligned}
\tag{D.1}
$$

where $\tilde{}$ represents the Laplace transformed variables, s is the Laplace variable, ω_n are the natural frequencies of the linear sloshing dynamics, ρ is the density of the liquid, g is the gravity acceleration, a_t and h_f represent, respectively, the tank-edge length in y-direction and the height of the liquid mass and b_t is tank-edge length in x-direction. Eq. D.1 can eventually be recast as

$$
\begin{Bmatrix} \tilde{F}_y \\ \tilde{M}_x^{(G)} \end{Bmatrix} = \mathsf{G}(s) \begin{Bmatrix} \tilde{Y} \\ \tilde{\varphi}^{(G)} \end{Bmatrix} \tag{D.2}
$$

where G is a linear sloshing operator derived here by analytical models, hereafter referred as generalized sloshing forces matrix. Considering a limited number of sloshing dynamics N_s and according with the Equivalent Mechanical Models (EMMs), the above equation can be rewritten as

$$
\mathsf{G}(s) = s^2\mathsf{A}_s + (s^2\mathsf{B}_s + \mathsf{C}_s)\left(s^2\mathsf{I} + s\mathsf{D}_s + \Omega_s^2\right)^{-1}(s^2\mathsf{B}_s + \mathsf{C}_s)^{\mathrm{T}} \tag{D.3}
$$

where:

$$\mathsf{A}_s = -\begin{bmatrix} \rho a b h_f & 0 \\ 0 & I_f \end{bmatrix} \qquad \mathsf{B}_s = -\begin{bmatrix} \sqrt{m_1} & \cdots & \sqrt{m_{N_s}} \\ \sqrt{m_1}h_1 & \cdots & \sqrt{m_{N_s}}h_{N_s} \end{bmatrix} \tag{D.4}$$

$$\mathsf{C}_s = g\begin{bmatrix} 0 & \cdots & 0 \\ \sqrt{m_1} & \cdots & \sqrt{m_{N_s}} \end{bmatrix} \qquad \Omega_s^2 = \begin{bmatrix} \omega_1^2 & & \\ & \ddots & \\ & & \omega_{N_s}^2 \end{bmatrix}$$

and D_s is a diagonal matrix, having as *i-th* diagonal element, a term associated with the modal damping of sloshing phenomenon. I_f is the effective sloshing fluid inertia moment (see Ref.[2]) and

$$m_n = 8\rho a_t b_t h_f \left(\frac{h_f}{a_t}\right)^2 \left[\frac{\tanh\left((2n-1)\pi\frac{h_f}{a_t}\right)}{\left((2n-1)\pi\frac{h_f}{a_t}\right)^3}\right] \tag{D.5}$$

$$h_n = h_f \left[\frac{1}{2} - \frac{\tanh\left((2n-1)\pi\frac{h_f}{2a_t}\right)}{\left((2n-1)\pi\frac{h_f}{2a_t}\right)}\right]$$

This allows us to express the Eq. D.2 as follows

$$\begin{aligned} \begin{Bmatrix} \tilde{F}_y \\ \tilde{M}_x^{(G)} \end{Bmatrix} &= s^2\mathsf{A}_s \begin{Bmatrix} \tilde{Y} \\ \tilde{\varphi}^{(G)} \end{Bmatrix} + \left(s^2\mathsf{B}_s + \mathsf{C}_s\right)\left(s^2\mathsf{I} + s\mathsf{D}_s + \Omega_s^2\right)^{-1}\left(s^2\mathsf{B}_s + \mathsf{C}_s\right)^{\mathsf{T}} \begin{Bmatrix} \tilde{Y} \\ \tilde{\varphi}^{(G)} \end{Bmatrix} \\ &= s^2\mathsf{A}_s \begin{Bmatrix} \tilde{Y} \\ \tilde{\varphi}^{(G)} \end{Bmatrix} + \left(s^2\mathsf{B}_s + \mathsf{C}_s\right)\tilde{\mathsf{r}} \end{aligned} \tag{D.6}$$

by defining as $\tilde{\mathsf{r}}$ the sloshing modal state space vector (in the Laplace domain) that collects the sloshing states, each of them representing a different dynamics of the liquid contained into the tank. For a wide range of applications in the framework of linear sloshing of simplified tanks, these Laplace-domain models allow to obtain sloshing forces and moments by having as time-domain counterpart a set of linear ordinary differential equations.

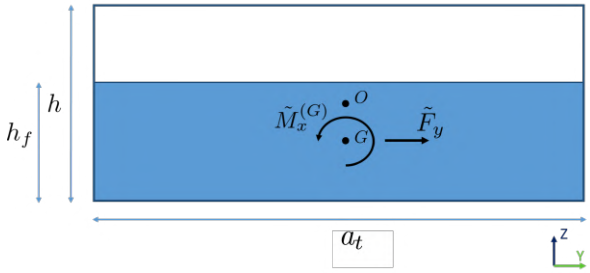

Figure D.1: Representation of 2D rectangular tank.

For finite elements applications, it is useful to express forces and moments with respect

to a fixed point, that can be associated to the geometric center of the tank (denoted as O in Fig. D.1). This needs to introduce a transformation matrix, indicated as S, that is given by

$$\mathsf{S} = \begin{bmatrix} 1 & -\frac{h-h_f}{2} \\ 0 & 1 \end{bmatrix} \tag{D.7}$$

and by which Eq. D.6 can be rewritten as follows:

$$\begin{Bmatrix} \tilde{F}_{y_o} \\ \tilde{M}_x^{(O)} \end{Bmatrix} = s^2\,\mathsf{S}^{\mathsf{T}}\mathsf{A}_s\mathsf{S}\begin{Bmatrix} \tilde{Y}_o \\ \tilde{\varphi}^{(O)} \end{Bmatrix} + \mathsf{S}^{\mathsf{T}}(s^2\mathsf{B}_s+\mathsf{C}_s)\,(s^2\mathsf{I}+s\mathsf{D}_s+\Omega_s^2)^{-1}\,(s^2\mathsf{B}_s+\mathsf{C}_s)^{\mathsf{T}}\mathsf{S}\begin{Bmatrix} \tilde{Y}_o \\ \tilde{\varphi}^{(O)} \end{Bmatrix} \tag{D.8}$$

where $\tilde{F}_{y_o}$ and $\tilde{M}_x^{(O)}$ are the sloshing force and moment about the geometric center of the tank resulting from its lateral motion Y_o and rotation $\varphi^{(O)}$. Note that the first addend of the second member of Eq. (3.33) represents the inertial force contribution of the liquid, in accordance with frozen sloshing modelling.

In order to integrate this contribution into the aircraft model, a transformation matrix indicated as T_t is applied to Eq. D.8 in order to express the state variables of the tanks with respect to the perturbation variables of the complete aircraft. T_t is defined for the *i-th* tank as

$$\mathsf{T}_t^{(i)} = \mathsf{R}^{(i)}(\alpha^{(i)})\mathsf{Z}_t^{(i)} \tag{D.9}$$

where $\mathsf{R}(\alpha)$ is the rotation matrix , related to the tank, that allows to pass from a "tank" frame of reference to the FE model frame of reference. The angle α measures the deviation between these two systems. $\mathsf{Z}_t^{(i)}$ instead, represents a $6 \times (6 + N_m)$ matrix whose columns are the modal shape vectors associated to the rigid and structural modes (assuming empty tank) and referred to the node where the *i-th* tank is located. It follows that the matrices in Eqs. 3.32 and 3.34 can be expressed as

$$\bar{\mathsf{A}}_s = \mathsf{T}_t^{\mathsf{T}}\mathsf{S}^{\mathsf{T}}\mathsf{A}_s\mathsf{S}\mathsf{T}_t \qquad \bar{\mathsf{B}}_s = \mathsf{T}_t^{\mathsf{T}}\mathsf{S}^{\mathsf{T}}\mathsf{B}_s \qquad \bar{\mathsf{C}}_s = \mathsf{T}_t^{\mathsf{T}}\mathsf{S}^{\mathsf{T}}\mathsf{C}_s$$

Appendix E

A viscous damping model for vertical sloshing

An alternative procedure for modeling vertical sloshing forces is proposed in this appendix. Specifically, a linearised viscous damping model is used whose coefficient is defined on the basis of the energy map obtained in the experimental characterisation presented in Chap. 1. For this purpose, a steady vertical harmonic motion $u\,(t)$ of the tank is considered to deduce the work (energy) dissipated by the sloshing forces approximated as $F_s \simeq c\,\dot{u}$. The law of motion $u\,(t)$ imposed on the tank is expressed as follows:

$$u\,(t) = u_0 \sin(\Omega t) \tag{E.1}$$

Thus, the energy dissipated by linearised vertical sloshing forces can be expressed as follows:

$$\begin{aligned} L_d \;&:=\; \oint_{cycle} F_s \,\mathrm{d}u \;=\; \int_t^{t+T} F_s\,\dot{u}(\tau)\,\mathrm{d}\tau \;=\; \int_t^{t+T} c\;\dot{u}^2(\tau)\,\mathrm{d}\tau \\ &=\; c\,u_0^2\,\Omega^2 \int_t^{t+T} \frac{1+\cos\left(2\,\Omega\,\tau\right)}{2}\mathrm{d}\tau \;=\; \pi\,c\,u_0^2\,\Omega \end{aligned} \tag{E.2}$$

The *viscous damping coefficient* c is derived using the energy map data obtained from the experimental characterisation of the dissipative behaviour of vertical sloshing. In particular, reference is made to the nondimensional dissipated energy Φ_d in the case with 50% filling level (see Sec. 1.4.2), which allows the dissipated work to be expressed as

$$L_d = m_l\,u_0^2\,\Omega^2\,\Phi_d\,(\bar{\omega},\bar{u}) \tag{E.3}$$

where $\bar{\omega} = \Omega/\sqrt{g/h}$ is the nondimensional frequency and $\bar{u} = u_0/h$ is the nondimensional amplitude. By imposing equivalence between Eqs. E.2 and E.3, the following expression for

viscous damping is obtained:

$$c = c(\bar{\omega}, \bar{u}) = \frac{m_l}{\pi} \Omega \, \Phi_d(\bar{\omega}, \bar{u}) = \frac{m_l}{\pi} \sqrt{\frac{g}{h}} \, \bar{\omega} \, \Phi_d(\bar{\omega}, \bar{u}) \tag{E.4}$$

Thus, the viscous damping coefficient distribution defined on the basis of the experimentally characterised energy information depends on both a dimensional term $m_l/\pi \sqrt{g/h}$, related to the height of the tank h and the mass of liquid stowed m_l, and a nondimensional term given by the product of the frequency $\bar{\omega}$ and the dissipated energy $\Phi_d(\bar{\omega}, \bar{u})$.
By selecting a tank with the same geometrical characteristics and the same liquid mass (of the case with 50% filling) as the one used in Chap. 1, the distribution of the viscous damping coefficient c in the nondimensional frequency and amplitude domain shown in Fig. E.1 is obtained.

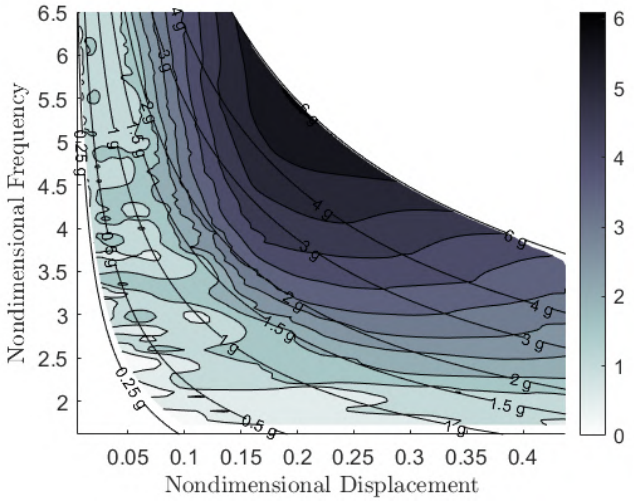

Figure E.1: Distribution of the viscous damping coefficient c based on the experimentally identified nondimensional dissipated energy

A representative scalar value of the viscous damping coefficient is required to be able to use this model to simulate vertical sloshing with the applications presented in the thesis. There is no clear-cut way to select this scalar value, however, it is possible to define different metrics based on the specific operational parameters of the application under consideration.

Sloshing beam with viscous sloshing force

In this section, the linear viscous damping model is used to describe vertical sloshing in the sloshing beam problem presented in Sec. 2.2.3, comparing the results obtained with those measured experimentally and those obtained by simulating the identified neural-network-based ROM. Since the tank mounted on the sloshing beam is the same as that used in

the energy characterisation in Chap. 1, the distribution of the viscous damping coefficient corresponds to that shown in Fig. E.1. With reference to it, the following three possible metrics are defined to select the unique value of the damping coefficient:

$$\begin{aligned} c_1 &= \frac{m_l}{\pi}\sqrt{\frac{g}{h}}\,\bar{\omega}_1\,\overline{\Phi_d\left(\bar{\omega}_1,\bar{u}\right)} = 3.40\ K_g/s \\ c_2 &= \frac{m_l}{\pi}\sqrt{\frac{g}{h}}\,\bar{\omega}_{max}\,\Phi_{d_{max}}\left(\bar{\omega}_{max},\bar{u}_{max}\right) = 4.69\ K_g/s \\ c_3 &= \frac{m_l}{\pi}\sqrt{\frac{g}{h}}\,\bar{\omega}_1\,\Phi_{d_{max}}\left(\bar{\omega}_{max},\bar{u}_{max}\right) = 4.40\ K_g/s \end{aligned} \tag{E.5}$$

where $\bar{\omega}_1 = 3.55$ is the nondimensional frequency corresponding to the first mode of the beam, $\overline{\Phi_d\left(\bar{\omega}_1,\bar{u}\right)}$ is the value of the nondimensional dissipated energy obtained at the frequency $\bar{\omega}_1$ by averaging over all nondimensional amplitudes $\bar{u}$ and $\bar{\omega}_{max} = 3.78$ is the nondimensional frequency corresponding the the maximum value of the nondimensional dissipated energy $\Phi_{d_{max}} = 1.65$. The coefficients given in Eqs. E.5 allow the generation of three linearised vertical sloshing models that can be used in free response simulations (see Sec. 2.2.3). The implementation is carried out similarly to what is shown in Sec. 2.2.4, where the Simulink block of vertical sloshing is replaced by a block capable of providing the generalised forces from the viscous damping forces acting at the point where the tank is located. Repeating the same free response analysis presented in Sec. 2.2.4 with the three viscous damping models yields the results shown respectively in Figs. E.2, E.3 and E.4. Figures E.3 and E.4 show how

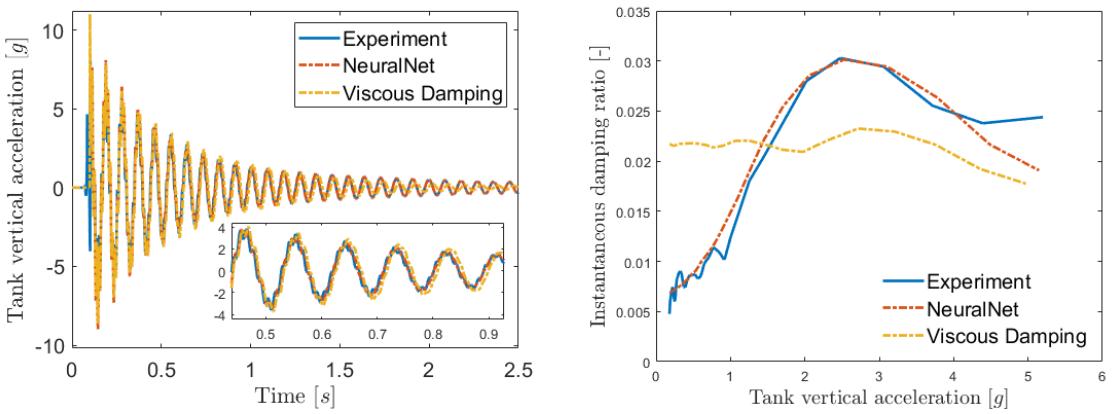

(a) Acceleration at tank location

(b) Instantaneous damping ratio (first mode)

Figure E.2: Comparison between sloshing beam experiment, network prediction and viscous damping model c_1 for tank vertical acceleration and instantaneous damping ratio of the first mode of vibration.

models with c_2 and c_3 cause an excessively damped response compared to the reference one,

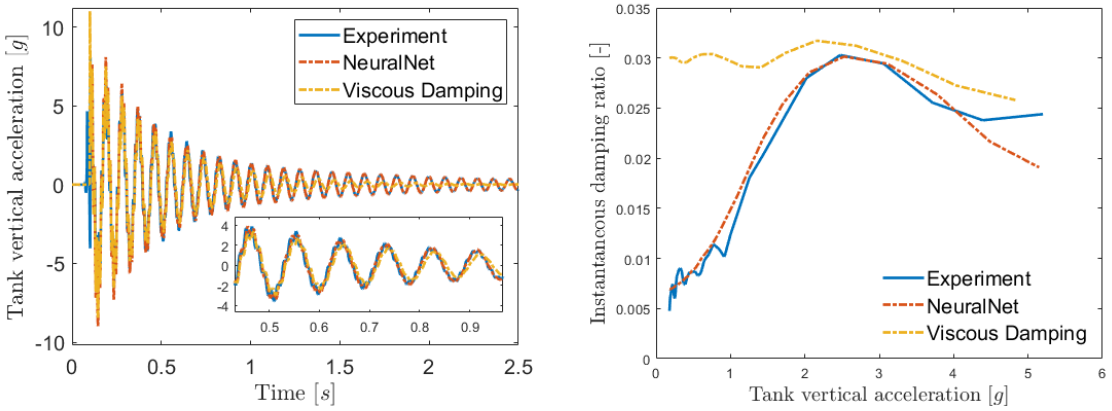

(a) Acceleration at tank location (b) Instantaneous damping ratio (first mode)

Figure E.3: Comparison between sloshing beam experiment, network prediction and viscous damping model c_2 for tank vertical acceleration and instantaneous damping ratio of the first mode of vibration.

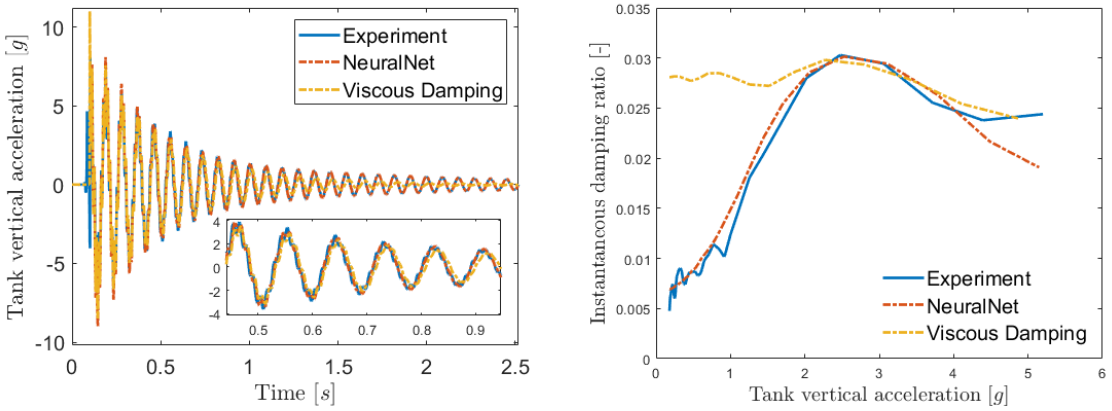

(a) Acceleration at tank location (b) Instantaneous damping ratio (first mode)

Figure E.4: Comparison between sloshing beam experiment, network prediction and viscous damping model c_3 for tank vertical acceleration and instantaneous damping ratio of the first mode of vibration.

providing an excessive damping contribution especially at low amplitudes. The model with the coefficient c_1 seems to be the one that on provides the most acceptable response, guaranteeing a damping that almost averages the experimental one over all response amplitudes (see Fig. E.2). The linearised vertical sloshing model based on viscous damping is highly dependent on the type of application being studied. The definition of the damping coefficient given in Eq. E.4 and the free response results just presented show how performance changes depending on how the nondimensional parameters $\bar{\omega}$ and Φ_d are chosen. Indeed, considering the problem with seismic excitation presented in Sec. 2.2.3, it is worth introducing a new viscous damping coefficient that is more representative of the specific operating conditions. The

random excitation imposed at the root of the beam promotes a variable amplitude vertical motion of the tank. In order to avoid overestimating the damping coefficient by averaging the nondimensional dissipated energy over all amplitudes as is done for c_1, it is preferable to estimate the average amplitude of vertical tank motion a priori and, based on this, directly evaluate Φ_d. Taking only the case with RMS: $0.4\,g$ into consideration, a new viscous model can be defined as follows

$$c_{rand} \;=\; \frac{m_l}{\pi}\sqrt{\frac{g}{h}}\;\bar{\omega}_1\,\Phi_d\left(\bar{\omega}_1,\bar{u}_m\right) \;=\; 3.686\;K_g/s \tag{E.6}$$

where $\bar{u} = 0.162$ is the average nondimensional vertical displacement measured in the sloshing beam seismic experiment and $\Phi_d\left(\bar{\omega}_1,\bar{u}_m\right) = 1.38$ is the nondimensional dissipated energy corresponding to it and to the nondimensional frequency of the first mode of the beam. Simulating this model in the Simulink® environment provides comparisons with the experiment and the neural network simulation in terms of tank acceleration over time (see Fig. E.5) and respective power spectral density (see Fig. E.6). From the comparisons

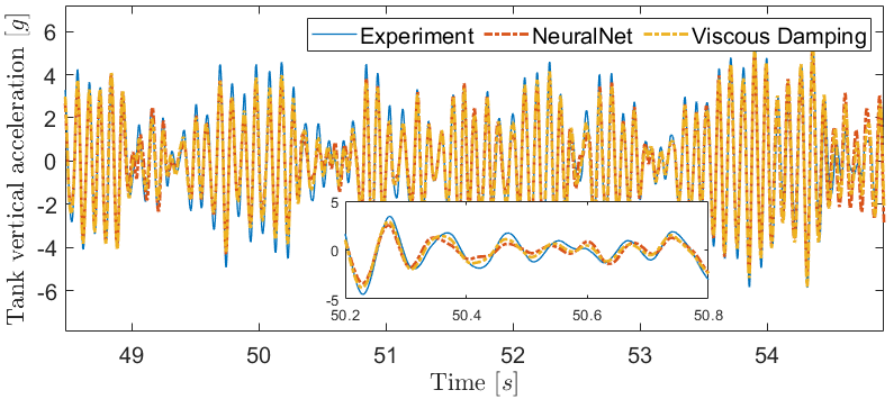

Figure E.5: Comparison between sloshing beam experiment, network prediction and viscous damping model c_{rand} for tank vertical acceleration in the case of RMS: $0.4\,g$.

shown in Figs. E.5 and E.6, it can be seen that the viscous model defined in Eq. E.6 is able to reproduce an accurate estimate of acceleration over time and provide a level of damping $\zeta_1 = 2.52$ which is almost equal to the experimental one ($\zeta_1 = 2.43$).

Although the performance obtained is quite good, it should be noted that it was possible to construct the c_{rand} viscous model on the basis of the experimental data measured in the specific problem to be analysed. Therefore, it is not possible to create a linearised vertical sloshing model that works for every application. Instead, one must be defined for each problem, selecting the most representative operating parameters (in terms of frequency, amplitude and dissipated energy).

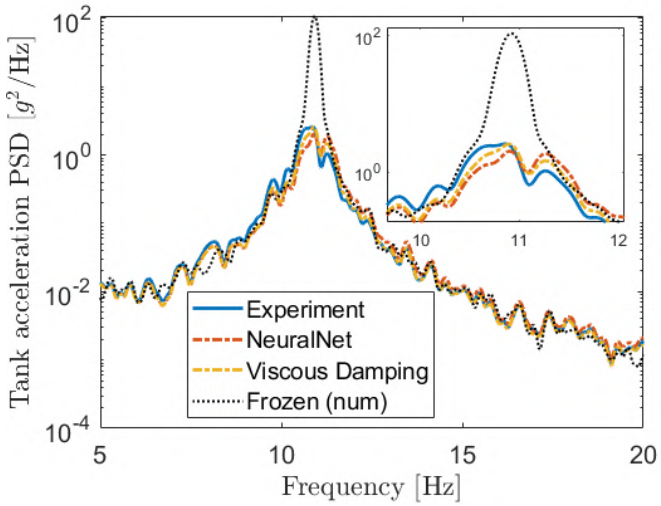

Figure E.6: Comparison between sloshing beam experiment, network prediction and viscous damping model c_{rand} for PSD of the tank vertical acceleration in the case of RMS: $0.4\,g$.

Wing prototype with viscous sloshing force

This section employs the linearised vertical sloshing model based on viscous damping in the aeroelastic model of the wing prototype introduced in Sec. 3.1. As already expressed in the previous section, depending on the application being studied, different criteria must be defined to obtain a representative damping coefficient. In the present case, it should first be noted that the wing contains eight tanks of different sizes inside it. Consequently, it is possible to define a viscous damping coefficient for each of the tanks due to the presence of a dimensional term that characterises each of them differently. The nondimensional amplitude and frequency domain distribution of the damping coefficient for the *i-th* tank is expressed as follows

$$c^{(i)} = c^{(i)}(\bar{\omega}, \bar{u}) = \frac{m_l^{(i)}}{\pi}\sqrt{\frac{g}{h^{(i)}}}\,\bar{\omega}\,\Phi_d(\bar{\omega}, \bar{u}) \tag{E.7}$$

Figure E.7 shows the distribution of the damping coefficient for two of the eight wing tanks, highlighting how the damping capacities change as the geometry and mass of liquid stowed vary. Tank number 3 (Fig. E.7(a)) has higher damping coefficient values than tank number 7 (Fig. E.7(b)), which is located almost at the wing tip.

The following three possible metrics are defined to select the unique value of the damping

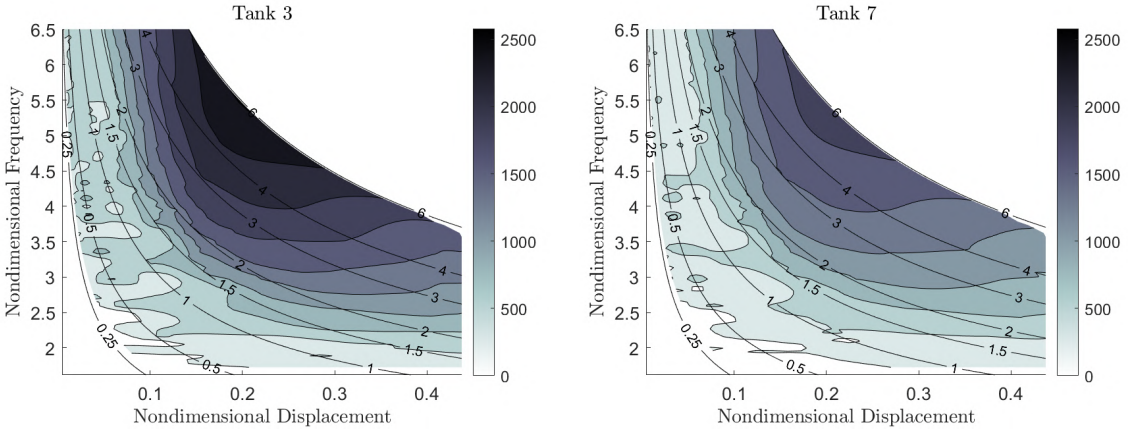

Figure E.7: Distribution of the viscous damping coefficient $c^{(i)}$ based on the experimentally identified nondimensional dissipated energy for two of the eight tanks of the wing prototype.

coefficient for each tank of the wing:

$$
\begin{aligned}
c_1^{(i)} &= \frac{m_l^{(i)}}{\pi}\sqrt{\frac{g}{h^{(i)}}}\;\bar{\omega}_{F_i}\;\overline{\Phi_d\left(\bar{\omega}_{F_i},\bar{u}\right)} \\
c_2^{(i)} &= \frac{m_l^{(i)}}{\pi}\sqrt{\frac{g}{h^{(i)}}}\;\bar{\omega}_{max}\,\Phi_{d_{max}}\left(\bar{\omega}_{max},\bar{u}_{max}\right) \\
c_3^{(i)} &= \frac{m_l^{(i)}}{\pi}\sqrt{\frac{g}{h^{(i)}}}\;\bar{\omega}_{F_i}\,\Phi_{d_{max}}\left(\bar{\omega}_{max},\bar{u}_{max}\right)
\end{aligned}
\tag{E.8}
$$

where $\bar{\omega}_{F_i}$ is the nondimensional frequency of the *i-th* tank corresponding to the flutter frequency $\omega_F = 1.95\,\omega_1$ (being ω_1 the first mode of vibration in the case of *dry* structure) $\overline{\Phi_d\left(\bar{\omega}_{F_i},\bar{u}\right)}$ is the value of the nondimensional dissipated energy obtained at the frequency $\bar{\omega}_{F_i}$ by averaging over all nondimensional amplitudes $\bar{u}$ for each tank. The two contributions $\bar{\omega}_{max}$ and $\Phi_{d_{max}}$ coincide with those introduced in the case of the sloshing beam problem.

In order to evaluate the performance of the linearised vertical sloshing model in the present case, we consider the same Simulink model presented in Sec. 3.1.1, in which, instead of the neural network block, another block is substituted to provide the generalised forces from the viscous ones (generated with the coefficients given in Eqs. E.8) acting in each of the wing tanks. Aeroelastic response analysis to vertical gust is then performed in the neighborhood of the flutter speed - in sub-critical condition - where the response is less damped and the sloshing plays a role of paramount relevance on damping aeroelastic vibrations. The same gust profile used in Sec. 3.1.2 is considered. The analysis is performed at a free stream velocity of $U_\infty = 315\,\mathrm{m/s}$, with a gust intensity of $w_{g_a} = 3\,\mathrm{m/s}$, for each one of the viscous damping

model defined in Eqs. E.8. Figure E.8 shows the gust responses in the case of $U_\infty = 315\,\mathrm{m/s}$

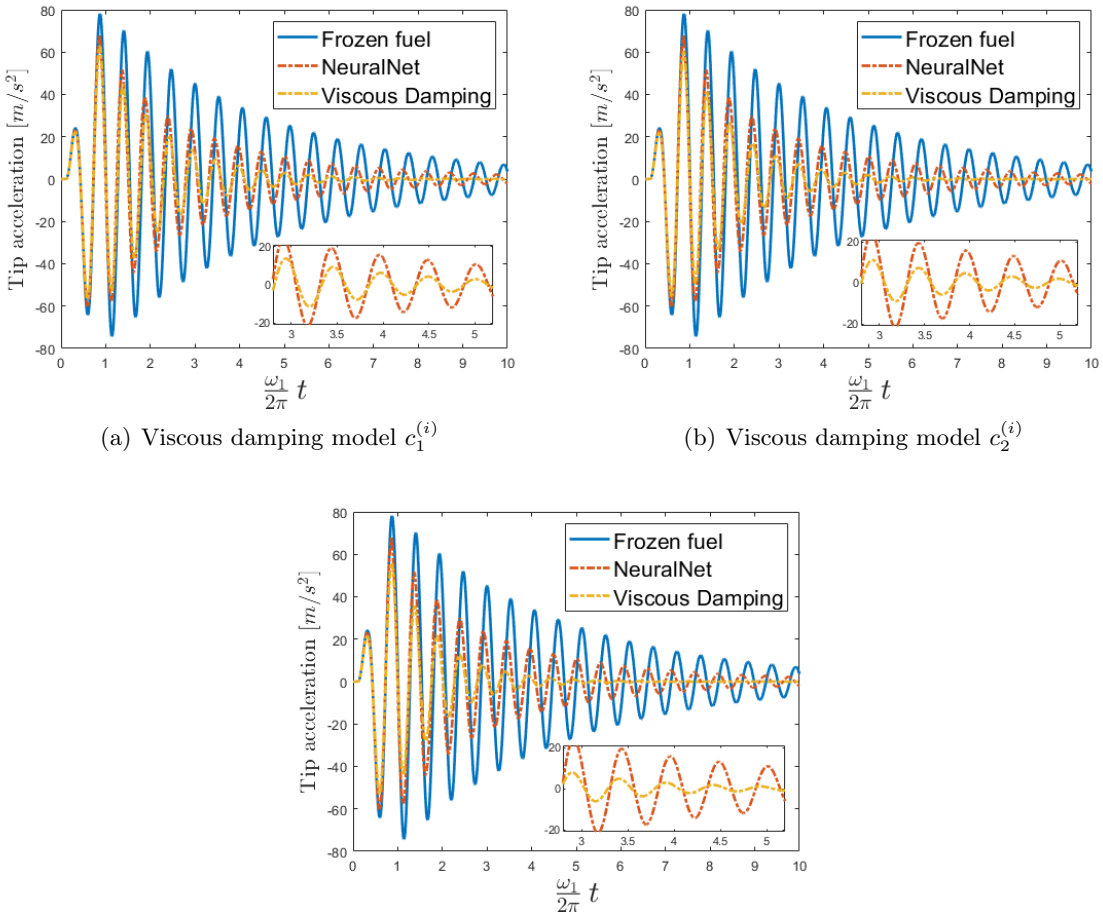

(a) Viscous damping model $c_1^{(i)}$

(b) Viscous damping model $c_2^{(i)}$

(c) Viscous damping model $c_3^{(i)}$

Figure E.8: Comparison of gust responses for $U_\infty = 315\,\mathrm{m/s}$

in terms of vertical wing tip acceleration, for each of the linearised models defined. Each of the models fails to provide a response over time comparable to that given by the nonlinear reduced-order model based on neural networks. The damping induced by viscous models is in fact significantly larger than expected. This is confirmed by Fig. E.9, which shows the trends of instantaneous damping ratio evaluated directly on the responses through logarithmic decay.

Leaving aside the more conservative models such as those with coefficients $c_2^{(i)}$ and $c_3^{(i)}$, it can be said that the model with coefficient $c_1^{(i)}$ provides an inaccurate estimate of the damping due to the fact that, in the process of averaging the dissipated energy, those values corresponding to amplitudes not reached during the gust response are also taken into account. This causes the viscous coefficient calculated for each tank to be overestimated. As a result, the linearised model of vertical sloshing again shows its limitations, since it must be redefined

each time the type of problem, and therefore the response to the gust changes. This is precisely because by changing the type of response, the amplitudes reached by the tank change and therefore the operation of averaging the nondimensional dissipated energy would require a redefinition according to the amplitude ranges reached in that specific problem.

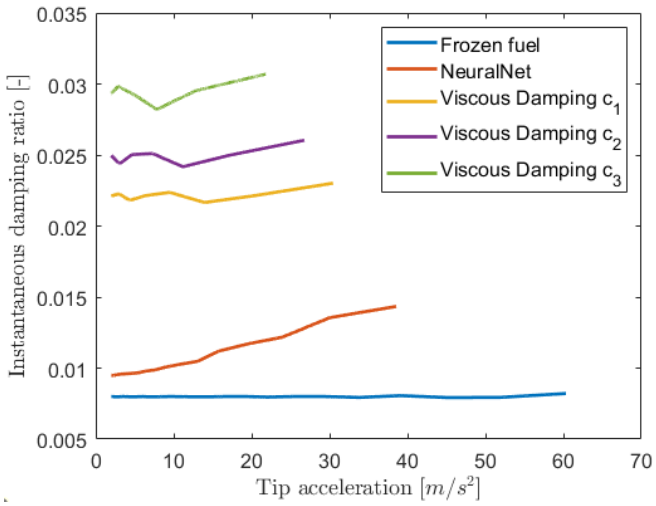

Figure E.9: Comparison of instantaneous damping ratio associated to the gust responses with $U_\infty = 315\,\mathrm{m/s}$ for each of the defined viscous damping models, for the neural network model and for the frozen fuel case.